Search for flavor-changing neutral current top quark decays $t \to Hq$, with $H \to b\bar{b}$, in pp collisions at $\sqrt{s} = 8$ TeV with the ATLAS detector

Ph.D. dissertation

Shota Tsiskaridze
Instituto de Física de Altas Energias
Universidad Autónoma de Barcelona
Departamento de Física
Facultad de Ciencias
Edificio Cn E-08193 Bellaterra (Barcelona)

Thesis director
Aurelio Juste Rozas
ICREA / Instituto de Física de Altas Energias
Universidad Autónoma de Barcelona
Edificio Cn E-08193 Bellaterra (Barcelona)

Thesis director
Sebastian Grinstein
ICREA / Instituto de Física de Altas Energias
Universidad Autónoma de Barcelona
Edificio Cn E-08193 Bellaterra (Barcelona)

Thesis tutor
Maria Pilar Casado Lechuga
Universidad Autónoma de Barcelona
Instituto de Física de Altas Energias
Edificio Cn E-08193 Bellaterra (Barcelona)

Contents

Introduction

Following the observation of a Standard Model-like Higgs boson with a mass of $\sim$ 125 GeV by the ATLAS and CMS collaborations [1, 2], a comprehensive program of measurements of its properties is underway looking for deviations from the Standard Model (SM) predictions. An interesting possibility is the presence of flavor-changing neutral current (FCNC) interactions between the Higgs boson, the top quark and a u or c quark, tqH $(q = u, c)$.

Since the Higgs boson is lighter than the top quark, such interactions would manifest themselves as FCNC top quark decays, $t \to Hq$. In the SM the $t \to Hq$ branching ratios, BR$(t \to Hq)$, are extremely small: BR$(t \to Hu) \sim 10^{-17}$ and BR$(t \to Hc) \sim 10^{-15}$. However, many beyond-SM scenarios predict enhancements for FCNC top decays orders of magnitude above the predicted rate in the SM. Examples include models with a quark-singlet, two Higgs doublet models (2HDM), the minimal supersymmetric SM (MSSM) or supersymmetry with R-parity violation. In these models typical branching ratios can be as high as BR$(t \to Hq) \sim 10^{-5}$. An even larger branching ratio, as high as BR$(t \to Hc) \sim 10^{-3}$, can be reached in 2HDMs without explicit flavor conservation. While other FCNC top couplings, $tq\gamma$, tqZ, tqg, are also enhanced relative to the SM prediction in those beyond-SM scenarios, the largest enhancement is typically for the tqH coupling, and in particular the tcH coupling.

Several searches for $t \to Hq$ decays have been performed by the ATLAS and CMS collaborations taking advantage of the large samples of $t\bar{t}$ events collected during Run 1 of the LHC, and assuming SM decays for the Higgs boson. The most sensitive single searches have been performed in the $H \to \gamma\gamma$ decay mode [3–5] which, despite the tiny branching ratio of BR$(H \to \gamma\gamma) \simeq 0.2\%$, is characterized by very small background and excellent diphoton mass resolution. Other searches performed by the ATLAS and CMS collaborations are focused on multilepton (three or four leptons) final states [4, 6, 7], resulting from the process $t\bar{t} \to WbHq$ with $H \to WW^*, ZZ^*, \tau\tau$. Multilepton searches are able to exploit a larger branching ratio for the Higgs boson decay, and are also characterized by relatively small backgrounds, but in general do not have any mass resolution (except for the $H \to ZZ^* \to 4\ell$ decay mode, which is negligible small), so any excess would be hard to interpret as originating from $t \to Hq$ decays.

The results presented in this dissertation fill a gap in the program of searches for $t \to Hq$ decays during Run 1 of the LHC by considering the dominant decay mode $H \to b\bar{b}$, which has BR$(H \to b\bar{b}) \simeq 58\%$. The search is focused on the $t\bar{t} \to WbHq$ $(q = u, c)$ process, with $W \to \ell\nu$ $(\ell = e, \mu, \tau)$ and $H \to b\bar{b}$, resulting in a lepton-plus-jets final state with high b-jet multiplicity, which can be effectively exploited to suppress the overwhelming $t\bar{t}$ background. The lepton-plus-jets final state also allows the kinematic reconstruction of the final state and in particular the dijet invariant

mass spectrum from the $H \to b\bar{b}$ decay, providing additional handles that would help in detecting $t\bar{t} \to WbHq$ events. Most of this dissertation is devoted to the discussion of this particular search, for which background estimation techniques, systematic uncertainties and statistical treatment closely follow those used in ATLAS searches using the same final-state signature [8, 9]. The results obtained have been published by the ATLAS collaboration in reference [10]. A combination of the three ATLAS searches for $t\bar{t} \to WbHq$, probing the $H \to b\bar{b}$, $H \to WW^*, \tau\tau$, and $H \to \gamma\gamma$ decay modes, has been performed and bounds have been set on BR($t \to Hc$) and BR($t \to Hu$), as well as on the corresponding non-flavor-diagonal Yukawa couplings.

The dissertation is organized as follows. Chapter 1 introduces the theoretical background relevant for this dissertation. This includes not only a brief introduction to the SM, as well as some of its possible extensions, but also a detailed discussion of the theoretical status and phenomenology of flavor-changing neutral currents interactions. In addition, the production and decay of top quark at hadron colliders are discussed. In Chapter 2 a description of the ATLAS detector and its different components is provided. The techniques used to obtain simulated event samples are described in Chapter 3. Starting from the computation of the matrix element of a particular physics process, Monte Carlo tools are combined to obtain the complete picture of how the event of interest evolves, including as a last step the simulation of the particles' interactions with the detector material. The reconstruction and performance of the physics objects needed in the analysis are described in Chapter 4. Chapter 5 describes the event selection criteria, the data samples and the modeling of the signal and background samples used in this analysis. In Chapter 6 the analysis strategy is discussed. This includes the event categorization used in this analysis, as well as the detailed description of the main variable used to discriminate between the signal and background. In Chapter 7, the different sources of systematic uncertainties are explained. An overview of the statistical methods used to interpret the analysis results is given in Chapter 8, including the profile likelihood method, which allows to incorporate the uncertainties in the limit calculation. Chapter 9 presents the results obtained by the three individual ATLAS searches as well as their combination. In Chapter 10 the prospects for future improvements in sensitivity for this analysis are discussed. Finally, the summary of this dissertation is provided in Chapter 11.

The analysis presented in this dissertation relies heavily on b-tagging, which in turn depends on the impact parameter resolution of the pixel detector. At the end of 2012 ATLAS installed a new innermost pixel layer (IBL) that improves the b-tagging performance. The author played a key role in the qualification of the 3D pixel technology used in the construction of the IBL [11].

Chapter 1

Theoretical Framework

The fundamental constituents of matter and their interactions (except for gravity) are described by the Standard Model (SM) of particle physics. Since its development in the 1960's, the validity of the SM has been tested by precision measurements at various experiments and confirmed by the observation of all the particles it predicts.

This chapter briefly reviews the theoretical aspects most relevant to this dissertation. In Sec. 1.1 the fundamental particles and interactions described by the SM are introduced. The experimental success and shortcomings of the SM are also presented in this section. In Sec. 1.2 some possible extensions of the SM, relevant for this dissertation, are introduced. The phenomenology of FCNC interactions is discussed in detail in Sec. 1.3, while Sec. 1.4 reviews the theoretical status of the top-quark FCNC sector. In Sec. 1.5 the production and decay of the top quarks at LHC are presented.

1.1 The Standard Model

The SM is a renormalizable quantum field theory [12–14] that describes the elementary particles, *fermions*, and their fundamental interactions through the exchange of force mediators, *bosons*.

Fermions have spin $\frac{1}{2}$ (in $\hbar$ units), and are classified into quarks and leptons. There are six species of quarks and leptons, which are divided into three families or generations. Generations of quarks and leptons are copies with the same quantum numbers except for their masses, having the 1^{st} generation the lighter particles and the 3^{rd} the heavier particles. The fermion generations, their masses and electric charges are summarized in Table 1.1.

In the SM neutrinos are assumed to be massless. However, in 1998 the K2K experiment at Super-Kamiokande observed neutrino oscillations [15] providing evidence that also neutrinos have a non-zero mass.

Additionally, for each quark and lepton exists an antiparticle, thus doubling the number of fermions. The antiparticles are characterized by having the same masses as their corresponding particles, but opposite quantum numbers.

The bosons of the SM are responsible for three of four interactions in Nature. Gravity is not (yet) included in the model, but its action on elementary particles is many order of magnitudes smaller than the others' and is, therefore, considered negligible at the fundamental components scale. Table 1.2 summarizes the bosons of the SM with the information about the interaction they mediate, their mass, their electric charge and the coupling strength of the force they are mediating at an energy

Generation	Name	Symbol	Mass	Electric charge
		Leptons		
1st	Electron neutrino	ν_e	< 2 eV	0
	Electron	e	0.51 MeV	-1
2nd	Muon neutrino	ν_μ	< 2 eV	0
	Muon	μ	105.66 MeV	-1
3rd	Tau neutrino	ν_τ	< 2 eV	0
	Tau	τ	1.77 GeV	-1
		Quarks		
1st	Up	u	2.3 MeV	$+2/3$
	Down	d	4.8 MeV	$-1/3$
2nd	Charm	c	1.275 GeV	$+2/3$
	Strange	s	95 MeV	$-1/3$
3rd	Top	t	173.5 GeV	$+2/3$
	Bottom	b	4.65 GeV	$-1/3$

Table 1.1: Table of lepton and quark families with their mass and electric charge according to the Particle Data Group [16].

corresponding to the Z boson mass. The mediators of the electromagnetic, weak and strong forces are vector bosons (usually referred to as *gauge bosons*) with spin 1, while the SM Higgs boson is a scalar particle with no spin.

Interaction	Mediator	Symbol	Mass	Electric charge	Coupling strength at $m(Z)$=91.2 GeV
Electromagnetic	Photon	γ	0	0	$1/127.934 \sim 10^{-2}$
Weak	W boson	$W^\pm$	91.19 GeV	± 1	$\sim 1/29.5 \sim 0.034$
	Z boson	Z	80.39 GeV	0	
Strong	8 gluons	g	0	0	0.1185
Mass	Higgs	H	125.4 GeV	0	

Table 1.2: Table of the bosons in the SM with their mass and electric charge.

The photon is massless, mediates the electromagnetic interaction and is its own antiparticle. The $W^\pm$ and the Z bosons mediate the weak forces. The W^+ boson has an electric charge of $+1$ and is an antiparticle of W^-. The Z boson has zero electric charge and is its own antiparticle. The weak vector bosons can interact among

themselves and the $W^{\pm}$ bosons can interact also with the photon. The gluons, g, are the massless mediators of the strong force. They exchange the *color charge* between the quarks and thus are "bicolored", carrying one positive unit of color and one negative unit. Being themselves color charged, trilinear and quartic gluon self couplings are also allowed.

Finally, the Higgs boson is the mediator of the Higgs field that gives masses to the vector bosons and fermions through the Higgs mechanism. It was the last missing particle of the SM and was discovered in 2012 by the ATLAS and CMS collaborations at the Large Hadron Collider (LHC) at CERN [1, 2].

1.1.1 Building the Standard Model

The theory describing the particle interactions is structured according to a gauge group, invariant under the following symmetry transformations:

$$SU\left(3\right)_C \times SU\left(2\right)_L \times U\left(1\right)_Y, \tag{1.1}$$

where $SU\left(3\right)_C$ is the unbroken *color* (C) symmetry, which represents the strong interactions described by the *Quantum Chromodynamics* (QCD) theory; and $SU\left(2\right)_L \times U\left(1\right)_Y$ is the symmetry with respect to the *isospin* (L) and *hypercharge* (Y) gauge groups, which accounts for the unified *electroweak* interactions described by the *Electroweak* (EW) theory.

The quantum number C is the *color charge*, carried only by quarks, anti-quarks and gluons. The quantum number I, the weak *isospin*, differentiates between left-handed ($I = \frac{1}{2}$) and right-handed ($I = 0$) fermions, with the latter not undergoing weak interactions. The quantum number Y, the *hypercharge*, is defined as $Y = 2(Q - I_3)$, where Q is the electric charge and I_3 the third component of the isospin which, in case of left-handed fermions, is $I_3 = +\frac{1}{2}$ for up-type quarks and neutrinos, and $I_3 = -\frac{1}{2}$ for down-type quarks and negatively-charged leptons (and *vice-versa* for the antiparticles).

The SM is then the combination of two theories, QCD and EW. The SM Lagrangian can be written as:

$$\begin{aligned}\mathcal{L}_{SM} = \mathcal{L}^{QCD}_{SU(3)} + \mathcal{L}^{EW}_{SU(2)\times U(1)} = \left[\mathcal{L}^{Gauge}_{SU(3)} + \mathcal{L}^{Matter}_{SU(3)}\right]^{QCD} + \\ + \left[\mathcal{L}^{Gauge}_{SU(2)\times U(1)} + \mathcal{L}^{Matter}_{SU(2)\times U(1)} + \mathcal{L}^{Higgs}_{SU(2)\times U(1)} + \mathcal{L}^{Yukawa}_{SU(2)\times U(1)}\right]^{EW}.\end{aligned} \tag{1.2}$$

The $\mathcal{L}^{Gauge}$ terms describe the dynamics of the gauge fields: the gluons in QCD, and the $W^{\pm}$, Z and γ bosons in the EW theories. The $\mathcal{L}^{Matter}$ terms describe the interaction of the particles with the gauge fields. The $\mathcal{L}^{Higgs}$ and $\mathcal{L}^{Yukawa}$ terms are arise from the Spontaneous Symmetry Breaking (SSB) of the $SU\left(2\right)_L \times U\left(1\right)_Y$ gauge theory via the Higgs mechanism. They are responsible for the interaction of the Higgs field with the other particles and force carriers, and for generating their masses. Each of the SM Lagrangian terms is described in detail below.

1.1.2 Quantum Chromodynamics

Quantum Chromodynamics (QCD) is the theory of strong interactions, a fundamental force describing the interactions between quarks and gluons. Quarks come in three colors, "red" (r), "blue" (b), and "green" (g). Typically, the quark color changes at a

quark-gluon vertex, and the difference is carried off by the gluon. Hence, each gluon carries one unit of color and one unit of anti-color. It would appear, then, that there should be nine species of gluons - $r\bar{r}$, $r\bar{b}$, $r\bar{g}$, $b\bar{r}$, $b\bar{b}$, $b\bar{g}$, $g\bar{r}$, $g\bar{b}$, $g\bar{g}$. However, gluons transform in the adjoint representation of $SU(3)_C$, which is 8-dimensional, therefore only 8 linear independent gluon fields, G^a_μ ($a \in \{1, 2, ..8\}$), may be created from those nine species of gluons.

The QCD lagrangian, involving only quarks and gluons, is then made of two terms:

$$\begin{cases} \mathcal{L}^{QCD}_{SU(3)_C} = \mathcal{L}^{Gauge}_{SU(3)_C} + \mathcal{L}^{Matter}_{SU(3)_C} = -\frac{1}{4} G^a_{\mu\nu} G^{a\mu\nu} + \bar{q}(i\gamma^\mu D_\mu)q \\ D_\mu = \partial_\mu + i g_s T_a G^a_\mu \\ G^a_{\mu\nu} = \partial_\mu G^a_\nu - \partial_\nu G^a_\mu - g_s f_{abc} G^b_\mu G^c_\nu \end{cases} . \tag{1.3}$$

where γ^μ are the Dirac γ-matrices and q is a vector of three components corresponding to the different colors of a given quark type. D_μ is a covariant derivative promoting the global gauge symmetry to a local one. T_a and f_{abc} ($a, b, c \in \{1, 2, ..8\}$) are, respectively, the generators and the structure constants of the $SU(3)_C$ group. G^a_μ are the gluon fields, that define the gluon field strength tensor $G^a_{\mu\nu}$, where the third term of the tensor describes the gluon self-interaction and is responsible for the non-Abelian nature of QCD. g_s is the strong coupling constant that usually referred to as $\alpha_s = g_s^2/4\pi$ in the literature.

The presence of the gluon self-interaction induces very particular features in the dependence of the strong coupling constant with the energy scale of the interaction. According to the renormalization group equation of quantum field theory, a beta function $\beta(\alpha_s)$ encodes the running of the strong coupling constant, α_s, as a function of the renormalization energy scale μ_R^2. The one-loop beta function in QCD, with the number of flavors n_f taking part in the interaction, is defined by the relation:

$$\beta(\alpha_s) = -\frac{\beta_0}{(4\pi)^2}\alpha_s^3, \quad \text{where} \quad \beta_0 = \frac{33 - 2 \cdot n_f}{3}, \tag{1.4}$$

and in the leading-order approximation, for the chosen scale Λ^2, the coupling constant can be expressed as:

$$\alpha_s(\mu_R^2, \Lambda^2) = \frac{4\pi}{\beta_0 \cdot \log\left(\frac{\mu_R^2}{\Lambda^2}\right)}. \tag{1.5}$$

The choice of scale to use as the renormalization energy scale μ_R^2 is not defined by first principles in QCD. Most commonly a "typical" scale of the process is used.

If $n_f \leq 16$, the ensuing beta function dictates that the coupling α_s decreases with increasing energy scale, a phenomenon known as *asymptotic freedom*, which means that in the high energy limit the quarks can propagate as if they were free. On the other hand, α_s becomes large at low energies, reaching the point of diverging. This property is known as *confinement*: quarks and gluons can not appear as free particles.

The Feynman diagram of the gluon-quark QCD vertex, with the coupling strength of the vertex, is shown in Fig. 1.1. The color of the depicted states is also given in a simplified way.

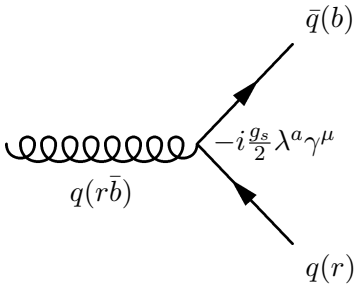

Figure 1.1: Gluon-quarks QCD vertex with color exchange.

1.1.3 Electroweak Theory

The electroweak theory describes the weak and the electromagnetic interactions. The electroweak eigenstate, ψ, is composed of left-handed doublet and right-handed singlets:

$$\psi = \begin{pmatrix} \psi_L \\ \psi_R \end{pmatrix}. \tag{1.6}$$

In the case of leptons, left-handed doublet and right-handed singlets can be written as:

$$\psi_L \equiv L_L \in \begin{pmatrix} \nu \\ l \end{pmatrix}_L = \left\{ \begin{pmatrix} \nu_e \\ e \end{pmatrix}_L, \begin{pmatrix} \nu_\mu \\ \mu \end{pmatrix}_L, \begin{pmatrix} \nu_\tau \\ \tau \end{pmatrix}_L \right\}, \quad \psi_R \equiv l_R \in \{e_R, \mu_R, \tau_R\}, \tag{1.7}$$

while in the case of quarks:

$$\psi_L \equiv Q_L = \begin{pmatrix} \mathcal{U} \\ \mathcal{D} \end{pmatrix}_L, \quad \psi_R \in \{\mathcal{U}_\mathcal{R}, \mathcal{D}_\mathcal{R}\}, \tag{1.8}$$

where the $\mathcal{U}$ represents all up-type quarks and $\mathcal{D}$ represents all down-type quarks and the above notations are shorthand for:

$$\begin{pmatrix} \mathcal{U} \\ \mathcal{D} \end{pmatrix}_L \in \left\{ \begin{pmatrix} u \\ d \end{pmatrix}_L, \begin{pmatrix} c \\ s \end{pmatrix}_L, \begin{pmatrix} t \\ b \end{pmatrix}_L \right\}, \quad \mathcal{U}_R \in \{u_R, c_R, t_R\}, \quad \mathcal{D}_R \in \{d_R, s_R, b_R\}, \tag{1.9}$$

The symmetry group of the weak interaction is the $SU(2)_L$ group. The generators of the group are the weak isospin operators, $\hat{I} = \frac{\sigma_i}{2}$ ($i \in \{1, 2, 3\}$), where σ_i are the three Pauli matrices:

$$\sigma_1 = \begin{pmatrix} 0 & 1 \\ 1 & 0 \end{pmatrix}, \quad \sigma_2 = \begin{pmatrix} 0 & -i \\ i & 0 \end{pmatrix} \quad \text{and} \quad \sigma_3 = \begin{pmatrix} 1 & 0 \\ 0 & -1 \end{pmatrix}. \tag{1.10}$$

Introducing the Weyl representation of the γ matrices:

$$\gamma^0 = \begin{pmatrix} 0 & 1 \\ 1 & 0 \end{pmatrix}, \quad \gamma^i = \begin{pmatrix} 0 & \sigma_i \\ \sigma_i & 0 \end{pmatrix} \quad \text{and} \quad \gamma^5 = \begin{pmatrix} -1 & 0 \\ 0 & 1 \end{pmatrix}, \tag{1.11}$$

the left- and right-handed components of the fermion fields can be expressed as:

$$\begin{aligned} \psi_L &= \frac{1}{2}\left(1-\gamma^5\right)\psi, \\ \psi_R &= \frac{1}{2}\left(1+\gamma^5\right)\psi. \end{aligned} \tag{1.12}$$

They transform differently under the operators of the weak symmetry group. The left-handed fermions transform as doublets, whereas right-handed fermions transform as singlets.

The "free matter" electroweak Lagrangian of the SM is then made of two terms [1]:

$$\mathcal{L}^{EW}_{SU(2)\times U(1)} = \mathcal{L}^{Gauge}_{SU(2)\times U(1)} + \mathcal{L}^{Matter}_{SU(2)\times U(1)}, \tag{1.13}$$

where:

$$\begin{cases} \mathcal{L}^{Gauge}_{SU(2)\times U(1)} = -\frac{1}{4}W^k_{\mu\nu}W^{\mu\nu k} - \frac{1}{4}B_{\mu\nu}B^{\mu\nu} \\ \qquad W^k_{\mu\nu} = \partial_\mu W^k_\nu - \partial_\nu W^k_\mu - g\epsilon^{ijk}W^i_\mu W^j_\nu \\ \qquad B_{\mu\nu} = \partial_\mu B_\nu - \partial_\nu B_\mu \end{cases}, \tag{1.14}$$

$$\begin{cases} \mathcal{L}^{Matter}_{SU(2)\times U(1)} = \bar{\psi_L} i\gamma_\mu D^\mu_L \psi_L + \bar{\psi_R} i\gamma_\mu D^\mu_R \psi_R \\ \qquad D^\mu_L = \partial^\mu + ig\frac{\overrightarrow{\sigma}\cdot\overrightarrow{W}^\mu}{2} + i\frac{g'}{2}Y_L B^\mu \\ \qquad D^\mu_R = \partial^\mu + i\frac{g'}{2}Y_R B^\mu \end{cases}. \tag{1.15}$$

The first Lagrangian term $\left(\mathcal{L}^{Gauge}_{SU(2)\times U(1)}\right)$ describes the vector bosons dynamics with self-couplings, including trilinear and quadrilinear terms. The second term $\left(\mathcal{L}^{Matter}_{SU(2)\times U(1)}\right)$ describes the transformation under the symmetry $SU(2)_L$ of weak isospin with coupling constant g, three boson fields $W^k_{\mu\nu}$ and their weak generators $\overrightarrow{\sigma}$, and under the symmetry $U(1)_Y$ of hypercharge with coupling constant $\frac{g'}{2}$, the boson field $B_{\mu\nu}$ and its hypercharge generator Y.

The physical electroweak bosons are the photon, and the $W^\pm$ and Z bosons, presented by gauge fields A_μ, $W^\pm_\mu$ and Z_μ, which are the linear combinations of W^i_μ and B_μ:

$$\begin{aligned} \begin{pmatrix} A_\mu \\ Z_\mu \end{pmatrix} &= \begin{pmatrix} \cos\theta_W & \sin\theta_W \\ -\sin\theta_W & \cos\theta_W \end{pmatrix} \begin{pmatrix} B_\mu \\ W^3_\mu \end{pmatrix}, \\ W^\pm_\mu &= \frac{1}{\sqrt{2}}(W^1_\mu \mp W^2_\mu), \end{aligned} \tag{1.16}$$

where the mixing between W^i_μ and B_μ fields is characterized by the weak mixing angle θ_W:

$$\cos\theta_W = \frac{g}{\sqrt{g^2+g'^2}}, \quad \sin\theta_W = \frac{g'}{\sqrt{g^2+g'^2}}. \tag{1.17}$$

[1] Note that when considering the sum $\mathcal{L}^{Matter}_{SU(3)} + \mathcal{L}^{Matter}_{SU(2)\times U(1)}$ in Eq. 1.2 the derivative ∂^μ must be included only once.

The Feynman diagrams of the photon-fermions vertex, W boson-fermions vertex and Z boson-fermions vertex with the corresponding coupling strengths are shown in Fig. 1.2. In natural units, the relation between e and the fine-structure constant α can be written as $e = g_e = \sqrt{4\pi\alpha}$, therefore α can be regarded as the QED coupling constant. g is the weak coupling strength of the W boson defined, through the Fermi constant G_F, as:

$$\frac{G_F}{\sqrt{2}} = \frac{g^2}{8m_W^2}, \tag{1.18}$$

where $G_F = 1.166 \times 10^{-5}$ GeV^{-2} and m_W is the mass of the W boson. g' is the weak coupling strength of the Z boson. The relation between the electroweak coupling constants is given by:

$$e = g \cdot \sin\theta_W = g' \cdot \cos\theta_W. \tag{1.19}$$

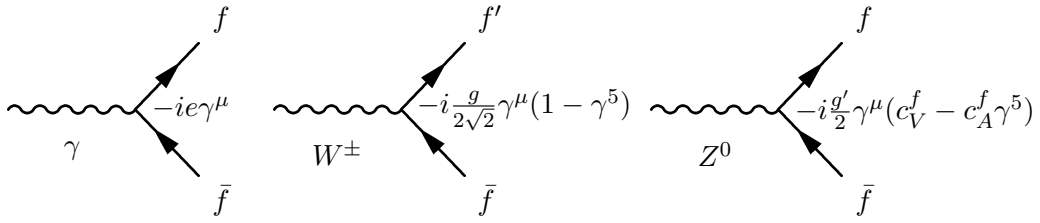

Figure 1.2: Electroweak interaction vertices with fermions: (a) QED vetex, (b) charged current mediated by the W boson, (c) neutral current mediated by the Z boson. The parameters c_V^f and c_A^f are the vector and axial coupling constants of the Z boson coupling to the fermions.

1.1.4 Spontaneous Symmetry Breaking

The Lagrangian in Eq. 1.13 is invariant under a local gauge transformation, but has the problem of including only massless fermions and gauge bosons. This problem can be solved through a Spontaneous Symmetry Breaking (SSB), where the symmetry group $SU(2)_L \times U(1)_Y$ breaks down to $U(1)_{EM}$. In order to generate the SSB, a new isospin doublet of complex scalar fields Φ, also known as Higgs field, is introduced:

$$\Phi \equiv \begin{pmatrix} \phi^+ \\ \phi^0 \end{pmatrix}, \tag{1.20}$$

where the "+" and "0" indices indicate the electric charge of the field.

The scalar Lagrangian with a quartic self-interaction can be then defined as:

$$\begin{cases} \mathcal{L}^{Higgs}_{SU(2)\times U(1)} = (D^\mu_\phi \phi)^\dagger (D_{\phi\mu}\phi) - V(\phi^\dagger\phi) \\ V = \mu^2\phi^\dagger\phi + \lambda(\phi^\dagger\phi)^2 \\ D^\mu_\phi = \partial^\mu + ig\dfrac{\bar{\sigma}\cdot\bar{W}^\mu}{2} + i\dfrac{g'}{2}Y_\phi B^\mu \end{cases} \tag{1.21}$$

The potential $V(\phi)$ depends on two parameters, μ^2 and λ. The case $\lambda < 0$ is unphysical and leads to a non stable minimum. For $\lambda > 0$ there are two possibilities: $\mu^2 > 0$ and $\mu^2 < 0$ which are illustrated on the Fig. 1.3.

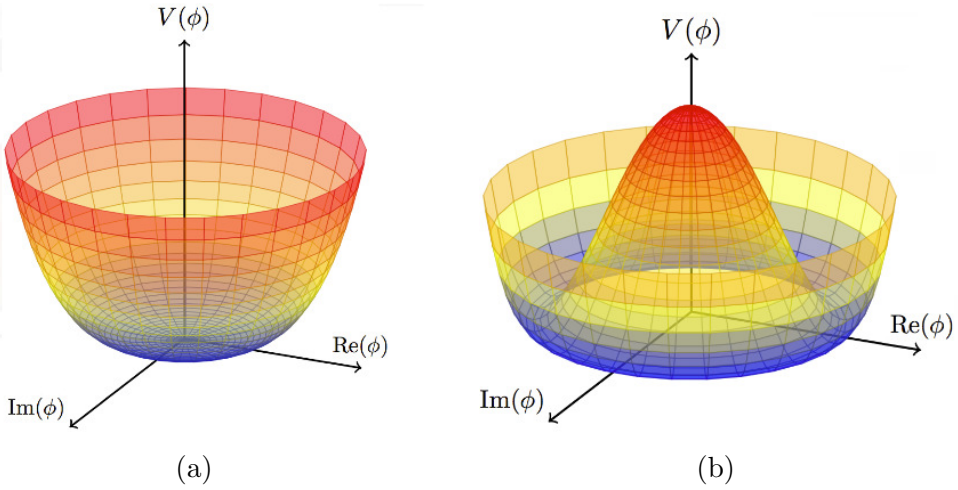

(a) (b)

Figure 1.3: Vacuum potential for $\lambda > 0$ and (a) $\mu^2 > 0$ and (b) $\mu^2 < 0$. Figures taken from reference [17].

If $\mu^2 > 0$, the potential $V(\phi)$ has one minimum, which corresponds to $|\Phi| = 0$ and gives the vacuum expectation value $\langle 0|\Phi|0\rangle = 0$. If $\mu^2 < 0$, the potential $V(\phi)$ has a minimum when:

$$\Phi^\dagger\Phi = -\frac{\mu^2}{2\lambda} \equiv \frac{v^2}{2}, \tag{1.22}$$

which means that the field Φ has a non-zero Vacuum Expectation Value (VEV) $\langle\Phi\rangle_0 \equiv \langle 0|\Phi|0\rangle = \frac{v}{\sqrt{2}}$, and there is no unique minimum. The fundamental vacuum state is not invariant under the symmetry group $SU(2)_L \times U(1)_Y$, i.e. these two symmetries are broken.

The Goldstone theorem states that *for every spontaneously-broken continuous symmetry, the theory must contain a massless particle* [18]. The massless fields that arise through spontaneous symmetry breaking are called *Goldstone bosons*. Since the photon is the only electroweak boson known to be massless, the minimum of the potential is chosen so that the Higgs field that acquires a VEV is the one with zero electric charge:

$$\Phi_0 \equiv \frac{1}{\sqrt{2}}\begin{pmatrix}0\\ v\end{pmatrix}, \tag{1.23}$$

where $v = \sqrt{-\mu^2/\lambda}$ is the VEV.

To represent all true minimum states of the theory, one can introduce the complex field $\Phi(x)$:

$$\Phi(x) \equiv \frac{1}{\sqrt{2}}\begin{pmatrix}0\\ v + H(x)\end{pmatrix}, \tag{1.24}$$

where $H(x)$ represents ground state fluctuations around the vacuum state in the direction perpendicular to the degenerate minima.

After the spontaneous symmetry breaking, the masses of the vector bosons can be obtained by computing the interaction terms between the Higgs field and the $W^{\pm}$, Z^0 and γ bosons at the minimum of the Higgs field. The mass of the Higgs boson (at the tree level) is found to be $m_H = \sqrt{2}\mu = \sqrt{2\lambda}v$. The W and Z boson masses are given by $m_W = g\frac{v}{2}$ and $m_Z = \frac{v}{2}\sqrt{g^2 + g'^2}$, respectively, and the mass of the photon remains equal to zero. The combination of these results gives the relation between the W and Z boson masses and the weak mixing angle:

$$m_W = m_Z \cdot \cos\theta_W. \tag{1.25}$$

Finally, a scalar-fermion interaction is introduced in order to give mass to the fermions. The interactions between the Higgs doublet and the fermion fields are added through the Yukawa Lagrangian term:

$$\mathcal{L}^{Yukawa}_{SU(2)\times U(1)} = -\bar{\psi_L} Y \Phi \psi_R + h.c. \tag{1.26}$$

where the matrices Y describe the Yukawa couplings between the Higgs doublet and the fermions.

The Feynman diagrams for the Higgs boson interaction vertices with the W and Z bosons, with fermions, and self-interactions are shown in Fig. 1.4. The strength of the coupling is proportional to the mass of the particle interacting with the Higgs boson, i.e. the heavier the particle, the stronger its coupling to the Higgs boson.

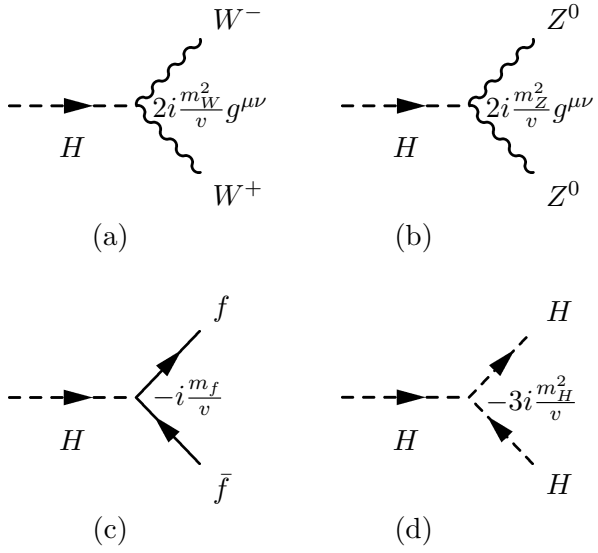

Figure 1.4: Higgs interaction vertices with the (a) $W^{\pm}$ bosons, (b) Z^0 bosons, (c) fermions and (d) itself. The strength of the coupling at each vertex is also shown.

1.1.5 Quark Mixing and CKM Matrix

To explain how the quarks and leptons get their masses one should replace Φ in Eq. 1.26 by its VEV (Eq. 1.24). Using the notations from the Eq. 1.7 and Eq. 1.8 the Yukawa

Lagrangian can be written as:

$$\begin{aligned}\mathcal{L}^{Yukawa}_{SU(2)\times U(1)} &= -\bar{L_L}Y^l\Phi l_R - \bar{Q_L}Y^u\Phi\mathcal{U}_R - \bar{Q_L}Y^d\Phi\mathcal{D}_R + h.c. \\ &= -\frac{v}{\sqrt{2}}\left[\bar{l_L}Y^l l_R + \bar{\mathcal{U}_L}Y^u\mathcal{U}_R + \bar{\mathcal{D}_L}Y^d\mathcal{D}_R\right] + h.c.\end{aligned} \tag{1.27}$$

The Y^l, Y^u and Y^d matrices should be diagonal to get the proper mass terms for the fermions, but they contain off-diagonal terms since the fermion fields compose a basis of the weak interaction, also called *flavor eigenstates*. To solve this problem one should change to *mass eigenstates*, by transforming to a new basis made up with fermion mass eigenstates introducing unitary matrices V:

$$\begin{aligned} {l'}_L = V^l_L l_L, \quad {l'}_R = V^R_L l_R, \\ {\mathcal{U}'}_L = V^l_u \mathcal{U}_L, \quad {\mathcal{U}'}_R = V^R_u \mathcal{U}_R, \\ {\mathcal{D}'}_L = V^l_d \mathcal{D}_L, \quad {\mathcal{D}'}_R = V^R_d \mathcal{D}_R. \end{aligned} \tag{1.28}$$

In this new basis the Yukawa Lagrangian takes the form:

$$\begin{aligned}\mathcal{L}^{Yukawa}_{SU(2)\times U(1)} &= -\frac{v}{\sqrt{2}}\left[\bar{l_L}V^{l\dagger}_L Y^l V^l_R l_R + \bar{\mathcal{U}_L}V^{u\dagger}_L Y^u V^u_R \mathcal{U}_R + \bar{\mathcal{D}_L}V^{d\dagger}_L Y^d V^{d\dagger}_R \mathcal{D}_R\right] + h.c. \\ &\equiv -\bar{l_L}Y^l_{mass} l_R - \bar{\mathcal{U}_L}Y^u_{mass}\mathcal{U}_R - \bar{\mathcal{D}_L}Y^d_{mass}\mathcal{D}_R + h.c.\end{aligned} \tag{1.29}$$

where the Y^l_{mass}, Y^u_{mass} and Y^d_{mass} matrices are now diagonal matrices with a real terms on the diagonal, i.e. proper mass terms for the fermions. This means that the mass states have observable eigenvalues and can be measured experimentally. But this feature comes with a cost.

The unitarity condition implies $V^{i\dagger}_j V^i_j = 1$ for $i \in \{l, u, d\}$ and $j \in \{L, R\}$. But one can also write the combination like $V^{u\dagger}_L V^d_L$, which contains non zero off-diagonal terms and leads to couplings of quarks from one doublet to quarks in other doublets during the weak interactions involving charged currents discussed in Sec. 1.3. This behavior is known as quark mixing and one can define a matrix V_{CKM}:

$$V_{CKM} \equiv V^{u\dagger}_L V^d_L = \begin{pmatrix} V_{ud} & V_{us} & V_{ub} \\ V_{cd} & V_{cs} & V_{cb} \\ V_{td} & V_{ts} & V_{tb} \end{pmatrix}, \tag{1.30}$$

which is a unitary matrix called Cabibo-Kobayashi-Maskawa (CKM) matrix and the square of its elements V_{ij} gives the probability of the coupling of down-type quark i to up-type quark j during the charged weak interactions. Its components are experimentally determined [19]:

$$V_{CKM} = \begin{pmatrix} V_{ud} \approx 0.974 & V_{us} \approx 0.225 & V_{ub} \approx 0.003 \\ V_{cd} \approx 0.225 & V_{cs} \approx 0.973 & V_{cb} \approx 0.041 \\ V_{td} \approx 0.009 & V_{ts} \approx 0.040 & V_{tb} \approx 0.999 \end{pmatrix}. \tag{1.31}$$

Additionally, it should be noted the relations resulting from the unitarity of the CKM matrix. By multiplying it on its hermitian conjugate one can get two set of relations, one for down-type quark mixing and one for up-type quark mixing:

$$V_{CKM}^{\dagger}V_{CKM} = \begin{pmatrix} V_{ud}^{*} & V_{cd}^{*} & V_{td}^{*} \\ V_{us}^{*} & V_{cs}^{*} & V_{ts}^{*} \\ V_{ub}^{*} & V_{cb}^{*} & V_{tb}^{*} \end{pmatrix} \begin{pmatrix} V_{ud} & V_{us} & V_{ub} \\ V_{cd} & V_{cs} & V_{cb} \\ V_{td} & V_{ts} & V_{tb} \end{pmatrix} = \begin{pmatrix} 1 & 0 & 0 \\ 0 & 1 & 0 \\ 0 & 0 & 1 \end{pmatrix}, \tag{1.32}$$

$$V_{CKM}V_{CKM}^{\dagger} = \begin{pmatrix} V_{ud} & V_{us} & V_{ub} \\ V_{cd} & V_{cs} & V_{cb} \\ V_{td} & V_{ts} & V_{tb} \end{pmatrix} \begin{pmatrix} V_{ud}^{*} & V_{cd}^{*} & V_{td}^{*} \\ V_{us}^{*} & V_{cs}^{*} & V_{ts}^{*} \\ V_{ub}^{*} & V_{cb}^{*} & V_{tb}^{*} \end{pmatrix} = \begin{pmatrix} 1 & 0 & 0 \\ 0 & 1 & 0 \\ 0 & 0 & 1 \end{pmatrix}. \tag{1.33}$$

There are overall 18 constrains, which can be split into 6 unitarity relations:

$$\begin{array}{ll} V_{ud}^2 + V_{cd}^2 + V_{td}^2 = 1, & V_{ud}^2 + V_{us}^2 + V_{ub}^2 = 1, \\ V_{us}^2 + V_{cs}^2 + V_{ts}^2 = 1, & V_{cd}^2 + V_{cs}^2 + V_{cb}^2 = 1, \\ V_{ub}^2 + V_{cb}^2 + V_{tb}^2 = 1, & V_{td}^2 + V_{ts}^2 + V_{tb}^2 = 1, \end{array} \tag{1.34}$$

and 12 orthogonal relations:

$$\begin{array}{ll} V_{ud}^{*}V_{us} + V_{cd}^{*}V_{cs} + V_{td}^{*}V_{ts} = 0, & V_{ud}^{*}V_{cd} + V_{us}^{*}V_{cs} + V_{ub}^{*}V_{cb} = 0, \\ V_{ud}^{*}V_{ub} + V_{cd}^{*}V_{cb} + V_{td}^{*}V_{tb} = 0, & V_{ud}^{*}V_{td} + V_{us}^{*}V_{ts} + V_{ub}^{*}V_{tb} = 0, \\ V_{us}^{*}V_{ud} + V_{cs}^{*}V_{cd} + V_{ts}^{*}V_{td} = 0, & V_{cd}^{*}V_{ud} + V_{cs}^{*}V_{us} + V_{cb}^{*}V_{ub} = 0, \\ V_{us}^{*}V_{ub} + V_{cs}^{*}V_{cb} + V_{ts}^{*}V_{tb} = 0, & V_{cd}^{*}V_{tb} + V_{cs}^{*}V_{ts} + V_{cb}^{*}V_{tb} = 0, \\ V_{ub}^{*}V_{ud} + V_{cb}^{*}V_{cd} + V_{tb}^{*}V_{td} = 0, & V_{td}^{*}V_{ud} + V_{ts}^{*}V_{us} + V_{tb}^{*}V_{ub} = 0, \\ V_{ub}^{*}V_{us} + V_{cb}^{*}V_{cs} + V_{tb}^{*}V_{ts} = 0, & V_{td}^{*}V_{cd} + V_{ts}^{*}V_{cs} + V_{tb}^{*}V_{cb} = 0. \end{array} \tag{1.35}$$

1.1.6 Experimental Successes of the Standard Model

Since its formulation in the 1960s, the SM has been tested in multiple experiments and its validity has been confirmed with precision measurements. All the particles predicted by the SM are already discovered and are accommodated nicely into the model.

The first significant success of the SM started in the *November Revolution* with the discovery of a new subatomic particle, the J/Ψ meson. The discovery was announced by two research groups at SLAC [20] and BNL [21] (who named it Ψ and J respectively) on 11 November 1974. The importance of the J/Ψ meson discovery is that it was the first particle contained a quark never seen before, the charm quark, which was predicted in order to explain the absence of flavor-changing neutral currents [16]. In the years following 1974, major advances in particle physics were made. Other composite particles, which were made from a combination of the charm quark and one or two of the "old" up, down and strange quarks, were discovered, which provided even more evidence for the quark model in general and allowed to study the charm quark in more detail.

In 1975, two more quarks - the top and bottom - were hypothesized, and in 1977, the bottom quark was discovered at Fermilab [22]. The W and Z bosons were discovered at the CERN $Sp\bar{p}S$ collider in 1983 [23–26]. The SM was thoroughly scrutinized with precision measurements of the W and Z bosons at the LEP collider started from 1989. The top quark mass was indirectly estimated from radiative corrections to the

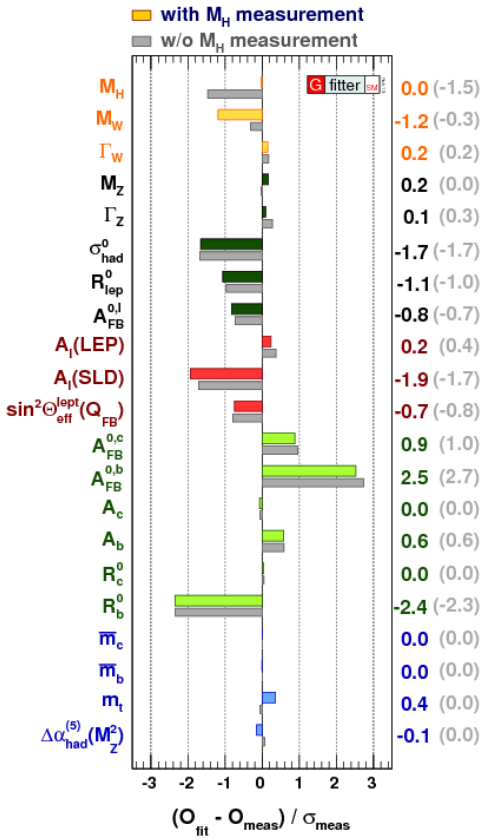

(a)

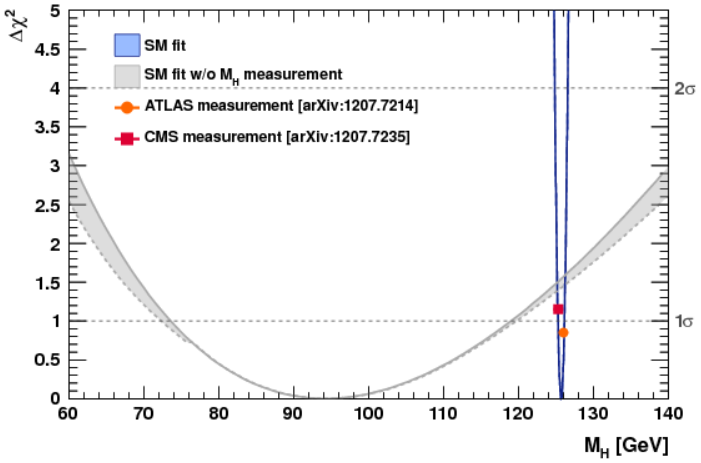

(b)

Figure 1.5: (a): Pull values for the SM fit with and without inclusion of M_H in the fit. The pull values are defined as deviations between experimental measurements and theoretical calculations in units of the experimental uncertainty. (b): $\Delta\chi^2$ as a function of Higgs boson mass M_H, with (blue band) and without the M_H measurements (gray band). Figures taken from reference [29].

W boson mass and the $Z \to b\bar{b}$ branching ratio, and was discovered in 1995 at the Tevatron [27, 28].

The last missing piece of the SM was the Higgs boson, whose mass was preffered to be low by indirect precision measurements [29]. The predicted and the measured quantities for several observables, obtained by the Gfitter Collaboration, are shown in Fig. 1.5. A good consistency between measured and expected quantities is found and none of differences exceeds three standard deviations.

The Higgs boson was discovered only in 2012 by the ATLAS and CMS collaborations at the LHC [1, 2]. The mass of the new particle was found to be ~ 125 GeV [30]. Further measurements of the newly discovered particle confirmed that it is a scalar and a positive CP eigenstate [31]. As of today, its couplings to the rest of the SM particles have been found to be consistent with those predicted for the SM Higgs boson.

1.1.7 Shortcomings of the Standard Model

Despite the fact that the gauge field theory of the SM has been proven to be extremely successful, it is not a complete theory. There are some critical questions that can not be answered within the SM framework. Thus, the SM has to be regarded as an effective theory, the low energy realization of a more complete theory, a "Theory of Everything", that would be able to explain the whole spectrum of observations. The investigation of the aspects where the SM fails to give a satisfactory answer can shed some light into the details of this more general theory.

1.1.7.1 Neutrino Oscillations

Neutrino oscillation is of great theoretical and experimental interest. Although neutrino masses are not measured directly, the measurement of oscillations requires that there is a mass difference between the different neutrino generations, i.e. the neutrino has a non-zero mass, which is not included as part of the SM of particle physics, but can be included by adding right-handed neutrinos, or Majorana masses through higher order operators violating lepton number.

1.1.7.2 Dark Matter Problem

Dark matter was postulated by Jan Oort in 1932 [32], albeit based upon insufficient evidence, to account for the orbital velocities of stars in the Milky Way. The first evidence of the presence of dark matter in the universe came in 1990 from the measurement of the rotation curves of the galaxies [33]. Dark matter doesn't interact through the electromagnetic force at any significant level and therefore can not be observed. According the SM of cosmology, the total mass-energy of the known universe contains 4.9% ordinary (baryonic) matter, 26.8% dark matter and 68.3% dark energy [34]. The SM has no candidate particle that can account for the large measured fraction of dark matter.

1.1.7.3 Matter-antimatter Asymmetry

According to the Big Bang Theory equal amount of matter and antimatter should have been created in the early universe. However, there is not much antimatter to be found. Although CP-violation is described by the presence of a phase in the CKM matrix, the amount of CP-violation is not big enough as to explain the current asymmetry.

1.1.7.4 Unification of Forces

The idea that at high energy the $SU(3)_C \times SU(2)_L \times U(1)_Y$ gauge group is embedded in a large simple group is known as *grand unification* [18]. The simplest choice for this large symmetry is $SU(5)$. In this theory three gauge interactions of the SM which define the electromagnetic, weak, and strong interactions or forces, are merged into one single force. This unified interaction is characterized by one larger gauge symmetry and thus several force carriers, but one unified coupling constant, g_5, which have the following relation with the coupling constant of $SU(3)_C \times SU(2)_L \times U(1)_Y$ gauge group:

$$g_5 = g_3 = g = \sqrt{\frac{5}{3}} g'. \tag{1.36}$$

One can extrapolate the values of the three coupling constants from the energy scale of m_Z upward. The result of this extrapolation for the SM is shown as solid lines in Fig. 1.6. The coupling constants do come close together at very high energies, though they do not actually meet. This means that in the SM no unification of the coupling constants can be achieved. However, unification can be realized at a scale of about 10^{16} GeV, for example, if the SM is extended to Minimal Supersymmetric Model (MSSM) by adding a supersymmetric multiplet of particles (dashed line in Fig. 1.6).

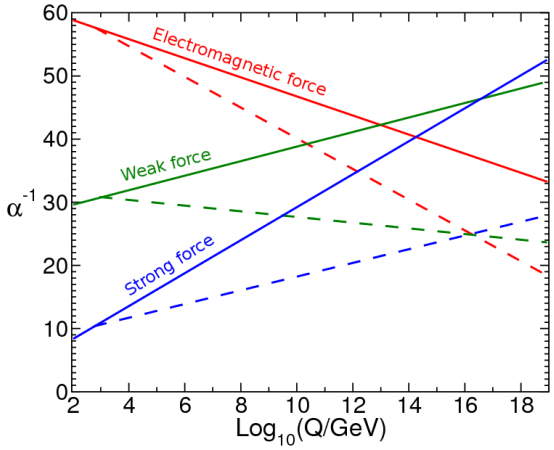

Figure 1.6: Running of the coupling constants for electromagnetic force (red), weak force (green) and strong force (blue). The solid lines represent the SM scenario and dashed one a minimal supersymmetric extension of the SM. Figure taken from reference [35].

1.1.7.5 Naturalness Problem

One of the principal objections to the SM as a "complete theory" is the high number of arbitrary parameters. The SM has 19 free parameters that are not predicted by the theory. Three of them are the couplings of the gauge groups g_s, g, g' for the strong, electromagnetic and weak interactions respectively. 13 parameters are associated with the nine charged fermion masses and the four parameters of the CKM matrix (three quark-mixing angles and one phase). Two more are the Higgs vacuum expectation value v and the quartic coupling constant λ, needed to describe the Spontaneous Symmetry Breaking mechanism, and the last one is the θ parameter of QCD.

The arbitrarity of parameters in the SM introduces the problem known as *naturalness problem*. A "natural" theory is characterized by free parameters with values at, more or less, the same order of magnitude. This does not happen in the SM: the top quark mass is 10^5 larger than the up quark one. The naturalness problem is not a problem to the theory itself, but such huge differences in arbitrary parameters are possible indications of unknown principles underlying a more complete theory encompassing the SM.

1.1.7.6 Quantum Theory of Gravity

A very important missing piece towards a "Theory of Everything" is the introduction of a quantum field theory for gravity. At energies of the order of the Planck scale, $M_P = 10^{18}$ GeV, quantum gravitational effects are not negligible and a new model should replace the SM. In the hypothetical absence of new physics below this scale, the requirement that the SM has to be valid up to the Planck scale introduces a new problem known as the "hierarchy problem".

1.1.7.7 Hierarchy Problem

The hierarchy problem can be expressed as the instability of the value of the Higgs boson mass when radiative corrections are included in presence of a physical energy scale cut-off, Λ, taken at energies far above the electroweak scale.

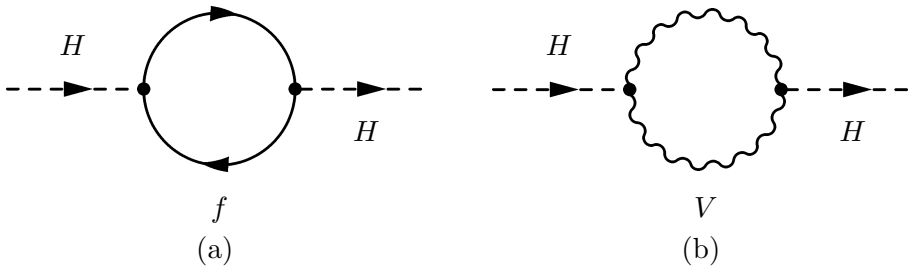

Figure 1.7: Example of one-loop quantum corrections to the Higgs boson mass due to (a) fermions and (b) bosons.

For illustration, one can consider the fermion one-loop radiative corrections, $\sum_H^f$, to the Higgs mass, like the one in Fig. 1.7a. Integrating over all possible loop momenta k, considering the N_f degrees for fermion f with mass m_f and Yukawa coupling y_f, gives:

$$\sum_H^f = -2N_f y_f^2 \int \frac{d^4k}{(2\pi)^4} \left[\frac{1}{k^2 - m_f^2} + \frac{2m_f^2}{(k^2 - m_f^2)^2} \right] \tag{1.37}$$

For $\Lambda \to \infty$ one can make the following types of replacements:

$$\begin{aligned} \int \frac{d^4k}{i\pi^2} \left(\frac{1}{k^2 - m_f^2} \right) &\to -\Lambda^2 + 2m_f \ln \frac{\Lambda}{m_f}, \\ \int \frac{d^4k}{i\pi^2} \left(\frac{1}{(k^2 - m_f^2)^2} \right) &\to 2 \ln \frac{\Lambda}{m_f}. \end{aligned} \tag{1.38}$$

From this, one finally gets the Higgs mass corrections as a function of Λ:

$$m_H^2 = (m_H)_0^2 + N_f \frac{y_f^2}{16\pi^2} \left[-2\Lambda^2 + 6m_f^2 \ln \frac{\Lambda}{m_f} + ... \right]. \tag{1.39}$$

where $(m_H)_0^2$ is the bare Higgs mass. Similar corrections arise also from gauge-boson loops, as shown in Fig. 1.7b.

The second term in Eq. 1.39 is quadratically divergent. The only solution to cancel this divergency is to have a bare mass $(m_H)_0^2 \sim \Lambda^2$, which is known as *fine tuning*. If the Λ is chosen to be $\sim 10^{16}$ GeV, which is the possible grand unification scale, then $m_H^2 \sim 10^{32}$ GeV^2. As it is known, the mass of the Higgs boson is measured to be $m_H \sim 125$ GeV, which means that m_H^2 is of the order of (100 GeV)^2, i.e. the experimentally measured value is many orders of magnitude smaller than theoretical one. This is so called *hierarchy problem*, which could be fixed within the SM by choosing a fine-tuned mass counter term, a solution considered not really elegant also because fine tuning will be required for every order in the perturbative expansion.

1.2 Beyond The Standard Model

Physics Beyond the Standard Model (BSM) refers to the theoretical developments needed to address one or several of the shortcomings of the SM. Over the years, many BSM extensions have been proposed. In the following, several of these theories relevant for this dissertation are reviewed.

1.2.1 Quark Singlet Model

One of the simplest extension of the SM is the Quark Singlet Model (QSM) with quarks whose left- and right-handed chiral components are both singlets (with charge $Q = \frac{2}{3}$ and $Q = -\frac{1}{3}$) with respect to the $SU(2)$ weak-isospin gauge group. Introduction of new quarks has an impact on the renormalization group equations, on the unification and perturbativity of gauge and Yukawa couplings. For more details see [36, 37].

1.2.2 Two-Higgs Doublet Model

Many BSM theories include an extended Higgs sector. A Two-Higgs-Doublet Model (2HDM) is an extension of the SM in which the electroweak symmetry is broken by two scalar Higgs doublet, Φ_1 and Φ_2, instead of one:

$$\Phi_1 \equiv H_u = \frac{1}{\sqrt{2}} \begin{pmatrix} 0 \\ v_u \end{pmatrix}, \quad \Phi_2 \equiv H_d = \frac{1}{\sqrt{2}} \begin{pmatrix} 0 \\ v_d \end{pmatrix}. \tag{1.40}$$

The two scalar Higgs doublets have in total eight initial degrees of freedom, three are used to provide masses for the $W^{\pm}$ and Z, and the remaining five corresponds to physical scalars: two neutral CP-even scalars Higgs bosons h and H, the one CP-odd pseudo-scalar A and two charged Higgs bosons $H^{\pm}$. Such a model has six free parameters: four Higgs masses (m_h, m_H, m_A, $m_{H^{\pm}}$), the ratio of the two vacuum expectation values ($\tan\beta = \frac{v_u}{v_d}$) and a mixing angle ($\alpha$).

1.2.3 Supersymmetry

One of the most popular BSM scenarios is the Supersymmetry (SUSY). In this theory each particle of the SM has an associated "superpartner". These superpartners have all of the quantum numbers identical to the corresponding SM particles, but differ by $\frac{1}{2}$ in the spin value.

Due to the difference in spin the isomorphic transformation, called *supersymmery*, between fermionic and bosonic sectors can be introduced:

$$\begin{aligned} Q|Fermion\rangle &\in |Boson\rangle, \\ Q|Boson\rangle &\in |Fermion\rangle. \end{aligned} \tag{1.41}$$

where Q is the supersymmetry operator. Q satisfies the following commutation and anti-commutation rules:

$$\begin{cases} \left\{Q, Q\right\} = \left\{Q^{\dagger}, Q^{\dagger}\right\} = 0 \\ \left\{Q, Q^{\dagger}\right\} = -\left\{Q^{\dagger}, Q\right\} = P^{\mu}\ , \\ \left[P^{\mu}, Q\right] = \left[P^{\mu}, Q^{\dagger}\right] = 0 \end{cases} \tag{1.42}$$

where $Q^{\dagger}$ is hermitian conjugate operator of Q and P^{μ} is time and space translations operator. From the commutation of the SUSY operators with P^{μ}, follows the commutation with the mass operator P^2, therefore all the particles in a supermultiplet are mass degenerate. Since the SUSY operators also commute with the generators of $SU(3)_C \times SU(2)_L \times U(1)_Y$ groups they also should have the same quantum numbers.

The transformation Q can be defined in many different ways. Therefore, supersymmetry is not a fixed model but a framework from which many SM extensions can be derived. So far, no SUSY particles have been found, which indicates that if supersymmetry exists it must be a spontaneously broken symmetry so that the SUSY particles can have a mass different from the electroweak symmetry breaking. Spontaneously broken supersymmetry could solve many problems in particle physics including the hierarchy and force unification problems.

The simplest realization of spontaneously broken supersymmetry is the Minimal Supersymmetric SM (MSSM), the one of the best studied candidates for physics beyond the SM. This is a model that introduces the minimal amount of new particles and no additional gauge interactions. In MSSM every SM particle is paired with one single superpartner. To form the names of superpartners of individual fermions the "s" prefix is used: squarks, sleptons, etc. The partners of the SM bosons are labeled with the suffix "ino": gluino, Higgsino, etc. The Higgs sector requires the introduction of an additional scalar Higgs doublet, as in the case of 2HDM, therefore producing five particles after giving mass to the SM bosons.

After electroweak symmetry breaking, the neutral W^0 and the B boson fields mix to produce the physical Z^0 and γ fields, while the corresponding $\tilde{W^0}$ and the $\tilde{B}$ mix to produce the zino ($\tilde{Z^0}$) degenerate with the Z^0, and a massless photino $\tilde{\gamma}$. The neutral gauginos, $\tilde{B}$ and $\tilde{W^0}$, and the neutral higgsinos, $\tilde{H_u^0}$ and $\tilde{H_d^0}$, combine to form four mass eigenstates named neutralinos. The charged higgsinos, $\tilde{H_u^+}$ and $\tilde{H_d^-}$, and the winos, W^+ and W^-, mix to form two mass eigenstates with electric charge ± 1, named charginos.

Also, the most general MSSM can contain operators that violate baryon or lepton numbers, thus allowing proton decays. To avoid having lepton and baryon number violating terms, a new symmetry, called *matter parity*, or *R-parity*, can be added. This introduces a new conserved quantum number, defined as:

$$P_R = (-1)^{3(B-L)+2s}, \tag{1.43}$$

where B and L are the baryon and lepton quantum numbers respectively and s is the spin of the particle. Thus all the SM particles have $P_R = +1$, while the SUSY partners have $P_R = -1$. The particle content for the MSSM is summarized in the Table 1.3.

SM Particle	Particle	Symbol	Spin	R-Parity	Superpartner	Symbol	Spin	R-parity
Fermions	Quarks	q	$\frac{1}{2}$	+1	Squark	$\tilde{q}$	0	-1
	Lepton	l	$\frac{1}{2}$	+1	Slepton	$\tilde{l}$	0	-1
Bosons	W bosons	W^0, $W^\pm$	1	+1	Wino	$\tilde{W^0}$, $\tilde{W^\pm}$	$\frac{1}{2}$	-1
	B bosons	B	1	+1	Bino	$\tilde{B}$	$\frac{1}{2}$	-1
	Gluon	g	1	+1	Gluino	$\tilde{g}$	$\frac{1}{2}$	-1
Higgs bosons	H_u	H_u^+, H_u^0	0	+1	Higgsinos	$\tilde{H_u^+}$, $\tilde{H_u^0}$	$\frac{1}{2}$	-1
	H_d	H_d^0, H_d^-	0	+1	Higgsinos	$\tilde{H_d^0}$, $\tilde{H_d^-}$	$\frac{1}{2}$	-1

Table 1.3: The predicted particle spectra in the MSSM.

The MSSM, with the requirement of R-parity conservation, provides an easy and natural solution for the hierarchy problem. Since for each SM particle SUSY has a superpartner, that also couples to the Higgs boson, the first order corrections in Eq. 1.39 will have an additional term, produced by the superparner, $\tilde{f}$:

$$\sum_H^{\tilde{f}} = -N_{\tilde{f}} \frac{y_{\tilde{f}}^2}{16\pi^2} \left[-2\Lambda^2 + 6m_{\tilde{f}}^2 \ln \frac{\Lambda}{m_{\tilde{f}}} \right], \tag{1.44}$$

where it has to be highlighted that this correction has opposite sign to the fermion contribution in Eq. 1.39. If $N_{\tilde{f}} = N_f$ and $|y_{\tilde{f}}| = |y_f|$, then all the fermion terms will have a counter term that naturally cancels the quadratic divergence introduced.

The residual correction terms to the Higgs mass, not written explicitly above and ignoring the logarithmic contributions, would be:

$$\Delta m_H^2 = \frac{N_f y_f^2}{8\pi^2} \left| m_f^2 - m_{\tilde{f}}^2 \right|. \tag{1.45}$$

Invoking "naturalness" arguments, the size of the corrections is expected to be smaller than m_H, leading to:

$$\left|m_f^2 - m_{\tilde{f}}^2\right| \leq 1 \quad \text{TeV}^2, \tag{1.46}$$

which can be understood as the range of validity of the SM: at the TeV scale superpartners of the SM particles can be produced and the SM is replaced by its supersymmetric extension.

The MSSM also gives a solution for the force unification problem. As it was already shown in Fig. 1.6 (dashed line), unification of the coupling constants can be achieved at a scale of about 10^{16} GeV.

Additionally, the conservation of the R-parity has one important phenomenological consequence: the Lightest Supersymmetric Particle (LSP) is absolutely stable, and if electrically neutral and interacts with matter through the weak interaction, it could be an attractive candidate for dark matter.

1.3 Flavor-Changing Neutral Current Interactions

This section presents an overview of the theoretical concepts behind the Flavor-Changing Neutral Current (FCNC) interactions in the SM. The absence of FCNC interactions at tree level in the SM is demonstrated. The presence of one-loop diagrams and their further suppresion are discussed in detail. The experimental evidence for FCNC interactions in light quarks is also presented.

1.3.1 FCNC Interactions in the SM

The SM Lagrangian in Eq. 1.15 for the weak interactions between quarks and gauge bosons can be written with three terms, the first one containing the electromagnetic current, J^μ_{em}, the second one containing the weak charged current, J^μ_{CC}, and the third one containing the weak neutral current, J^μ_{NC}:

$$\mathcal{L}^{Matter}_{SU(2)\times U(1)} = -eJ^\mu_{em}A_\mu - \frac{g}{2}\left(J^\mu_{CC}W^+_\mu + J^{\mu\dagger}_{CC}W^-_\mu\right) - \frac{g}{2\cos\theta_W}J^\mu_{NC}Z_\mu, \tag{1.47}$$

where the currents are given by:

$$\begin{aligned}
J^\mu_{em} &= \sum_f q_f \bar{f}\gamma^\mu f = \frac{2}{3}\bar{\mathcal{U}}\gamma^\mu\mathcal{U} + \frac{1}{3}\bar{\mathcal{D}}\gamma^\mu\mathcal{D}.\\
J^\mu_{CC} &= \bar{\mathcal{U}}_L\gamma^\mu\mathcal{D}_L,\\
J^\mu_{NC} &= \bar{\mathcal{U}}_L\gamma^\mu\left(1 - \frac{4}{3}\sin^2\theta_W\right)\mathcal{U}_L - \bar{\mathcal{U}}_R\gamma^\mu\frac{4}{3}\sin^2\theta_W\mathcal{U}_R -\\
&\quad - \bar{\mathcal{D}}_L\gamma^\mu\left(1 - \frac{2}{3}\sin^2\theta_W\right)\mathcal{D}_L + \bar{\mathcal{D}}_R\gamma^\mu\frac{4}{3}\sin^2\theta_W\mathcal{D}_R,
\end{aligned} \tag{1.48}$$

and gauge fields A_μ, $W^\pm_\mu$ and Z_μ are defined in Eq. 1.16.

From Eq. 1.48 one can note the crucial things for these currents:

- The charged current is between down-type quarks and anti-up-type quarks, i.e. it is a flavor changing interaction.

- The neutral and electromagnetic currents are only between up-type quarks and anti-up-type quarks, or between down-type quarks and anti-down-type quarks, therefore it does not change flavors of quarks, i.e. there are no transitions like $t \to c$ or $t \to u$ at tree level.

Unlike the situation with the charged currents, the neutral currents do couple quarks to only same-flavored quarks. Therefore the SM does not allow FCNC interactions at tree level, i.e. there are no transitions like $t \to c$ or $t \to u$ at tree level.

1.3.2 One-Loop FCNC Diagrams

As mentioned before, FCNC processes can not occur at tree level in the SM, but it can occur at higher order loop diagrams within the SM framework. Nevertheless, even these higher-order FCNC interactions are further suppressed, they are discussed in the following.

Each higher-order loop contribution for FCNC process contains the following interaction terms:

$$\sum_{\mathcal{U} \neq \mathcal{U}'} \sum_{\mathcal{D}} V^*_{\mathcal{U}'\mathcal{D}} V_{\mathcal{U}\mathcal{D}} \cdot \bar{\mathcal{U}}' \mathcal{U}, \tag{1.49}$$

where $\mathcal{D} \in \{d, s, b\}$, $\mathcal{U} \in \{u, c, t\}$, $\mathcal{U}' \in \{u, c, t\}$ and $V_{\mathcal{U}\mathcal{D}}$ are the components of the CKM matrix. The internal quarks from $\mathcal{D}$ enter the Feynman diagrams as a virtual particles. If one assumes that all down-type quarks have equal mass these interactions will be proportional to the orthogonal relations from Eq. 1.35, i.e. equal to zero. However, there is no complete cancellation since the mass of the internal quarks have to be taken into consideration and each term in equation should get a factor of $1/m_q$ for every internal down-type quark and the total sum would add up to a small non-zero value. This suppression was first theorized by Glashow, Iliopoulos and Maiani, and is known as the GIM mechanism [16].

For example, there are two types of first order Feynman diagrams for FCNC interactions, called *box* diagrams and *penguin* diagrams, as shown in Fig. 1.8. Left (right) diagram presents the strange (bottom) quark undergoing a flavor change to down (strange) quark, while the net current is neutral. In this case the internal quarks, u, c or t, are the virtual particles. Assuming that masses of the quarks are equal, these interactions become proportional to:

$$V^*_{us} V_{ud} + V^*_{cs} V_{cd} + V^*_{ts} V_{td}, \tag{1.50}$$

for the left diagram and:

$$V^*_{us} V_{ub} + V^*_{cs} V_{cb} + V^*_{ts} V_{tb}, \tag{1.51}$$

for the right diagram. According the Eq. 1.35 these equations are equal to zero. However, the quarks are not degenerate in mass, i.e. these terms should also get factors proportional to the inverse mass of internal quarks: $\frac{1}{m_u}$, $\frac{1}{m_c}$, $\frac{1}{m_t}$. This results in non-zero but still highly suppress contribution in the SM.

Additionally, one can note that the suppression of FCNC interactions in the up-type quark sectors is more pronounced than in the down-type quark sectors, because the masses for down-type quarks are more similar than those for the up-type quarks.

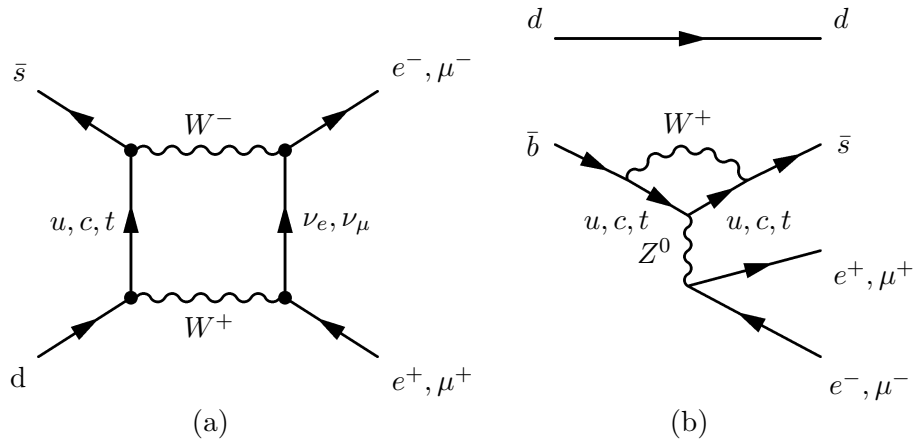

Figure 1.8: First-order FCNC Feynman diagrams: (a) example of a *box* diagram for the $K^0 \to l^+l^-$ decay; (b) example of *penguin* diagram for the $B^0 \to K^0 l^+ l^-$ decay.

1.3.3 FCNC Interactions in Light Quarks

The search for FCNC interactions in the light quarks sector has been a rich field of study. Based on the large datasets available from different experiments (collider: CLEO, BaBar, Belle; fixed target: KTeV, FOCUS), it has been confirmed that the branching ratios for FCNC decays of light quarks are small and in accordance with the SM expectations.

The smallness of FCNC decays was first discovered for the *strange* quark in the $K_L^0 \to \mu^+\mu^-$ decay. At that time only one box diagram, shown in Fig. 1.8a, with the internal u-quark, was known. The obtained branching ratio was far below that expected from this diagram. To explain the rareness of this decay the existence of another quark, *charm* quark, whose box diagram would cancel the contribution from the box diagram with internal u-quark, was proposed. Later this led to the GIM mechanism conception. From the KTeV experiment the branching ratio for the $K_L^0 \to \mu^+\mu^-$ decay has been measured to be $\mathrm{BR}(K_L^0 \to \mu^+\mu^-) = (6.87 \pm 0.11) \times 10^{-9}$ [38]. The branching ratio for the $K_L^0 \to e^+e^-$ decay is even smaller: $\mathrm{BR}(K_L^0 \to e^+e^-) = (9^{+6}_{-4}) \times 10^{-12}$ [19].

FCNC processes in the *charm* sector have received less attention, due to fact that the GIM mechanism suppression in the up-type sector is more severe than in the down-type sector, as mentioned in the previous section. Therefore, only experimental upper limits have been set by many searches from Fermilab charm hadroproduction experiments: $\mathrm{BR}(D^0 \to \mu^+\mu^-) < 1.3 \times 10^{-6}$ at 90% C.L. [19], $\mathrm{BR}(D^+ \to \pi^+e^+e^-) < 7.4 \times 10^{-6}$ at 90% C.L. [19] and $\mathrm{BR}(D_s^+ \to K^+\mu^+\mu^-) < 3.6 \times 10^{-5}$ at 90% C.L. [19].

FCNC decay of the *bottom* quark was first discovered at CLEO in 1993 for the quark-level process $b \to s\gamma$ in the $B^0 \to K^{*0}\gamma$ and $B^- \to K^{*-}\gamma$ decays with the

average branching ratio of $\mathrm{BR}(B \to K^*\gamma) = (4.5 \pm 1.5 \pm 0.9) \times 10^{-5}$ [39]. This value was consistent with the SM predictions from electromagnetic penguin diagrams. The electroweak penguin quark-level process $b \to sZ^0$, shown in Fig. 1.8b, was observed with the Belle detector in $B \to Kl^+l^-$ decay process with the branching ratio of $\mathrm{BR}(B \to Kl^+l^-) = (0.75^{+0.25}_{-0.21} \pm 0.09) \times 10^{-6}$ [40]. The branching ratio for this decay is also consistent with the SM predictions.

A full list of FCNC decays in light quarks can be found in *The Review of Particle Physics* [19].

1.4 Top FCNC Interactions

The top quark is the heaviest particle in the SM. Having a mass of 173.34 ± 0.76 GeV [41], it is about 35 times heavier than the b-quark, which is the reason why it was discovered only in 1995 at the Tevatron by the CDF and DØ collaborations [27, 28]. The large mass of the top quark results in a short lifetime ($\sim 10^{-25}$) sec, which is less than the characteristic time scale of the strong interaction, i.e the top quark decays before it can hadronize.

Within the SM the top quark decays almost exclusively to a W boson and a b-quark ($t \to Wb$), since the CKM matrix element V_{tb} is close to unity. Other SM decay channels are predicted to be several orders of magnitude smaller than $t \to Wb$ decay. The next most likely decays are $t \to Ws$ and $t \to Wd$ with branching ratios of $\mathrm{BR}(t \to Ws) \approx 1.6 \times 10^{-3}$ and $\mathrm{BR}(t \to Wd) \approx 1 \times 10^{-4}$ respectively. Other rare decays include those that occur via FCNC interaction at one loop level and are highly suppressed by the GIM mechanism. Example of *penguin* diagram with FCNC top interaction is shown in Fig. 1.9. The Feynman diagrams of the top quark decays are shown in Fig. 1.10.

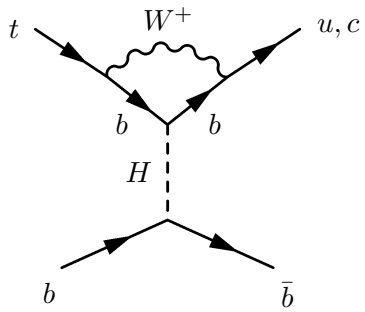

Figure 1.9: Example of the SM *penguin* diagram with FCNC top interaction.

1.4.1 Top FCNC Interactions in the SM

The most general effective SM Lagrangian describing the FCNC interactions of the top quark with the light quark $q = \{u, c\}$ and a gauge or Higgs bosons can be written

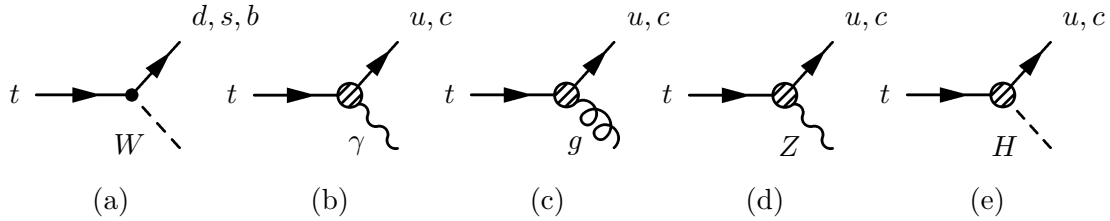

Figure 1.10: Feynman diagrams of the top quark decays. SM decay: (a) $t \to Wb, Ws, Wd$, and FCNC decays: (b) $t \to \gamma u, \gamma c$, (c) $t \to gu, gc$, (d) $t \to Zu, Zc$, (e) $t \to Hu, Hc$.

as:

$$\begin{aligned}\mathcal{L}_{eff} = &-e\frac{\kappa_{tq\gamma}}{\Lambda}\bar{t}\sigma^{\mu\nu}\left(f^L_{tq\gamma}P_L + f^R_{tq\gamma}P_R\right)qA_{\mu\nu} - \\ &-\sqrt{2}g_s\frac{\kappa_{tqg}}{\Lambda}\bar{t}\sigma^{\mu\nu}T_a\left(f^L_{tqg}P_L + f^R_{tqg}P_R\right)qG^a_{\mu\nu} - \\ &-\frac{g}{\sqrt{2}\cos\theta_W}\frac{\kappa_{tqZ}}{\Lambda}\bar{t}\sigma^{\mu\nu}\left(f^L_{tqZ}P_L + f^R_{tqZ}P_R\right)qZ_{\mu\nu} - \\ &-\frac{g}{\sqrt{2}}\frac{\kappa_{tqH}}{\Lambda}\bar{t}\left(f^L_{tqH}P_L + f^R_{tqH}P_R\right)qH + h.c.,\end{aligned} \tag{1.52}$$

where $\kappa_{tq\gamma}$, κ_{tqg}, κ_{tqZ} and κ_{tqH} are dimensionless parameters that relate the strength of new coupling to the coupling constants e, g_s and g accordingly. Λ is the physics scale, related to the mass cutoff scale above which the effective theory breaks down. T^a are the Gell-Mann matrices and $\sigma^{\mu\nu} = \frac{i}{2}\left[\gamma^\mu, \gamma^\nu\right]$ transforms as a tensor under the Lorentz group. The $f^{L,R}_{tq\gamma}$, $f^{L,R}_{tqg}$, $f^{L,R}_{tqZ}$ and $f^{L,R}_{tqH}$ are chiral parameters normalized to one: $|f^L_{tqi}|^2 + |f^R_{tqi}|^2 = 1$ for $i = \{\gamma, g, Z, H\}$. The operator $P_L = \frac{1}{2}\left(1 - \gamma^5\right)$ performs a left-handed projection, while $P_R = \frac{1}{2}\left(1 + \gamma^5\right)$ performs a right-handed projection and $G^a_{\mu\nu}$ is the gauge-field tensor of the gluon from Eq. 1.3.

To express the limits on the new coupling constants in terms of the top decay branching ratios one needs to move to the partial width expressions, Γ, for FCNC decays, which for a generic decay channel X is related with the branching ratio as:

$$\mathrm{BR}(t \to X) = \frac{\Gamma(t \to X)}{\Gamma(t \to Wb)_{SM} + \sum_X \Gamma(t \to X)} \simeq \frac{\Gamma(t \to X)}{\Gamma(t \to Wb)_{SM}}, \tag{1.53}$$

assuming that $\Gamma(t \to Wb)_{SM} \gg \sum_X \Gamma(t \to X)$.

The partial width of the tree level prediction for $t \to Wb$ decay is given by:

$$\Gamma(t \to Wb) = \frac{\alpha}{16\sin^2\theta_W}|V_{tb}|^2\frac{m_t^3}{M_W^2}\left[1 - 3\frac{M_W^4}{m_t^4} + 2\frac{M_W^6}{m_t^6}\right], \tag{1.54}$$

while the partial widths of the FCNC decays are given by:

$$\begin{aligned}
\Gamma(t \to q\gamma) &= \frac{\alpha}{2}|\kappa_{tq\gamma}|^2 m_t, \\
\Gamma(t \to qg) &= \frac{2\alpha_s}{3}|\kappa_{tqg}|^2 m_t, \\
\Gamma(t \to qZ) &= \frac{\alpha_s}{4\sin^2 2\theta_W}|\kappa_{tqZ}|^2 m_t \left[1 - \frac{M_Z^2}{m_t^2}\right]^2 \left[2 + \frac{M_Z^2}{m_t^2}\right], \\
\Gamma(t \to qH) &= \frac{\alpha}{32\sin^2\theta_W}|\kappa_{tqH}|^2 m_t \left[1 - \frac{M_H^2}{m_t^2}\right]^2.
\end{aligned} \tag{1.55}$$

On the other hand, the partial width depends on the values of the free parameters of the SM. In this dissertation the following values for the free parameters are used: $m_W = 80.4$ GeV, $m_H = 125$ GeV, $m_t = 172.5$ GeV, $\alpha(m_t) = 1/128.921$, $\alpha_s(m_t) = 0.108$, $\sin^2\theta_W(m_t) = 0.2342$.

According to this, $\Gamma(t \to Wb) = 1.61$ GeV. This value is taken as the total top width Γ_t. The corresponding branching rations within the SM are:

$$\begin{aligned}
\mathrm{BR}(t \to q\gamma) &= 0.4280 \cdot |\kappa_{tq\gamma}|^2, \\
\mathrm{BR}(t \to qg) &= 7.9300 \cdot |\kappa_{tqg}|^2, \\
\mathrm{BR}(t \to qZ) &= 0.3670 \cdot |\kappa_{tqZ}|^2, \\
\mathrm{BR}(t \to qH) &= 0.0388 \cdot |\kappa_{tqH}|^2.
\end{aligned} \tag{1.56}$$

The difference in the branching ratios between the top quark decay to u-quark and the top quark decay to c-quark via FCNC interaction is a factor $|V_{ub}/V_{cb}|^2 \simeq 0.0079$ and according to reference [42] they are:

$$\begin{aligned}
\mathrm{BR}(t \to u\gamma) &\simeq 3.7 \times 10^{-16}, & \mathrm{BR}(t \to c\gamma) &\simeq 1.0 \times 10^{-14}, \\
\mathrm{BR}(t \to ug) &\simeq 3.7 \times 10^{-14}, & \mathrm{BR}(t \to cg) &\simeq 4.6 \times 10^{-12}, \\
\mathrm{BR}(t \to uZ) &\simeq 8.0 \times 10^{-17}, & \mathrm{BR}(t \to cZ) &\simeq 1.0 \times 10^{-14}, \\
\mathrm{BR}(t \to uH) &\simeq 2.0 \times 10^{-17}, & \mathrm{BR}(t \to cH) &\simeq 3.0 \times 10^{-15}.
\end{aligned} \tag{1.57}$$

1.4.2 Top FCNC Interactions Beyond the SM

Contributions of beyond the SM physics to the effective Lagrangian in Eq. 1.52 can enhance the rates of the top FCNC decays by several orders of magnitude, leading to observable branching ratios. Several BSM scenarios, listed in Sec. 1.2, predict the presence of FCNC contributions already at tree level. Theoretical predictions of the branching ratios of these models are summarized in Table 1.4 [42]. It should be noted, that $t \to qH$ is the FCNC decay mode with the largest enhancement in the BSM theories.

In QS models, due to the extra quarks, the CKM matrix is no longer unitary, which means that FCNC decays may occur at tree level. The branching ratios for different FCNC decays of the top quark for the model with a $Q = 2/3$ quark singlet is present in Table 1.4. In the model with a $Q = 1/3$ quark singlet, however, the level of non-unitarity of the CKM matrix is severely constrained by experiments and, therefore, the branching ratios are much smaller.

Channel	SM	QS	2HDM	FC 2HDM	MSSM	$\not{R}$ SUSY
$t \to u\gamma$	3.7×10^{-16}	7.5×10^{-9}	–	–	2×10^{-6}	1×10^{-6}
$t \to ug$	3.7×10^{-14}	1.5×10^{-7}	–	–	8×10^{-5}	2×10^{-4}
$t \to uZ$	8.0×10^{-17}	1.1×10^{-4}	–	–	2×10^{-6}	3×10^{-5}
$t \to uH$	2.0×10^{-17}	4.1×10^{-5}	5.5×10^{-6}	–	1×10^{-5}	1×10^{-6}
$t \to c\gamma$	4.6×10^{-14}	7.5×10^{-9}	1×10^{-6}	1×10^{-9}	2×10^{-6}	1×10^{-6}
$t \to cg$	4.6×10^{-12}	1.5×10^{-7}	1×10^{-4}	1×10^{-8}	8×10^{-5}	2×10^{-4}
$t \to cZ$	1.0×10^{-14}	1.1×10^{-4}	1×10^{-7}	1×10^{-10}	2×10^{-6}	3×10^{-5}
$t \to cH$	3.0×10^{-15}	4.1×10^{-5}	1.5×10^{-3}	1×10^{-5}	1×10^{-5}	1×10^{-6}

Table 1.4: Branching ratios for top FCNC decays in the SM, models with $Q = 2/3$ quark singlet (QS), a general (Type-III) 2HDM, a flavor-conserving (FC) 2HDM, in the MSSM and R-parity violating SUSY. Table taken from reference [42].

2HDM introduces FCNC interactions with three different types of models, depending on what fermions couple to what doublet Φ. All three type of models are summarized in Table 1.5. In Type-I models, the fermions couple to only one of the doublets, in Type-II models, down-type quarks and charged leptons couple to one doublet and the other fermions couple to the other doublet, while in Type-III models fermions couple to both doublets. Type-I and -II models impose a symmetry that forbids FCNC interactions at tree level. Nevertheless, the FCNC interactions at loop level are enhanced by charged and neutral Higgs bosons contributions. These models are also called Flavor-Conserving 2HDM (FC 2HDM). In Type-III models such restriction does not exist and FCNC interactions involving h, H and A Higgs bosons, as well as $H^{\pm}$, are allowed at tree level. The branching ratios for the general (Type-III) 2HDM and flavor-conserving 2HDM are presented in the Table 1.4.

Type	up-type quarks couple to	down-type quarks couple to	charged leptons couple to	Description
Type I	Φ_2	Φ_2	Φ_2	Fermiophobic
Type II	Φ_2	Φ_1	Φ_1	MSSM-like
Type III	Φ_1, Φ_2	Φ_1, Φ_2	Φ_1, Φ_2	FCNC at tree level

Table 1.5: Types of Two-Higgs-Doublet Model (2HDM).

In the MSSM, which is a Type-II 2HDM, the possible misalignment between the rotation matrices, which diagonalize the quark and squark sectors can lead to flavor violation with enhanced FCNC rates. In this case, where R-parity is conserved, the FCNC decays is enhanced in average by eight orders of magnitude compared to the SM. In SUSY models with R-parity violation [43], new baryon-number-violating interactions arise and the FCNC branching ratios can increase by about one order of magnitude with respect to MSSM. The branching ratios for MSSM and SUSY with R-parity violation are presented in Table 1.4.

1.5 Top Quark Production and Decay at the LHC

The top quark is a key element in the studies for deviations from SM predictions. Because of the large mass, it plays a significant role in radiative corrections to the Higgs boson mass, which suggests a special role in electroweak symmetry breaking. In this section the SM and FCNC production and decay of the top quark at the LHC are presented in detail.

1.5.1 Top Quark Production and Decay within the SM

At hadron colliders, top quarks are mainly produced in pairs ($t\bar{t}$) via the strong interaction or singly (*single top*) via the electroweak interaction. At the LHC $t\bar{t}$ events are produced mainly through *gluon-gluon fusion* $gg \to t\bar{t}$ ($\sim 85\%$ of the time), followed by *quark-antiquark annihilation* $q\bar{q} \to t\bar{t}$ ($\sim 15\%$ of the time). The Feynman diagrams for $t\bar{t}$ pair production processes are shown in Fig. 1.11.

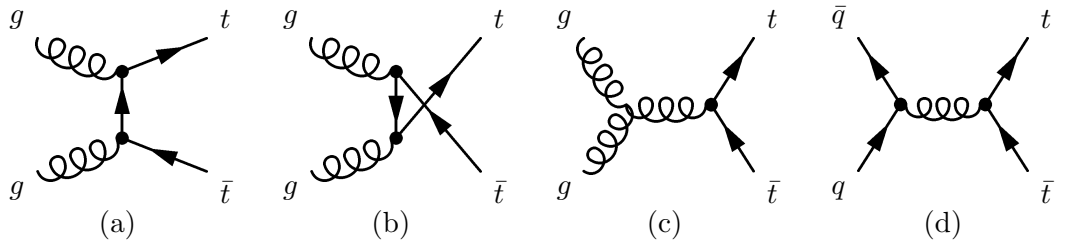

Figure 1.11: Feynman diagrams for top pair production processes at tree level: (a), (b), and (c) gluon-gluon scattering diagrams, (d) quark-antiquark diagram.

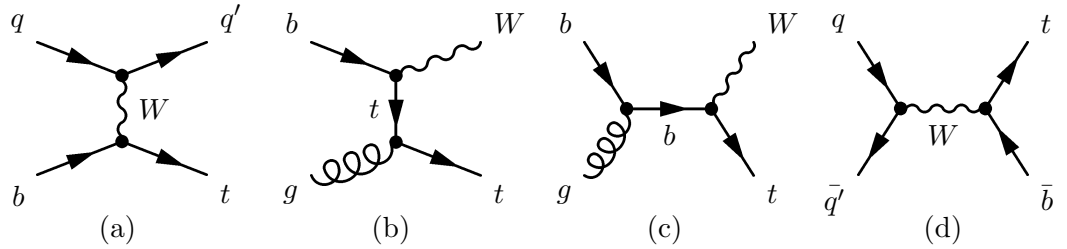

Figure 1.12: Feynman diagrams for single top production processes at tree level: (a) t-channel diagram, (b) and (c) Wt associated diagrams, (d) s-channel diagram.

The cross-section for $t\bar{t}$ production in pp collisions as a function of center-of-mass energy is shown in Fig. 1.13. The inclusive $t\bar{t}$ production cross sections at $\sqrt{s} = 8$ TeV measured by the ATLAS and CMS collaborations are $\sigma_{t\bar{t}} = 260 \pm 1(\text{stat.})^{+22}_{-23}(\text{syst.})\pm$ $\pm 8(\text{lumi.})\pm 4(\text{beam.})\text{pb}$ and $\sigma_{t\bar{t}} = 257 \pm 3(\text{stat.})\pm 24(\text{syst.})\pm 7(\text{lumi.})\text{pb}$ respectively. Both measurements are in agreement with the SM predictions.

Additionally, top quarks are produced singly with about half of the pair-production rate. Single top production can be categorized in three sub-processes: the exchange of a virtual W boson in the t-channel, or in the s-channel, and the associated production of a top quark and an on-shell W boson. The corresponding Feynman diagrams are shown in Fig. 1.12.

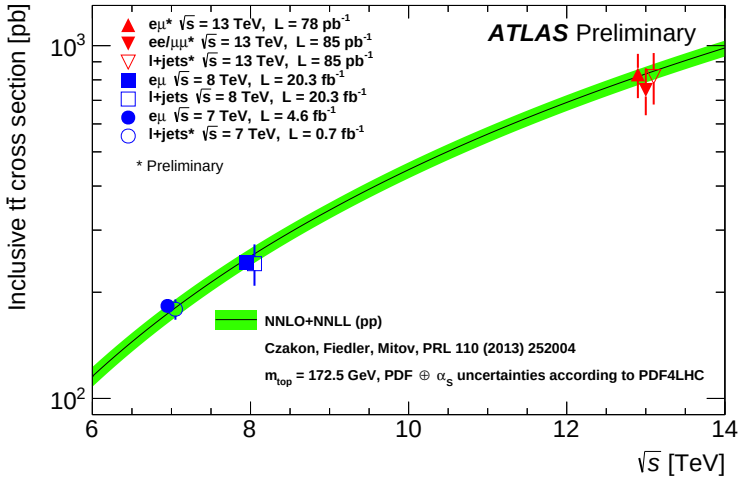

Figure 1.13: Cross-section for $t\bar{t}$ pair production in pp collisions as a function of center-of-mass energy. Results from the ATLAS experiment at $\sqrt{s} = 7$, 8 and 13 TeV are compared to the NNLO+NNLL theory predictions. Figure taken from reference [44].

As discussed in Sec. 1.4, within the SM the top quark decays in almost all cases into a W boson and a b-quark. The W boson itself decays in one third of the cases into a charged lepton and the corresponding anti-neutrino (*leptonic* decay), and two thirds of the cases into a quark-antiquark pair (*hadronic* decay). In the first case signature will be a high energetic lepton and missing energy, due to inability to detect the neutrino, while in the second case it will be two light-jets. Therefore, the final states corresponding to a $t\bar{t}$ pair can be classified in three categories, based on the decays of the two W bosons originating from the decays of the top and the anti-top quarks:

- **Fully hadronic**. Both W bosons decay to quark-antiquark pairs and cover 4/9 of the decay rate of $t\bar{t}$. The event topology of this decay is six jets, two of which are b-jets. This channel is difficult to distinguish from QCD multijet background and the kinematic reconstruction of both top quark is a challenging task because of the large combinatorial background.

- **Semi-leptonic**. One of the W boson decays hadronically, while the other decays leptonically. The event topology is therefore one isolated lepton, four jets, from which two are b-jets, and missing energy. The rate of this decay is also 4/9 of the $t\bar{t}$ decay rate, but semi-leptonic events are much easier to distinguish from QCD multijet background than fully hadronic ones due to the energetic lepton.

- **Di-leptonic**. In this channel both W bosons decay leptonically and the two leptons in the final state give a clear experimental signature. However, because of the high amount of missing energy and the inability to compute the neutrino contributions to the missing energy, the reconstruction of the top quarks is a rather difficult task. The rate of this decay is only 1/9 of the total $t\bar{t}$ decay rate.

The corresponding branching fractions are illustrated in Fig. 1.14.

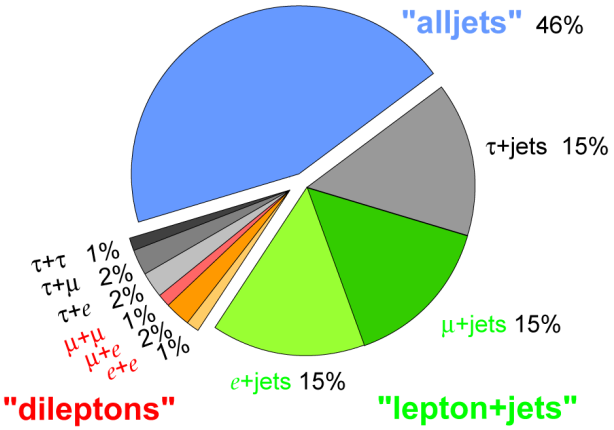

Figure 1.14: $t\bar{t}$ pair branching fractions. Figure taken from reference [45].

1.5.2 FCNC-Mediated Top Quark Production and Decay

The two main processes involving the FCNC tqH interaction at the LHC are:

- **$t\bar{t}$ production, with $t \to Hq$ decay:**. The dominant contribution is *gluon fusion*, $gg \to t\bar{t} \to tH\bar{q}$ (see Fig. 1.15a), followed by $q\bar{q}$ *annihilation*, $q\bar{q} \to t\bar{t} \to tH\bar{q}$.

- **Associated Top-Higgs production**. The associated production of a top quark and the SM Higgs boson, $pp \to tH + X$ (see Fig. 1.15b-e).

The total cross section of $pp \to tqH$ is larger than the cross section for $pp \to t\bar{t} \to tqH$ by a factor of 1.16 at $\sqrt{s} = 8$ [46]. Additionally, the associated top-Higgs production can result from the process $qg \to tH$, where the light quark participating in the FCNC interaction comes from the proton PDF (see Fig. 1.15f). Cross-sections for the different production mechanisms as a function of the hadronic center of mass energy, and normalized to the corresponding tqH couplings, are shown in Fig. 1.16 [47]. For the event selection considered in the analysis presented in this dissertation, the associated top-Higgs production mechanism is negligible. Therefore, this analysis will only consider the $t\bar{t} \to WbHq$, with $q = (u, c)$, process.

Similar to the $t \to Wb$ decay, the $t \to Hq$ decay signature depends on the Higgs boson decay modes. The Higgs boson decay branching ratios assuming $M_H = 125$ GeV are summarized in Table 1.6 [48]. The dominant decay channel is $H \to b\bar{b}$, with a branching ratio of about $\sim 58\%$, which is the Higgs boson decay mode considered in this dissertation.

Neglecting the process with two FCNC top quark decays, the final states for the $t\bar{t} \to WbHq$ process can be classified in two categories:

- **Hadronic top quark decay**. In this channel one top quark decays hadronically, $t \to Wb \to qq'b$, while the other top quark decays to a Higgs boson and light quark, $t \to Hq$. In the case of the $H \to b\bar{b}$ decay, the event topology consists of six jets, three of which are b-jets and the other jets originate from light-quarks.

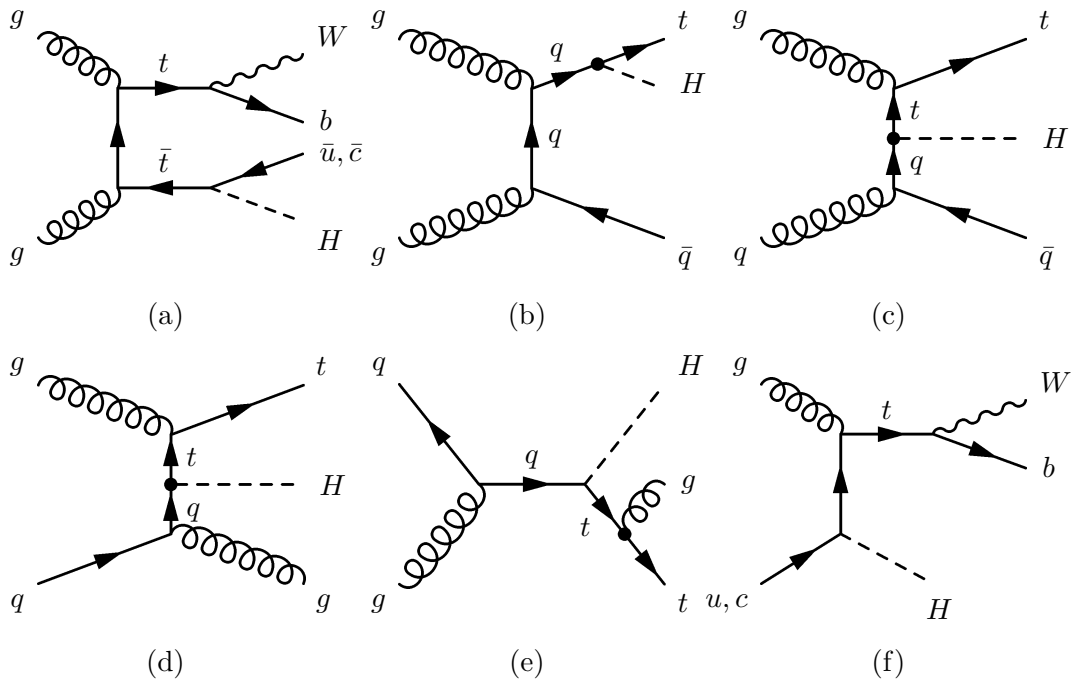

Figure 1.15: Illustrative Feynman diagrams for top-Higgs FCNC production and decay: (a) $gg \to t\bar{t} \to WbHq$, and (b-f) associated top-Higgs production.

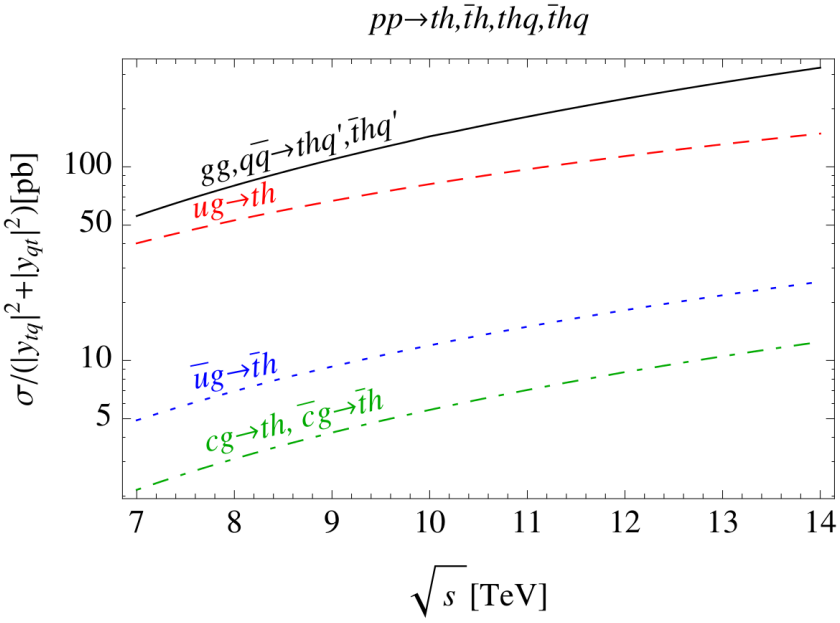

Figure 1.16: Cross-sections for $pp \to tH, \bar{t}H, tqH, \bar{t}Hq$ production induced by flavor violating top-Higgs couplings as a function of the hadronic center of mass energy and normalized to the corresponding tqH couplings. Figure taken from reference [47].

Decay Mode	Prediction
$H \to b\bar{b}$	57.70%
$H \to WW$	21.50%
$H \to gg$	8.57%
$H \to \tau\tau$	6.32%
$H \to cc$	2.91%
$H \to ZZ$	2.64%
$H \to \gamma\gamma$	0.23%
$H \to Z\gamma$	0.15%
$H \to ss$	0.02%
$H \to \mu\mu$	0.02%

Table 1.6: The SM Higgs decay branching ratios for $M_H = 125$ GeV. Values taken from reference [48].

This channel is very challenging to analyze due to the large multijet background as well as combinatorial background.

- **Leptonic top quark decay**. In this channel one top quark decays leptonically, $t \to Wb \to \ell\nu_\ell b$, while the other top quark decays to a Higgs boson and a light quark, $t \to Hq$. In the case of the $H \to b\bar{b}$ decay, the event topology consists of one isolated lepton, four jets, three of which are b-jets and one originates from a light quark, and missing energy.

Depending on the Higgs boson decay modes, different searches have been performed. For example, the $t \to Hq$, $H \to \gamma\gamma$ search considers both leptonic and hadronic top quark decays. Other searches, particularly that for $H \to b\bar{b}$ decay, as well as searches in multilepton final states exploiting $H \to WW^*, \tau\tau$ decays, rely on leptonic top quark decays.

The analysis presented in this dissertation is focused on the process $t\bar{t} \to WbHq \to \ell\nu_\ell b b\bar{b} q$.

Chapter 2

The ATLAS Experiment at the Large Hadron Collider

The Large Hadron Collider (LHC) is the world's largest and most powerful particle accelerator, designed to collide protons at a center of mass energy of 14 TeV. It was built by the European Organization for Nuclear Research (CERN) between 1998 and 2008, and is the latest addition to CERN's accelerator complex. There are four main experiments at the LHC, all run by international collaborations. There are over 10,000 scientists and engineers from more than 100 countries, as well as hundreds of universities and laboratories working at CERN's experiments. The two largest and multi-purpose experiments, ATLAS and CMS, are built to analyze the myriad of particles produced by the LHC. They have been conceived to pursuit an ambitious physics program, where at the head of the list was the discovery of the Higgs boson, achieved in 2012. Having two independently designed detectors is vital for cross-confirmation of any new discoveries made.

This chapter introduces CERN's accelerator complex (Sec. 2.1) and describes the ATLAS detector (Sec. 2.2), used to perform the physics analysis described in this dissertation.

2.1 The Large Hadron Collider

The Large Hadron Collider (LHC) [49] is a two-ring, superconducting, hadron collider located at the European Organization for Nuclear Research ("*Conseil Européen pour la Recherche Nucléaire*", CERN) facility near Geneva, Switzerland. The LHC is installed approximately 175 meters underground in a 27 km circumference tunnel. It is designed to collide protons at a center of mass energy of up to $\sqrt{s} = 14$ TeV. The accelerator rings consist of superconducting magnets and accelerating cavities. The magnets bend and focus the proton beams into a circular trajectory while radio-frequency cavities boost their energy.

The proton beams undergo several acceleration steps before reaching the desired energy. A schematic view of the acceleration chain is shown in Fig. 2.1. First, protons are obtained by ionization of hydrogen gas and accelerated up to 50 MeV in the linear accelerator LINAC2. Then they are transferred into the Proton Synchrotron Booster (PSB), where the energy is increased up to 1.4 GeV. Then the Proton Synchrotron (PS) accelerates the protons up to 25 GeV and injects them into the Super Proton

Synchrotron (SPS), which brings the energy of protons to 450 GeV. Finally the protons enter the two LHC beam pipes where the energies are boosted up to 7 TeV.

To record and study the collisions delivered by the LHC four main-experiment detectors have been built around four different interaction points, as shown in Fig. 2.1:

- **ALICE**. A Large Ion Collider Experiment [50], designed to study heavy-ion collisions;
- **ATLAS and CMS**. A Toroidal LHC ApparatuS [51] and Compact Muon Solenoid [52], the multipurpose experiments designed to study a broad range of physics processes;
- **LHCb**. LHC-beauty [53], experiment specialized in the study of heavy particles containing a b-quark;

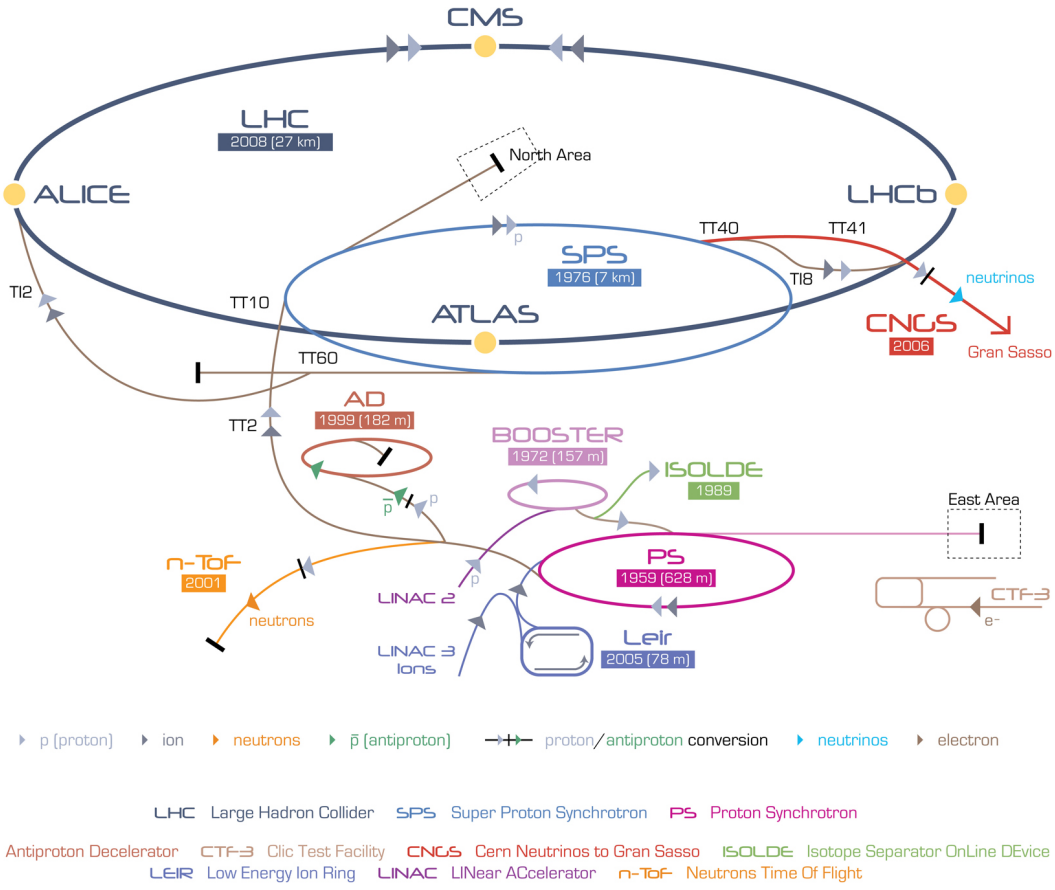

Figure 2.1: Schematic view of the CERN particle accelerator complex. The four main LHC experiments are shown at the interaction points. Figure taken from reference [54].

One of the main parameters of the accelerator is the *instantaneous luminosity* $\mathcal{L}$, defined as:

$$\mathcal{L} \equiv f_r \times \frac{n_b \times n_1 \times n_2}{A}, \tag{2.1}$$

where f_r is the collider revolution frequency, n_b is the number of bunches, n_1 and n_2 are the number of particles in each of the two bunches, and A is the beam cross-section. The event rate of a certain process, R can be obtained as the product of the process cross section and the instantaneous luminosity:

$$R \equiv \frac{dN}{dt} = \mathcal{L} \times \sigma. \tag{2.2}$$

Integrating the instantaneous luminosity over a certain accelerator active time one can obtain the *integrated luminosity*, L, which is used to describe the amount of collision data delivered by the accelerator over that period:

$$L \equiv \int \mathcal{L} dt = \frac{n_{\text{tot}}}{\sigma}, \tag{2.3}$$

where n_{tot} is the total number of produced events and σ is the process cross-section.

The first collisions at the LHC were observed on November 30, 2009. During 2010 and 2011 the LHC delivered proton collisions at a center-of-mass energy $\sqrt{s} = 7$ TeV, while in 2012 the collisions were at a center-of-mass energy $\sqrt{s} = 8$ TeV. The total integrated luminosity recorded by the ATLAS and CMS experiments in 2010 was about 45 pb^{-1} (47 pb^{-1} delivered) with a final uncertainty of $\pm 2.8\%$. In 2011 and 2012 the total integrated luminosity reached about 5.1 fb^{-1} (5.5 fb^{-1} delivered) with a final uncertainty of $\pm 1.8\%$ and 21.3 fb^{-1} (22.8 fb^{-1} delivered) with a final uncertainty of $\pm 2.8\%$ accordingly. By the time the first proton physics run (Run 1) ended in February 2013, the total integrated luminosity delivered to ATLAS and CMS had reached nearly 30 fb^{-1} and enabled the discovery of a Higgs boson.

The peak instantaneous luminosity delivered to ATLAS per day versus time during the 2012 year is shown in Fig. 2.2a. In Fig. 2.2b the delivered luminosity by the LHC to ATLAS and the luminosity recorded by ATLAS during stable beam conditions are shown. The difference in luminosity delivered to and recorded by the ATLAS experiment is due to different Data Acquisition (DAQ) inefficiencies. Of the recorded luminosity, only a part is usable for analysis, which is referred to as "good data", i.e. the data that satisfy Data Quality (DQ) requirements assessed after reprocessing (see Sec. 2.2.8).

Due to the high frequency of collisions and the high density of the bunches necessary to achieve such a high luminosity, there is a non-zero probability that several events, originating from different pp collisions, may occur simultaneously. These events are referred to as "pile-up" and are categorized as *in-time* or *out-of-time* pile-up. The first one are caused by multiple inelastic interactions of protons in the same bunch collision, while the second one occurs when the detector records events originated in different bunch-crossings. The mean number of interactions per bunch crossing $\langle\mu\rangle$, which is taken as measure of the pile-up activity, is defined as:

$$\langle\mu\rangle = \frac{A \cdot \Delta\mathcal{L}}{f \cdot n_b}, \tag{2.4}$$

where $\Delta\mathcal{L}$ is the average instantaneous luminosity over a time period $\Delta t \gg 600$ ns. The number of mean interactions per bunch crossing in 2011 and 2012 is summarized in Fig. 2.3. It amounts to $\langle\mu\rangle = 9$ and $\langle\mu\rangle = 21$ in 2011 and 2012 respectively, while in 2010 $\langle\mu\rangle$ was smaller than 3.

In Table 2.1 the relevant parameters for the LHC performance is summarized for the Run 1 operation in 2010-2013. On 13 February 2013 the LHC's Run 1 officially

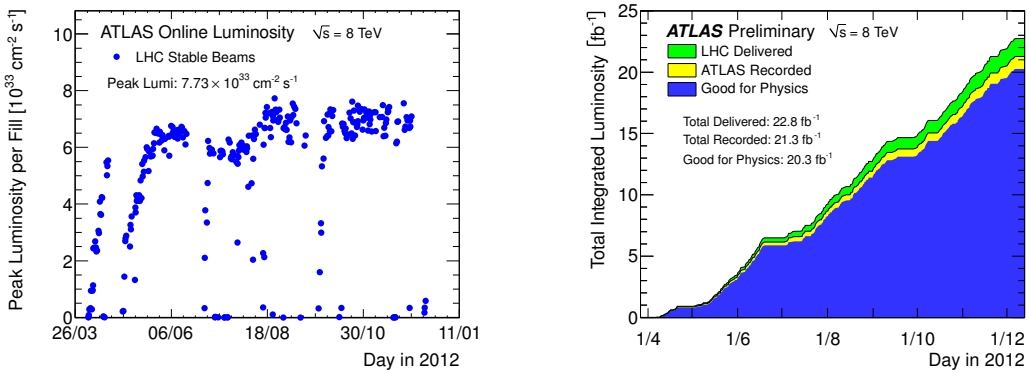

(a) (b)

Figure 2.2: (a) The peak instantaneous luminosity delivered to the ATLAS experiment per day versus time during the *pp* runs in 2012. (b) Total integrated luminosity versus time delivered by the LHC to ATLAS (in green), recorded by the experiment (in yellow) and selected as good data for analysis (in blue) for *pp* collisions at $\sqrt{s} = 8$ TeV in 2012. Figures taken from reference [55].

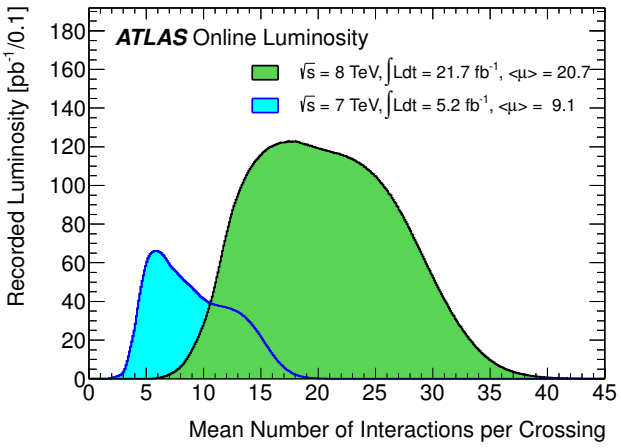

Figure 2.3: Mean number of interactions per beam crossing during the 2011 (green) and 2012 (blue) LHC runs. Figure taken from reference [55].

ended, and it was shut down for planned upgrades. "Test" collisions restarted in the upgraded collider on 5 April 2015, reaching 6.5 TeV per beam on 20 May 2015. The LHC's Run 2 commenced on schedule on 3 June 2015 and by the end of 2015 it had delivered an integrated luminosity of 4.2 fb^{-1} to the ATLAS and CMS experiments.

Parameters	Design value	2010	2011	2012
Beam energy (TeV/c)	7	3.5	3.5	4
Beta function β^*(m)	0.55	2.0/3.5	1.5/1.0	0.6
Bunch spacing (ns)	25	150	75/50	50
Max. # bunches/beam	2808	368	1380	1380
Max. # protons/bunch	1.15×10^{11}	1.2×10^{11}	1.45×10^{11}	1.7×10^{11}
Peak luminosity ($cm^{-2}s^{-1}$)	1.00×10^{34}	2.1×10^{32}	3.70×10^{33}	7.7×10^{33}
Emittance $\epsilon_n(\mu rad)$	3.75	2.0	2.4	2.5
Max. $\langle\mu\rangle$	19	4	17	37

Table 2.1: Overview of the parameters for the LHC performance comparing the design values with their time evolution during the Run 1 operation in 2010-2013.

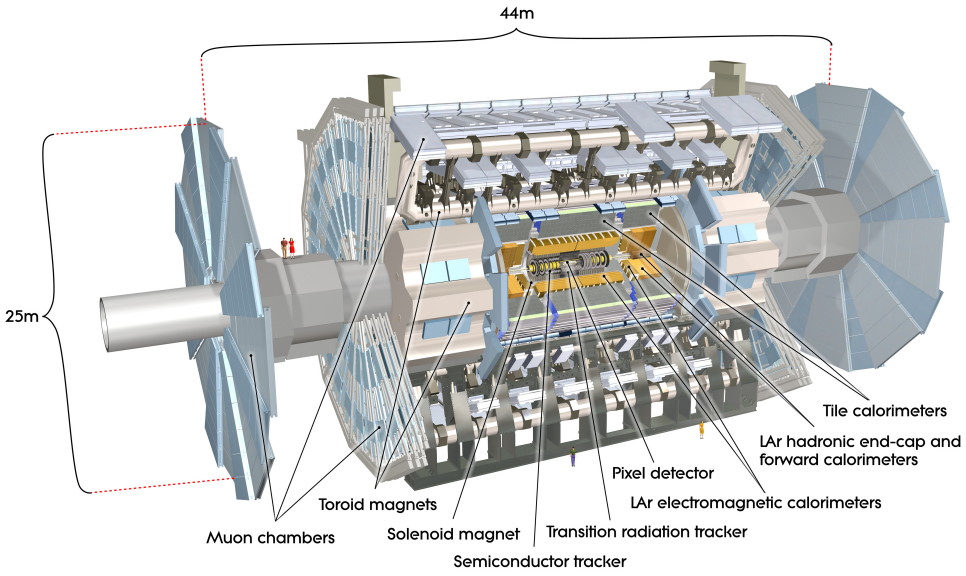

Figure 2.4: Drawing of the ATLAS detector showing the different subdetectors and the magnet systems. Figure taken from reference [51].

2.2 The ATLAS Experiment

ATLAS (A Toroidal LHC ApparatuS) [51] is one of two general-purpose experiments at the LHC, aimed at exploring a vast range of physics scenarios and designed to measure the particles at unprecedented energies and instantaneous luminosity. It is the biggest detector of its kind ever built: about 46 m long, 25 m wide and weights

7000 t. The ATLAS detector is characterized by a full coverage of the space around the *pp* interaction point and complete containment of the particles produced in the collision.

When a collision which may be of interest occurs, this usually means that some heavy and therefore short-lived particle or resonance has been created. In general these short lived particles quickly decay into two or more new particles, which in turn continue into the detector. These new particles carry information from the original event which produced them, and the purpose of the ATLAS detector is to record as much information as possible about the outgoing particles. This is accomplished through different detecting subsystems, that identify the particles and measure their momentum and energy (see Fig. 2.4):

- **Magnets**. The magnet system, which curves the charged particles so their momenta can be measured.

- **Inner Detector**. Immersed in a solenoidal magnetic field, it is used to identify and measure the momenta of charged particles and to identify the interaction vertices and the displaced vertices.

- **Calorimeters**. Consists of electromagnetic and hadronic calorimeters, used to identify and measure the energy of neutral and charged particles. They are designed to stop most types of particles, except muons and neutrinos.

- **Muon Spectrometer**. A muon detection system used to detect and measure the properties of muons. Because muons minimally interact with the other parts of the detector and have long lifetimes, they are identified and measured in the outermost detector layer.

The reason that detectors are divided into many components is that each component measures a specific set of particle properties. In Fig. 2.5 the interactions of various particles with the different components of the detector are shown. Each particle type has its own "signature" in the detector. For example:

- Charged particles, like electrons and protons, are detected both in the tracking system and the calorimeters.

- Neutral particles, like neutrons and photons, are not detectable in the tracking system. Photons are detected by the electromagnetic calorimeter, while neutrons are evidenced by the energy they deposit in the hadronic calorimeter.

- Muons are hard to stop and generally exit the detector completely. Similar to the tracking system, the muon detection employs a series of tracking chambers to measure the trajectories of muons, which are bent by a toroidal magnet field.

- Neutrinos do not produce a signal in any of the detectors because they rarely interact with matter. Their presence is inferred as missing transverse momentum.

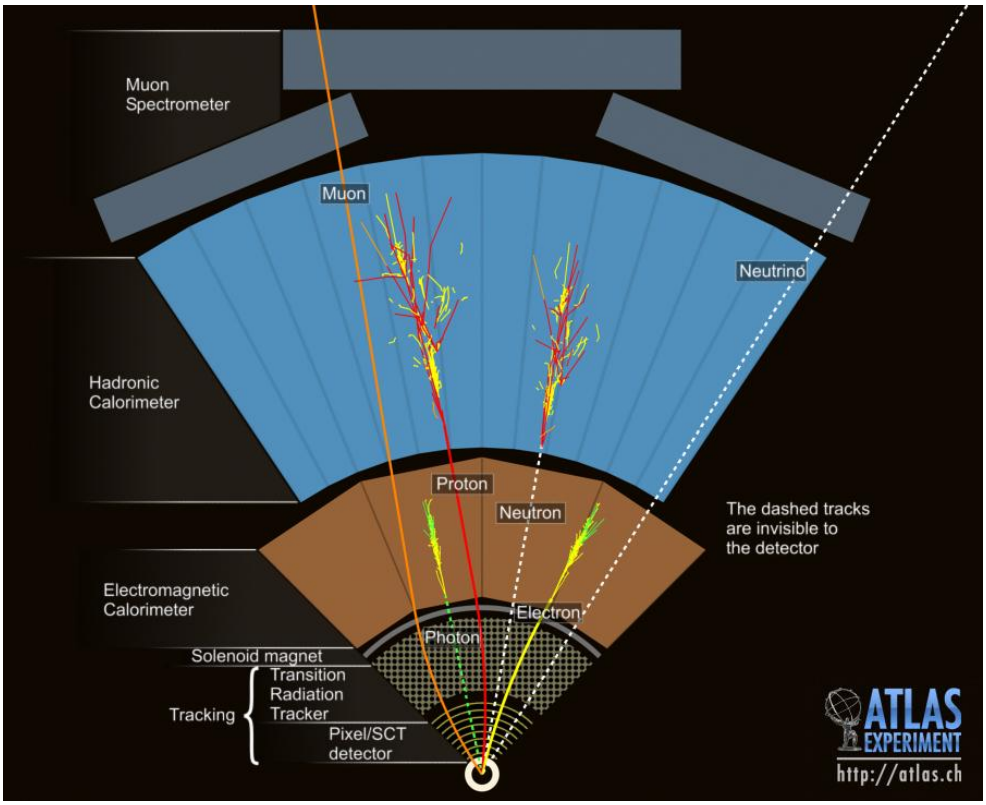

Figure 2.5: Drawing of the detection of particles going from the interaction point through the whole detector. Figure taken from reference [56].

2.2.1 Coordinate System

In Fig. 2.6 the coordinate system used in the ATLAS detector is shown. The origin of three dimensional XYZ right-handed coordinate system is taken at the nominal Interaction Point (IP) in the center of the detector. The X-axis points toward the center of the LHC ring, the Y-axis points upward, and the Z-axis is along the beam direction. The detector half at positive Z-values is referred to as the "A-side", the other half the "C-side". The transverse plane is often described in terms of $R-\phi$ coordinates, with the azimuthal angle ϕ measured around the beam axis, ranging between $-\pi$ and $+\pi$ with respect to the X-axis. The polar angle θ is measured from the positive Z-axis and varies from 0 to π.

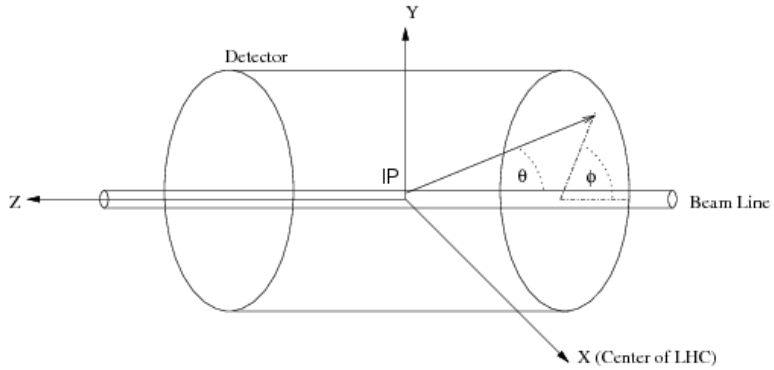

Figure 2.6: The ATLAS coordinate system. Figure taken from reference [57].

Since the momentum and initial energy of the colliding partons along the Z-axis is unknown, it is useful to define the transverse component of variables of interest, like the energy and the momentum, as their projection on the XY plane, which are boost-invariant along the Z-axis:

$$E_T = E \sin\theta, \quad p_T = p \sin\theta. \tag{2.5}$$

Another common variable used at hadron colliders to describe the polar distribution and preferred to the simple polar angle θ is the rapidity:

$$y \equiv \frac{1}{2} \ln\left(\frac{E + p_Z}{E - p_Z}\right), \tag{2.6}$$

which, for vanishing particle mass, is equal to the pseudorapidity η:

$$\eta \equiv -\ln\left(\tan\frac{\theta}{2}\right). \tag{2.7}$$

The advantage of pseudorapidity over θ is that pseudorapidity difference $\Delta\eta$ is boost-invariant along the Z-axis. For visualization the correspondence between the polar angle and the pseudorapidity for some values are reported in Table 2.2.

The distance between two particles in $\eta - \phi$ space is then defined as:

$$\Delta R \equiv \sqrt{(\Delta\eta)^2 + (\Delta\phi)^2}. \tag{2.8}$$

ATLAS covers the pseudorapidity region up to $|\eta| < 4.9$, while physics analyses typically consider objects restricted to $|\eta| < 2.5$.

θ	0^o	5^o	10^o	20^o	30^o	45^o	60^o	80^o	90^o
η	∞	3.13	2.44	1.74	1.31	0.88	0.55	0.18	0

Table 2.2: Pseudorapidity vs polar angle values.

2.2.2 Magnet System

A magnetic field is used in the ATLAS detector to measure the momenta of charged particles. When a charged particle moves in a magnetic field, it bends in a circular motion in the plane perpendicular to the magnetic field. High momentum particles bend very little while low momentum particles bend more. The deflection can be measured, and thus the particle momentum can be determined. In addition, the direction in which the deflection occurs determines the charge of the particles.

The magnet system in the ATLAS detector is composed of four large superconducting magnets: one central solenoid and three "open-air" toroids, as shown in Fig. 2.7.

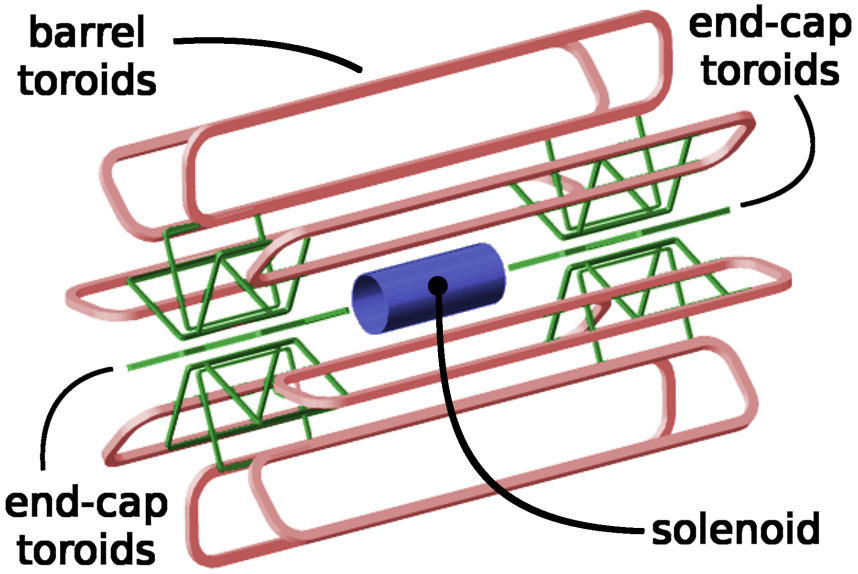

Figure 2.7: Schematic view of the magnet system of the ATLAS detector. Figure taken from reference [58].

The central solenoid magnet provides a 2 Tesla axial magnetic field which bends charged particles in the ϕ-direction and gives rise to its curvature in the Inner Detector. Placed between the Inner Detector and the Electromagnetic CALorimeter (ECAL), it is only 5.8 m long, has an inner diameter of 2.46 m and is 45 mm thick. The cooling of the magnets is done with liquid Helium, sharing the cryostat with the ECAL.

The toroidal magnet system produces the magnetic field needed by the muon spectrometer to bend muons in the η direction. It consists of the eight air-core superconducting barrel loops and two end-cap air toroidal magnets. The barrel toroid generates a magnetic field of 3.9 Tesla, has a length of 25 m, an inner radius of 4.7 m and an outer radius of 10.05 m. The end-cap magnet produces a magnetic field of 4.1 Tesla and is rotated by 22.5^o with respect to the barrel toroid to give a radial overlap and to optimize the bending power in the transition region between the two. Each coil of the

barrel toroid has an individual vacuum vessel, while the end-caps toroid systems have a single integrated cooling system each. The choice of the "open air" toroid configuration was made to improve the muon reconstruction performance without relying on the Inner Detector. Such configuration allows to efficiently generate the magnetic field over a large volume with a reduced amount of material. This minimizes the amount of multiple scattering, [1] which represents one of the factors limiting the muon momentum resolution.

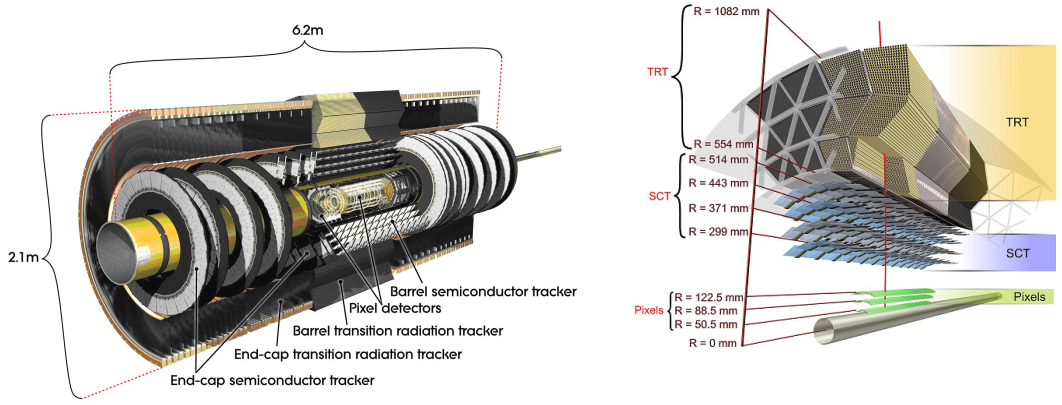

(a) (b)

Figure 2.8: (a) Cut-away view of the ATLAS Inner Detector. (b) Detailed schematic of the barrel section of the ID showing the three subsystems and reporting the distance to the center of the beam pipe. Figures taken from reference [51].

2.2.3 Inner Detector

The Inner Detector (ID) is the subsystem closest to the IP, tracking the charged particles arising from collisions and allowing the measurement of their momentum and the reconstruction of vertices with excellent position resolution. It combines the Pixel Detector as the innermost component followed by microstrip detectors of the Semi-Conductor Tracker (SCT) with tracking straw tubes in the outer Transition Radiation Tracker (TRT). Typically, for each track about 36 measurement points are provided by the ID, to which the SCT contributes four space points and the pixel detector three points. The ID system provides coverage for tracks with $|\eta| < 2.5$.

The outer radius of the ID is 1.15 m, and the total length is about 7 m. In the barrel region the high-precision detectors are arranged in concentric cylinders around the beam axis, while the end-cap detectors are mounted on disks perpendicular to the beam axis. A schematic view of the ID is shown in Fig. 2.8a.

2.2.3.1 Pixel Detector

The pixel detector is the innermost part of the ID. It faces the highest amount of particle flux due to its closeness to the beam pipe, corresponding to the largest radiation

[1] Multiple scattering is defined as the electromagnetic interaction of a charged particle with the atomic structure of the medium. The result of the interaction with the very large number of nuclei and electrons results into a random smearing of the momentum of the incoming particle.

damage and hit occupancy in ATLAS. The silicon detectors are chosen to fit this requirement. Due to the fine granularity of the detector segments, they also provide a high precision set of measurements close to the IP. Each pixel of silicon detector has a size of $50 \times 400\ \mu m^2$, resulting in total ~ 80.4 million readout channels, achieving a very fine granularity. The pixel detector is subdivided into three barrel layers in its center, at radii of 50.5, 88.5 and 122.5 mm respectively, and three disks on either side for the forward detection, at a distance of 49.5, 58 and 65 cm respectively in the ϕ-direction from the center of the detector, as shown in Fig. 2.8b. With the total length of approximately 1.4 m, it typically detects three hits per traversing particles with $|\eta| < 2.5$, with the transition between barrel and disk structures being at $|\eta| \approx 1.9$. The position resolution achieved is 10 μm in $R-\phi$, and 115 μm in Z (R) in the barrel (end-cap) region. The very first layer is called B-layer and, thanks to its position really close to the IP (50.5 mm), it allows for the reconstruction of secondary vertices associated with the production of long-lived particles such as b-hadrons. This information is very useful to identify jets originating from the fragmentation of b-quarks.

2.2.3.2 Semiconductor Tracker

The SCT forms the middle subdetector of the ID. It consists of four nested cylindrical barrels in the center and nine disks in each of two end-caps, as shown in Fig. 2.8a. The barrels cover a region from 30 to 52 cm in the ϕ-direction and have an active length of 153 cm, centered around the IP. The respective barrel layers are fully covered by 32, 40, 48 and 56 rows of twelve identical modules, overlapping in a tile structure in order to ensure full coverage, making a total 2112 modules. The end-caps consist of nine disks each placed between Z=83.5 to Z=278.8 cm and ϕ-direction ranging from 25.9 to 56 cm. The discs are placed in three rings overlapping azimuthally, two on one side, one on the other side, in order to achieve full coverage.

The SCT barrel modules are made of four sensors, glued in pairs on either side of a thermally highly conductive baseboard. The sensors are approximately 6×6 cm^2 p-in-n silicon wafers of 300 μm thickness. Each sensor has 768 strips with 80 μm pitch.

The end-cap modules are made of two or four wedge-shaped sensors of varying size depending on their position on the end-cap rings. The strip pitch varies from 57 μm on the inner edge of the innermost sensors to 94 μm on the outer edge of the outermost sensors. The sensor pairs are mounted on a thermally highly conductive carbon base board that provides cooling. The SCT sensors are operated at -7^oC to prevent reverse annealing radiation damage. The spatial resolution achieved is 17 μm in $R-\phi$ and 580 μm in Z (R) in the barrel (end-cap) region.

2.2.3.3 Transition Radiation Tracker

The TRT is the outermost part of the ID. It provides charged particle tracking based on the use of straw detectors with 420,000 readout channels, as well as electron identification through transition radiation measurements. The TRT consists of 144 cm long cylindrical barrel layers ranging from 56 to 108 cm in the ϕ-direction and two end-caps ranging from 84 to 271 cm in Z and 64 to 103 cm in the ϕ-direction. Both barrel and end-cap parts contain similar carbon-polyimide straw tubes of 4 mm in diameter which are equipped with a 30 μm diameter gold-plated W-Re wire. The straws are filled with a nonflammable gas mixture of 70% Xe, 27% CO_2 and 3% O_2, the first component being the main gas in which ionization occurs and the latter had to be

added to avoid etching problems with the glass joints that hold the wires. The straws are operated in proportional mode with the electrodes being on approximately 1530 V bias. The 52544 straws in the barrel form two modules embedded in polypropylene radiator foils in which transition radiation is produced. The modules are then formed into three rings to compose the entire barrel such that the straws are parallel to the z-axis. The end-caps are composed of 160 planes of 122880 radially arranged straws of 37 cm length. The TRT is only segmented in $R-\phi$, and it provides a resolution of 130 μm per straw. The covered pseudorapidity region is $|\eta| < 2.0$. A schematic view of the TRT is presented in Fig. 2.8b.

2.2.3.4 Inner Detector Combined Performance

The three ID subsystems give very precise $R-\phi$ and Z measurements, as well as good track pattern recognition. Using the combined information from the three subdetectors the transverse momentum resolution, measured with cosmic muons calibration runs [59], is:

$$\frac{\sigma_{p_T}}{p_T} = P_1 \oplus P_2 \times p_T, \tag{2.9}$$

where $P_1 = 1.6 \pm 0.1\%$ and $P_2 = (53 \pm 2) \times 10^{-5}$ GeV^{-1}. This gives a resolution of $\sim 1.6\%$ for tracks with $p_T \sim 1$ GeV and $\sim 50\%$ for tracks with $p_T \sim 1$ TeV.

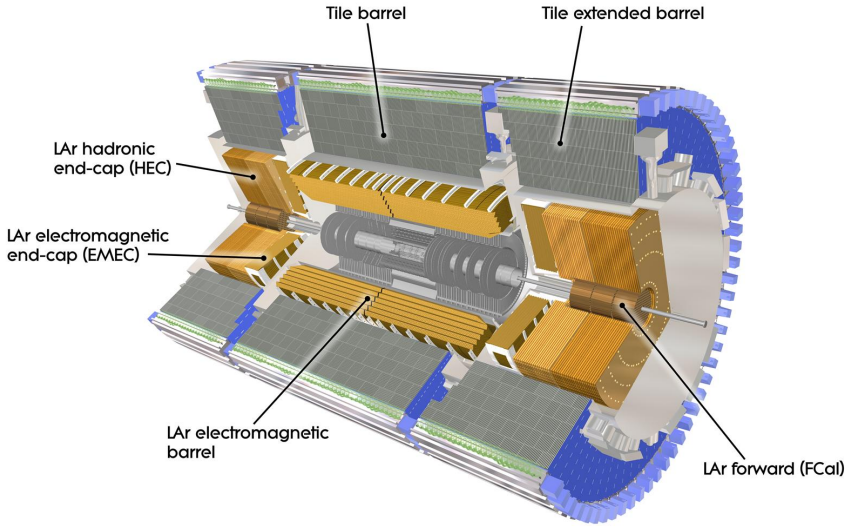

Figure 2.9: Schematic view of the calorimeter system of the ATLAS detector. Figure taken from reference [51].

2.2.4 Calorimeters

The calorimeter system is located directly outside the magnetic solenoid and consists of two parts: the Electromagnetic CALorimeter (ECAL), made of liquid argon and forming the innermost layer, and the hadronic calorimeter, which is made up of the Tile Calorimeter (TileCal) and the Liquid Argon (LAr) calorimeters, forming the outer

layer. The ECAL absorbs the energy from particles that interact electromagnetically while the hadronic calorimeter absorbs the energy of particles that interact via the strong force. A schematic view of the calorimeter system is presented in Fig. 2.9.

Besides particles energy measurement, the calorimeters provide particle identification information, discriminating electrons, photons and jets, and the determination of the missing transverse energy. The coverage area of the full system is up to $|\eta| < 5$ and an almost full coverage in the ϕ-direction. The relative energy resolution of the calorimeter is usually parameterized by:

$$\frac{\sigma_E}{E} = \frac{a}{\sqrt{E}} \oplus \frac{b}{E} \oplus c, \tag{2.10}$$

where a is the *stochastic* term, related to how the shower develops in the sampling calorimeter; b is the *noise* term, which includes the contribution from electronic noise and pile-up energy fluctuation; c is the *constant* term, that depends on calibration, shower containment, inactive material and on the linearity of the response. The experimental values for these terms are respectively $a \simeq 10\%$, $b \simeq 17\%$ (without pile-up) and $c = 0.7\%$ for the ECAL [60], while for the hadron calorimeter the values are $a \simeq 50\%$ and $c = 5\%$ [61].

Electromagnetic Calorimeter

The ECAL [60] is designed to measure electrons and photons energies in the range from 50 MeV to 3 TeV and cover a range of $|\eta| < 3.2$. It uses liquid argon detector with accordion-shape electrodes as active material and lead plates as absorber. The liquid argon solution was adopted for its intrinsic linear behavior, high ionization yield, stability and resistance to radiation. To collect the ionization electrons from the interaction a high voltage is applied between absorber plates, which also amplifies the signal strength. In the barrel region the ECAL is referred to as ElectroMagnetic Barrel (EMB), which is divided into two identical semi-barrels EMBA and EMBC, and covers the pseudorapidity region $|\eta| < 1.457$. Two end-cap detectors, referred to as ElectroMagnetic End-Cap (EMEC), are divided into two coaxial wheels and cover the pseudorapidity region $1.375 < |\eta| < 3.2$.

The EMB is segmented into layers with very different depths and cell structure in the $\eta - \phi$ plane, as shown in Fig. 2.10. The first layer has a thickness of 4.3 X_0 and is segmented in η with thin readout strips of $\Delta\eta \times \Delta\phi = 0.0031 \times 0.098$, providing precise measurement of the direction in pseudorapidity of the particles. The second layer has a thickness of 16 X_0 and represents most of the thickness of the calorimeter ($\sim 70\%$). It is divided in towers of size of $\Delta\eta \times \Delta\phi = 0.025 \times 0.025$ and provides the position measurement of the cluster. Most of the shower energy ($\sim 95\%$) is deposited in a matrix of 3×7 towers in $\Delta\eta \times \Delta\phi$. The third layer, only 2 X_0 thick, is used to estimate the amount of energy lost beyond the ECAL. Towers in this section have a dimension of $\Delta\eta \times \Delta\phi = 0.05 \times 0.0245$.

A design similar to the EMB has been used for the EMEC, which is divided into two wheels covering the ranges $1.375 < |\eta| < 2.5$ and $2.5 < |\eta| < 3.2$. The inner wheel has a coarser granularity in $\eta - \phi$, limiting the region devoted to precision physics to $|\eta| < 2.5$. In the central region an additional pre-sampler layer is placed in front of the EMB and the EMEC at $|\eta| < 1.8$ to correct for energy lost in front of the calorimeter.

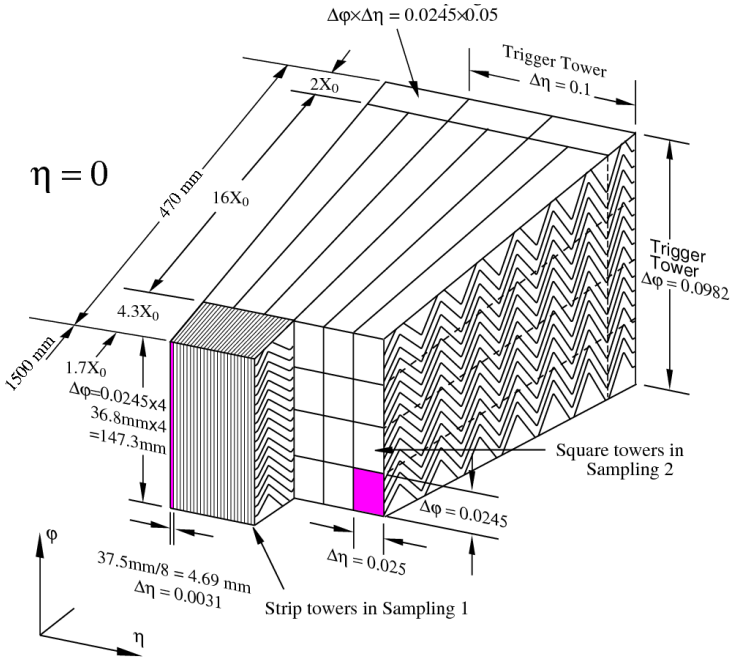

Figure 2.10: Schematic view of the Electromagnetic barrel calorimeter. Figure taken from reference [60].

Hadronic Calorimeter

Hadronic calorimeters are designed to completely absorb high-energy hadrons, which will deposit only part of their energy in the electromagnetic calorimeter. It is divided in three components: the Tile Calorimeter (TileCal) in the central barrel and the two extended barrels, the LAr Hadronic End-Cap (HEC) calorimeter, and the LAr Forward CALorimeter (FCAL). Each component has its own particular technology and choice of material.

The TileCal [62] is placed just after the ECAL and measures the energy and position of jets and isolated hadrons. It is divided into one long barrel with $|\eta| < 1.0$ and two extended barrels with $0.8 < |\eta| < 1.7$. Both type of barrels are segmented into 64 modules in ϕ, each of $\Delta\phi \sim 0.1$. Each module is further segmented radially into three layers, with the thickness of approximately 1.5, 4.1, 1.8 hadronic interaction lengths (λ) in the long barrel and 1.5, 2.6, 3.3 λ in the extended barrels. The $\Delta\eta \times \Delta\phi$ segmentation of each module is 0.1×0.1 in the first two radial layers and 0.2×0.1 in the third one.

The TileCal in the barrel region is made of steel tiles as absorber with plastic scintillator tiles as active material. Wavelength-shifting fibers coupled to the scintillator tiles on either ϕ edge of the cells collect the light produced and are read out by two photo-multiplier tubes (PMT), each linked to one readout channel. The readout channels are grouped into cells forming a pseudo-projective geometry in η. A schematic view of TileCal is shown in Fig. 2.11.

The HEC collects the energy from particles that are not completely contained in the EMEC and in particular is used to reconstruct jets and the missing transverse

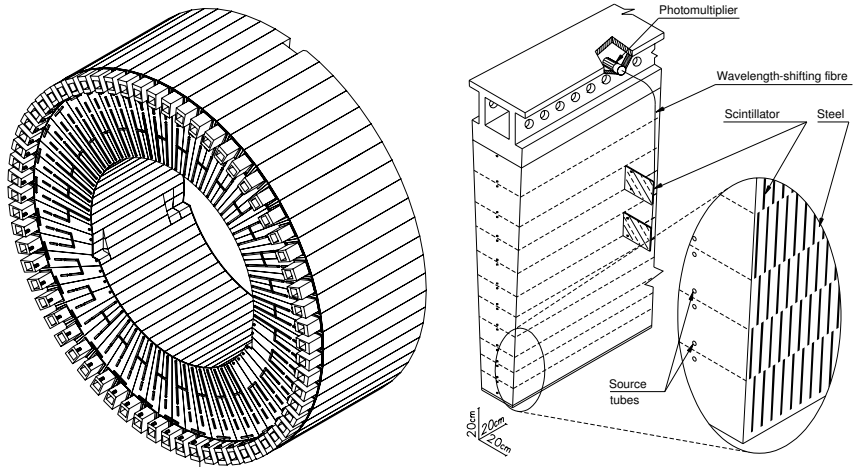

Figure 2.11: Schematic view of the Hadronic barrel calorimeter. Figure taken from reference [60].

energy. It is made of copper as passive material and LAr as active material, chosen for its radiation hardness in a region exposed to a significant amount of particle flux. Each HEC is composed of two independent wheels with different segmentation, varying with η. In the region $1.5 < |\eta| < 2.5$, the $\Delta\eta \times \Delta\phi$ segmentation is 0.1×0.1 in the first two longitudinal layers, and 0.2×0.1 in the last one. In the region $2.5 < |\eta| < 3.2$, the $\Delta\eta \times \Delta\phi$ segmentation is 0.2×0.2 in all three samples.

The FCAL covers the very forward region of pseudorapidity $3.1 < |\eta| < 4.9$, making the calorimeter system achieve its good hermeticity and minimize the energy losses. It has an electromagnetic part that uses copper as absorber and two hadronic compartments with tungsten as passive material. The liquid argon is used as active material.

2.2.5 Muon Spectrometer

The last subsystem of ATLAS detector is the muon spectrometer [63]. It is designed to detect charged particles exiting the barrel and end-cap calorimeters. Due to the total large value of λ of the previous systems, muons are the only charged particles expected to reach this detector. The muon spectrometer consists of four subdetectors: Monitored Drift-Tube (MDT) chambers, Cathode Strips Chambers (CSC), Resistive Plate Chambers (RPC) and Thin Gap Chambers (TGC), as shown in Fig. 2.12.

MDTs and CSCs chambers have precise position and momentum measurement for track detection. These chambers, with a combination of toroidal superconducting magnets, provides a measurement of the momentum of muons for $|\eta| < 2.7$.

RPCs and TGCs chambers are for the triggering and time measurements. These chambers provide p_T thresholds, the possibility to identify the bunch-crossing thanks to their time resolution, and the measurement of the track coordinate in the ϕ plane with a precision ranging between 2 and 10 mm.

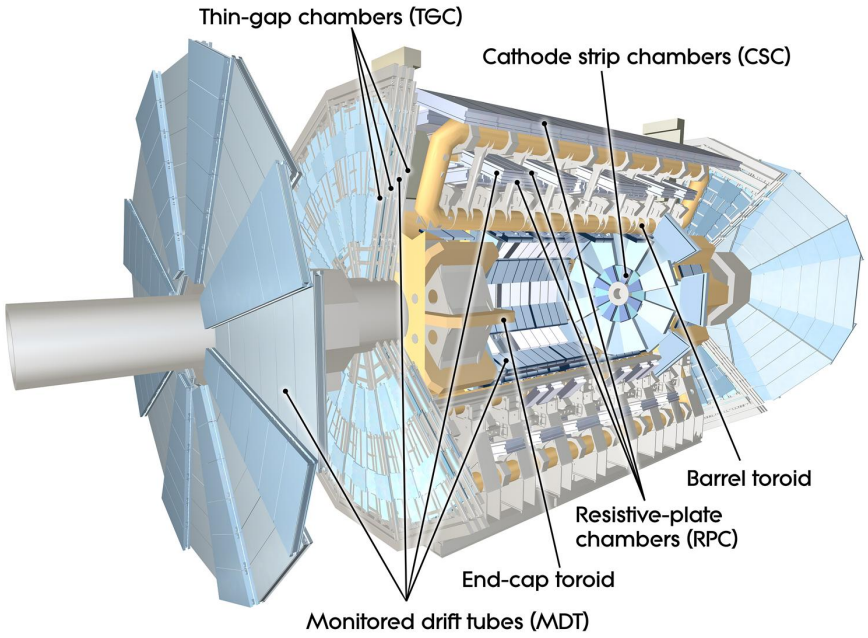

Figure 2.12: Schematic view of the muon spectrometer of the ATLAS detector. Figure taken from reference [51].

In standalone measurements the muon spectrometer has 10% resolution for a 1 TeV muon track, and muon tracks can be measured with good precision in the p_T range from 3 GeV to 3 TeV.

Monitored Drift-Tube Chambers

MDTs are proportional chambers used in the barrel region with pseudorapidity coverage of $|\eta| < 2.0$. It is based on pressurized drift tubes made of aluminum with a diameter of 30 mm and length varying from 0.9 m to 6.2 m. Tubes are filled with a 93% argon and 7% carbon dioxide mixture and the anode is a 50 μm tungsten-rhenium wire producing a radial electric field. Each chamber is composed by a group of six or eight tubes placed transverse to the beam axis. This number of tubes allows for a very good track reconstruction and high reduction of fake tracks from random associations of background hits, providing a resolution on position of 80 μm for an individual tube, 40 μm for a chamber and 30 μm for the three layers of MDTs.

Cathode Strip Chambers

CSCs are multi-wire proportional chambers used in end-cap regions and cover the pseudorapidity region of $2.0 < |\eta| < 2.7$. They are arranged in a system of two end-caps with eight chambers each. Each chamber contains four multi-wire proportional chambers with wires oriented in the radial direction, spaced by 2.5 mm and filled with the same gas mixture of argon and carbon dioxide as for the MDT chambers. The cathode strips are oriented either perpendicularly to the anode wires, giving the precision coordinate, or parallel to the wires, giving the transverse coordinate. The

resolution provided by the interpolation between the charges induced in neighboring cathode strips ranges between 50 and 70 μm.

Resistive Plate Chambers

For the trigger system RPCs are used in the barrel region and cover the pseudo-rapidity region of $|\eta| < 1.05$. They are filled with a gas mixture of $C_2H_2F_4$ (94.7%), Iso-C_4H_{10} (5%) and SF_6 (0.3%) between two resistive Bakelite plates, spaced by 2 mm. RPCs measure six points per coordinate for each particle, quickly collecting the avalanches with two orthogonal sets of pick-up strips that provides a position resolution of 1 cm in each plane and 1 ns time resolution, allowing for individual bunch crossing discrimination. RPCs also provide the ϕ coordinate for the tracks, since MDT chambers only give the η coordinate.

Thin Gap Chambers

TGCs are multi-wire proportional chambers, similar to the CSCs. They are used in the end-cap regions and cover the pseudorapidity region of $|\eta| < 2.4$. For a fast collecting time, they have 1.8 mm wire-to-wire separation and 1.4 mm wire-to-cathode separation. Each chamber is filled with a highly quenching gas mixture of 55% CO_2 and 45% n-C_5H_{12}, and provide a spatial resolution of about 1 mm and a time resolution of 5 ns.

2.2.6 Forward Subdetectors and Luminosity Measurement

To reach the ultimate precision in measurement of processes of interest a good determination of the integrated luminosity is needed. The instantaneous luminosity, $\mathcal{L}$, defined in Eq. 2.1, can be rewritten as:

$$\mathcal{L} = \frac{\mu_{vis} \times n_b \times f_r}{\sigma_{vis}}, \tag{2.11}$$

where f_r is the collider revolution frequency, n_b the number of bunches and σ_{vis} the visible inelastic cross section (total inelastic cross section times the detector acceptance and efficiency). The visible interaction rate per bunch crossing is denoted as μ_{vis}. It is extracted mainly from the signals coming from specific luminosity detectors. The simplest algorithm consists in "simple counting of bunch crossings where detectors reported a signal, but more refined algorithms are used [64], in particular when the pile-up contamination is no longer negligible. In order to use the measured μ_{vis} for luminosity determination, each detector and algorithm must be calibrated by determining its visible cross section σ_{vis}. The calibration technique exploits the *van der Meer* scans [65]. These are special low-intensity LHC runs where the beam separation in the transverse planes is varied (scanned) in order to determine the beams overlap profile. Through the determination of the beam lateral profile the absolute luminosity of the particular run can be inferred using Eq. 2.1, and σ_{vis} can be determined for each subdetector.

ATLAS is equipped with subdetectors in the forward regions used for monitoring tasks. The Minimum Bias Trigger Scintillators (MBTS), embedded in the structure of TileCal extended barrel modules, consist of 32 scintillator paddles assembled in two

disks covering the pseudorapidity region $2.09 < |\eta| < 3.84$ and are used to detect minimum bias activity and to indirectly measure the luminosity. The main detectors for luminosity measurement are listed below:

LUCID (Luminosity Measurements Using Cherenkov Integrating Detector)

LUCID is a Cherenkov detector specifically designed for luminosity measurement. It consists of 16 aluminum tubes surrounding the beam pipe at 17 m from the interaction point. Each tube is filled with C_4F_{10} and is coupled to a photo-multiplier in the back-end.

BCM (Beam Conditions Monitor)

BCM consists of 1 cm^2 diamond detectors located at $Z = \pm 184$ cm around the beam pipe. Their fast readout and good time resolution (0.7 ps) allow them to provide luminosity information for each bunch crossing. At the same time, they are also employed to trigger on beam losses and induce the dump of the beam, thus protecting the silicon detectors from damage that might result from an uncontrolled beam.

ALFA (Absolute Luminosity For ATLAS)

ALFA is a subdetector that is only activated during special runs. It consists of eight scintillating fibers detectors placed at 240 m from the interaction point inside roman pots, above and below the beam pipe.

In addition, cross-checks of the luminosity measurement have been performed using information from other standard subdetectors: counting of primary vertices reconstructed by the ID and integrated signals from the Tile and forward calorimeter. The precision achieved is of a few % depending on the data-taking year.

2.2.7 Trigger and Data Acquisition System

Due to technical limitations (space, bandwidth), not every LHC collision can be recorded by the ATLAS detector. At nominal operation conditions, bunches of 10^{11} protons will cross each other at 40 MHz, resulting in ∼25 proton-proton interactions per bunch crossing. Nevertheless, only a small fraction of this ∼1 GHz event rate results in interesting physics processes. The Trigger and Data Acquisition (TDAQ) system of the ATLAS detector was designed to select a manageable rate of such events for permanent storage and further analysis, reducing the event rate from about ∼1 GHz to ∼200 Hz. The ATLAS trigger system [67] has a three-layer structure with increasingly detailed levels of information used in the reconstruction: the first level trigger (LVL1), the second level trigger (LVL2) and the Event Filter (EF) system. A schematic view of TDAQ systems of the ATLAS detector is shown in Fig. 2.13.

Level 1 Trigger

The LVL1 is completely based on the hardware of the detector, using coarse in-

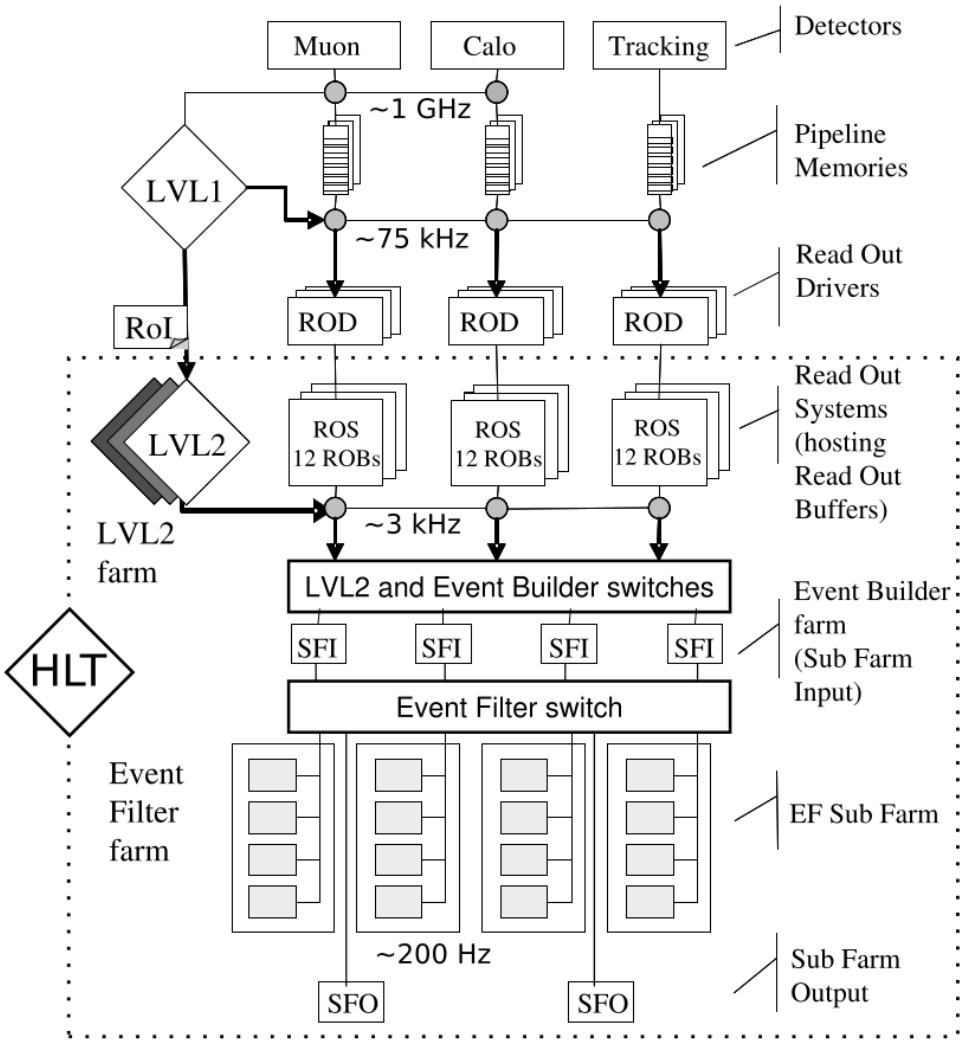

Figure 2.13: Schematic view of the Trigger and Data Acquisition Systems of the ATLAS detector. Figure taken from reference [66].

formation from calorimeters, muon spectrometer trigger systems and from the MBTS. At this level the event rate is reduced from 40 MHz to 75 kHz by choosing events with high transverse momentum or high missing transverse energy. The LVL1 takes decisions within 2.5 μs, while the front-end electronics of the several subdetectors keep the complete data in the pipeline memories. The data is then moved to the Readout Buffers (ROB) via the Readout Drivers (ROD).

Level 2 Trigger

The LVL2 receives a list with Regions of Interest (RoI), which contains the positions of the objects selected by the LVL1. Starting from the RoI, the LVL2 reduces the rate from 75 kHz to 3.5 kHz with an average decision time of 40 ms. At this stage the information from the trackers is incorporated to the RoI to build candidate object (electrons, photons, muons) and better obtain its position and energy with simplified algorithms quick enough to respect the limit on the decision time. The event information is then passed to the Sub-Farm Input (SFI), which provides the full data to the EF.

Event Filter

The final trigger level is the EF, which together with LVL2, is referred to as High Level Trigger (HLT). At this point the physics objects are built using the same algorithms as used in the offline reconstruction. With an execution time amounting to 4 s, the EF reduces the event rate to the goal value of 200 Hz. Events passing the EF are assigned to streams defined to separate the events into different datasets for different analysis interests, e.g. electron streams, muon streams, jet streams etc. The selected events are then moved into the Sub-Farm Output (SFO) and stored to be analyzed later.

Trigger Menu

The trigger system is configured via a trigger *menu* which defines trigger *chains*. Each chain is defined by a sequence of steps at each trigger level. Thresholds are increasingly tightened at each level in order to maximize selection efficiencies. For each HLT level, a sequence of read-out, reconstruction and selection steps is specified. A trigger is defined as the combination of the LVL1 seeding item and the two HLT (LVL2 and EF) chains. Triggers are categorized based on the object reconstructed (jets, muons, etc..), and the selection requirements, such as energy thresholds, multiplicity or isolation. This categorization, together with other distinctions, depending on the reconstruction algorithm and its configuration, are encoded in the trigger name. The naming convention is as follow:

$$\text{[LEVEL][N][TYPE(S)][THRESHOLD][ISOLATION][QUALITY]}, \tag{2.12}$$

where the components, from left to right, are: the trigger level used, the multiplicity of the type, the object candidate, the threshold applied to the transverse momentum or energy of the object candidate, the object isolation, and additional requirements related to the type of algorithm used.

Defining the data taking period time unit as Luminosity Block (LB), typically one minute of data taking, information on beam conditions, detector performance and events passing any of the trigger chains of the trigger menu are stored to be then used in the analyses. All the LBs occurring between the start and the end of a stable beam collision period compose a "run". Runs are finally grouped in "Data Periods", labeled with capital letters ("Period A", "Period B", etc.), when they pertain to the same general detector condition, machine configuration and trigger menu.

2.2.8 Data Quality

The totality of *pp* collisions recorded by ATLAS, which differs from the amount delivered by the LHC because of data-taking inefficiencies, is still not 100% usable by physics analyses. Indeed, every subdetector needs to perform some routine checks on the quality of the data they recorded in order to certify that its performance was conform to the expectations. Therefore, so-called "Good Runs Lists" (GRL) are compiled recording for each LB which subdetectors satisfied the requirements. The single analyses will then decide which GRL to use, based on their specific needs of the individual subsystems. The fraction of data considered as "good" is $\sim 95\%$, giving a total integrated luminosity of 20.3 fb^{-1} satisfying data quality that is used for this analysis.

Chapter 3

Event Simulation

To quantify the consistency of observed data with the SM, or some of its possible extensions, the comparison with theoretical predictions is necessary. These predictions are obtained by simulating the physics processes and the interaction of the particles with the detector, taking into account the expected contributions from signal and background sources. Most computer programs used to simulate the different physics processes are based on Monte Carlo (MC) generators. The MC method employs pseudorandom numbers to simulate both hadron-hadron collisions, and the interaction of particles with the detector material and the read-out of the detector.

In this chapter, a brief overview of the simulation of pp collisions (Sec. 3.1) is presented, followed by a description of the MC generators (Sec. 3.2), the ATLAS detector simulation (Sec. 3.3), and the corrections applied to the MC simulation to improve the agreement with data (Sec. 3.4).

3.1 Simulation of pp Collisions

The simulation requires the modeling of physics processes at very different energy scales, starting from the high-energy scales characteristic of deep inelastic scattering between the partons in pp collisions, and ending with the low-energy scales of the final state when the partons transform into stable hadrons. The most challenging aspect of the simulation is the description of QCD phenomenology in the low-energy regime, where the physics involved can not be described by perturbative QCD, making an analytical description of the process not possible.

Fortunately, the factorization of the different energy scales involved in the simulation of pp collisions is possible. The simulation of the deep inelastic scattering can be computed at a fixed order (LO or NLO) in perturbation theory. Since the partons involved in the collision are color charged, they emit gluons, which in turn radiate further gluons or split into quark/anti-quark pairs, leading to the formation of *parton showers*. Emissions associated with the initial partons are referred to as *Initial State Radiation* (ISR), while *Final State Radiation* (FSR) is emitted by the partons produced in the collision. The radiation process continues until the partons reach an energy scale of $Q \approx 1$ GeV. At this stage, the *hadronization* process takes place, and partons recombine into colorless hadrons. The hadronization step, as well as the decay of the hadrons into the final state particles, are described by phenomenological models. The different steps involved in the simulation of a pp collision, presented in Fig.3.1, are discussed in detail below.

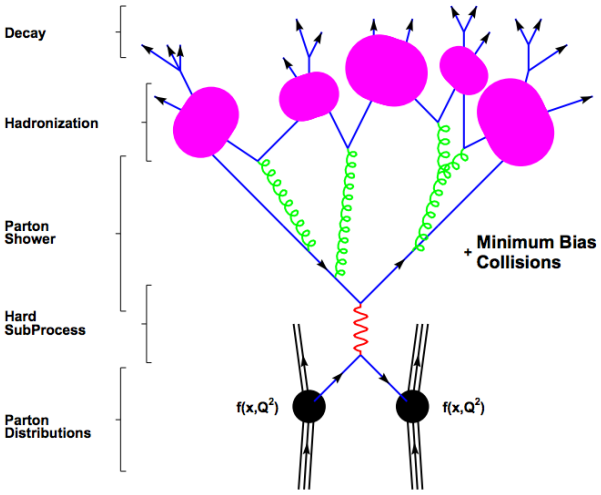

Figure 3.1: Representation of the different steps involved in the simulation of a pp collision. Figure taken from reference [68].

3.1.1 Factorization Theorem

According to the factorization theorem [69], the cross section for a hadron collision, illustrated in Fig. 3.2, can be factorized into short- and long-distance effects delimited by a *factorization scale*, μ_F:

$$\sigma_{pp\to X} = \sum_{a,b} \int dx_a dx_b f_a(x_a, \mu_F^2) f_b(x_b, \mu_F^2) \cdot \hat{\sigma}_{ab\to X}(x_a p_a, x_b p_b, \mu_F^2, \mu_R^2), \tag{3.1}$$

where $f_i(x_i, \mu_F^2)$ $(i = a, b)$ are the standard parton distribution function (PDF) for partons $a, b \in \{g, u, \overline{u}, d, ...\}$. $f_i(x_i, \mu_F^2)$ $(i = a, b)$ encodes the probability of finding a parton of type i within the proton, carrying a fraction of the proton's momentum x_i. The PDFs are universal since they dont depend on the particular process. Several groups, e.g. CTEQ, MSTW, NNPDF, HeraPDF [70–74], extract the PDFs by fitting the results from different measurements of deep-inelastic scattering experiments at particle colliders. An example of PDFs from the NNPDF collaboration is shown in Fig. 3.3 for two interaction energy scales $Q^2 = 10$ GeV^2 and $Q^2 = 10^4$ GeV^2.

The cross section for the partonic process $\hat{\sigma}_{ab\to X}(x_a p_a, x_b p_b, \mu_F^2, \mu_R^2)$ is computed explicitly at a fixed order in perturbation theory, which introduces a dependence on a renormalization scale μ_R, that is usually chosen to be equal to the factorization scale μ_F. This step is also referred to as *matrix element* calculation, because it involves the calculation of the scattering matrix relating the initial and final state particles of the process.

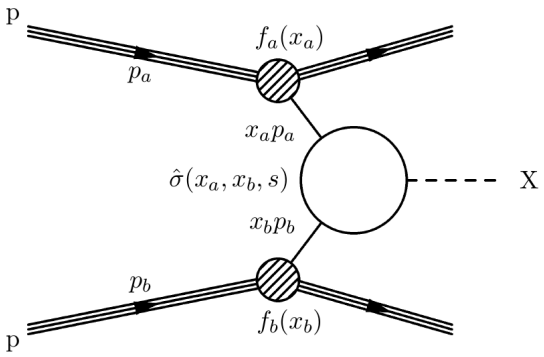

Figure 3.2: Diagram of a generic hard scattering process. The partons, extracted from the colliding pp pair, carry a momentum fraction with respect to the proton energy described by a parton distribution function. The scattering of the partons is computed perturbatively and hence the kinematic properties of the final state object X are predicted.

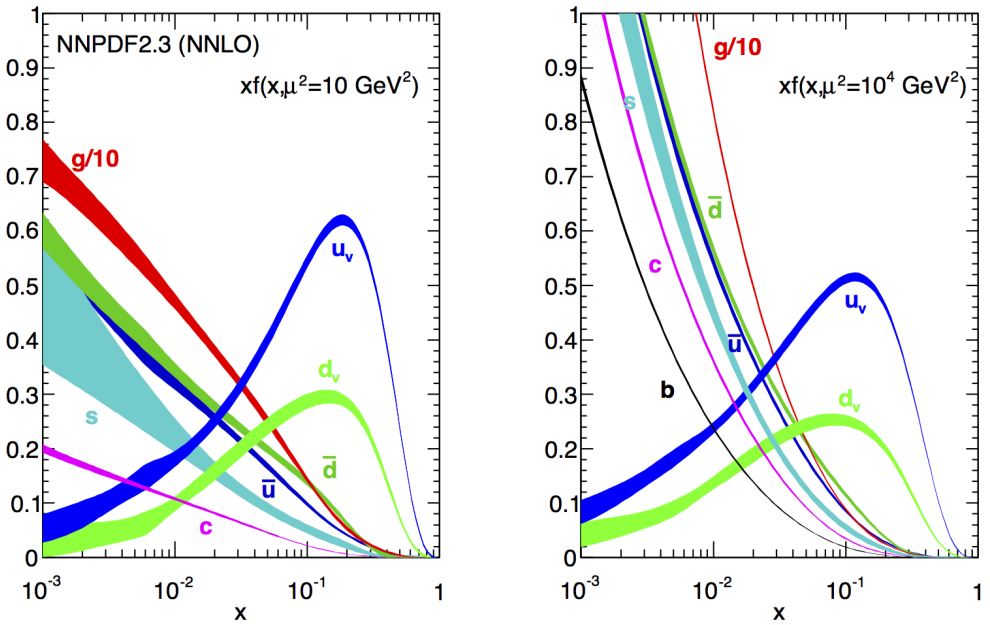

Figure 3.3: Parton density functions at (a) $Q^2 = 10$ GeV^2 and (b) $Q^2 = 10^4$ GeV^2 obtained by the NNPDF collaboration. Figures taken from reference [75].

3.1.2 Fixed Order QCD: Matrix Elements

Let us consider the production of $pp \to X+$anything, with X an arbitrary final state. Schematically, the all-orders differential cross section can be written as:

$$\hat{\sigma}_{ab\to X} \sim \underbrace{\sum_{k=0}^{\infty} \int d\Phi_{X+k}}_{\Sigma \text{ legs}} | \underbrace{\sum_{\ell=0}^{\infty} \mathcal{M}^{\ell}_{X+k}}_{\Sigma \text{ loops}} |^2 , \tag{3.2}$$

where, for compactness, all PDF and luminosity normalization factors are suppressed. $\mathcal{M}^{\ell}_{X+k}$ is the amplitude for producing X in association with k additional final-state partons (referred to as "legs") and with ℓ additional corrections (refereed as "loops"). The sums start at $k = 0$ and $\ell = 0$, corresponding to the Leading Order (LO) for producing X, while higher terms represent "real emission" and "virtual" corrections, respectively. Φ_{X+k} represents the phase space of the configuration with k legs.

The various fixed-order truncations of a perturbative QCD calculation can be recovered by limiting the nested sums in Eq. 3.2 to include only specific values of $k + \ell$:

- $k = 0$, $\ell = 0$: LO for inclusive X production.
- $k = n$, $\ell = 0$: LO for $X + n$ jets.
- $k + \ell \leq n$: N^{n}LO for X (includes N^{n-1}LO for $X + 1$ jet, N^{n-2}LO for $X + 2$ jets, and so on up to LO for $X + n$ jets).

For $\ell \geq 1$, the virtual amplitudes are divergent for any point in phase space. According to the KLN theorem [76,77], the divergences originated in the loops exactly cancel against those from the real emissions, order by order in perturbation theory, making the complete answer for fixed $k + \ell = n$ finite. However, for $k \geq 1$, $\ell = 0$ in a fixed-order calculation, the integration over the full momentum phase space will include configurations in which one or more of the k partons become *collinear* or *soft*. Such configurations are infrared divergent in QCD and hence the integration region needs to be modified to include only "hard, well-separated" momenta. The remaining part of the phase space is then considered by the parton shower generators.

3.1.3 Parton Shower

Parton shower represent higher-order corrections to the hard scattering $2 \to n$, corresponding to the production of additional partons in the process $2 \to n + X$. At a fixed order in the perturbative expansion, these corrections are divergent at low energies (*infrared divergence*) or small angles (*collinear divergence*) and their explicit calculation is not possible. Therefore an approximation scheme (*leading logarithm*) is used, where only the dominant contributions are considered.

There are three possible processes for QCD emission (*splitting*): $q \to qg$, $g \to gg$, $g \to q\bar{q}$. In the almost collinear splitting of a parton, the $n+1$-parton differential cross section can be related to the n-parton differential cross section before splitting as:

$$d\sigma_{2\to n+1} \approx d\sigma_{2\to n} dP_i(z, q^2) \approx d\sigma_{2\to n} \frac{\alpha_s}{2\pi} \frac{dq^2}{q^2} dz P_i(z, q^2), \tag{3.3}$$

where $dP_i(z, q^2)$ is the probability that the parton i will split into two partons at a virtuality scale or invariant mass q^2, with parton j carrying a fraction z of the

momentum of parton i. An illustration of this process is given in Fig. 3.4. The simulation algorithm develops the shower by applying Eq. 3.3 iteratively, for each parton involved in the hard interaction.

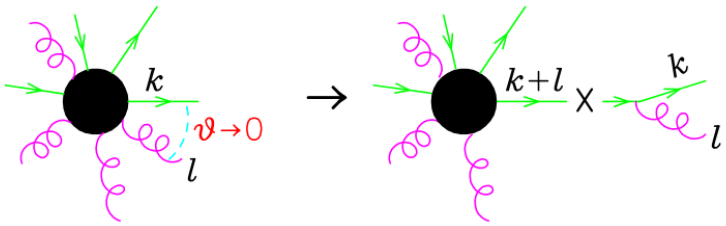

Figure 3.4: Representation of an $n+1$-parton process described as a splitting from an n-parton process. Figure taken from reference [78].

The implementation of the parton shower in MC generator programs is done via the *Sudakov form factors*, which represent the probability that a parton evolves from an initial scale q_1 to a lower scale q_2 without splitting:

$$\delta_i(q_1^2, q_2^2) = \exp\left(-\sum_j \int_{q_2^2}^{q_1^2} \int_{z_{min}}^{z_{max}} dP_i(z, q^2)\right). \tag{3.4}$$

In the case of parton showers for FSR, the branching algorithm operates in the following steps:

- Given the initial scale Q^2, partons emit radiation at a scale q_2 determined by sampling Eq. 3.4.
- If the scale q_2^2 is below the hadronization scale, $q_2^2 < Q_0^2 \approx 1$ GeV^2, the shower development is terminated and hadronization takes place.
- Otherwise, the procedure is repeated for each new parton produced by the splitting, taking q_2^2 as initial scale.

In the case of parton showers for ISR, the radiation is emitted by the colliding partons, and the final energy scale is the one entering the hard interaction. MC generators implement a *backward evolution* that starts by setting the correct parton momentum for the hard scatter, and then develops the shower backwards, with ancestor partons gaining energy at each emission. The Sudakov form factors are then slightly different from Eq. 3.4, being rescaled by a factor that takes into account the particle density functions of the parton before and after splitting.

3.1.4 Matrix Element and Parton Shower Matching

Matrix element calculations in multi-leg or NLO generators include ISR and FSR emissions computed at fixed order in QCD with a cut-off to prevent collinear and soft divergences. Therefore the parton shower algorithm is used to simulate only soft and collinear emissions. The interface of parton shower algorithms with LO or NLO matrix element generators requires a criterium to define which portion of the phase space is simulated by which algorithm in order to avoid double-counting of partonic

configurations generated by both algorithms. The procedure to distinguish between hard and large-angle emissions, described by the matrix element, and soft and collinear emissions, described by the parton shower, is referred to as ME-PS *matching*.

The most widely-used matching schemes are the CKKW [79] and the MLM [80] algorithms. Both methods rely on re-clustering the final state partons, using a jet algorithm (k_T or cone, respectively), in order to identify the radiation patterns generated at matrix element level. The generation of parton shower emissions in the same phase space is then prevented by vetoing hard and large-angle radiation (CKKW) or rejecting events where the re-clustered partons after parton shower do not match the matrix element final state (MLM).

3.1.5 Hadronization

As partons radiate and the shower evolution brings the parton virtuality below the hadronization scale, $Q_0^2 \approx 1$ GeV, the confining effects of QCD become important. The dynamics of the partons enters a non-perturbative phase, which leads to the formation of the final-state colorless hadrons. Therefore, calculations based on first-principles are absent and event generators have to rely on phenomenological models whose parameters are tuned to measurements in data.

The simplest model for fragmentation is based on the hypothesis of the so-called *parton-hadron duality*, the intuitive assumption that the basic flow of momentum and quantum numbers found at the parton-level is maintained at the hadron level. QCD predicts that development of the parton shower will result in color preconfinement and a decrease in the invariant mass of the color-connected partons. These color-connected pairs form the seed for the hadronization, so it is natural to expect the quark content of the hadrons in a region of the detector to be similar to that of the partons before hadronization. This simple idea is implemented quantitatively in the two most common hadronization models: *string fragmentation* [81,82], and the *cluster model* [83,84], used in `PYTHIA` and `HERWIG` respectively (see Sec. 3.2), illustrated in Fig. 3.5.

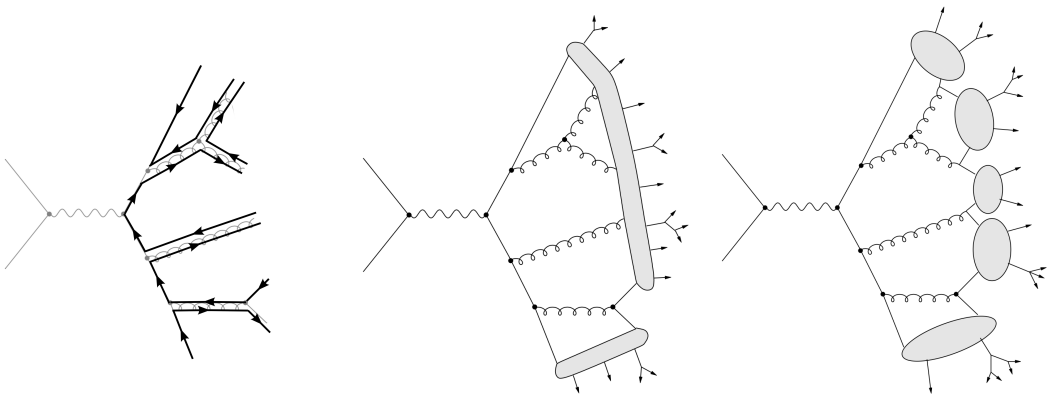

Figure 3.5: Possible radiation pattern from (a) $q\bar{q}$ pair, and (b) illustration of string fragmentation and (c) cluster hadronization. Figures taken from reference [85].

In the string model, the confinement between partons induced by the color force is represented by a gluonic string. For a quark-antiquark pair, as the color charges

move apart, the string is stretched, and its potential energy grows. When the energy becomes of the order of hadron masses, it becomes energetically favorable for the string to break and create a new quark-antiquark pair. The two segments of string will stretch and break again, until all the energy has been converted into quark-antiquark pairs connected by short strings.

The cluster model relies on groupings of partons to form colorless clusters, after forcing the final state gluons to split into quark-antiquark pairs. The heaviest clusters can decay and split into smaller clusters. Most clusters will have masses below 3 GeV, and their decay into hadrons is simulated with three-body models with intermediate resonances.

3.1.6 Underlying Event

The low-energy interactions between the proton remnants, referred to as *underlying event* (UE), are described with phenomenological models. The phenomenological model parameters are tuned based on experimental data [86], such as the charged particle density shown in Fig. 3.6. The dominant sub-process of the UE is gluon-gluon scattering, with a cross section larger than the total pp scattering cross section, indicating that multiple gluon scatterings per proton collision are very likely. For this reason the generic soft scattering of partons is referred to as *multiple parton interactions* (MPI). The color connection with the beam remnants that are not interacting is also simulated with phenomenological models [87, 88].

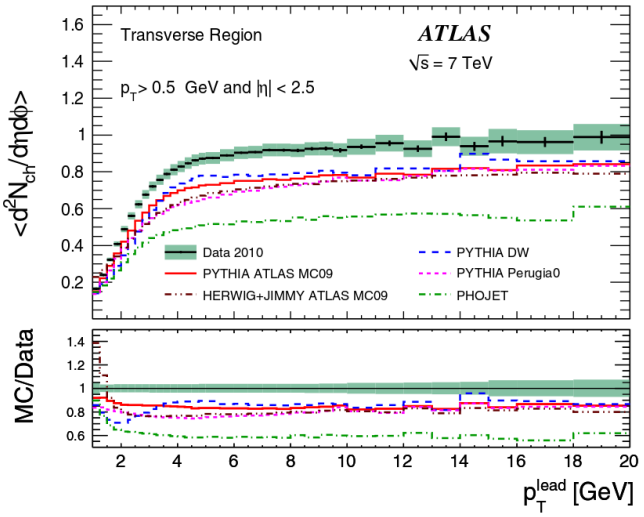

Figure 3.6: Density of charged particles with $p_T > 0.5$ GeV and $|\eta| < 2.5$ as a function of the leading particle p_T in ATLAS data at $\sqrt{s} = 7$ TeV compared with simulations from different tunes of MC generators. Figure taken from reference [86].

3.1.7 Pile-up

In-time pile-up events are originated from the scattering of protons in the same bunch of the hadron generating the hard process of interest. They mainly consist of soft QCD interactions and are modeled in a similar way as the UE. Out-of-time pile-up

is modeled with the same physics process, but considering interactions in past bunch crossings and simulating the time response of the readout electronics.

3.2 Monte Carlo Generators

Generators can be classified as either *multi-purpose* or *specialized* matrix element generators. The multi-purpose generators are capable of performing the full simulation chain described above, while the specialized matrix element generators are optimized for the calculation of complicated MEs, either at LO or NLO, and have to be interfaced with an additional parton shower. The following sections summarize the main characteristics of the MC generators that are used in this dissertation.

3.2.1 General Purpose Generators

- **PYTHIA** [87]. A multi-purpose MC generator using LO calculations for $2 \to n$ ($n \leq 3$) processes and parton showers with emissions ordered in transverse momentum instead of angle. The Lund string model is used for hadronization, and UE simulation is included.

- **HERWIG** [89]. A multi-purpose MC generator using LO calculations for $2 \to 2$ processes and parton shower with emissions ordered in opening angle. The cluster model is used for hadronization and for the UE description, `HERWIG` is typically interfaced with the standalone software `JIMMY` [88] that simulates UE as MPI.

3.2.2 Multi-leg Leading-order Generators

- **ALPGEN** [90]. A MC generator providing LO calculations of $2 \to n$ ($n \leq 9$) processes. It can be interfaced with either `PYTHIA` or `HERWIG` for parton shower evolution, hadronization and UE modeling. ME-PS matching is applied with the MLM algorithm.

- **MADGRAPH** [91]. A MC generator specialized in the computation of matrix element involving $2 \to n$ ($n \leq 6$) processes at LO. It is interfaced with `PYTHIA` for the parton shower evolution and the ME-PS matching is performed with the MLM algorithm.

- **SHERPA** [92]. A MC generator that can provide multi-leg leading-order calculations. It contains its own parton shower algorithm based on the Catani-Seymour dipole formalism [93]. The ME-PS matching is implemented with an improved version of the CKKW algorithm [94].

3.2.3 NLO Generators

- **MC@NLO** [95]. A MC generator using NLO calculations. The full NLO matrix element provides precise cross section estimates, but higher-multiplicity parton emissions are simulated via `HERWIG` parton shower with a poor description of hard emissions. The ME-PS matching is performed by a built-in CKKW-like subtraction procedure. Hadronization and UE are simulated through `HERWIG` and `JIMMY`. It should be noted that MC@NLO is not used for the analysis of this dissertation, but used for the jet charge studies presented in Chapter 10.

- **POWHEG** [96]. A MC generator using NLO calculations and typically interfaced either with `PYTHIA` or `HERWIG` for the modeling of parton shower, hadronization and UE. It generates only positive-weighed events. The use of a different ME-PS matching scheme with respect to MC@NLO leads to a better modeling of the jet multiplicity in the event.

- **SHERPA**. A MC generator that can generate events at NLO after being interfaced with additional libraries to compute the loop amplitudes. Sherpa in conjunction with Open-Loops [97] is used to model the $t\bar{t} + b\bar{b}$ process at NLO, which is one of the largest backgrounds for the analysis discussed in this dissertation.

3.3 ATLAS Detector Simulation

An overview of the ATLAS simulation data flow is shown in Fig. 3.7. Algorithms and applications to be run are placed in square-cornered boxes, and persistent data objects are placed in round-cornered boxes. The optional steps required for pile-up are shown with a dashed outline.

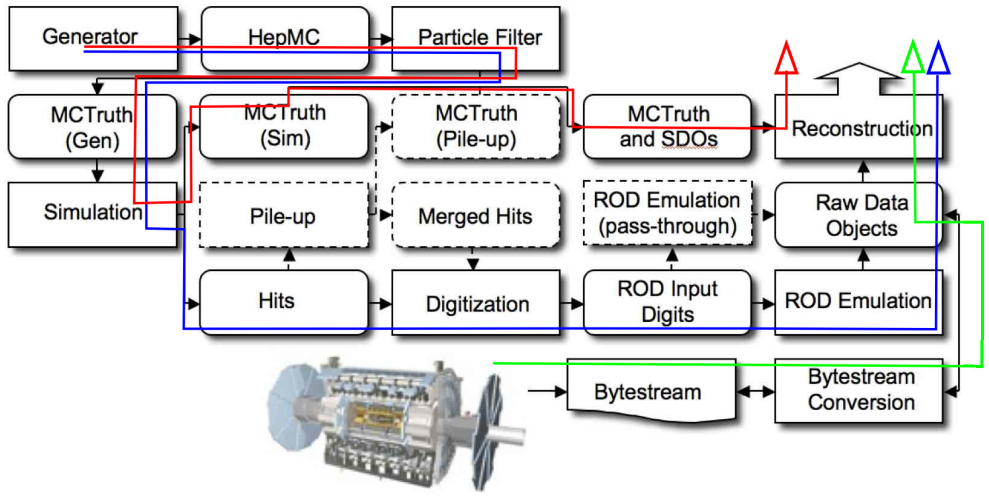

Figure 3.7: The flow of the ATLAS simulation software, from event generators (top left) through reconstruction (top right). The red path leads to *particle level* physics objects, the blue path to *reconstructed level* physics objects, while the green path shows the real data flow to physics objects. Monte Carlo truth information is saved in addition to energy depositions in the detector (Hits). This truth is merged into Simulated Data Objects (SDOs) during the digitization. Also, during the digitization stage, the Read Out Driver (ROD) electronics are simulated. Figure taken from reference [98].

The MC generator produces events in standard HepMC format [99]. These events can be directly used at *particle level*, i.e. without any further operation on the generated particles, in order to study the physics processes. In order to compare it with the recorded data, the MC events have to go through detector simulation and object reconstruction, to obtain the so-called *reconstructed level*. The detector simulation software, known as `ATHENA` [100], is integrated into the ATLAS software framework and uses the `GEANT4` simulation toolkit [101], which models the interaction of the par-

ticles with the detector and converts the energy deposits into electronic signals taking into account the geometry, materials and readout system of the ATLAS detector. The GEANT4 parameters are tuned using test-beam and *pp* collision data. Two databases are used to construct the detector geometry: the ATLAS *geometry database*, that contains the fundamental constants of the detector construction like dimensions, rotations and positions, as well as element and material properties including density, and ATLAS *conditions database*, that stores information on the real detector real-time conditions as dead channels, misalignments, temperature. Since conditions vary from run to run, it is important that the detector simulation reproduces as close as possible the real status of ATLAS during a particular data period. To ensure this, simulation samples are reprocessed for each *data release*.

Large computing resources are required to accurately model the complex detector geometry and physics descriptions in the standard ATLAS detector simulation. This has led to the development of several varieties of fast simulation, which reduces considerably the CPU time necessary to process the events by applying a parameterized description of the parton showers in the calorimeters.

For the analysis presented in this dissertation, the Monte Carlo production tagged as mc12 is used. Release versions 17.2.7.4 and 17.2.6.5 of ATHENA are used for processing the dataset and simulation at $\sqrt{s} = 8$ TeV. A fast simulation, known as Atlfast-II or AF2 [102], is also available.

3.4 Monte Carlo Simulation Corrections

In order to compare with the distributions observed in data, simulated events are normalized to the most precise available theoretical cross section of the process (usually at NLO or NNLO) and to the number of expected data events, which comes from the integrated luminosity. The applied event weight, w, is defined as:

$$w = \frac{\sigma \times L}{N}, \tag{3.5}$$

where σ is the process theoretical cross section, N is the number of Monte Carlo events, and L is the integrated luminosity.

While simulated events are generated for the whole spectrum of number of interactions per bunch crossing $< \mu >$, the proportions are not the same as in data. Therefore, the simulated events are weighted to account for the pile-up conditions, to ensure that the $< \mu >$ distribution in simulated samples matches the one in data.

To ensure an accurate modeling of the detector effects, reconstruction and selection efficiencies (ϵ) are calibrated with *scale factors* (SF) defined as:

$$SF = \frac{\epsilon_{data}}{\epsilon_{MC}}, \tag{3.6}$$

where ϵ_{data} and ϵ_{MC} are measured in dedicated data calibration samples and in the equivalent MC simulation, respectively. Analogously, energy scale and resolution of the different physics objects in the simulation are corrected to match the corresponding measurements in data.

Chapter 4

Event Reconstruction

This chapter describes the main physics objects considered in the analysis presented in this dissertation: electrons, muons, jets, b-jets and missing transverse momentum. This analysis uses the standard object selection criteria recommended by the ATLAS Top Group for the full 2012 dataset and documented in reference [103]. More detailed studies based on a partial 2012 dataset are documented in reference [104].

4.1 Tracks

In the solenoidal magnetic field of the ID, a charged particle moves along a helicoidal trajectory, *track*, with a curvature inversely proportional to its momentum. Therefore, the reconstruction of tracks is necessary to be able to identify charged particles and measure their momenta. In addition, the extrapolation of the trajectories allows the identification of the hard interaction vertices and the reconstruction of decays of long-lived particles such as b-hadrons.

The parameters describing a track are shown in the double-view drawing of Fig. 4.1. A reconstructed track in the X-Y and R-Z planes is fully specified by the following parameters:

- d_0 - impact parameter, or the minimum distance to the center of the detector in the transverse plane direction.
- z_0 - impact parameter, or the minimum distance to the center of the detector in the longitudinal direction.
- ϕ - the azimuthal angle, or the angle with respect to the X axis in the X-Y plane measured from the perigee.
- θ - the polar angle, or the angle with respect to the Z axis in the R-Z plane measured from the perigee.
- q/p - the charge divided by the momentum.

Impact parameters and direction are often expressed with respect to the main primary vertex in the event (see Sec. 4.2).

In order to reconstruct the track three algorithms [105] are used:

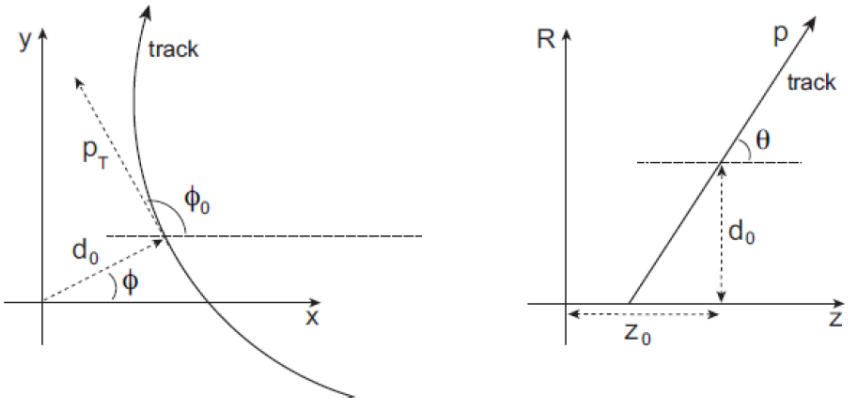

(a) (b)

Figure 4.1: Track parameters in the (a) X-Y and (b) R-Z planes where the origin is the beam spot, i.e. where the protons collide and interact.

- *Inside-out* algorithm. This algorithm uses hit information from the ID, converted into three-dimensional space points, and is used to reconstruct the tracks of primary particles, i.e. particles with a mean life time $\tau > 3 \times 10^{-11}$ sec. The track is reconstructed iteratively, by combining space points one by one, starting from three seed hits in the pixel detector or in the SCT, and adding the other compatible hits, extending the track to the TRT. The compatibility between the track and the new point is checked using a Kalman filter algorithm [106]. A cleaning procedure then removes incomplete tracks or tracks sharing hits with others, or composed by noise hits. A threshold of $p_{\mathrm{T}} > 0.4$ GeV is required for a track to be retained. Finally, the track quality is improved by taking into account the signal from the TRT and the effects from the interaction of the charged particle with the detector material.

- *Outside-in* or *Back-tracking* algorithm. This algorithm identifies the tracks coming from the decay products of primary particles, the so called secondaries. It takes into account all the hits not considered by the inside-out algorithm and reconstructs the tracks in opposite order: it starts from track fragments reconstructed in the TRT, that are not associated to any track candidate by the inside-out reconstruction, and extrapolate them back to the SCT and pixel detector.

- *TRT-standalone* algorithm. This algorithm reconstructs the tracks with no associated segment in the pixel nor in the SCT detector.

In a low pile-up environment, the tracking reconstruction algorithms perform well and the agreement between data and simulation is good [107]. With the increase of the mean number of interactions per bunch crossing a balance has to be found between tighter requirements, to decrease the number of fake tracks and vertices, and the loss in reconstruction efficiency.

The baseline requirements for a good track are at least seven hits in the pixel + SCT detectors and not more than two holes (a missing hit that, given the track trajectory, would have been expected to be measured) in the pixel detector. The "robust" requirements used to minimize the number of reconstructed fake tracks, are at least nine hits in the pixel + SCT detectors and no holes in the pixel detector.

The track reconstruction efficiency for primary particles versus the track p_{T} is shown in Fig. 4.2a. The efficiencies are shown for tracks passing the default (dashed) and robust (solid) requirements. The efficiency is defined as the fraction of primary particles with $p_{\mathrm{T}} > 400$ MeV and $|\eta| < 2.5$ matched to a reconstructed track, where the matching criterion is based on the fraction of hits on the track in each subdetector that were produced by the primary particle. It is stable in different pile-up conditions with the robust as well as with the default track requirements. A 5% loss in efficiency is observed when applying the robust selection. The robust requirements, though, are very effective in eliminating the pile-up dependency of the ratio of secondaries and combinatorial fake tracks over the primary tracks by rejecting most of the fake tracks. This ratio as a function of the track p_{T} is shown in Fig. 4.2b for the different pile-up conditions studied and the two reconstruction selections, default and robust.

4.2 Primary Vertices

Due to the large number of protons per bunch crossing, multiple interaction vertices can be reconstructed in the event. The reconstruction of the interaction points of the primary particles, referred to as *Primary Vertices* (PV), is essential to identify which one corresponds to the hard-scattering process and reconstruct the physics objects accordingly.

The reconstruction of PVs exploits an iterative χ^2 algorithm. The maximum in the distribution of the z_0 parameter of reconstructed tracks is taken as seeds. A compatibility weight is then associated to each track to assess the probability that it belongs to a certain vertex. Tracks incompatible with any PV by more than 7σ are used to seed a new vertex. This procedure is repeated until there are no tracks left without being assigned to a vertex.

A PV must have at least two associated tracks and its position must be consistent with the beam collision region in the X-Y plane. The vertex with the highest sum of squared p_{T} of its associated tracks is chosen as the hard-scatter PV. The rest of the PVs are identified with pile-up interactions. Vertices incompatible with the beam collision region are considered secondary vertices.

The vertex reconstruction efficiency and fake vertex probability are shown in Fig. 4.3, as a function of the average number of interactions in a simulated sampled of minimum bias events. As can be seen, the vertex reconstruction efficiency decreases from 80% to 50% with increasing μ, from $\mu = 1$ to $\mu = 41$. When considering only vertices with at least two tracks in the acceptance region of the inner detector and applying the pile-up robust selection, the PV reconstruction efficiency can exceed 90%. The robust requirements also ensure that the fake vertex contribution remains below the percent level, even when a high number of interactions per bunch crossing are recorded, without decreasing sensibly the reconstruction efficiency.

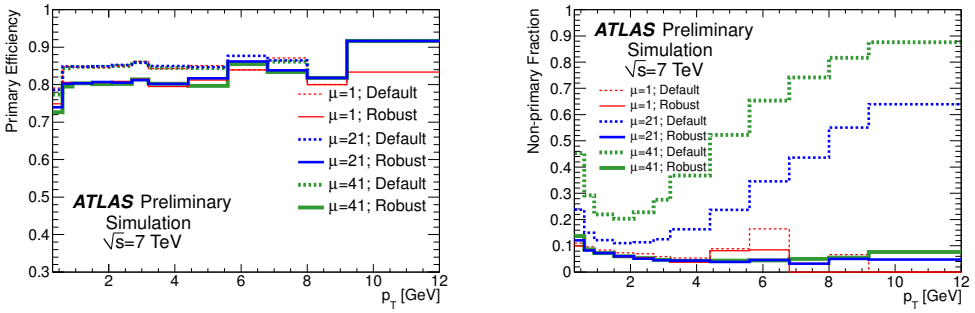

(a) (b)

Figure 4.2: (a) Primary particle track reconstruction efficiency as a function of the track p_{T}. (b) Fraction of non primary tracks as a function of the track p_{T}. To monitor the pile-up dependence of the track reconstruction, three simulated samples with different pile-up conditions have been used: in red a sample with no pile-up ($\mu = 1$), in blue a sample with medium pile-up ($\mu = 21$) and in green a sample with high pile-up ($\mu = 41$). Figures taken from reference [108].

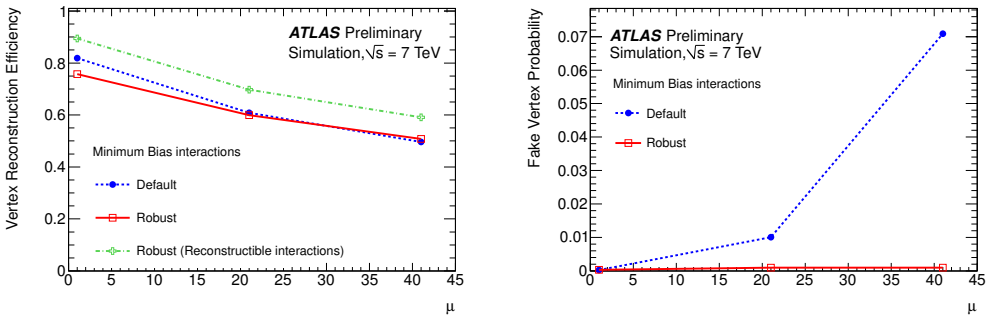

(a) (b)

Figure 4.3: (a) Vertex reconstruction efficiency and (b) fake vertex probability as a function of the average number of interactions in a minimum bias Monte Carlo simulation. Reconstructable interactions (green dashed line) are defined as the vertices with at least two primary tracks with $p_{\mathrm{T}} > 0.4$ GeV and $|\eta| < 2.5$. Figures taken from reference [109]

4.3 Leptons

The reconstruction and identification of leptons (electrons and muons) are discussed in this section. Tau-lepton reconstruction is not considered since tau leptons not explicitly be used in the analysis described in this dissertation. Although no attempt is made to identify tau-leptons, their decay products can still contribute to the object reconstruction. Leptonic tau decays can be identified as isolated electrons or muons, whereas hadronic tau decays are reconstructed as narrow jets in the detector.

4.3.1 Electrons

Detection of the electrons is based on the energy deposition in the EM calorimeter by electromagnetic showers. Electrons provide a clear signature and have a very good performance in terms of reconstruction and identification efficiencies. They also have low systematic uncertainties related to the determination of their energy scale and resolution. Electrons candidates are reconstructed from energy deposits in the EM calorimeter with the *sliding window* algorithm [110]. The sliding algorithm consists of three steps.

The first step is to search for local maxima of energy in the calorimeter cells and group them into *electromagnetic clusters* of dimensions 3×5 in $\Delta\eta\times\Delta\phi = 0.025\times0.025$ units.

The second step is the matching of the tracks from the ID to the selected clusters. Tracks with $p_{\mathrm{T}} > 0.5$ GeV are selected and extrapolated to the middle layer of the electromagnetic calorimeter and matched to the cluster seed. The matching criteria are:

- $|\Delta\eta| < 0.05$, where $\Delta\eta$ is the distance between the cluster and the track in η.
- $-0.05 < q \cdot \Delta\phi < 0.10$, where $\Delta\phi$ is the distance between the cluster and the track in ϕ-direction, and q is a charge of the track.
- In the case of multiple matches, the track with the minimum $\Delta R = \sqrt{(\Delta\phi)^2 + (\Delta\eta)^2}$ is chosen.

For the 8 TeV dataset, additional track-matching criteria have also been taken into account to properly reconstruct electrons that lost significant amount of energy in the dead material in front of the calorimeter due to bremsstrahlung [111]. Matched clusters are then optimized to account for the energy deposited in all layers of the calorimeter. The size of the cluster windows are hence enlarged to 3×7 cells in the barrel and 5×5 in the end-cap regions.

The electron four-momentum is built then from the cluster energy and the direction of the associated track. The final energy of the cluster is obtained by correcting for the energy losses in the material in front of the calorimeter, energy not included into the cluster because of its limited size (*lateral leakage*) and energy deposited in the hadronic calorimeter (*longitudinal leakage*).

In order to suppress the misidentification of other particles as electrons, an electron identification procedure, based on cluster shape, track quality and track-cluster matching, is applied as a last step. For example, using the fact that the shower development is narrower for electrons than for hadrons, different conditions on cluster shape are applied. Track quality requirements reduce the impact of accidental track association

with photons, energetic π^0 or η mesons with electromagnetic decays reconstructed as a single energy cluster.

There are six electron identification criteria used in ATLAS in order to discriminate real electrons from misidentified ones. Each identification criteria applies additional requirements with respect to the previous one:

- `Loose`. Electron candidates have low hadronic leakage and requirements on the variables defining the shower shape. The identification efficiency is above 95%, but the jet rejection is low, about 500.

- `Loose++`. Electron candidates are `loose` electrons whose track has at least one hit in the pixel detector and at least 7 hits in the combined silicon detectors. The absolute value of the distance in η between the track extrapolated to the first EM layer and the matched cluster, $|\Delta\eta_{\text{firstEM}}|$, must be lower than 0.015. The identification efficiency is similar to the loose one but the rejection is ten times higher.

- `Medium`. Electron candidates are `loose++` electrons with the additional requirements $|d_0| < 5$ mm and $|\Delta\eta_{\text{firstEM}}| < 0.01$. The efficiency is about 88% and the rejection is better than for `loose++` electrons.

- `Medium++`. Electron candidates are `medium` electrons whose track has at least one hit in the first pixel detector layer and a high fraction of high-threshold TRT hits. $|\Delta\eta_{\text{firstEM}}|$ is required to be smaller than 0.005, and more stringent requirements are applied to the shower shape of clusters at $|\eta| < 2.01$. The efficiency is about 85% and rejection is about 5×10^4.

- `Tight`. Electron candidates are `medium++` electrons with additional requirements on the distance between the track and the matched cluster ($|\Delta\phi| < 0.02$, $|\Delta\eta| < 0.005$). In addition, a higher fraction of high-threshold TRT hits is required, as well as an impact parameter $|d_0| < 1$ mm. The efficiency is about 75% and the rejection is slightly higher than for medium++.

- `Tight++`. Electron candidates are `tight` electrons with asymmetric $\Delta\phi$ requirements, yielding higher efficiency (about 80%) and rejection (about 5×10^4) with respect to tight criteria.

The `Tight++` electron identification criteria is used in the analysis discussed in this dissertation, since the largest possible rejection of "fake" electrons from misidentifications is required. To estimate the misidentification rate of jets as an electrons for the multijet events the `Medium++` identification criteria is used, which will be described in detail in Sec. 7.3.4. In addition to the identification requirements, electrons are required to have $|\eta_{\text{cluster}}| < 2.47$ and to be outside the transition region $1.37 < |\eta_{\text{cluster}}| < 1.52$, since this region shows worse reconstruction and energy resolution performance.

Finally, electron isolation is required to reject electrons from semileptonic hadron decays. The track isolation variable p_{T}^R is defined as the sum of the transverse momenta of all the tracks in a cone of radius R around the electron direction. Only tracks with $p_{\text{T}} > 1$ GeV and compatible with being originated from the primary vertex are considered with the exception of the track used to build the electron object. The calorimetric isolation variable called E_{T}^R represents the sum of the transverse energy

of the calorimetric cells in the cone of radius R around the electron with the deposit associated with the electron itself subtracted. The variables $E_{\mathrm{T}}^{0.2}$ and $p_{\mathrm{T}}^{0.3}$ have been chosen, with variable cut values in order to obtain a constant efficiency of 90% as a function of p_{T} and η for real electrons already fulfilling the `Tight++` identification criteria.

In Fig. 4.4 the comparison of the identification efficiency for each electron identification criteria discussed above is shown. The efficiencies are estimated applying the so called "Tag-and-probe" method to $Z \to e^+e^-$, $W \to e\nu$ and $J/\Phi \to e^+e^-$ data and MC samples [112]. This method selects a clean and unbiased sample of leptons (probe leptons) from Z boson decays using selection cuts on one of the leptons in the decay (tag leptons). The efficiency is determined by applying the selection to the probe leptons.

The modeling in simulation differs slightly from what is observed in data, therefore a calibration scale factor is applied in MC samples. These scale factors typically deviate from unity by only a few %. The combined uncertainties on the reconstruction, identification and isolation requirement scale factors are at the level of 2 %. For $t\bar{t}$-related analyses, an additional uncertainty of 2 % is assumed for the isolation efficiency, due to the extrapolation from the $Z \to e^+e^-$ - environment to the $t\bar{t}$ environment, involving higher jet multiplicity and therefore smaller angular separation between the electron and surrounding jets [113].

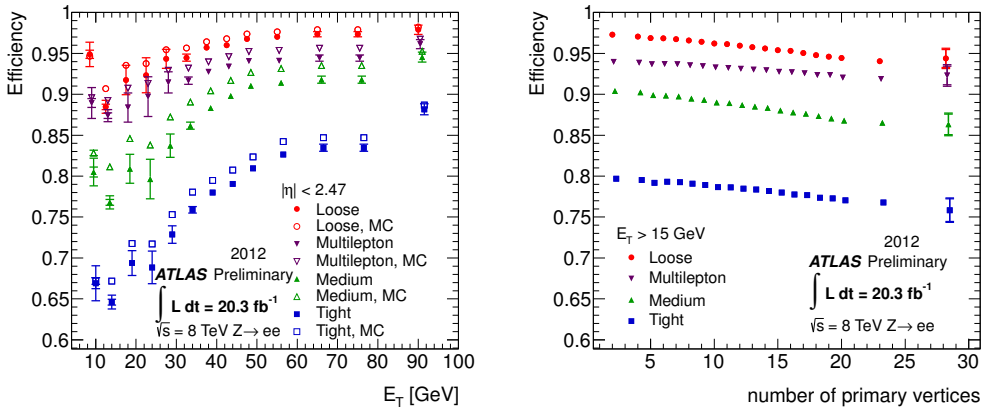

Figure 4.4: (a) Electron identification efficiency as a function on electron E_T for the benchmark selections in data and MC. (b) Measured electron identification efficiency in data for the different benchmark selection as a function of the number of reconstructed primary vertices in the event. Figures taken from reference [112].

4.3.1.1 Electron Energy Scale and Resolution

The $Z \to e^+e^-$ and $J/\Phi \to e^+e^-$ data samples have been used to measure the electron energy scale. In order to obtain the correction factors as a function of the electron η, the dielectron invariant mass distributions of the two resonances are fitted. The total uncertainty on the electron in-situ calibration is $< 1\%$ in the central region and increases up to a few % in the most forward region of the calorimeter. An additional procedure, profiting from the very large sample of collected $W \to e\nu_e$ events, has been

used. It exploits the combined measurement of the track momentum in the inner detector and the energy in the calorimeter (E/p).

The electron energy resolution is mainly probed via the study of the $Z \to e^+e^-$ resonance width. It is found that the resolution in data is slightly worse than that in simulation, so appropriate corrections are derived and applied to the simulation to match the data.

4.3.2 Muons

Muons interact with all of ATLAS subdetectors, even though they act as minimum ionizing particles (MIP) and hence will deposit only a very small fraction of their energy in the material. Their tracks are reconstructed in the muon spectrometer (MS) by identifying track segments in each layer of the chambers, that are then combined to form a full track. Muon candidates are classified in different types based on their reconstruction:

- `Stand-Alone` muons (SA). The muon trajectory is reconstructed using only the hits in the MS (used mainly in the region $2.5 < |\eta| < 2.7$ not covered by the ID).
- `Combined` muons (CB). The muon trajectory is reconstructed by matching a track reconstructed in the MS with a track from the ID. This type has the highest muon purity and is the one recommended for physics analyses.
- `Segment-tagged` muons (ST). Muons are reconstructed by matching the tracks from the ID with the track segments in the MDT or CSC chambers. They are used to recover the acceptance that may be lost by the CB muons.
- `Calorimeter-tagged` muons (CaloTag). Muons are reconstructed by matching the tracks from the ID to the energy deposit in the calorimeter compatible with a MIP. This type has the lowest purity of all the muon types but it recovers acceptance in the uninstrumented region of the MS, i.e. recover the acceptance at $|\eta| < 0.1$ where no MS layers are present.

The analysis presented in this dissertation makes use only of `combined` muons, reconstructed using the `Muid` algorithm [114]. This algorithm searches for track segments in the RPC and TGC in $\Delta\eta \times \Delta\phi = 0.4 \times 0.4$ regions where the trigger fired, and combine them into a single MS track by means of a least-square fitting method. These tracks are then extrapolated back to the interaction point, taking into account the energy losses in the calorimeter material. To obtain the final muon candidate track, a χ^2 test, that matches the candidate MS track and the tracks reconstructed in the ID, is performed. The momentum of the muon candidate is computed as a weighted average of ID and MS measurements and calibrated using $Z \to \mu^+\mu^-$ events.

To further improve the quality of the muon and reduce the misidentification rate, additional selection criteria are applied:

- Combined muons are required to have pseudo-rapidity $|\eta| < 2.5$, in order to be confined to the region with ID coverage.
- The longitudinal impact parameter $|z_0| < 2$ mm, to ensure the track comes from the hard-scatter PV.

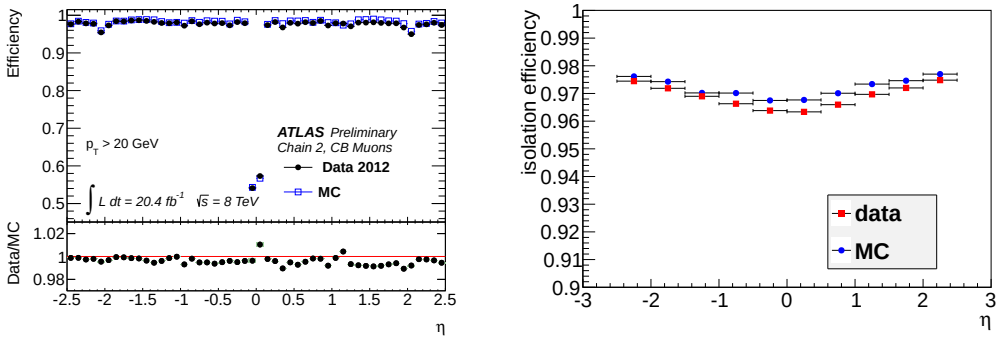

(a) (b)

Figure 4.5: (a) `Combined` muon reconstruction efficiencies using the `Muid` algorithm measured from $Z \to \mu^+\mu^-$ events in data and simulation as a function of η. (b) Mini Isolation efficiency as a function of muon η for data and MC. Figure taken from reference [104].

- A minimal number of hits in the Pixel, SCT and TRT subdetectors is required, together with a hit in the innermost pixel layer when the track crosses an active module.

The reconstruction, identification and isolation efficiencies have been measured in data with the tag-and-probe method using $Z \to \mu^+\mu^-$ and $J/\Psi \to \mu^+\mu^-$ events. The data/MC comparison for the reconstruction plus identification efficiency and the isolation efficiency are shown in Fig. 4.5. The level of agreement and the corresponding uncertainties are $\sim 1\%$ and found to be very stable versus other kinematic quantities as well as versus the number of primary vertices in the event.

A further separation between prompt muons arising from the hard interaction and muons originating from decay chains of b/c-hadrons or kaons, is achieved through an isolation requirement. A "mini-isolation" variable, I^{μ}_{mini}, is introduced [104] to reject non-isolated muons and reduce sensitivity to the high pileup conditions of $\sqrt{s} = 8$ TeV collision events:

$$I^{\mu}_{mini} = \sum_{tracks} p_{\mathrm{T}}^{track}/p^{\mu}_{\mathrm{T}}, \tag{4.1}$$

where p^{μ}_{T} is the transverse momentum of the reconstructed muon and the sum is done over all tracks with $p_{\mathrm{T}}^{tracks} > 1$ GeV, found within cone radius $\Delta R(\mu, track) = 10\ \mathrm{GeV}/p^{\mu}_{\mathrm{T}}$. The mini-isolation requirement is $I^{\mu}_{mini}/p^{\mu}_{\mathrm{T}} < 0.05$, yielding a 97% efficiency for identifying hard-scatter muons.

A second muon definition, with looser selection criteria, will also be used to estimate the contribution from non-prompt muons arising from semi-leptonic hadron decays. This looser definition removes the isolation requirement in order to increase the contribution from multijet events. The use of this second set of muons will be described in detail in section 7.3.4.

4.3.2.1 Muon Momentum Scale and Resolution

A simultaneous determination of the muon momentum scale and resolution is possible due to the large number of clean $Z \to \mu^+\mu^-$ and $J/\psi \to \mu^+\mu^-$ events collected. For

this a fit to the di-muon invariant mass distributions of the Z and J/ψ resonances [115] is performed. Correction factors for the momentum scale and resolution are determined separately for the MS and ID. The central value and the uncertainty of the correction to the muon momentum scale in the MS are shown in Fig. 4.6. The amount of the correction, as well as the uncertainty, are at the few per mille level.

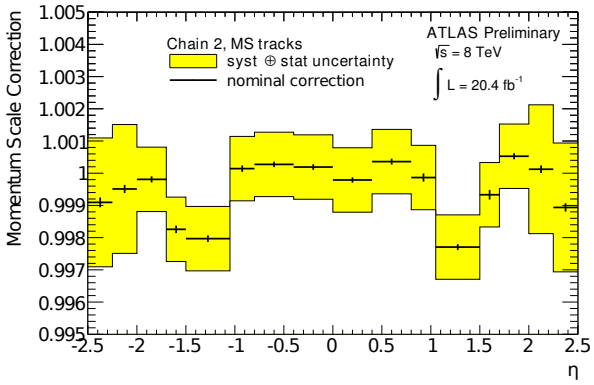

Figure 4.6: Scale correction for the muon momentum in the muon spectrometer as a function of muon η. Figure taken from reference [115].

These factors, and their relative uncertainties, are used to correct the MC scaling the muon p_{T} and introducing additional smearing to match the data. The di-muon invariant mass for data and MC, before and after such corrections have been applied, are shown in Fig. 4.7.

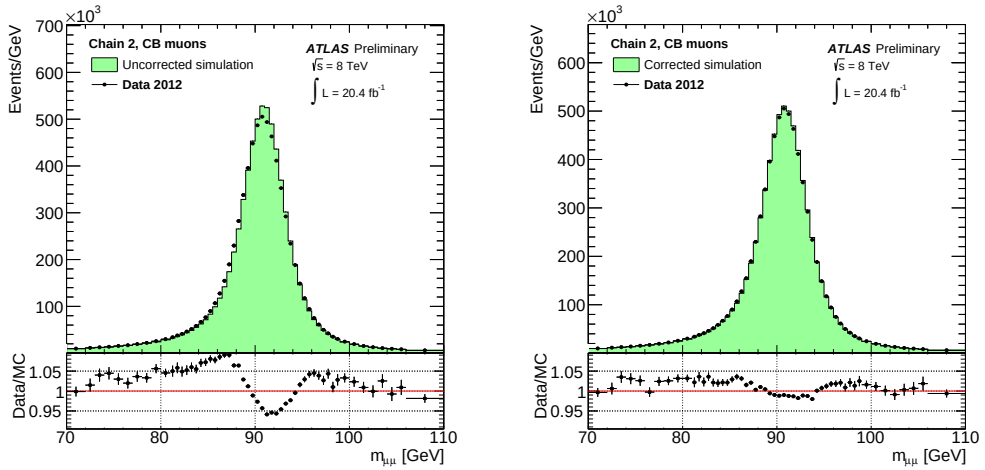

(a) (b)

Figure 4.7: Comparison of di-muon invariant mass in data, before (a) and after (b) MC smearing and scale corrections are applied. Figures taken from reference [115].

4.4 Jets

One of the consequences of color confinement is that quarks and gluons cannot be found isolated and therefore cannot be directly observed. Instead, they clump together to form hadrons. This process is called *hadronization*. The spray of calorimeters particles created by the hadronization of a quark or gluon is called a *jet*. Jets are measured in particle detectors and studied in order to determine the properties of the initial parton.

Jets can be categorized according the type of inputs and the algorithm used to combine them and build a jet:

- *Particle jets*. Jets reconstructed from truth stable particles in MC samples.
- *Track jets*. Jets built from reconstructed tracks in the detector.
- *Calorimeter jets*. Jets built from energy deposits in the calorimeter and most commonly used in ATLAS analyses.

In the following, only the calorimeter jets are considered.

4.4.1 Cluster Formation

In order to interpret the detector information, neighboring calorimeter cells are grouped into topological clusters, known as *topo-clusters*, by means of the *topological clustering* algorithm [110]. This algorithm reconstructs three-dimensional clusters based on the significance of the energy deposit in the calorimeter cells, E_{cell}, with respect to their noise level σ. The σ is defined as the RMS of the energy distribution measured in events triggered at random bunch crossings, and it takes into account electronic noise and pile-up fluctuations.

Cells with a significant signal-to-noise ratio of $|E_{cell}|/\sigma > 4$ are selected as seeds, and all the neighboring cells in the three dimensions with a signal-to-noise ratio of $|E_{cell}|/\sigma > 2$ are then added to the topo-cluster. Finally, cells in the perimeter are also added to the topo-cluster, to ensure that the tails of showers are not discarded. A schema of a topological cluster formation is presented in Fig. 4.8a.

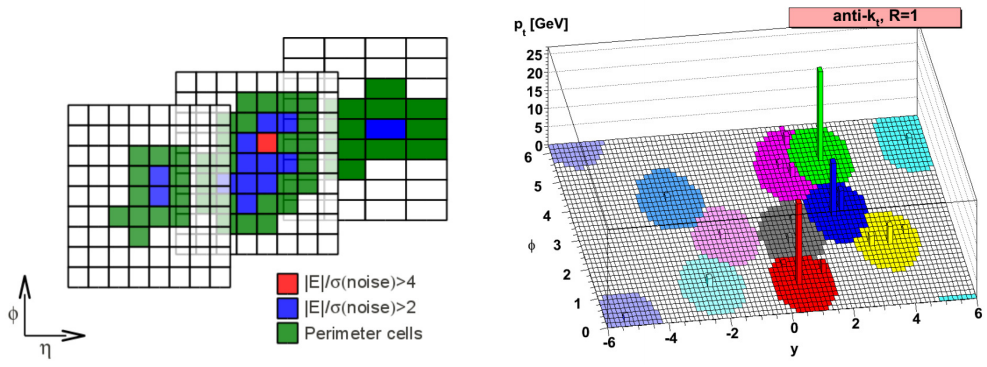

(a) (b)

Figure 4.8: (a) Grid representing calorimeter cells, showing topo-cluster formation in the three hadronic layers in the barrel. (b) Illustration of the clustering of jets with the anti-k_T algorithm. Figures taken from reference [116–118].

4.4.2 Jet-finding Algorithm

A jet-finding algorithm is needed to decided which inputs are aggregated into individual jets. A class of jet algorithms, known as *sequential recombination* algorithms [116–118], combine topo-clusters into jets using an iterative method based on a distance parameter criterion, defined as:

$$\begin{aligned} d_{ij} =& min\left(p_{\mathrm{T}_i}^{2p}, p_{\mathrm{T}_j}^{2p}\right)\frac{\Delta R_{ij}^2}{R^2}, \\ d_i =& p_{\mathrm{T}_i}^{2p}. \end{aligned} \tag{4.2}$$

Here, d_{ij} is the distance between the constituents i and j, while d_i is the distance between the constituent i and the beam, introduced to separate constituents coming from the hard-scatter interaction from those coming from proton remnants. p_{T_i} is the transverse momentum of topo-cluster i, $\Delta R_{ij}^2 = \Delta\eta_{ij}^2 + \Delta\phi_{ij}^2$ is the distance between constituents i and j, R is a parameter of the algorithm that approximately controls the size of the jet , and p is the parameter that defines the type of algorithm:

$$\begin{aligned} p = \quad 1: &\quad k_T \quad \text{algorithm;} \\ p = \quad 0: &\quad \text{Cambridge/Aachen} \quad \text{algorithm;} \\ p = -1: &\quad \text{anti}{-}k_T \quad \text{algorithm;} \end{aligned} \tag{4.3}$$

At each iterative step the jet-finding algorithms compute all possible distances d_{ij} and d_i. If the smallest distance is a d_{ij}, it removes the constituents i and j, and replaces them with a merged one, while if the smallest distance is d_i, the algorithm calls i a jet and removes it from the list of constituents. The iterative procedure is repeated until no constituents are left.

The default jet-finding algorithm used at the LHC experiments, and in particular in ATLAS, is the anti-k_T algorithm. This algorithm has been chosen for its theoretical properties of infrared and collinear safety [119], and for the fact that it produces rather circular jets in the $\eta - \phi$ plane. Fig. 4.8b illustrates the clustering of hard and soft particles into jets when the anti-k_T algorithm is applied. The analysis described in this dissertation uses anti-k_T jets with a radius of $R = 0.4$. During jet reconstruction, no distinction is made between identified electrons and jet energy deposits. Therefore, if any of the jets lie within $\Delta R = 0.2$ of a selected electron, the closest jet is discarded in order to avoid double-counting of electrons as jets.

4.4.3 Jet Calibration

Initially, the topo-clusters are reconstructed at the electromagnetic scale (EM), which measures the energy in the calorimeter deposited by particles produced in an electromagnetic shower. To correctly measure the energy deposited by particles produced in a hadronic shower the local cluster weights (LCW) [120] calibration scheme, that calibrates the jets at the hadronic scale, is applied. This scheme classifies topo-clusters as either electromagnetic or hadronic based on the measure energy density and the longitudinal shower depth. Then, energy corrections are applied according to this classification from single pion MC simulations. Further dedicated corrections are introduced for the effects of non-compensation response of the calorimeter, signal losses

due to noise threshold effects, and energy lost in non-instrumented regions (dead material). The analysis described in this dissertation use jets built from LCW-calibrated clusters, which are also referred to as LCW-jets. Jets built from non-calibrated clusters are usually named EM-jets.

Further corrections are applied to the reconstructed jet energy in order to reduce the impact of pile-up contamination and recover the energy of the truth particle jets on average. The calibration scheme consists of four steps, illustrated in Fig. 4.9 and described below:

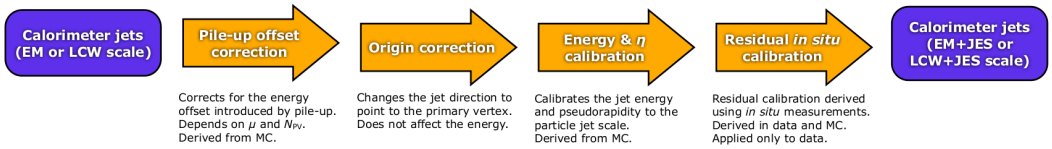

Figure 4.9: Overview of the ATLAS jet calibration scheme. Figure taken from reference [121].

4.4.3.1 Pile-up Offset Correction

The measured energy of calorimeter jets can be affected by contributions produced by additional pile-up activity. An offset correction to subtract this contribution is defined as:

$$p_{\mathrm{T}}^{corr} = p_{\mathrm{T}} - \rho \cdot A - \alpha \cdot (N_{\mathrm{PV}} - 1) - \beta \cdot \langle \mu \rangle \,, \tag{4.4}$$

where:

- ρ is the pile-up energy density of the event, which provides a direct estimate of the global pile-up activity.
- A is the *jet area*, which is estimated jet-by-jet and provides a measure of the susceptibility of the jet to pile-up [122].
- $\alpha = \frac{\partial p_{\mathrm{T}}}{\partial N_{\mathrm{PV}}}$ - the coefficient of a residual term proportional to the number of reconstructed pile-up vertices $N_{\mathrm{PV}} - 1$ (to account for in-time pile-up).
- $\beta = \frac{\partial p_{\mathrm{T}}}{\partial \mu}$ - the coefficient of a residual term proportional to the number of average interactions in a luminosity block $\langle \mu \rangle$ (to account for out-of-time pile-up).

The dependence of jet p_{T} on N_{PV} and $\langle \mu \rangle$ as a function of jet pseudo-rapidity, η, at each step of the correction process, is shown in Fig. 4.10.

4.4.3.2 Origin Correction

Initially, calorimeter jets are reconstructed using the geometrical center of the ATLAS detector as reference to calculate the direction of jets and their constituents. The jet four-momentum is corrected for each event such that the direction of each topo-cluster points back to the hard-scatter PV. This correction improves the angular resolution and results in a small improvement ($< 1\%$) in the jet p_{T} response. The jet energy remains unaffected.

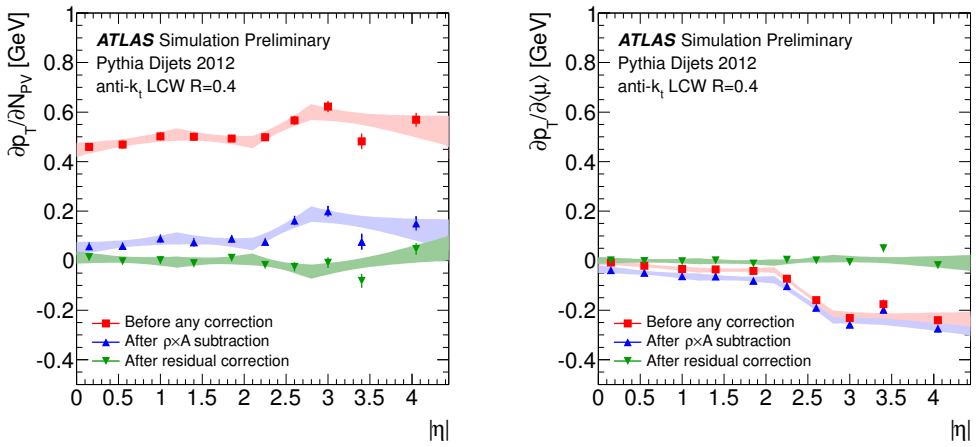

(a) (b)

Figure 4.10: Dependence of the reconstructed jet p_{T} on (a) in-time pile-up and (b) out-of-time pile-up at various correction stages: before any correction, after $\rho \cdot A$ subtraction, and after the residual correction. Figures taken from reference [123].

4.4.3.3 Jet Energy Calibration

The jet energy calibration restores the reconstructed jet energy to the energy of the truth particle jet. Since pile-up effects have already been corrected for, the MC samples used to derive the calibration do not include multiple proton-proton interactions. The calibration is derived using all isolated jets reconstructed in the calorimeter that have a matching isolated truth particle jet within $\Delta R < 0.3$. Here, an isolated jet is defined as a jet having no other jet with $p_{\mathrm{T}} > 7$ GeV within a cone of radius $\Delta R = 2.5R$, where $R = 0.4$ is the jet radius. For each pair of matching isolated calorimeter and truth jets the *jet energy response* is computed as:

$$R_{\mathrm{jet}}^{\mathrm{EM(LCW)}} = \frac{E_{\mathrm{jet}}^{\mathrm{EM(LCW)}}}{E_{\mathrm{jet}}^{\mathrm{truth}}}, \tag{4.5}$$

where $\mathrm{E}_{\mathrm{jet}}^{\mathrm{EM}}$ and $\mathrm{E}_{\mathrm{jet}}^{\mathrm{LCW}}$ are the energy measured in the reconstructed EM and LCW jets respectively, while $\mathrm{E}_{\mathrm{jet}}^{\mathrm{truth}}$ is the truth particle jet energy. The jet energy response as a function of the calorimeter jet detector pseudo-rapidity η_{det} is shown in Fig. 4.11. The correction factor needed for LCW jets is closer to unity than for EM jets since the input topo-clusters used for LCW jets have been calibrated at the hadronic scale.

4.4.3.4 In-situ Calibration

As a last step data-to-MC differences are assessed using *in-situ* techniques, which exploit the transverse momentum balance between the jet and a well-measured photons, Z bosons or jets. Such correction is applied to jets in data in order to match the jet energy scale of the MC simulation. The calibration of jets in the forward and central regions of the detector is done differently. Central jets are calibrated combining in-situ techniques as Z+jets, γ+jets and multi-jet balance calibration [121]. Fig. 4.12 shows the ratio of the jet response, defined as $p_{\mathrm{T}}^{\mathrm{measured}}/p_{\mathrm{T}}^{\mathrm{reference}}$, between data and MC. In

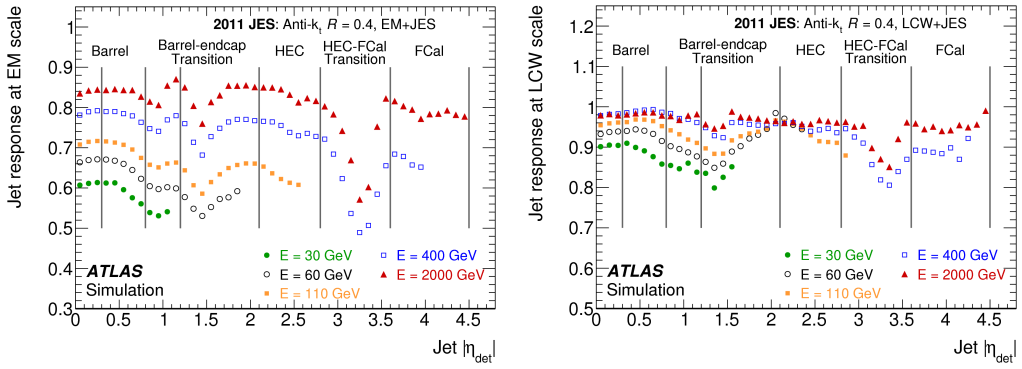

(a) (b)

Figure 4.11: Average response for jets built from topo-clusters at (a) the EM scale and (b) the LCW scale. The response is shown separately for various particle-jet energies as function of the jet detector pseudo-rapidity η_{det}. Also indicated are the different calorimeter regions. Figures taken from reference [121].

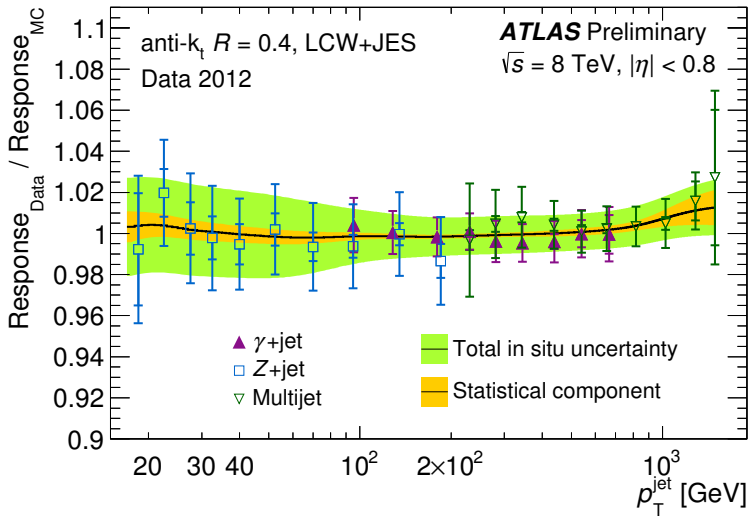

Figure 4.12: Ratio of the average jet response $\langle p_{\mathrm{T}}^{\mathrm{jet}}/p_{\mathrm{T}}^{\mathrm{ref}}\rangle$ measured in data to that measured in MC simulations for jets within $|\eta| < 1.2$ as a function of the jet transverse momentum, $p_{\mathrm{T}}^{\mathrm{jet}}$, shown separately for the three in-situ techniques, used in the combined calibration. Figure taken from reference [121]

contrast, forward jets are calibrated using the η-intercalibration technique. This technique exploits the p_{T}-balance between jets in different η regions where forward jets are calibrated against central jets, whose energy scale can be assessed in a more precise way.

4.4.3.5 Semileptonic *b*-jet Corrections

In addition to the standard jet calibration, further correction is applied for semileptonic[1] decays of heavy-flavored hadrons. In the case of semileptonic b-hadron decays the energy of the jet containing that hadron is underestimated since both the muon and the neutrino can carry a substantial part of the hadron energy and they are not considered in the jet clustering process.

In b-hadron decays muons are produced in $\sim 20\%$ of the cases, including direct decays and decays via decays via c-hadrons and τ leptons. The effect of this production is important for analyses with a large number of b-quarks in the final state. Therefore, the jet four-momentum is corrected by combining it with the muon:

$$\mathbf{p}_{\text{jet}}^{\text{corr}} = \mathbf{p}_{\text{jet}} + \sum_{i}^{\text{muons}} (\mathbf{p}_{\mu_i} - \mathbf{E}_{\text{loss}}(\mu_i)) \tag{4.6}$$

where p_{μ_i} is the combined muon and $E_{\text{loss}}(\mu_i)$ is the estimated energy loss of the muon in the calorimeter which is subtracted to avoid double-counting. Only muons passing the standard *MuId* selection cut ($p_{\text{T}} > 4$ GeV and distance ΔR to the jet axis < 0.4) are considered in the correction term.

The correction is applied to all jets overlapping with muons, independently of whether they are tagged as b-jets. The energy losses due to the escaping neutrino are not considered since a correction term was derived based on a different category of muons, *Staco* and not *MuId*, as used in this analysis. The effect of each correction on a b-jets from $t\bar{t}$ events are shown in Fig. 4.13.

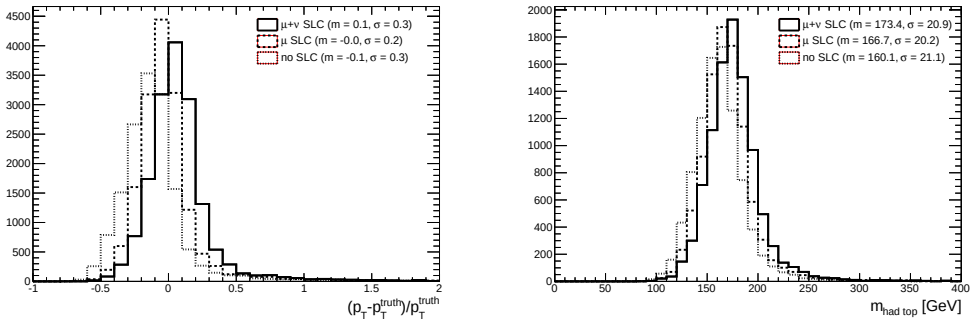

(a) (b)

Figure 4.13: (a) Jet p_{T} resolution and (b) reconstructed hadronic top mass for an inclusive jet sample in MC $t\bar{t}$ events. The dotted line describes calibrated jets, the dashed line jets after the muon correction and the solid line jets after both the muon and the neutrino corrections. Figures taken from reference [124].

4.4.4 Jet Cleaning

Further jet cleaning criteria have been developed in order to identify fake jets, also referred to as "bad jets". Two sets of cuts are implemented, one to reject jets related to

[1] The notation *semileptonic* is used to denote any decay chain of the type: $B \to X + \mu + \nu_{\mu}$. Decays in the electron channel don't require a special treatment since the electron energy is deposited in the calorimeter and clustered into the jet.

detector problems, and one to discriminate against cosmic rays and non-pp-collisions. Such non-pp-collisions can originate from interactions of the incoming protons with residual gas inside the LHC beam pipe or with the beam collimators in the forward region. The jet cleaning cuts applied are:

- The shape of the electrical signal collected in every calorimeter cell is compared to the reference (quality factor), and a jet quality factor is computed weighting the cell quality with the cell energy squared. Jets with significant deviation from the reference quality factor are rejected.
- The energy of the jet deposited in the electromagnetic calorimeter must be between 5% and 95%. This helps reducing noise effects from the EM calorimeter and from non-collision backgrounds.
- Due to the larger noise in the HEC, the fraction of the jet energy in this subdetector has to be smaller than 50%.
- The energy fraction of a jet contained in one single layer of the calorimeter should be smaller than 99%.

4.4.5 Jet Vertex Fraction

Due to the high pile-up environment with many interactions per bunch crossing it is necessary to introduce dedicated cuts to suppress jets that do not originate from the interaction vertex of interest. This is accomplished via a selection of the so-called jet vertex fraction (JVF), which is used in ATLAS to estimate the jet energy that comes from the hard-scatter PV [122]. Using tracks reconstructed in the ID, the JVF variable is defined for the pair $(\text{jet}_i, \text{PV}_j)$ as the ratio of the sum of transverse momentum of matched tracks that originate from a chosen PV, to the sum of transverse momentum of all matched tracks in the jet, independently of their origin:

$$\text{JVF}(\text{jet}_i, \text{PV}_j) = \frac{\sum_k p_{\text{T}}(\text{track}_k^{\text{jet}_i}, \text{PV}_j)}{\sum_{n=1}^{N_{\text{PV}}} \sum_{k=1}^{N_{\text{tracks}}} p_{\text{T}}(\text{track}_k^{\text{jet}_i}, \text{PV}_n)}. \tag{4.7}$$

The JVF variable has a good separation power between the jets originating from the hard-scatter PV and for jets originating from pile-up interactions, as illustrated in Fig. 4.14a. Four distinct populations can be distinguished in the JVF variable:

- JVF $= -1$ is assigned to calorimeter jets which do not have associated tracks (mainly at large rapidity).
- JVF $= 0$ indicates that all tracks originate from pile-up vertices.
- $0 <$ JVF < 1 indicates that some tracks originate from the hard-scatter PV and some from pile-up vertices.
- JVF $= 1$ indicates that all tracks originate from the hard-scatter PV.

In the analysis presented in this dissertation, a requirement on the absolute value of the JVF variable above 0.5 is applied to jets with $p_{\text{T}} < 50$ GeV and $|\eta| < 2.4$. The effect of the cut has been tested on data and MC using $Z \to \ell^+\ell^-$ events where specific selections are applied to obtain a sample of hard-scatter jets and pile-up jets. This cut

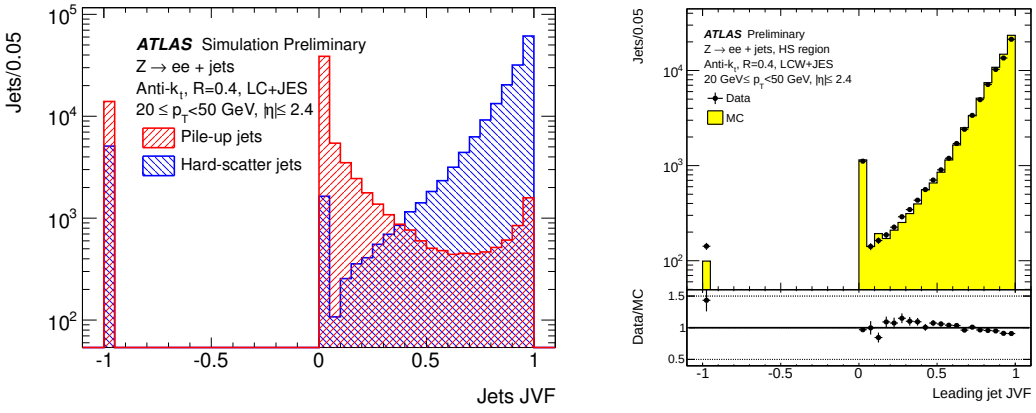

(a) (b)

Figure 4.14: (a) JVF distribution for hard-scatter (blue) and pile-up (red) jets with $20 \leq p_{\mathrm{T}} \leq 50$ GeV and $|\eta| < 2.5$ in simulated Z+jets events. (b) JVF distribution for jets well balanced against $Z \to e^+e^-$ candidates in data and MC simulation. Figures taken from reference [122].

gives a 95% selection efficiency for jets from the primary interaction while rejecting 75% of pile-up jets.

The comparison between data and MC for a sample enriched in hard-scatter jets is presented in Fig. 4.14b.

4.5 *b*-tagging

The identification of jets originating from the hadronization of b-quarks, b-jets, is an important ingredient for analyses with b-quarks in the final state. When a b-quark is produced in an event, it hadronizes into a b-hadron, which has relative long lifetime, τ, of the order 10^{-12} s. Therefore, a b-hadron travels about 3-5 mm before decaying, generating a secondary vertex (SV) that can be separated from the hard-scatter PV, and if correctly reconstructed, can allow for the identification of the b-jet. A schematic view of a b-hadron decay is shown in Fig. 4.15.

Several characteristics can be exploited to identify the b-hadron decay, based on the SV identification. If the SV can be identified within a jet, the distance L_{xy} between the SV and PV, referred to as *decay length* [2], as well as the mass of all the particles associated to the vertex can be used for the identification. SV from b-hadron decays are expected to be significantly displaced from the PV and to have a vertex mass of up to ~ 5 GeV (due to neutral decay products not being included). If the SV is not reconstructed the *impact parameter* of the tracks in the jet can be used for the b-hadron decay identification. The impact parameter is divided between the longitudinal and transverse components in the z-direction and in the x-y plane. The sign of the impact parameter is positive if the track extrapolation crosses the jet direction in front of the PV, and negative otherwise. For a jet originating from a b-quark, typically one or more tracks are expected to show a large and positive impact parameter significance.

[2] The decay length is divided by its error to obtain the *decay length significance*, L/σ_L, in order to reduce the effect of poorly-measured vertices.

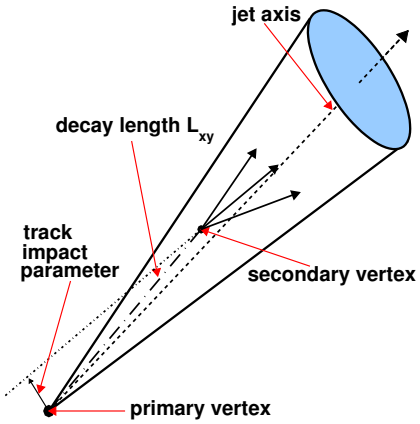

Figure 4.15: Schematic view of a b-hadron decay inside a jet resulting in a SV with three charged particle tracks. The vertex is significantly displaced with respect to the PV, thus the decay length is macroscopic and measurable. The track impact parameter is shown in addition for one of the secondary tracks. Figure taken from reference [125].

The advantage of the impact parameter approach is that it can be obtained without the need to reconstruct the SV.

4.5.1 *b*-tagging Algorithms

The algorithms that identify the jets coming from a b-quark are referred to as b-tagging algorithms [126]. The b-tagging algorithms developed within the ATLAS collaboration exploit either the properties of the tracks IP or the presence of a SV. Both methods rely on the measurement of the tracks in the ID and therefore the jets originating from a b-hadron can be identified only for $|\eta| < 2.5$.

The baseline b-tagging algorithms are summarized below:

- **IP3D**. An IP-based algorithm, where the longitudinal and transverse IP of the tracks are used in a 2D likelihood ratio discriminant. Input variables are compared to templates for both the b-jet and light-jet hypotheses, obtained from MC simulation.

- **SV1**. An SV-based algorithm, where different variables are combined using a likelihood ratio technique, such as the SV decay length significance, the invariant mass of all tracks associated with the vertex, the ratio of the sum of the energies of the tracks in the vertex to the sum of the energies of all tracks in the jet, and the number of two-track vertices.

- **JetFitter**. An algorithm based on the discrimination between light- and b-jets by taking advantage of the topology of the weak b- and c-hadron decays in the jets and the identification of secondary and tertiary vertices with the assumption that they lie on the flight direction of the b-hadron. The final discrimination is achieved by combining the discriminating variables used also by SV1 and the flight length significance of the vertex with a likelihood ratio method.

- **JetFitterCombNN**. A neural network algorithm that combines the output of the IP3D and JetFitter algorithms, used for the analysis of the $\sqrt{s} = 7$ TeV dataset. A different version called JetFitterCombNNc is also available where the neural network is explicitly trained to separate c-jets from b-jets.

- **MV1**. A neural network algorithm that combines the output of the IP3D, SV1 and JetFitterCombNN weights, used for the analysis of the $\sqrt{s} = 8$ TeV dataset. In order to obtain better separation between jets originating from b-quarks and jets originating from c-quarks a new version of this algorithm, so-called MV1c algorithm, has been developed.

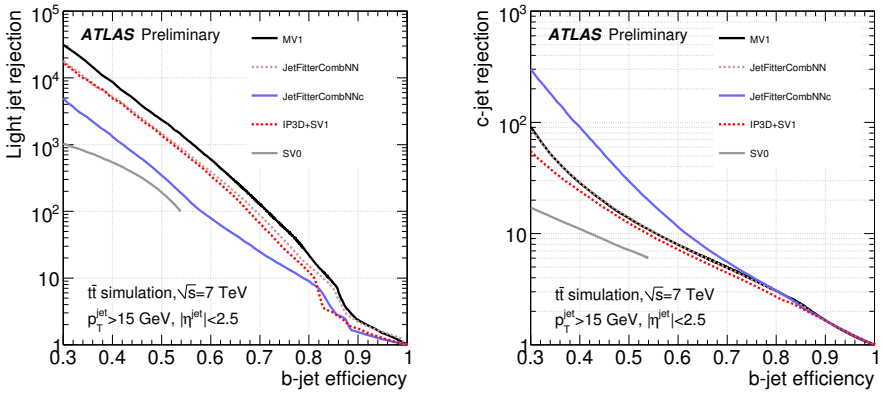

(a) (b)

Figure 4.16: (a) Light-jet rejection and (b) c-jet rejection as a function of the b-jet efficiency for different available b-tagging algorithms, based on simulated $t\bar{t}$ events. Figures taken from reference [126].

The b-tagging algorithms are characterized by their capability to correctly identify jets coming from a real b-quark (b-tagging efficiency) compared to the probability of mistakenly b-tagging a jet originating from a c-quark or a light-flavor parton (u, d, s-quark or gluon), referred to as the c-tagging efficiency [3] and mistag rate respectively. The performance of some of the algorithms discussed above is summarized in Fig. 4.16. Here, the rejection is defined as the inverse of the mistag or c-tagging rate. The MV1 algorithm shows the best performance in rejecting light quark jets and is therefore used as the b-tagging algorithm of choice for the analysis presented in this dissertation.

Several operating points have been considered based on the average efficiency of the algorithm on simulated $t\bar{t}$ events. Some of them are listed in Table 4.1.

The 70 % operating point has been chosen for most of the $t\bar{t}$-based analyses given the good compromise between efficiency and rejection. The efficiency, obtained from the simulation, of the 70 % MV1 operating point for b-jet, c-jet and light-jets as a function of the jet p_{T} and $|\eta|$, are presented in Fig. 4.17. The b-tagging efficiency increases at high p_{T} where the identification of displaced vertices is more efficient. The mistag rate is more important for large $|\eta|$ values due to the worse track resolution.

[3] Dedicated algorithms to identify c-jets are also available [127]. In the context of this dissertation, c-tagging refers to mistakenly b-tagging a c-jet.

b-jet efficiency	c-jet rejection	light-jet rejection
50%	13.7	2330
60%	7.9	590
70%	5.0	140
80%	3.1	25

Table 4.1: The MV1 algorithm's operating points and their performance. The b-jet efficiency is the average obtained for b-jets from a simulated $t\bar{t}$ sample.

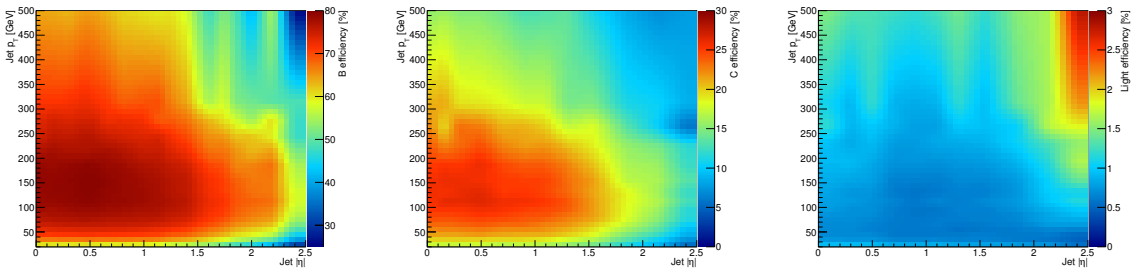

(a) (b) (c)

Figure 4.17: b-tagging efficiency for the MV1 70% operating point as a function of the jet p_{T} and $|\eta|$. Efficiencies are shown separately for (a) b-jets, (b) c-jets and (c) light-jets from simulated $t\bar{t}$ events. Figures taken from reference [124].

4.5.2 *b*-tagging Calibration

The efficiency of each operating point has been calibrated in order to correct for mismodeling in the input variables used in the b-tagging algorithms. The calibration is performed using data samples enriched in b-jets, c-jets and light jets, respectively, and presented in terms of scale factors, SF$= \epsilon_{\mathrm{data}}/\epsilon_{\mathrm{MC}}$, used to correct the per-jet tagging efficiency in the simulation. Several methods have been used for the calibration according to the sample they use:

- ***b*-jet calibration**. The tagging calibration on b-quarks has been derived on a high-purity sample of b-jets that can be obtained from dileptonic $t\bar{t}$ events in data. The calibration is based on a likelihood approach which uses correlated information from multiple jets in the event [128], and achieves a precision of a few % for jets with p_{T} ranging between 30 and 200 GeV. Since the calibration has been derived using a dileptonic $t\bar{t}$ sample, no overlap of data events exists with analyses performed in the single-lepton final state.

- ***c*-jet calibration**. The calibration has been derived by reconstructing D-mesons within a jet from the decay chain $D^{*+} \to D^0(\to K^-\pi^+)\pi^+$ [129].

- ***light*-jet calibration**. Light-jets are expected to have a rather symmetric track impact parameter or vertex decay length significance distribution. Therefore, the "negative tag" method [130] is used for the mistag rate estimation. The

performance of the tagger is evaluated by using tracks (vertices) with negative impact parameter (decay length significance) and reversing their sign within the algorithm.

The scale factors obtained are applied to MC samples as event weight corrections. If a jet in simulation satisfies the b-tagging algorihtm criterion, a weight equal to the b-tagging scale factor, SF, of the corresponding jet flavor is considered. Otherwise, a weight corresponding to $(1 - \mathrm{SF} \cdot \epsilon_{\mathrm{MC}})/(1 - \epsilon_{\mathrm{MC}})$ is assumed. The event-level weight is obtained as the product of all the selected individual jet weights. Scale factors as a function of jet p_{T} for b-jet, c-jet and light-jets are shown in Fig. 4.18.

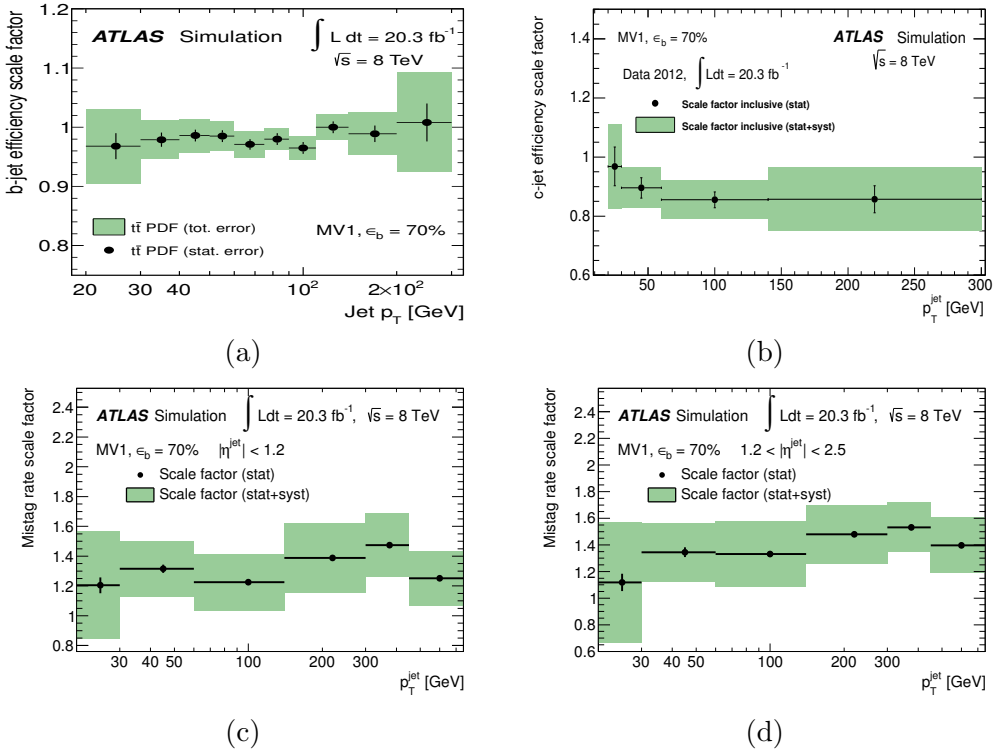

Figure 4.18: Data/MC scale factor for the tagging efficiency of (a) b-jets, (b) c-jets and (c) light jets in the central and (d) forward region with the 70 % MV1 operating point. The total uncertainty is shown as well as the statistic components. Scale factors are measured as a function of jet p_{T} and, in the case of mistag rate, the result for two $|\eta|$ bins are shown. Figures taken from reference [124].

There are multiple systematic uncertainties affecting the b-tagging scale factors and the diagonalization method is used in order to to propagate them in a manageable way. The covariance matrix of the scale factors in the different jet p_{T} bins is diagonalized. The eigenvectors of the covariance matrix represent the variations which are needed to describe the b-tagging efficiency uncertainty induced in the analysis. After diagonalization, these variations can be considered as independent variations and are treated in the analysis as uncorrelated uncertainties. A total of six eigenvectors are considered to describe the systematic uncertainties related to the b-tagging calibration. The same procedure is performed to derive four (twelve) eigenvectors on the c-tagging (mistag) calibration.

The b-tagging calibration for b-jets and c-jets only extends to 300 GeV in jet p_{T}, with the light-jet calibration extending to 750 GeV. A MC-based analysis is used to assess an extrapolation uncertainty on the b-tagging efficiency from the last calibrated p_{T} bin up to 1200 GeV, to judge how systematic effects could impact the higher p_{T} jets compared to the last calibrated bin. An additional uncertainty is included for jets with p_{T} above the calibrated range.

4.6 Missing Transverse Momentum

To estimate the momentum of weakly-interacting particles that escaped without being measured, i.e. neutrinos and other particles predicted in BSM scenarios, the missing transverse momentum, $\overrightarrow{p_{\mathrm{T}}}^{\mathrm{miss}}$, is used. The $\overrightarrow{p_{\mathrm{T}}}^{\mathrm{miss}}$ is obtained from the negative vector sum of the p_{T} of all particles detected in a pp collision. The magnitude of this vector is the missing transverse energy, $E_{\mathrm{T}}^{\mathrm{miss}}$.

The $E_{\mathrm{T}}^{\mathrm{miss}}$ along the x and y axis is defined as the sum of the missing energy measured in the calorimeters and muons measured in the muon spectrometer:

$$E_{x,y}^{\mathrm{miss}} = E_{x,y}^{\mathrm{miss,calo}} + E_{x,y}^{\mathrm{miss},\mu}. \tag{4.8}$$

Isolated muons are measured by combining the information in the muon spectrometer and the inner detector. In the case of non-isolated muons, the momentum measurement is taken from the muon spectrometers only and an additional term for the energy deposit in the calorimeter is considered.

Energy deposits in calorimeter cells are associated with identified physics objects and are considered in the calculation with the calibration of these associated objects. Double counting is avoided by considering physics objects in a specific order: electrons, jets and muons.

$$E_{\mathrm{x(y)}}^{\mathrm{miss,calo}} = E_{\mathrm{x(y)}}^{\mathrm{miss,e}} + E_{\mathrm{x(y)}}^{\mathrm{miss,jet}} + \left(E_{\mathrm{x(y)}}^{\mathrm{miss,muon-calo}}\right) + E_{\mathrm{x(y)}}^{\mathrm{miss,soft-jet}} + E_{\mathrm{x(y)}}^{\mathrm{miss,cell-out}} \tag{4.9}$$

where the sum is the missing momentum contributions of electrons, photons, hadronically decaying taus, jets, softjets, muons and cells not associated to any other objects (CellOut).

The effects of systematic uncertainties in the $E_{\mathrm{T}}^{\mathrm{miss}}$ computation are divided into two main sources: uncertainties affecting high-p_{T} objects and uncertainties affecting the soft-jet and the cell-out terms. For the former, systematic uncertainties on the physics object calibrations are directly translated into the missing transverse energy computation through Eq. 4.8. The uncertainties on $E_{\mathrm{T}}^{\mathrm{miss,soft-jet}}$ and $E_{\mathrm{T}}^{\mathrm{miss,cell-out}}$ are considered to be fully correlated, and they are evaluated in events with no real source of $E_{\mathrm{T}}^{\mathrm{miss}}$, such as $Z \to \mu^+\mu^-$ events with no jets with $p_{\mathrm{T}} > 20$ GeV. An uncertainty of 2.3% and 3.6% has been assigned respectively to the resolution and scale of both terms [131].

Chapter 5

Event Samples and Preselection

This chapter describes the event selection criteria, the data samples and the modeling of the signal and background samples used in the analysis. The event preselection criteria is described in Sec. 5.2. Sec. 5.1 presents the data samples used, while Sec. 5.3 describes the signal and background modeling with the simulation. The *tag rate function* (TRF) method, that helps to improve the statistical precision in the background prediction, is introduced in Sec. 5.4. Finally, the quality of the modeling is illustrated in Sec. 5.5 with the comparison between data and prediction for a number of kinematic distributions.

5.1 Data Sample

The search is based on pp collision data at a center-of-mass energy of $\sqrt{s} = 8$ TeV collected by the ATLAS experiment between April and December 2012. The total integrated luminosity recorded, after requiring all subdetectors to be fully operational during the data taking, is 20.3 ± 0.6 fb^{-1}. Events collected during stable beam periods are required to pass data quality requirements and are selected online by single-electron or single-muon triggers.

In order to maximize the trigger efficiency, different p_{T} thresholds are combined in a logical OR. The triggers with the lower-p_{T} threshold include isolation requirements on the candidate lepton, resulting in inefficiencies at high p_{T} that are recovered by the triggers with higher-p_{T} threshold. The p_{T} thresholds are 24 or 60 GeV for the electron triggers and 24 or 36 GeV for the muon triggers. The electron triggers used are `EF_e24vhi_medium1` and `EF_e60_medium1`, while the muon triggers are `EF_mu24i_tight` and `EF_mu36_tight`.

The isolation requirement that is applied offline is more stringent than the one included in the trigger, therefore, the analyses are not affected by the isolation requirement applied at the trigger level. The p_{T} and isolation requirements for each trigger are detailed in Table 5.1.

5.2 Event Preselection

As mentioned in Sec. 1.5.2, the analysis discussed in this dissertation is focused on the $t\bar{t} \to WbHq$ ($q = u, c$) process, with $W \to \ell\nu$ ($\ell = e, \nu$) and $H \to b\bar{b}$. Therefore, the event signature is one electron or muon, at least four jets of which three are b-quark jets, and missing transverse energy $E_{\mathrm{T}}^{\mathrm{miss}}$.

	electron (e)		muon (μ)	
Trigger	`EF_e24vhi_medium1`	`EF_e24vhi_medium1`	`EF_mu24i_tight`	`EF_mu36_tight`
Lepton $p_{\mathrm{T}_{min}}$	24 GeV	60 GeV	24 GeV	36 GeV
Lepton isolation	$p^{0.2}_{\mathrm{T,tracks}}/E_{\mathrm{T}_e} < 0.1$	–	$p^{0.2}_{\mathrm{T,tracks}}/p_{\mathrm{T}_\mu} < 0.12$	–

Table 5.1: Lepton p_{T} and isolation requirements for the lepton triggers during 2012 data taking.

The reconstructed electron or muon must satisfy the quality and kinematic criteria discussed in Sec. 4.3. The lepton selected offline is required to match the corresponding lepton at the trigger level within $\Delta R = 0.15$. The p_{T} requirement on both electron and muon is $p_{\mathrm{T}} > 25$ GeV in order to be in the region where the trigger is fully efficient. Events satisfying either the electron or muon selections are combined and treated coherently, regardless of the lepton flavor. A veto on a second lepton allows reducing the contamination from backgrounds with two isolated leptons such as dileptonic $t\bar{t}$ and Z+jets events.

In addition to the lepton, a minimum of four jets, satisfying the requirements of Sec. 4.4, with $p_{\mathrm{T}} > 25$ GeV and $|\eta| < 2.5$ are required to be reconstructed in the event. Given the high number of b-quarks in the final state, a requirement of at least two b-tagged jets is included in the preselection. This condition has a high efficiency for the FCNC signal, while being very effective in removing non-$t\bar{t}$ backgrounds.

Additional requirements to the event preselection, referred to as "event cleaning", are listed below:

- *Data quality.* Only the luminosity blocks from the "Good Runs List" are considered (see Sec. 2.2.8). From the total recorded luminosity, only $\sim 6\%$ of events do not satisfy this requirement.

- *Corrupted data removal.* Detector problems happening for periods shorter than a lumiblock are rejected with event-level flags without losing the entire luminosity block. This is the case for data integrity problems or noise bursts in the calorimeters. Only 0.1% of the events fail this requirement.

- *Non-collision background removal.* Events are required to have at least one reconstructed vertex with at least five associated tracks with $p_{\mathrm{T}} > 400$ MeV, consistent with originating from the beam collision region in the x–y plane. If more than one vertex is found, the hard-scatter primary vertex is taken to be the one which has the largest sum of the p^2_{T} of its associated tracks. This requirement ensures a good position resolution for the vertex and rejects events produced by the interaction of cosmic muons and other non-collision sources. About 2% of the events are removed with this requirement.

- *Bad jets removal.* Events that include a "bad jet" (see Sec. 4.4.4) with $p_{\mathrm{T}} > 20$ GeV and $|\eta| < 4.5$ events are removed. This procedure avoids having mismeasured jets contribute to the $E^{\mathrm{miss}}_{\mathrm{T}}$ computation. Only 0.1% of the events fail this requirement.

The preselection requirements are summarized in Table 5.2.

Preselection	
Leptons	Exactly one electron or muon
Number of jets	$\geq$4 jets with $p_{\mathrm{T}} > 25$ GeV and $\lvert\eta\rvert < 2.5$
Number of b-jets	$\geq$2 b-tagged jets
Additional req.	"Event cleaning"

Table 5.2: Event preselection requirements.

Since the background from multijet production is very small in the $\geq$ 2 b-tags region, as it will be shown in Chapter 6, no requirements on $E_{\mathrm{T}}^{\mathrm{miss}}$ or transverse mass of the lepton and $E_{\mathrm{T}}^{\mathrm{miss}}$ ($m_{\mathrm{T}}^{\mathrm{W}}$) [1] are applied in this analysis.

5.3 Signal and Background Modeling

After event preselection, the main background (about 90%) is $t\bar{t} \to WbWb$ production, in association with jets, denoted by $t\bar{t}$+jets in the following. Subdominant background contributions originate from single top quark production and the production of a W boson in association with jets (W+jets). Small contributions arise from multijet, Z+jets and diboson (WW, WZ, ZZ) production, as well as from the associated production of a vector boson V ($V = W, Z$) or a Higgs boson and a $t\bar{t}$ pair ($t\bar{t}V$ and $t\bar{t}H$). Multijet events contribute to the selected sample via the misidentification of a jet or a photon as an electron or the presence of a non-prompt lepton, e.g. from a semileptonic b- or c-hadron decay. Signal and all backgrounds are modeled using MC simulation and normalized to their theoretical cross sections, with the exception of the multijet background, which is estimated with data-driven methods [132].

A value for the top quark mass of 172.5 GeV and for the Higgs boson mass of 125 GeV, respectively, are used in all generated samples. Photos 2.15 [133] is used to simulate photon radiation, while for the simulation of τ decays the generator used is Tauola 1.20 [134]. All generated samples are processed through a full simulation [98] of the detector geometry and response using Geant4 [135]. Additional minimum-bias pp interactions are simulated with the Pythia 8.1 generator with the MSTW 2008 LO PDF set and the A2 UE tune [136]. They are overlaid on the simulated signal and background events according to the luminosity profile of the recorded data. The contributions from these pileup interactions are modeled both within the same bunch crossing as the hard-scattering process and in neighboring bunch crossings. All simulated samples are processed through the same reconstruction software as the data. Simulated events are corrected so that the object identification efficiencies, energy scales, and energy resolutions match those determined from data control samples.

5.3.1 $t\bar{t}$+jets Background

The modeling of $t\bar{t}$+jets background takes a central part in the analysis discussed in this dissertation. An accurate simulation of the different topologies is required, es-

[1] $m_{\mathrm{T}}^{\mathrm{W}} = \sqrt{2p_{\mathrm{T}}^{\ell}E_{\mathrm{T}}^{\mathrm{miss}}(1-\cos\Delta\phi)}$, where p_{T}^{ℓ} is the transverse momentum (energy) of the muon (electron) and $\Delta\phi$ is the azimuthal angle separation between the lepton and the direction of the missing transverse momentum.

pecially the emission of additional jets and the heavy-flavor fraction. Not only the normalization, but also the kinematics of the full final state have to be correctly modeled for this background.

It has been observed that POWHEG-BOX+PYTHIA is currently the MC generator that best models inclusive $t\bar{t}$ production. However, some corrections need to be applied to improve its prediction. These corrections are described in detail below.

The $t\bar{t}$ sample is generated with the NLO generator POWHEG-BOX 2.0 [137–140] using the CT10 [141] set of parton distribution functions (PDF). The nominal sample is interfaced to PYTHIA 6.425 [142] for parton showering and hadronization with the CTEQ6L1 PDF set and the Perugia2011C [143] set of optimized parameters for the underlying event (UE) description, referred to as the "UE tune". An alternative sample, used to study the uncertainty related to the hadronization model, is interfaced to HERWIG v6.520 [89] with the CTEQ6L1 PDF set and JIMMY v4.31 [88] to simulate the UE.

The $t\bar{t}$ sample is normalized to a cross section of 253^{+15}_{-16} pb, computed using TOP++ v2.0 [144] at next-to-next-to-leading order (NNLO) in QCD, including resummation of next-to-next-to-leading logarithmic (NNLL) soft gluon terms [145–149], and using the MSTW 2008 NNLO [150,151] PDF set. Theoretical uncertainties result from variations of the factorization and renormalization scales, as well as from uncertainties on the PDF and α_S. The latter two represent the largest contribution to the overall theoretical uncertainty on the cross section and were calculated using the PDF4LHC prescription [152] with the MSTW 2008 68% CL NNLO, CT10 NNLO [141, 153] and NNPDF2.3 5f FFN [154] PDF sets.

In the case where a non-zero BR($t \to Hq$) is assumed, an additional normalization factor of $[1 - \mathrm{BR}(t \to Hq)]^2$ is applied to the $t\bar{t}$ sample. It is not possible to generate the $t\bar{t} \to WbHq$ signal with POWHEG-BOX, and a different event generator is used instead, as discussed in the following sections.

5.3.1.1 $t\bar{t}$+jets Background Categorization

The $t\bar{t}$+jets samples are generated inclusively, but events are categorized depending on the flavor content of additional particle jets not originating from the decay of the $t\bar{t}$ system. The classification is based on an algorithm matching hadrons to particle jets built from stable particles. Particle jets are reconstructed by clustering stable particles excluding muons and neutrinos using the anti-k_T algorithm with a radius parameter $R = 0.4$ (see Sec. 4.4). All particle jets with $p_{\mathrm{T}} > 15$ GeV and $|\eta| < 2.5$ are matched to a selected set of b- and c-hadrons. This algorithm considers the set of b- and c-hadrons with $p_{\mathrm{T}} > 5$ GeV that are not originating from $t\bar{t}$ decay products, i.e. excluding those hadrons originating from b-quarks from top-quark decays, or from c-quarks from hadronic W-boson decays. If the ΔR between the particle jet and b- or c-hadron is less than 0.4, then the particle jet is labeled as a b- or c-jet respectively. The p_{T} threshold for particle jets of 15 GeV is chosen to be 10 GeV below the reconstructed-jet p_{T} threshold, in order to allow for resolution effects.

Events with at least one b-jet not originated from top decay products are labeled as a $t\bar{t}+b\bar{b}$ events. Events that fail this criteria, and containing at least one c-jet not from a W-decay are labeled as $t\bar{t} + c\bar{c}$. The remaining events are labeled as $t\bar{t}$+light-jets events. In this way, a distinction is made between $t\bar{t} + b\bar{b}$, $t\bar{t} + c\bar{c}$ and $t\bar{t}$+light-jets events. The first two categories are generically referred to as $t\bar{t}$+HF events (with HF

standing for "heavy flavor"), while the latter category also includes events with no additional jets.

In order to study the modeling of $t\bar{t}$+jets production by different generators another subcategorization of the $t\bar{t}+b\bar{b}$ and $t\bar{t}+c\bar{c}$ events is performed as follows. An event is labeled as $t\bar{t}+b$ if it has only one particle jet matched to a b-hadron. If the event has two particle jets matched to two different b-hadrons, the event is labeled as $t\bar{t}+b\bar{b}$, while if the event has one particle jet matched to two b-hadrons, the event is given the label $t\bar{t}+B$, representing unresolved gluon splitting to $b\bar{b}$. A similar classification is performed for $t\bar{t}+c\bar{c}$ events.

5.3.1.2 $t\bar{t}$ Reweighting

Although POWHEG-BOX+PYTHIA is the MC generator that best models inclusive $t\bar{t}$ production, it overpredicts the data for the some observables. Differential cross section measurements at $\sqrt{s} = 7$ TeV [155] as a function of the top-quark transverse momentum, $p_{\mathrm{T}}^{\mathrm{top}}$, and the transverse momentum of the $t\bar{t}$ system, $p_{\mathrm{T}}^{t\bar{t}}$, showed a visible difference between data and the MC simulation not covered by the statistical and systematic uncertainties of the measurements. Different MC generator predictions for the differential cross sections compared to the experimental measurement are shown in Fig. 5.1.

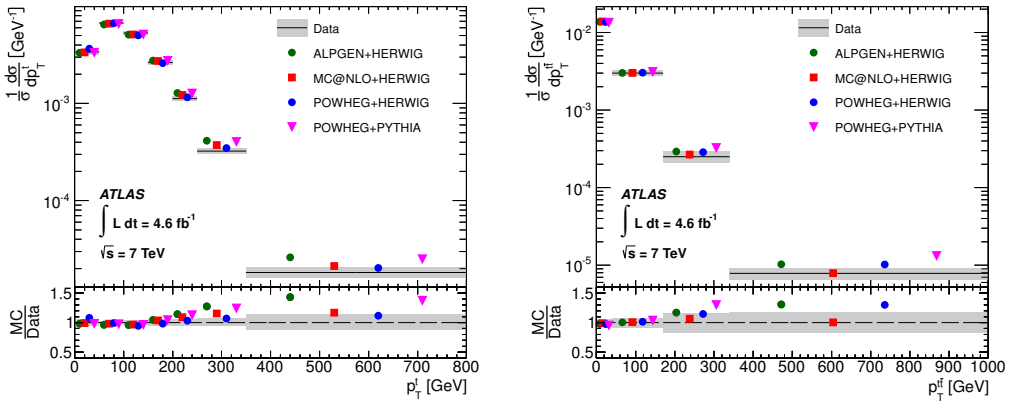

(a) (b)

Figure 5.1: Normalized differential cross sections for (a) the transverse momentum of the hadronically-decaying top quark, $p_{\mathrm{T}}^{\mathrm{top}}$, and (b) the transverse momentum of the $t\bar{t}$ system, $p_{\mathrm{T}}^{t\bar{t}}$. The prediction for POWHEG-BOX+PYTHIA generator is shown with a triangle marker. The gray bands indicate the total uncertainty on the experimental measurement in each bin. Figures taken from reference [155].

To correct this difference, a two-step reweighting procedure to the initial POWHEG-BOX+PYTHIA prediction is performed. A first reweighting corrects the $p_{\mathrm{T}}^{t\bar{t}}$ distribution in POWHEG-BOX+PYTHIA to match the differential cross section measurement. A second reweighting is applied to the prediction including the first reweighting, in order to correct the $p_{\mathrm{T}}^{\mathrm{top}}$ distribution. Table 5.3 summarizes the correction factors and total uncertainties for the binning considered in each variable.

This reweighting procedure, referred to as "$t\bar{t}$ reweighting", is applied inclusively to all three sub-samples: $t\bar{t}$+light-jets, $t\bar{t}+b\bar{b}$ and $t\bar{t}+c\bar{c}$. The effect of the $t\bar{t}$ reweight-

$t\bar{t}$ reweighting							
$p_{\mathrm{T}}^{\mathrm{top}}$ bin [GeV]	[0, 50]	[50, 100]	[100, 150]	[150, 200]	[200, 250]	[250, 350]	[350, 800)
Rew. Factor	1.01±0.01	1.01±0.02	1.01±0.01	1.00±0.01	0.96±0.04	0.91±0.09	0.88±0.17
$p_{\mathrm{T}}^{t\bar{t}}$ bin [GeV]	[0, 40]	[40, 170]	[170, 340]	[340, 1000)			
Rew. Factor	1.04±0.12	0.99±0.14	0.81±0.18	0.68±0.22			

Table 5.3: Reweighting factors for the PowHeg+Pythia sample as a function of the top quark p_{T} (top) and $t\bar{t}$ system p_{T} (bottom). The product of both factors is used as the event weight correction.

ing procedure on the data/MC agreement in regions with exactly two b-tagged jets, which are dominated by the $t\bar{t}$+light-jets background, is presented in Fig. 5.2. An improvement in the prediction is clearly visible in the jet multiplicity and the scalar sum of the jet p_{T} ($\mathrm{H}_{\mathrm{T}}^{\mathrm{had}}$) distributions. The former is driven by the first reweighting factor while the latter is mainly due to the second reweighting factor. The validation of the $t\bar{t}$ reweighting for the $t\bar{t}$+HF background is discussed in the next section.

5.3.1.3 $t\bar{t}$+HF Modeling

The modeling of $t\bar{t}$+HF background is a key aspect of this analysis. This analysis follows the same strategy for the modeling of this background as used in the $t\bar{t}H$, $H \to b\bar{b}$ search [8].

The main contribution for selections with high b-tag multiplicity (typically ≥ 4 b-tagged jets) is $t\bar{t} + b\bar{b}$ production, where fixed-order NLO calculations can reduce perturbative uncertainties on the cross section from 70-80% of the LO calculation, down to 15-20% [156–158]. In the Powheg-Box generator only diagrams of the type $gb \to t\bar{t}b$ are directly included, while the production of $b\bar{b}$ pairs is obtained with the parton shower evolution. Therefore, the modeling of $t\bar{t}$+$b\bar{b}$ has only leading-logarithmic (LL) accuracy. In order to study uncertainties related to this simplified description, different MC generators are tested and compared to Powheg-Box+Pythia.

An alternative $t\bar{t}$+jets sample is generated with Madgraph5 1.5.11 [91] using the CT10 PDF set and interfaced to Pythia 6.425 for showering and hadronization. It includes tree-level diagrams with up to three additional partons, including b- and c-quarks. A five-flavor scheme is used, where b- and c-quarks are treated as massless partons in the matrix element calculation and can be originated inside the proton.

Another $t\bar{t}$+jets sample is also available within the Sherpa framework, interfaced with the OpenLoops library [97, 159]. The Sherpa+OpenLoops NLO sample is generated following the four-flavor scheme using the Sherpa 2.0 pre-release and the CT10 PDF set. In this scheme the b-quark is generated as a massive final state and does not contribute to the proton PDF. The renormalization scale, μ_R is set to $\mu_R = \prod_{i=t,\bar{t},b,\bar{b}} E_{\mathrm{T},i}^{1/4}$, where $E_{\mathrm{T},i}$ is the transverse energy of parton i, and the factorization and resummation scales are both set to $\mu_F = \mu_Q = (E_{\mathrm{T},t} + E_{\mathrm{T},\bar{t}})/2$. The matrix element is then interfaced to the Sherpa parton shower.

In contrast to Madgraph and Powheg-Box, where only inclusive $t\bar{t}$ samples are generated, the Sherpa+OpenLoops sample is an exclusive $t\bar{t} + b\bar{b}$ sample at NLO. However, the presence of massive b-quarks in the generation allows the computation to cover the full $t\bar{t} + b\bar{b}$ phase space, including collinear gluon splitting into $b\bar{b}$.

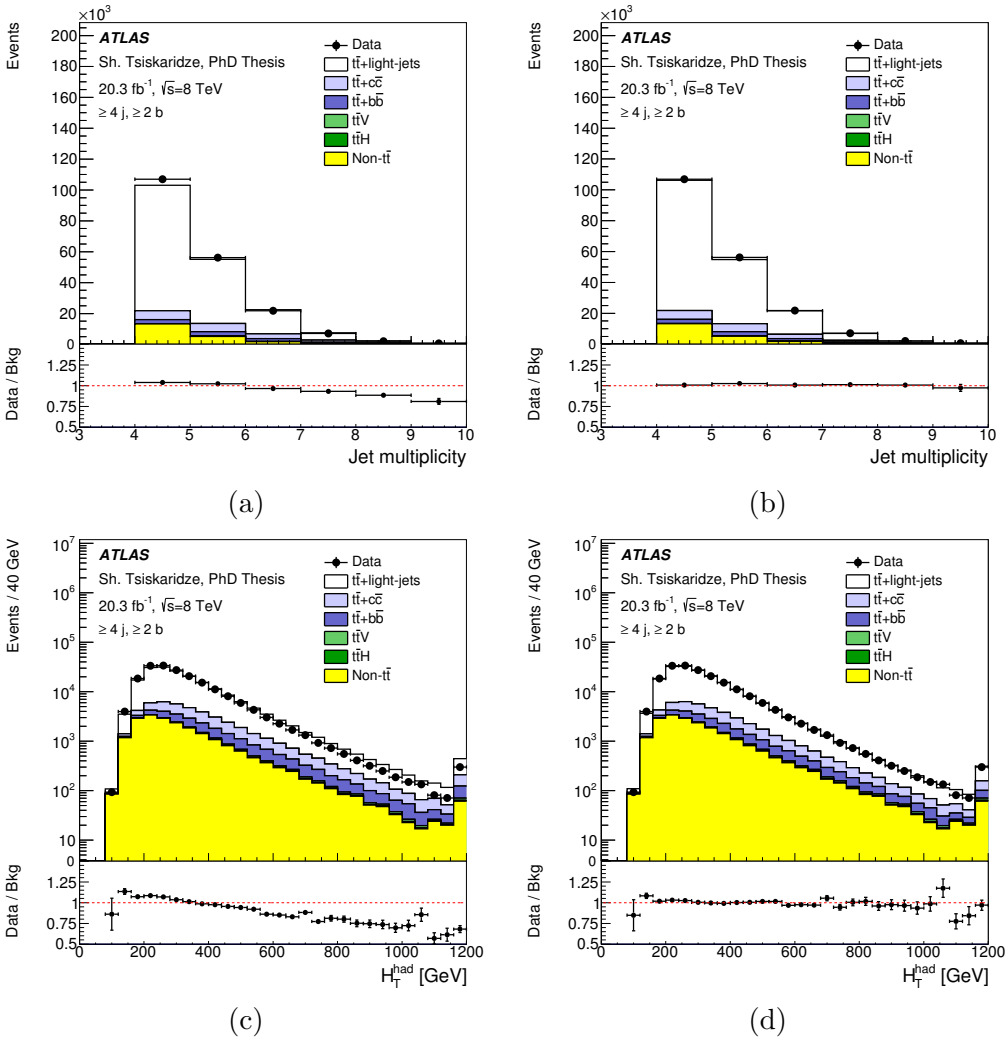

Figure 5.2: Comparison between data and prediction in the combined e+jets and μ+jets channels for events with ≥ 4 jets and ≥ 2 b-tagged jets before and after applying the reweighting of the p_{T} of $t\bar{t}$ system and the p_{T} of the top quark to the POWHEG-BOX+PYTHIA $t\bar{t}$ sample. Shown are: the jet multiplicity distribution (a) before and (b) after the reweighting; and the $\mathrm{H_T^{had}}$ distribution (see text for definition) (c) before and (d) after the reweighting.

There are small contributions that are not included in the SHERPA+OPENLOOPS sample and have to be identified and excluded from the comparison to the POWHEG-BOX+PYTHIA sample. One contribution results from additional $b\bar{b}$ pairs resulting from multiple parton interactions (MPI) overlaying $t\bar{t}$+jets events. Another contribution originates from final-state radiation (FSR), where the production of a $b\bar{b}$ pair results from the splitting of a gluon radiated off top decay products.

The comparison of the absolute contribution of $t\bar{t}+b\bar{b}$ subcategories to the $t\bar{t}+b\bar{b}$ cross section between the different MC generators is shown in Fig. 5.3a. A difference in the inclusive $t\bar{t}+b\bar{b}$ cross section is observed, with the POWHEG-BOX prediction being about 20% above SHERPA+OPENLOOPS. While the relative distribution across categories is such that SHERPA+OPENLOOPS predicts higher contribution of the $t\bar{t}+B$ category, as well as every category where the production of a second pair of $b\bar{b}$ is required.

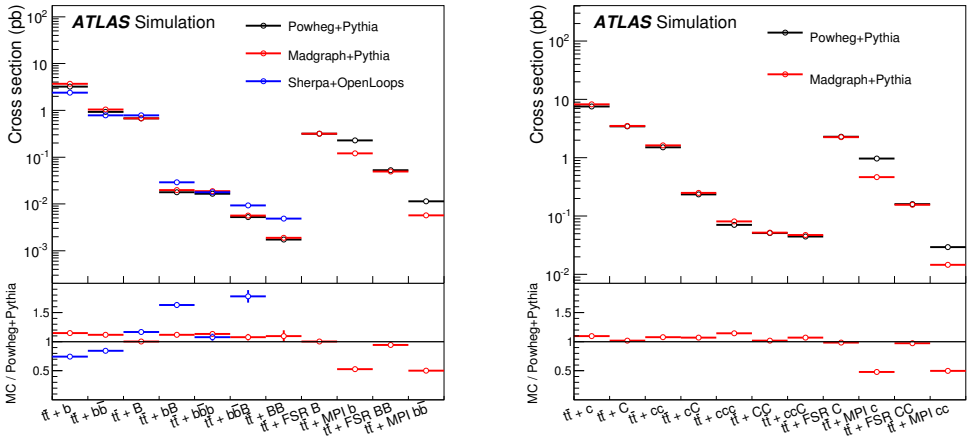

(a) (b)

Figure 5.3: Comparison of (a) $t\bar{t}+b\bar{b}$ and (b) $t\bar{t}+c\bar{c}$ subcategories between different MC generators. Figures taken from reference [124].

In order to improve the modeling of the $t\bar{t}+b\bar{b}$ background, a reweighting procedure is implemented, based on the differences observed between the predictions of POWHEG-BOX+PYTHIA and SHERPA+OPENLOOPS. The inclusive $t\bar{t}+b\bar{b}$ cross section is kept constant throughout all the reweightings, but the relative cross section in each category is adjusted to the NLO prediction. Furthermore, two independent kinematic reweightings are derived to improve the agreement of the different variables in each category. The first reweighting is based on the p_{T} of the top and $t\bar{t}$ systems. The second reweighting is chosen to be on the p_{T} and η of the heavy-flavor jet in the topologies with only one additional heavy-flavor jet. In the topologies with two or more heavy-flavor jets the reweighting is based on the ΔR and p_{T} of the dijet system. This reweighting improves the modeling of the rest of the variables, though some minor differences remain. The effect of the reweighting is illustrated in Fig. 5.4.

In contrast with the $t\bar{t}+b\bar{b}$ background, no NLO calculations are available for the $t\bar{t}+c\bar{c}$ background. Therefore the $t\bar{t}+c\bar{c}$ prediction from POWHEG-BOX is taken without any additional calibration, apart from the $t\bar{t}$ reweighting. The $t\bar{t}+c\bar{c}$ modeling in POWHEG-BOX+PYTHIA is validated by comparing to the multi-leg LO prediction

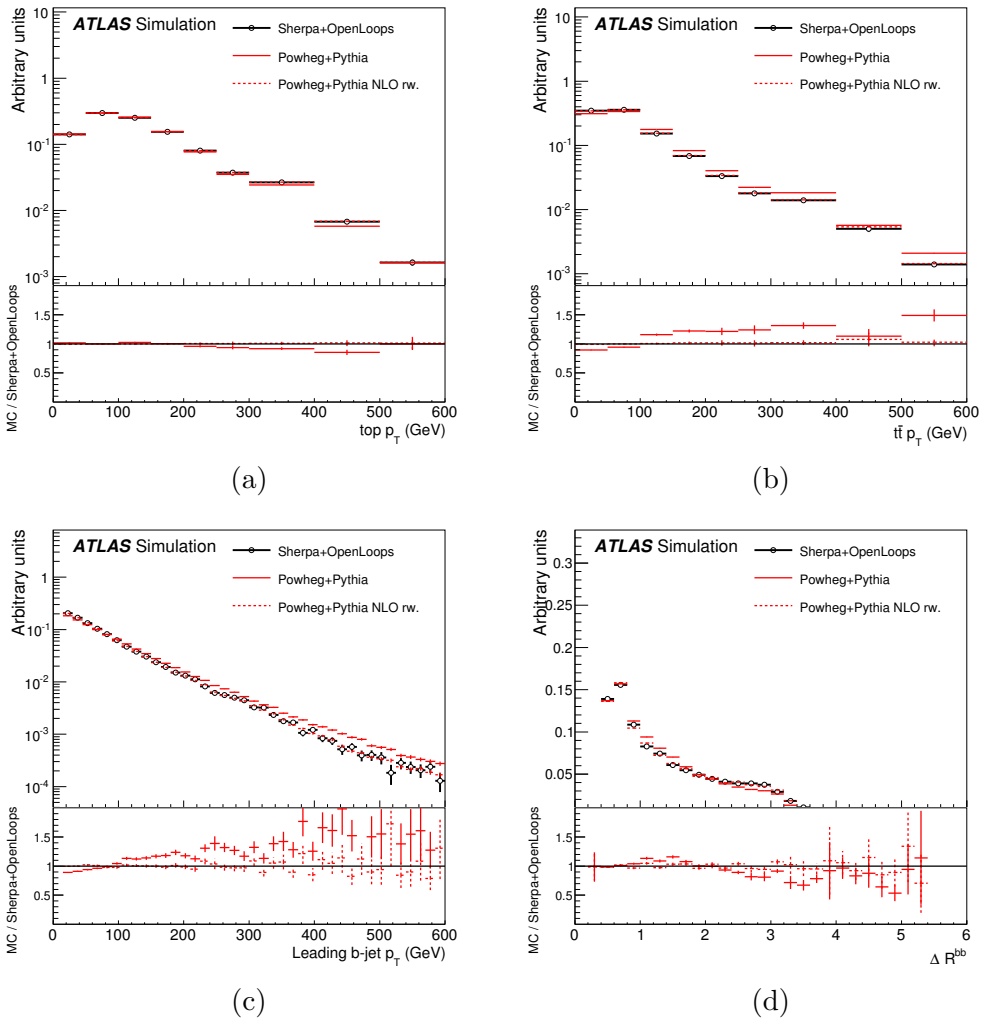

Figure 5.4: Comparison of some kinematic variables in $t\bar{t} + b\bar{b}$ events between the NLO prediction from Sherpa+OpenLoops (black) and Powheg-Box+Pythia (after the $t\bar{t}$ reweighting) before (red solid) and after (red dashed) the additional reweighting to the Sherpa+OpenLoops prediction. The different topologies shown are: (a) $p_{\mathrm{T}}^{\mathrm{top}}$ in $t\bar{t} + b$, (b) $p_{\mathrm{T}}^{t\bar{t}}$ in $t\bar{t} + b$, (c) leading b-jet p_{T} in $t\bar{t} + B$ and (d) $\Delta R^{b\bar{b}}$ in $t\bar{t} + b\bar{b}$. Figures taken from reference [124].

from MADGRAPH. Reasonable agreement between both generators can be seen in Fig. 5.3b and a selection of kinematic variables is shown in Fig. 5.5.

More detailed studies and validation of the reweighing procedure for the $t\bar{t}+b\bar{b}$ and $t\bar{t}+c\bar{c}$ backgrounds can be found in reference [124].

5.3.2 W/Z+jets Background

Samples of W/Z+jets events are generated with up to five additional partons using the ALPGEN v2.14 [90] LO generator with the CTEQ6L1 PDF set and interfaced to PYTHIA v6.426. To avoid double-counting of partonic configurations generated by both the matrix-element calculation and the parton shower, a parton–jet matching scheme ("MLM matching") [160] is employed.

The W+jets samples are generated separately for W+light-jets, $Wb\bar{b}$+jets, $Wc\bar{c}$+jets and Wc+jets, while the Z+jets samples are generated separately for Z+light-jets, $Zb\bar{b}$+jets and $Zc\bar{c}$+jets. Overlap between $VQ\bar{Q}$+jets ($V=W,Z$ and $Q=b,c$) events generated from the matrix-element calculation and those generated from parton-shower evolution in the W/Z+light-jets samples is avoided via an algorithm based on the angular separation between the extra heavy quarks: if $\Delta R(Q,\bar{Q})>0.4$, the matrix-element prediction is used, otherwise the parton-shower prediction is used.

Both the W+jets and Z+jets background contributions are normalized to their inclusive NNLO theoretical cross sections [161]. Further corrections are applied to W/Z+jets events in order to better describe data in the preselected sample. Normalization factors for each of the W+jets categories ($Wb\bar{b}$+jets, $Wc\bar{c}$+jets, Wc+jets and W+light-jets) are derived for events with one lepton and at least four jets by simultaneously analyzing six different event categories, defined by the b-tag multiplicity (0, 1 and $\geq$2) and the sign of the lepton charge [162]. The b-tag multiplicity provides information about the heavy-flavor composition of the W+jets background, while the lepton charge is used to determine the normalization of each component, exploiting the expected charge asymmetry for W+jets production in pp collisions as predicted by ALPGEN. In the case of Z+jets events, a correction to the heavy-flavor fraction is derived to reproduce the relative rates of Z+2-jets events with zero and one b-tagged jet observed in data.

In addition, the Z boson p_{T} spectrum is compared between data and the simulation in Z+2-jets events, and a reweighting function is derived in order to improve the modeling. This reweighting function is also applied to the W+jets simulated sample and it was verified that this correction further improves the agreement between data and simulation for W+jets events. In any case, W/Z+jets events constitute a very small background in this analysis after final event selection.

5.3.3 Other Simulated Backgrounds

Samples of single-top-quark backgrounds corresponding to the t-channel, s-channel, and Wt production mechanisms are generated with POWHEG-BOX 2.0 [163,164] using the CT10 PDF set and interfaced to PYTHIA 6.425 with the CTEQ6L1 PDF set in combination with the Perugia2011C UE tune. Overlaps between the $t\bar{t}$ and Wt final states are avoided using the "diagram removal" scheme [165]. The single-top-quark samples are normalized to the approximate NNLO theoretical cross sections [166–168], calculated using the MSTW 2008 NNLO PDF set.

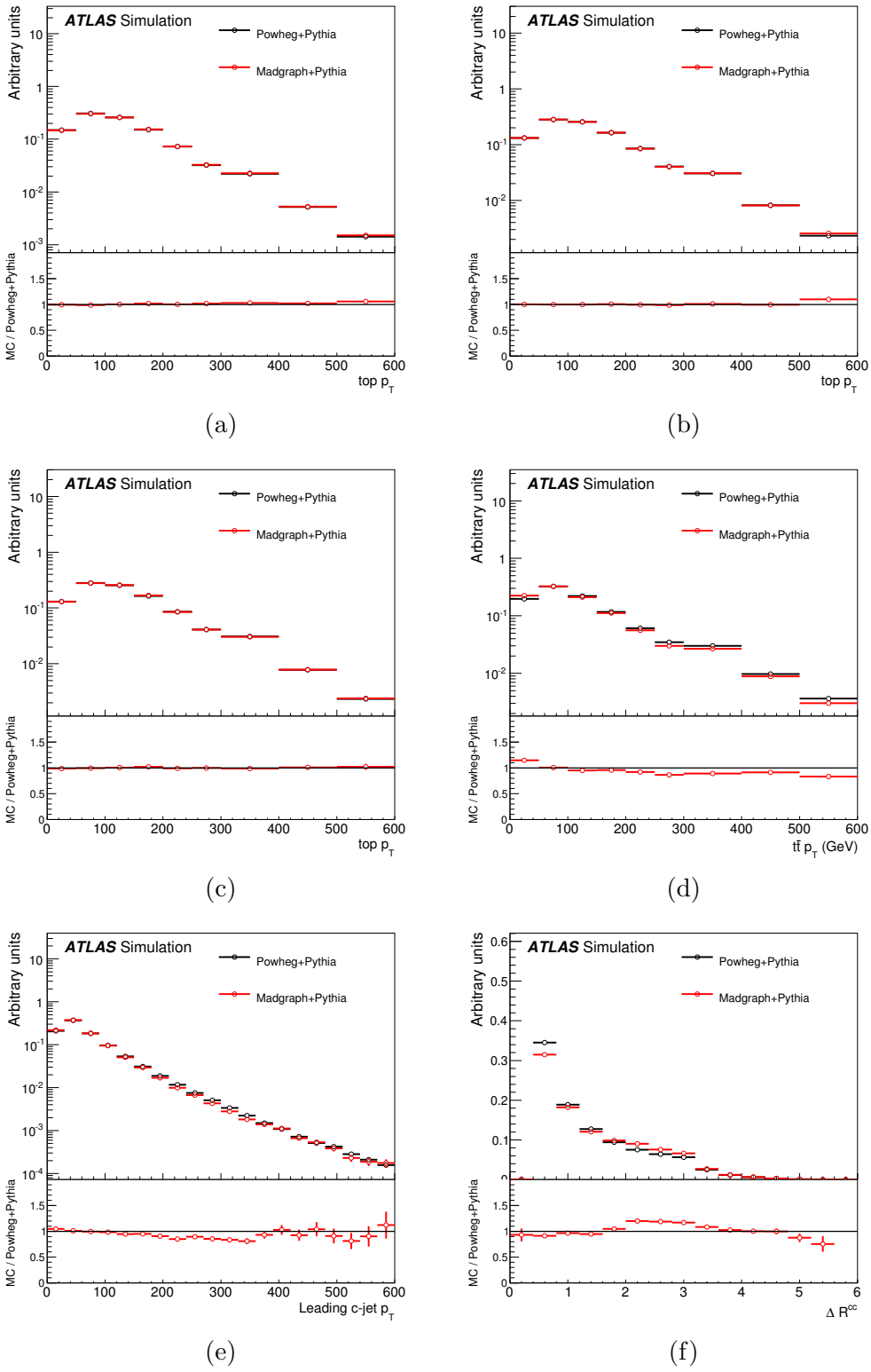

Figure 5.5: Comparison of some kinematic variables in $t\bar{t}+b\bar{b}$ events between the POWHEG-BOX+PYTHIA and MADGRAPH+PYTHIA predictions. The different topologies shown are: (a) $p_{\mathrm{T}}^{\mathrm{top}}$ in $t\bar{t}+c$, (b) $p_{\mathrm{T}}^{\mathrm{top}}$ in $t\bar{t}+B$, (c) $p_{\mathrm{T}}^{\mathrm{top}}$ in $t\bar{t}+c\bar{c}$, (d) $p_{\mathrm{T}}^{t\bar{t}}$ in $t\bar{t}+c\bar{c}$, (e) leading c-jet p_{T} in $t\bar{t}+c\bar{c}$, (f) $\Delta R^{c\bar{c}}$ in $t\bar{t}+c\bar{c}$ (f). Figures taken from reference [124].

Samples of $WW/WZ/ZZ$+jets events are generated with up to three additional partons using ALPGEN v2.13 and the CTEQ6L1 PDF set, interfaced to HERWIG v6.520 and JIMMY v4.31 for parton showering, hadronization and UE modeling. The MLM parton–jet matching scheme is used. The WW+jets samples require at least one of the W bosons to decay leptonically, while the WZ/ZZ+jets samples require one Z boson to decay leptonically and other boson decays inclusively. Additionally, WZ+jets samples requiring the W boson to decay leptonically and the Z boson to decay hadronically, are generated with up to three additional partons (including massive b- and c-quarks) using SHERPA v1.4.1 and the CT10 PDF set. All diboson samples are normalized to their NLO theoretical cross sections [169].

Samples of $t\bar{t}V$ events, including $t\bar{t}WW$, are generated with up to two additional partons using MADGRAPH5 1.3.28 with the CTEQ6L1 PDF set, and interfaced to PYTHIA 6.425 with the AUET2B UE tune [170]. The $t\bar{t}V$ samples are normalized to the NLO cross-section predictions [171].

A sample of $t\bar{t}H$ events is generated with the POWHEL framework [172], which combines the POWHEG-BOX generator and NLO matrix elements obtained from the HELAC-Oneloop package [173]. The sample is generated using the CT10nlo PDF set [141]. Showering is performed with PYTHIA 8.1 [174] using the CTEQ6L1 PDF set and the AU2 UE tune [170, 175]. Inclusive decays of the Higgs boson are assumed in the generation of the $t\bar{t}H$ sample. The $t\bar{t}H$ sample is normalized using the NLO cross-section [176–178] and the Higgs decay branching ratios [179–182] collected in reference [183].

5.3.4 Multijet Background

Multijet background events can pass the preselection criteria via several production and misreconstruction mechanisms. In the electron channel, it consists of non-prompt electrons from semileptonic b- or c-hadron decays, as well as misidentified photons, e.g. from a conversion of a photon into an e^+e^- pair, or jets with a high fraction of their energy deposited in the EM calorimeter. In the muon channel, the main contributions come from non-prompt leptons from semileptonic b- and c-hadron decays.

While the probability of misreconstruction of a lepton is very low, the production cross-section for multijet events is orders of magnitude larger than for $t\bar{t}$ production. Therefore, the contribution to the total background from QCD multijet events cannot be neglected.

The QCD multijet background is very difficult to model with the MC simulation with the desired level of accuracy. Therefore, its normalization and shape are estimated directly from data using the so-called "Matrix Method" (MM) [132]. The MM exploits the differences in lepton-identification-related properties between prompt and isolated leptons from W and Z boson decays, referred to as "real leptons", and leptons that are either non-isolated or result from the misidentification of photons or jets, referred to as "fake leptons".

The basic idea is to divide the data sample into two categories: one of events that satisfy "tight" lepton selection requirements, and the other that satisfy "loose" lepton selection requirements. The tight selection requirements are described in Sec. 4.3, while the loose selections are obtained by applying looser isolation and identification criteria.

The number of events in the loose and tight sample, N^{loose} and N^{tight} respectively,

can be expressed as a linear combination of the numbers of events with real and fake leptons, as given by:

$$\begin{aligned} N^{\text{loose}} &= N^{\text{loose}}_{\text{real}} + N^{\text{loose}}_{\text{fake}}, \\ N^{\text{tight}} &= \epsilon_{\text{real}} \cdot N^{\text{tight}}_{\text{real}} + \epsilon_{\text{fake}} \cdot N^{\text{tight}}_{\text{fake}}, \end{aligned} \tag{5.1}$$

where ϵ_{real} (ϵ_{fake}) represents the probability for a real (fake) lepton satisfying the loose criteria to also satisfy the tight one. Both probabilities are measured in data control samples. The predicted yields for the multijet background satisfying the tight selections is obtained by resolving the above system of equations, yielding:

$$N^{\text{tight}}_{\text{fake}} = \frac{\epsilon_{\text{fake}}}{\epsilon_{\text{real}} - \epsilon_{\text{fake}}} \left(\epsilon_{\text{real}} \cdot N^{\text{loose}} + N^{\text{tight}} \right). \tag{5.2}$$

To reach the desired level of accuracy, the following conditions must be satisfied in the MM:

- $\epsilon_{\text{real}} \gg \epsilon_{\text{fake}}$, i.e. the loose sample should have real and fake efficiencies sufficiently different numerically, so that the statistical precision of the misidentified background estimation is not compromised by the denominator.
- ϵ_{real} and ϵ_{fake} efficiencies should not be dependent strongly on the event topology, i.e. it must be similar for leptons originating from W+jets, Z+jets and $t\bar{t}$, so that they can be determined in control samples and be applied to the analysis sample.
- Any significant dependence of the efficiencies on the kinematics or topology must be parameterized in order to obtain an accurate modeling.

The efficiency ϵ_{real} is measured using the tag-and-probe method from $Z \to e^+e^-$ and $Z \to \mu^+\mu^-$ control regions, being on average $\epsilon_{\text{real}} \approx 0.75$ in the electron channel and $\epsilon_{\text{real}} \approx 0.98$ in the muon channel. For the measurement of efficiency ϵ_{fake}, samples enriched in multijet background are selected by requiring either low $E_{\text{T}}^{\text{miss}}$ or m_{T}^{W} in the electron channel, and high impact parameter significance for the lepton track in the muon channel. On average it is $\epsilon_{\text{fake}} \approx 0.15$ in both electron and muon channels. Dependencies of ϵ_{real} and ϵ_{fake} on quantities such as lepton p_{T} and η, ΔR between the lepton and the closest jet, or number of b-tagged jets, are parameterized in order to obtain a more accurate estimate.

5.3.5 Signal Modeling

The FCNC $t\bar{t} \to WbHq$ signal process is modeled using the PROTOS v2.2 [184, 185] LO generator with the CTEQ6L1 PDF set, and interfaced to PYTHIA 6.426 and the Perugia2011C UE tune.

Two separate samples of 1M events are generated corresponding to $t\bar{t} \to WbHc$ and $t\bar{t} \to WbHu$. The W boson is forced to decay leptonically, $W \to \ell\nu$ ($\ell = e, \mu, \tau$), while the Higgs boson is allowed to decay to all SM particles with branching ratios shown in Table 1.6. The signal sample is normalized to the same NNLO cross section as used for the $t\bar{t} \to WbWb$ sample, and the corresponding branching ratios: $\sigma(t\bar{t} \to W(\to \ell\nu)bHq) = 2\text{BR}(t \to Hq)[1 - \text{BR}(t \to Hq)]\text{BR}(W \to \ell\nu)\sigma_{t\bar{t}}$, with $\text{BR}(W \to \ell\nu) =$

0.324 and BR($t \to Hq$) depending on the branching ratio being tested. Typically a reference branching ratio of BR($t \to Hq$) = 1% is used. The case of both top quarks decaying into Hq is considered to be numerically irrelevant (for the allowed region of BR($t \to Hq$) $\leq$ 1%) and neglected in this analysis.

In order to improve the modeling of the signal kinematics, a two-step reweighting procedure is applied: the first step is designed to correct the spectrum of top quark p_{T} and $t\bar{t}$ system p_{T} to match that of the uncorrected $t\bar{t} \to WbWb$ POWHEG-BOX+PYTHIA sample; the second step involves the same correction to the top quark p_{T} and $t\bar{t}$ system p_{T} applied to the $t\bar{t}$+jets background (see Sec 5.3.1). The comparison of the $t\bar{t}$ and top quark p_{T} in PROTOS+PYTHIA to that in POWHEG-BOX+PYTHIA before and after applying this sequential reweighted is shown in Fig. 5.6. After the sequential reweighting, the agreement is significantly improved up to p_{T} values of approximately 300 GeV. Although the agreement is not perfect at high p_{T} values, we consider it sufficient for our purpose. More details on the correction, its validation and impact on the signal acceptance and shape are provided in App. A.

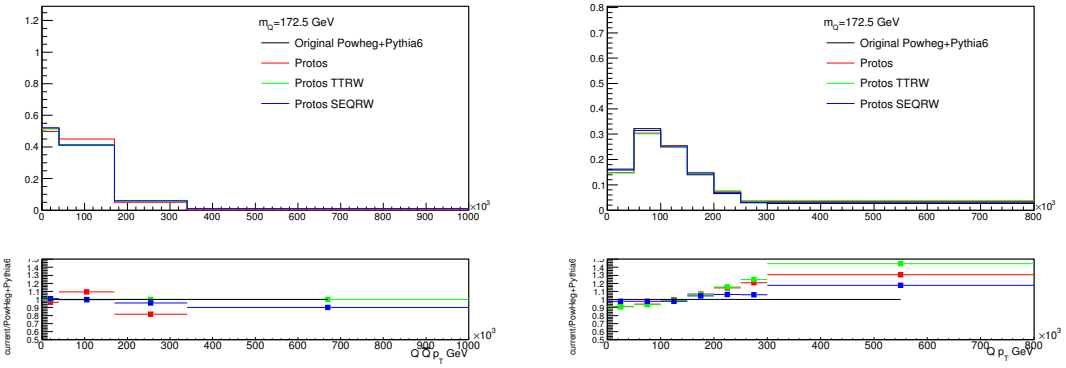

(a) (b)

Figure 5.6: Comparison of the distributions of (a) $t\bar{t}$ p_{T} and (b) top quark p_{T} between original POWHEG-BOX+PYTHIA (black), nominal PROTOS+PYTHIA (red), PROTOS+PYTHIA after $t\bar{t}$ p_{T} reweighting (green) and PROTOS+PYTHIA after sequential $t\bar{t}$ p_{T} plus top quark p_{T} reweighting (blue).

5.4 Tag Rate Function Method

When requiring high b-jet multiplicity in the analysis, the number of available MC events is significantly reduced, leading to large fluctuations in the resulting distributions. This can negatively affect the sensitivity of the analysis, as the corresponding statistical uncertainties on the background templates need to be taken into account in the determination of exclusion limits, and lead to unreliable systematic uncertainties in the predicted distribution shapes. In addition, the observed limits may be biased, depending on how the MC distributions fluctuate with respect to the data in the signal region.

In order to mitigate this problem, a *tag-rate-function* (TRF) method is applied to all MC samples. Instead of direct application of the cut on the b-tagging algorithm output (see Sec. 4.5), referred to as "direct tagging" (DT), the TRF method assigns

a probability, referred to as "TRF weight", to the given event to contain the desired number of b-jets. The TRF weight for the event is computed based on parameterized b-tagging efficiencies of the jets in the event, which are extracted from $t\bar{t}$ MC events as a function of the p_{T}, $|\eta|$ and flavor [2](f) of the jet: $\varepsilon\,(f, |\eta|, p_{\mathrm{T}})$. Given the b-tagging efficiency, each jet can be considered as "tagged" with ε probability and "un-tagged" with $(1-\varepsilon)$ probability.

For a given number of jets in the event (N) and for a given requirement on the number of b-tagged jets in the event (n), the TRF weight is calculated as the sum of all the possible permutations of n "tagged" jets and $N-n$ "un-tagged" jets:

$$P_{=n} = \sum_{S=n} \left(\prod_{s_i=1} \varepsilon_i \cdot \prod_{s_i=0} (1-\varepsilon_i) \right), \quad S = \sum_{i=1}^{N} s_i, \tag{5.3}$$

where s_i identify the tagging of the jets ("tagged" or "un-tagged") and take values of 0 or 1. In the same way, it can be used to compute the probability for inclusive b-tagging selections:

$$P_{\geq n} = 1 - \sum_{i=0}^{n-1} P_{=i}. \tag{5.4}$$

This allows the use of all events in the pre-b-tagged sample to predict the normalization and shape after any b-tagging selection.

For the distributions built using the b-tagged jet information, it is necessary to know which jets in the event are b-tagged. In this case, one of the possible permutations is randomly chosen, based on the relative probability of each permutation. Note that a TRF-assigned b-tagged jets in the selected permutation may not correspond to the actual b-tagged jets by the application of a cut on the b-tagging algorithm output. Therefore a "new" per-jet b-tagging output value, referred to as "TRF discrete weight", is introduced for the selected permutation.

The TRF discrete weights for the jets and various studies performed to validate the TRF method for the FCNC signal and the $t\bar{t}$ background samples are discussed in detail in App. B. A comparison between the cut-based and TRF prediction of the $\mathrm{H_T^{had}}$ variable (defined as the scalar sum of jet p_{T}) at the preselection level for the FCNC signal and the $t\bar{t}$+jets background are presented in Fig. 5.7 and Fig. 5.8 respectively.

Small discrepancies in the normalization between cut based selection and TRF prediction are corrected for the FCNC signal and $t\bar{t}$+jets background samples, in order to ensure that no bias is introduced.

5.5 Data-to-Monte Carlo Comparison

In order to validate the modeling of the main backgrounds by the simulation, detailed comparisons between data and MC are performed. Basic kinematic variables at the preselection level are shown in Fig. 5.9. Figure 5.10 displays the same kinematic variables but without the preselection requirement of ≥ 2 b-tagged jets. As can be

[2] The flavor of the jet is defined by looking at partons with $p_{\mathrm{T}} > 5$ GeV within $\Delta R < 0.3$ around the jet direction. If a b-quark is found, the jet is labeled as "b". If no b-quarks are found, c-quarks are considered and if found, the jet is labeled as "c". The remaining jets are labeled as "light".

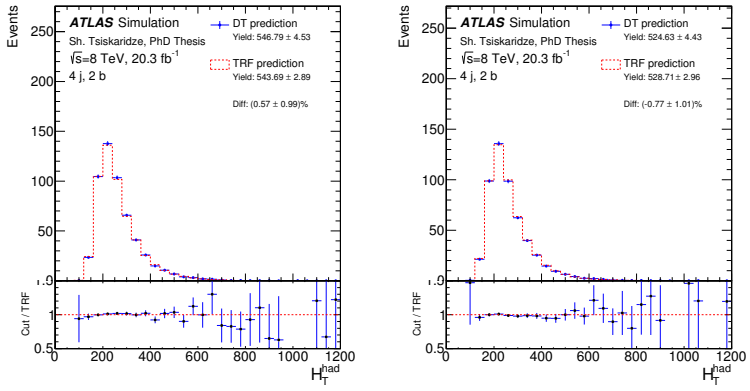

(a) (b)

Figure 5.7: Comparisons between the cut-based and TRF-based prediction at the preselection level for (a) $t\bar{t} \to WbHc$ and (b) $t\bar{t} \to WbHu$ FCNC signal events. The comparison is performed for the $\mathrm{H_T^{had}}$ distribution.

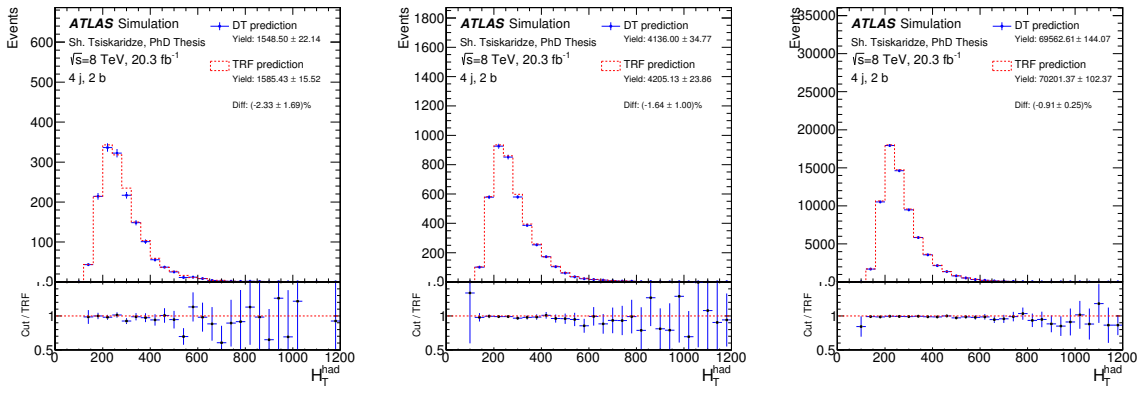

(a) (b) (c)

Figure 5.8: Comparisons between the cut-based and TRF-based prediction at the preselection level for (a) $t\bar{t}+b\bar{b}$, (b) $t\bar{t}+c\bar{c}$ and (c) $t\bar{t}$+jets background events. The comparison is performed for the $\mathrm{H_T^{had}}$ distribution.

appreciated, the requirement of $\geq$ 2 b-tagged jets effectively suppresses the non-$t\bar{t}$ background (dominated by W+jets), leaving a sample dominated by $t\bar{t}$+jets.

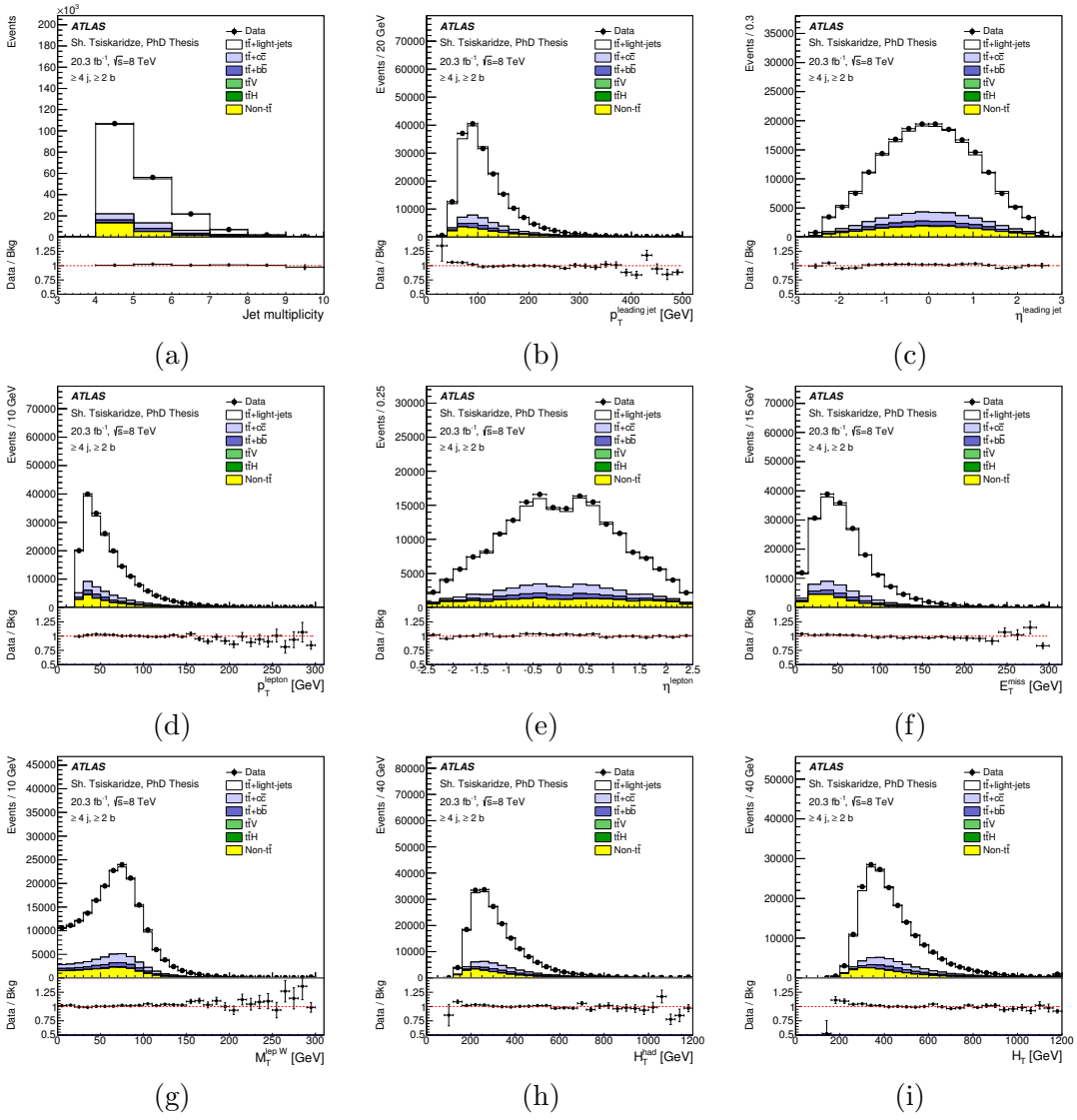

Figure 5.9: Comparison between data and prediction for a number of kinematic variables in the combined e+jets and μ+jets channels after the preselection requirement of $\geq$ 4 jets and $\geq$ 2 b-tagged jets. The variables displayed are: (a) jet multiplicity, (b) leading jet p_{T}, (c) leading jet η, (d) lepton p_{T}, (e) lepton η, (f) missing transverse energy, (g) W transverse mass, (h) $H_{\mathrm{T}}^{\mathrm{had}}$ and (i) H_{T} (defined as the scalar sum of the lepton p_{T}, $E_{\mathrm{T}}^{\mathrm{miss}}$ and $H_{\mathrm{T}}^{\mathrm{had}}$).

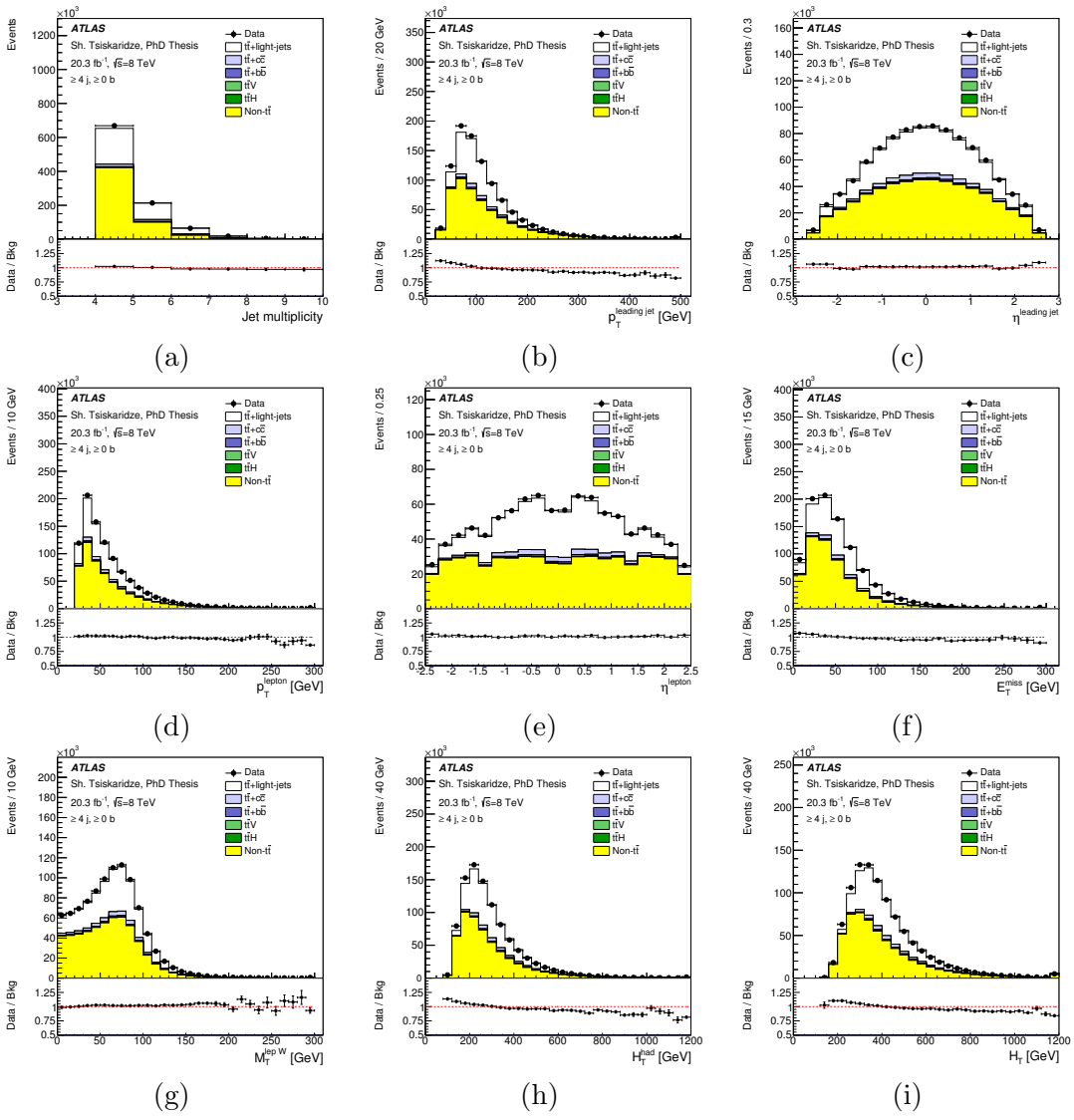

Figure 5.10: Comparison between data and prediction for a number of kinematic variables in the combined e+jets and μ+jets channels after the preselection requirement of ≥ 4 jets and ≥ 0 b-tagged jets. The variables displayed are: (a) jet multiplicity, (b) leading jet p_{T}, (c) leading jet η, (d) lepton p_{T}, (e) lepton η, (f) missing transverse energy, (g) W transverse mass, (h) $H_{\mathrm{T}}^{\mathrm{had}}$ and (i) H_{T} (defined as the scalar sum of the lepton p_{T}, $E_{\mathrm{T}}^{\mathrm{miss}}$ and $H_{\mathrm{T}}^{\mathrm{had}}$).

Chapter 6

Analysis Strategy

This chapter presents an overview of the analysis strategy followed in the $t\bar{t} \to WbHq, H \to b\bar{b}$ search. The event categorization is described in Sec. 6.1, while Sec. 6.2 introduces the variable used to discriminate signal from background.

6.1 Event Categorization

As previously discussed, this search is focused on the $t\bar{t} \to WbHq$ process, with $W \to \ell\nu$ and $H \to b\bar{b}$. Therefore, the signal is expected to have typically four jets, of which three or four are b-tagged. The latter case corresponds to the $t\bar{t} \to WbHc$ signal where the charm quark, as well as the three b-quark jets, are b-tagged. Additional jets can also be present because of initial- or final-state radiation. The high b-tag multiplicity can be effectively exploited to suppress the background, as illustrated in Fig. 6.1.

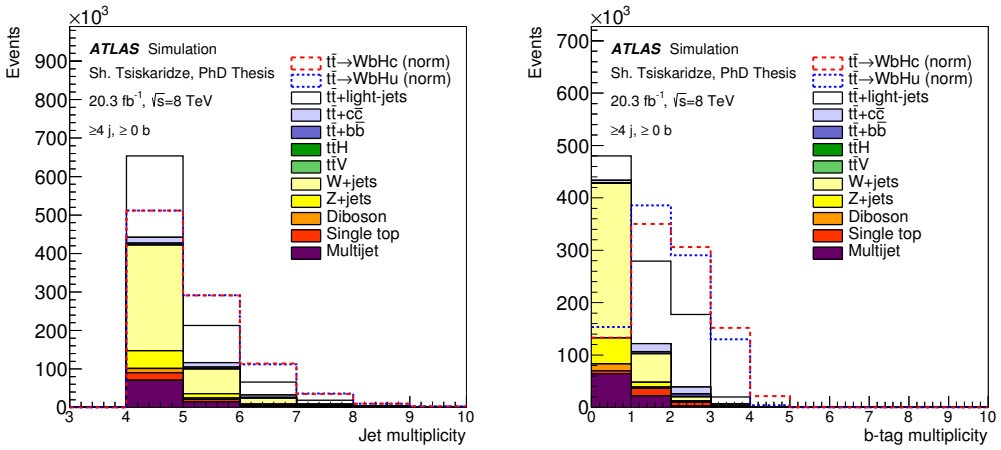

(a) (b)

Figure 6.1: Comparison of the shape of (a) the jet multiplicity and (b) the b-tag multiplicity distributions between total background and the $t\bar{t} \to WbHc$ and $t\bar{t} \to WbHu$ signals events satisfying the preselection requirements. The background prediction is absolute while the signal distributions have been normalized to the total background yield for the purpose of comparing the shape.

In order to optimize the sensitivity of the search, the preselected events are cate-

gorized into different channels depending on the number of jets (4, 5 and ≥6) and on the number of b-tagged jets (2, 3 and ≥4). Therefore, the total number of analysis channels considered in this search is nine: (4 j, 2 b), (4 j, 3 b), (4 j, 4 b), (5 j, 2 b), (5 j, 3 b), (5 j, ≥4 b), (≥6 j, 2 b), (≥6 j, 3 b), and (≥6 j, ≥4 b), where (n j, m b) indicates n selected jets and m b-tagged jets. Table 6.1 presents the observed and predicted yields in each of the analysis channels considered, also displayed in Fig. 6.3. Comparisons between data and prediction for selected kinematic variables in different channels are provided in App. C.

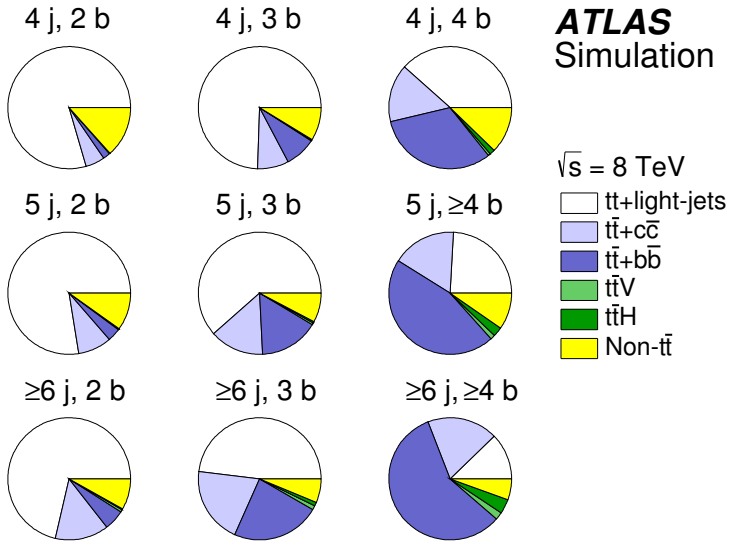

Figure 6.2: Fractional contributions of the various backgrounds to the total background prediction in each analysis channel.

The overall rate and composition of the $t\bar{t}$+jets background strongly depends on the jet and b-tag multiplicities, as illustrated in Fig. 6.2. The $t\bar{t}$+light-jets background is dominant in events with exactly two or three b-tagged jets, with the two b-quarks from the top quark decays being tagged in both cases, and a charm quark from the hadronic W boson decay also being tagged in the latter case. Contributions from $t\bar{t}+c\bar{c}$ and $t\bar{t}+b\bar{b}$ become significant as the jet and b-tag multiplicities increase, with the $t\bar{t}+b\bar{b}$ background being dominant for events with ≥6 jets and ≥4 b-tags.

Tables 6.2 and 6.3 show the fractional contribution from the different Higgs boson decay modes to the selected $t\bar{t} \to WbHc$ and $t\bar{t} \to WbHu$ signals in each of analysis channels considered. As can be appreciated, in the channels with four or five jets and three or at least four b-tags, which dominate the sensitivity of this search, selected signal events have a $H \to b\bar{b}$ decay in more than 95% of the events.

In the case of the $t\bar{t} \to WbHc$ signal, the (4 j, 4 b) channel has the highest signal fraction, although other channels contain also significant amount of signal, albeit with a much larger background fraction. In the case of the $t\bar{t} \to WbHu$ signal, the (4 j, 3 b) channel has the highest sensitivity, since the expected signal yield with ≥ 4 b-tags is very small (comes through mistagging of a light jet) and with 2 b-tags is overwhelmed by background. Therefore, it is expected that the analysis will have better sensitivity for $t\bar{t} \to WbHc$ than for $t\bar{t} \to WbHu$ signal.

The rest of the channels have significantly lower signal-to-background ratios, but

	4 j, 2 b	4 j, 3 b	4 j, 4 b
$t\bar{t} \to WbHc$	890 ± 100	394 ± 54	41.6 ± 7.2
$t\bar{t} \to WbHu$	851 ± 98	339 ± 49	3.81 ± 0.71
$t\bar{t}$+light-jets	77400 ± 8100	6170 ± 860	53 ± 12
$t\bar{t} + c\bar{c}$	4900 ± 2600	680 ± 370	21 ± 11
$t\bar{t} + b\bar{b}$	1870 ± 990	680 ± 370	44 ± 23
$t\bar{t}V$	121 ± 21	15.5 ± 2.9	0.89 ± 0.19
$t\bar{t}H$	30.5 ± 4.2	12.7 ± 1.9	1.91 ± 0.34
W+jets	4700 ± 1600	217 ± 78	5.4 ± 2.0
Z+jets	1080 ± 450	50 ± 22	0.90 ± 0.50
Single top	4900 ± 1400	340 ± 100	6.8 ± 2.3
Diboson	212 ± 75	11.5 ± 4.1	0.24 ± 0.11
Multijet	1540 ± 550	100 ± 36	3.4 ± 1.2
Total background	96800 ± 9600	8300 ± 1100	138 ± 32
Data	98049	8752	161

	5 j, 2 b	5 j, 3 b	5 j, ≥4 b
$t\bar{t} \to WbHc$	483 ± 96	242 ± 50	35.1 ± 7.7
$t\bar{t} \to WbHu$	473 ± 95	217 ± 46	8.4 ± 2.0
$t\bar{t}$+light-jets	37600 ± 6600	3480 ± 750	61 ± 18
$t\bar{t} + c\bar{c}$	4300 ± 2300	810 ± 460	43 ± 28
$t\bar{t} + b\bar{b}$	1670 ± 860	890 ± 470	115 ± 61
$t\bar{t}V$	145 ± 24	26.5 ± 4.5	3.10 ± 0.60
$t\bar{t}H$	40.9 ± 4.8	22.3 ± 2.9	5.96 ± 0.98
W+jets	1850 ± 790	131 ± 57	5.8 ± 2.7
Z+jets	400 ± 200	29 ± 14	1.47 ± 0.76
Single top	1880 ± 740	195 ± 78	8.3 ± 3.1
Diboson	96 ± 41	8.0 ± 3.5	0.40 ± 0.19
Multijet	450 ± 160	68 ± 24	8.3 ± 3.0
Total background	48400 ± 7800	5700 ± 1100	252 ± 75
Data	49699	6199	286

	≥ 6 j, 2 b	≥6 j, 3 b	≥6 j, ≥4 b
$t\bar{t} \to WbHc$	267 ± 68	145 ± 37	31.1 ± 8.3
$t\bar{t} \to WbHu$	259 ± 67	132 ± 34	10.3 ± 2.8
$t\bar{t}$+light-jets	18800 ± 4800	2000 ± 730	52 ± 40
$t\bar{t} + c\bar{c}$	3700 ± 2000	850 ± 500	79 ± 46
$t\bar{t} + b\bar{b}$	1430 ± 760	970 ± 520	240 ± 130
$t\bar{t}V$	182 ± 32	44.6 ± 8.1	8.4 ± 1.7
$t\bar{t}H$	64.2 ± 8.2	39.8 ± 5.4	16.1 ± 2.6
W+jets	880 ± 440	95 ± 47	8.5 ± 4.5
Z+jets	180 ± 100	19 ± 11	1.5 ± 0.9
Single top	840 ± 410	122 ± 62	11.9 ± 6.2
Diboson	50 ± 26	6.0 ± 3.0	0.54 ± 0.29
Multijet	176 ± 62	20.3 ± 7.2	0.93 ± 0.50
Total background	26400 ± 6100	4200 ± 1200	420 ± 160
Data	26185	4701	516

Table 6.1: Predicted and observed yields in each of the analysis channels considered. The prediction is shown before the fit to data. Also shown are the signal expectations for $t\bar{t} \to WbHc$ and $t\bar{t} \to WbHu$ assuming $\mathcal{B}(t \to Hc) = 1\%$ and $\mathcal{B}(t \to Hu) = 1\%$ respectively. The $t\bar{t} \to WbWb$ background is normalised to the SM prediction. The quoted uncertainties are the sum in quadrature of statistical and systematic uncertainties on the yields.

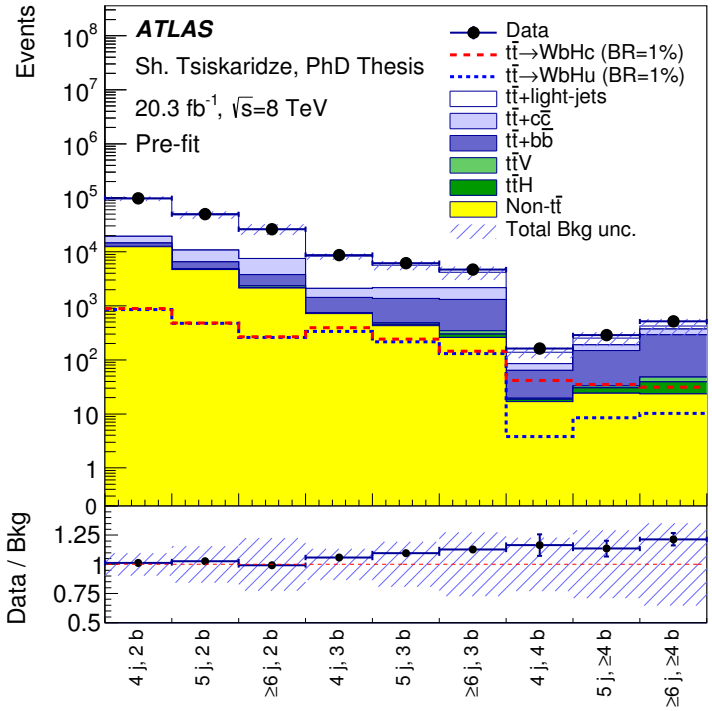

Figure 6.3: Comparison between the data and background prediction for the yields in each of the analysis channels considered. Backgrounds are normalized to their nominal cross sections discussed in Sec. 5.3. The expected $t\bar{t} \to WbHc$ and $t\bar{t} \to WbHu$ signals (dashed histograms) are shown separately normalized to BR($t \to Hq$) = 1%. The $t\bar{t} \to WbWb$ background is normalized to the SM prediction. The small contributions from W/Z+jets, single top, diboson and multijet backgrounds are combined into a single background source referred to as "Non-$t\bar{t}$". The bottom panel displays the ratio of data to the SM background ("Bkg") prediction. The dashed area represents the total uncertainty on the background.

$t\bar{t} \to WbHc$									
Decay Mode	4 j, 2 b	4 j, 3 b	4 j, 4 b	5 j, 2 b	5 j, 3 b	5 j, ≥4 b	≥6 j, 2 b	≥6 j, 3 b	≥6 j, ≥4 b
$H \to b\bar{b}$	84.35 %	96.71 %	98.64 %	80.76 %	95.54 %	97.91 %	76.82 %	93.2 %	96.11 %
$H \to W^+W^-$	7.49 %	1.11 %	0.19 %	9.89 %	1.79 %	0.48 %	13.23 %	3.24 %	1.41 %
$H \to \tau^+\tau^-$	1.71 %	0.13 %	0.02 %	2.13 %	0.26 %	0.05 %	2.7 %	0.62 %	0.33 %
$H \to c\bar{c}$	2.62 %	0.51 %	0.16 %	2.7 %	0.59 %	0.21 %	2.46 %	0.72 %	0.47 %
$H \to ZZ$	2.41 %	0.86 %	0.48 %	2.8 %	1.06 %	0.63 %	2.73 %	1.09 %	0.61 %
$H \to \gamma\gamma$	1.28 %	0.64 %	0.5 %	1.51 %	0.71 %	0.67 %	1.78 %	0.95 %	0.88 %
$H \to Z\gamma$	0.08 %	0.00 %	0.00 %	0.13 %	0.01 %	0.01 %	0.11 %	0.01 %	0.00 %
$H \to s\bar{s}$	0.06 %	0.02 %	0.02 %	0.08 %	0.03 %	0.04 %	0.16 %	0.16 %	0.18 %
$H \to \mu^+\mu^-$	0.01 %	0.00 %	0.00 %	0.01 %	0.00 %	0.00 %	0.01 %	0.00 %	0.00 %

Table 6.2: Fractional contribution from the different Higgs boson decay modes to the selected $t\bar{t} \to WbHc$ signal in each of the analysis channels considered.

$t\bar{t} \to WbHu$									
Decay Mode	4 j, 2 b	4 j, 3 b	4 j, 4 b	5 j, 2 b	5 j, 3 b	5 j, ≥4 b	≥6 j, 2 b	≥6 j, 3 b	≥6 j, ≥4 b
$H \to b\bar{b}$	90.6 %	98.32 %	98.51 %	88.19 %	97.55 %	96.59 %	84.51 %	95.9 %	95.28 %
$H \to W^+W^-$	4.16 %	0.38 %	0.23 %	5.89 %	0.76 %	0.82 %	8.66 %	1.76 %	1.55 %
$H \to \tau^+\tau^-$	0.55 %	0.03 %	0.01 %	0.87 %	0.08 %	0.03 %	1.14 %	0.24 %	0.24 %
$H \to c\bar{c}$	1.55 %	0.17 %	0.13 %	1.5 %	0.27 %	0.3 %	1.75 %	0.41 %	0.46 %
$H \to ZZ$	1.98 %	0.48 %	0.4 %	2.26 %	0.61 %	0.53 %	2.32 %	0.76 %	0.8 %
$H \to \gamma\gamma$	1.05 %	0.56 %	0.68 %	1.19 %	0.7 %	1.71 %	1.47 %	0.85 %	1.62 %
$H \to Z\gamma$	0.02 %	0.00 %	0.00 %	0.04 %	0.00 %	0.00 %	0.06 %	0.00 %	0.00 %
$H \to s\bar{s}$	0.07 %	0.05 %	0.04 %	0.07 %	0.04 %	0.02 %	0.07 %	0.05 %	0.05 %
$H \to \mu^+\mu^-$	0.00 %	0.00 %	0.00 %	0.01 %	0.00 %	0.00 %	0.01 %	0.02 %	0.01 %

Table 6.3: Fractional contribution from the different Higgs boson decay modes to the selected $t\bar{t} \to WbHu$ signal in each of the analysis channels considered.

they are useful for calibrating the $t\bar{t}$+jets background prediction and constraining the related systematic uncertainties (see Chapter 7) through a likelihood fit to data (see Chapter 8). It should be noted that all nine channels (signal-rich and signal-depleted) are fitted simultaneously. This strategy was first used in the ATLAS search for $t\bar{t}H$ associated production, with $H \to b\bar{b}$ [8], and is adapted for this analysis. In the following, the results before the fit are denoted as "pre-fit", while results after the fit are denoted as "post-fit".

One of the reasons for the splitting of channels in jet multiplicity (4, 5 and ≥ 6) is the fact that at high b-tag multiplicity the $t\bar{t}$+jets background typically has higher jet multiplicity than the signal because additional heavy flavor jets (from $t\bar{t} + b\bar{b}$ and $t\bar{t} + c\bar{c}$) are necessary in order to have so many b-tags. The other reason is that the main discriminating variable for this analysis will be based on an event likelihood discriminant (below referred to as $\mathcal{D}$), and the signal-to-background separation of such likelihood degrades at higher jet multiplicity. Details about the discriminating variable are provided in Sec. 6.2.

6.2 Discriminating Variable

After event categorization, the signal-to-background ratio is very low even in the most sensitive analysis channels, and a suitable discriminating variable between signal and background is constructed in order to improve the sensitivity of the search. A powerful discriminant between signal and background can be obtained by evaluating the probability density (pdf) of a given event under the signal hypothesis ($t\bar{t} \to WbHq$), $P^{\text{sig}}(\mathbf{x})$, and under the background hypothesis ($t\bar{t} \to WbWb$), $P^{\text{bkg}}(\mathbf{x})$, as:

$$D(\mathbf{x}) = \frac{P^{\text{sig}}(\mathbf{x})}{P^{\text{sig}}(\mathbf{x}) + P^{\text{bkg}}(\mathbf{x})}. \tag{6.1}$$

Both pdfs are functions of $\mathbf{x}$, representing the four-momentum vectors of all final-state particles at the reconstruction level: the lepton (ℓ), the neutrino (ν; reconstructed as discussed below), and the number of selected jets, N_{jets}, in a given analysis channel.

Possibly the most optimal way to construct P^{sig} and P^{bkg} would be via the *Matrix Method* (see Sec. 7.3.4), but this is very computationally-expensive and, for the purpose of this analysis, a simpler approach is followed.

Since both signal and background result from the $t\bar{t}$ decay, there are few experimental handles available to discriminate between them. The most prominent features are the different resonances present in the decay (i.e. the Higgs boson in the case of $t\bar{t} \to WbHq$ and a hadronically decaying W boson in the case of $t\bar{t} \to WbWb$), and the different flavor content of the jets forming those resonances. This is the main information exploited in the construction of $P^{\text{sig}}(\mathbf{x})$ and $P^{\text{bkg}}(\mathbf{x})$ in this analysis, so that $\mathbf{x}$ is extended to include not only the four-momenta of jets $\mathbf{p}_{\text{jet}}$, but also the value of their multivariate b-tagging discriminant w_{jet}, i.e., $\mathbf{x} \equiv \{p_\ell, p_\nu, (p_{\text{jet}_i}, w_{\text{jet}_i})\}$ $(i = 1, \ldots, N_{\text{jets}})$. There is also some angular information from the different spins of the daughter resonances (Higgs and W boson) that could be exploited, but it is expected to be subleading in importance and is neglected in this analysis.

In the following, b_ℓ denotes the b-quark jet from the semileptonic top quark decay, q_h and b_h denote the light-quark jet ($q_h = u$ or c) and b-quark jet from the hadronic top quark decay in background and signal events respectively, q_1 and q_2 denote the up-type-quark jet (u or c) and down-type-quark jet (d or s) from the W boson decay respectively, and b_1 and b_2 denote the two b-quark jets from the Higgs boson decay. This notation, along with the parton jet assignments, is illustrated for the signal and background probabilities in Fig. 6.4(a) and Fig. 6.4(b,c) respectively.

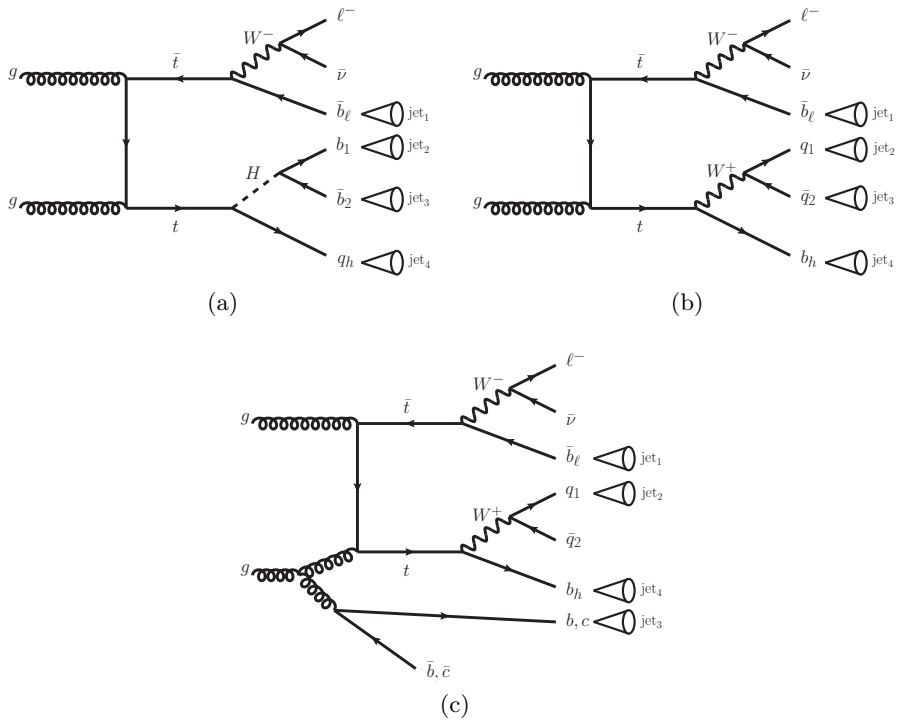

Figure 6.4: Representative Feynman diagrams illustrating the partonic configurations and parton–jet assignments considered in the construction of (a) the signal probability and (b) and (c) the background probability used in the definition of the final discriminant (see text for details).

The calculation of $P^{\text{sig}}(\mathbf{x})$ and $P^{\text{bkg}}(\mathbf{x})$ is discussed in detail in Sec. 6.2.1 and Sec. 6.2.2 respectively. The smoothing procedure for the pdfs is described in Sec. 6.2.3. The level of separation achieved between signal and background with the resulting

discriminant D is illustrated in Sec. 6.2.4.

6.2.1 Signal Probability

The construction of $P^{\text{sig}}(\mathbf{x})$ will be described step by step to illustrate the method. If the partonic origin of each jet were known, as shown in Fig. 6.4(a), then $P^{\text{sig}}(\mathbf{x})$ would be defined in this analysis as the product of the normalized pdfs for each of the reconstructed invariant masses in the event, i.e the semileptonic top quark mass ($M_{\ell\nu b_\ell}$), the hadronic top quark mass ($M_{b_1b_2q_h}$) and the Higgs boson mass ($M_{b_1b_2}$).

The above factorization assumes no correlation between each of the three variables. This is not a good approximation in the case of $M_{b_1b_2q_h}$ and $M_{b_1b_2}$, since the former contains the latter. To improve this, the $M_{b_1b_2q_h}$ variable is replaced by the difference in quadrature between $M_{b_1b_2q_h}$ and $M_{b_1b_2}$:

$$X_{b_1b_2q_h} \equiv M_{b_1b_2q_h} \ominus M_{b_1b_2}, \tag{6.2}$$

where $\ominus$ denotes the quadratic difference ($a \ominus b = \sqrt{a^2 - b^2}$). As shown in Fig. 6.5, the correlation between $M_{b_1b_2}$ and $X_{b_1b_2q_h}$ is significantly smaller compared to that between $M_{b_1b_2}$ and $M_{b_1b_2q_h}$.

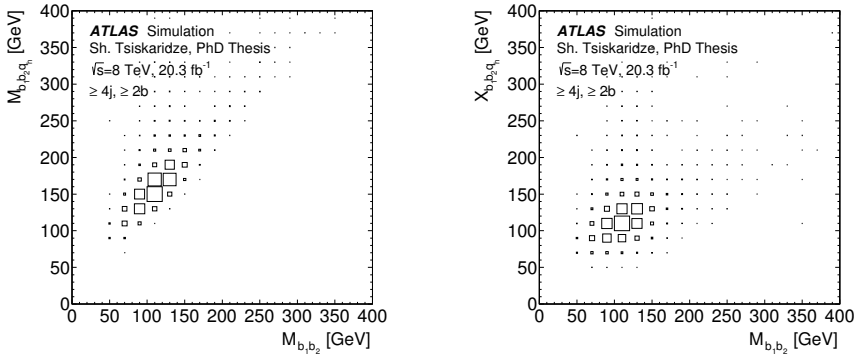

(a) (b)

Figure 6.5: Scatter plot of (a) $M_{b_1b_2q_h}$ vs $M_{b_1b_2}$ and (b) $X_{b_1b_2q_h}$ vs $M_{b_1b_2}$ in $t\bar{t} \to WbHc$ signal events with ≥ 4 jets and ≥ 2 b-tags.

Therefore, the expression for P^{sig} just making use of the above kinematic information, denoted by $P^{\text{sig}}_{\text{kin}}$, is:

$$P^{\text{sig}}_{\text{kin}}(\mathbf{x}) = P^{\text{sig}}(M_{\ell\nu b_\ell})P^{\text{sig}}(X_{b_1b_2q_h})P^{\text{sig}}(M_{b_1b_2}). \tag{6.3}$$

The distributions of these invariant masses are obtained from simulated signal events using the reconstructed lepton and/or jets corresponding to the correct parton–jet assignment, determined by matching a given quark (before final-state radiation) to the closest jet with $\Delta R < 0.3$. The corresponding pdfs are constructed as unit-normalized one-dimensional histograms, and are discussed below.

- **Leptonic Top Mass PDFs**

To compute $M_{\ell\nu b_\ell}$, the neutrino four-momentum is needed, which is reconstructed as follows. Initially, the x and y components of the neutrino momentum, $p_{x,\nu}$ and $p_{y,\nu}$, are identified with those of the reconstructed $E_{\mathrm{T}}^{\mathrm{miss}}$ vector. The z component of the neutrino momentum, $p_{z,\nu}$, is inferred by solving the following quadratic equation:

$$M_W^2 = (p_\ell + p_\nu)^2, \tag{6.4}$$

where $M_W = 80.4$ GeV is the W boson mass.

If two real solutions ("2sol") exist, they are sorted according to their absolute value of $|p_{z,\nu}|$ i.e., $|p_{z,\nu 1}| < |p_{z,\nu 2}|$. It is found that in 62% of the cases $p_{z,\nu 1}$ is closer than $p_{z,\nu 2}$ to the generator-level neutrino $p_{z,\nu}$. In this case, two different pdfs are constructed, one for each solution, and $P_{\mathrm{2sol}}^{\mathrm{sig}}(M_{\ell\nu b_\ell})$ is defined as the average of the two pdfs weighted by their fractions (0.62 for $p_{z,\nu 1}$ and 0.38 for $p_{z,\nu 2}$).

If no real solution ("nosol") exists, which happens in about 30% of the cases, the $p_{x,\nu}$ and $p_{y,\nu}$ components are scaled by a common factor until the discriminant of the quadratic equation is exactly zero, yielding only one solution for $p_{z,\nu}$. This solution for $p_{z,\nu}$ is used to compute $M_{\ell\nu b_\ell}$, from which the corresponding $P_{\mathrm{nosol}}^{\mathrm{sig}}(M_{\ell\nu b_\ell})$ is constructed.

In the calculation of $P_{\mathrm{kin}}^{\mathrm{sig}}(\mathbf{x})$ from Eq. 6.3, $P^{\mathrm{sig}}(M_{\ell\nu b_\ell})$ is identified with $P_{\mathrm{2sol}}^{\mathrm{sig}}(M_{\ell\nu b_\ell})$ or with $P_{\mathrm{nosol}}^{\mathrm{sig}}(M_{\ell\nu b_\ell})$, depending on how many neutrino solutions can be found for the event. A comparison of the resolution in the neutrino momentum obtained in each of the cases ("Solution 1", "Solution 2" and "No solution") is shown in Fig. 6.6.

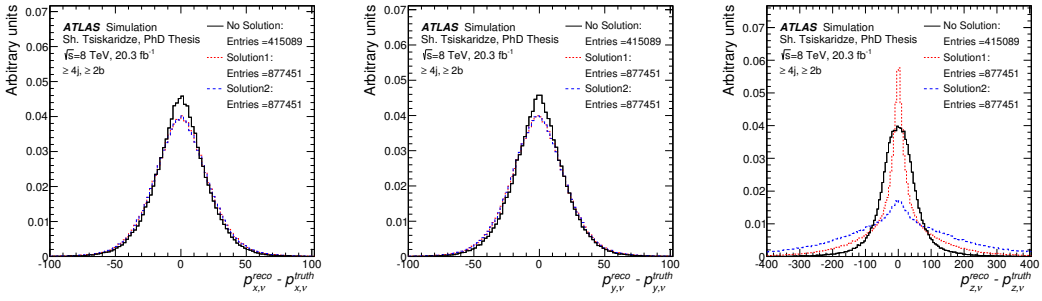

(a) (b) (c)

Figure 6.6: Resolution of the reconstructed neutrino momentum computed as (a) $p_{x,\nu}^{\mathrm{reco}} - p_{x,\nu}^{\mathrm{true}}$, (b) $p_{y,\nu}^{\mathrm{reco}} - p_{y,\nu}^{\mathrm{true}}$ and (c) $p_{z,\nu}^{\mathrm{reco}} - p_{z,\nu}^{\mathrm{true}}$, for the "Solution 1", "Solution 2" and "No solution" cases. The distributions are obtained in $t\bar{t} \to WbWb$ background events with ≥ 4 jets and ≥ 2 b-tags.

Three different pdfs are obtained for $M_{\ell\nu b_\ell}$, corresponding to each of the cases discussed above, and are presented in Fig. 6.7. These pdfs are found to be consistent between $t\bar{t} \to WbHc$ and $t\bar{t} \to WbHu$ signal events, and independent of the analysis channel and so they are measured for events with $\geq$4 jets and $\geq$2 b-tags, to ensure high statistics. They are also very close to the ones derived in $t\bar{t} \to WbWb$ events, used in the calculation of P^{bkg}, discussed in Sec. 6.2.2.

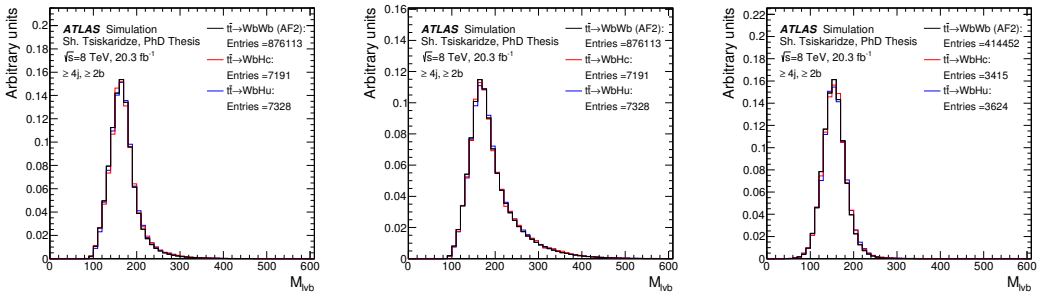

(a) (b) (c)

Figure 6.7: Pdfs for $M_{\ell\nu b_\ell}$ for the (a) "Solution 1", (b) "Solution 2", and (c) "No solution" cases. The distributions are compared between $t\bar{t} \to WbHc$ signal, $t\bar{t} \to WbHu$ signal and $t\bar{t} \to WbWb$ background events with ≥ 4 jets and ≥ 2 b-tags.

- **Hadronic Top Mass and Higgs Mass PDFs**

  The $P^{\text{sig}}(M_{b_1 b_2})$ and $P^{\text{sig}}(X_{b_1 b_2 q_h})$ pdfs are obtained by matching the jets with the correct quarks as discussed above, and can be found in Fig. 6.8. These pdfs are found to be consistent between $t\bar{t} \to WbHc$ and $t\bar{t} \to WbHu$ signal events, and independent of the analysis channel, so they are measured for $t\bar{t} \to WbHc$ events with $\geq$4 jets and $\geq$2 b-tags, to ensure high statistics. Also shown are pdfs for $t\bar{t} \to WbWb$ to illustrate the separation between signal and background on the leading kinematic variables exploited by the likelihood discriminant.

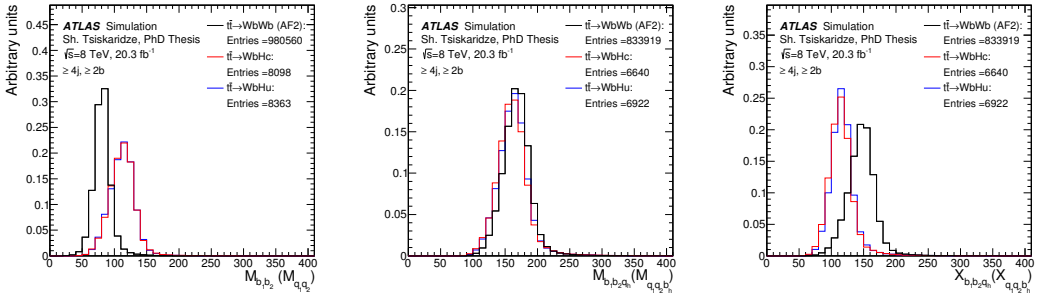

(a) (b) (c)

Figure 6.8: Pdfs for (a) $M_{b_1 b_2}$, (b) $M_{b_1 b_2 q_h}$ and (c) $X_{b_1 b_2 q_h}$. The $M_{b_1 b_2 q_h}$ pdf is not used as such and only shown here to illustrate the peak at the correct top quark mass. Also show are pdfs for $t\bar{t} \to WbWb$ corresponding to similar variables ($M_{q_1 q_2}$, $M_{q_1 q_2 b_h}$ and $X_{q_1 q_2 b_h}$) that will be used in the construction of the P^{bkg} probability.

In practice, the partonic origin of the jets is not known, so it is necessary to evaluate $P^{\text{sig}}(\mathbf{x})$ by averaging over the possible parton–jet assignments, N_p, which dilutes the kinematic information. At this point b-tagging information can be used to suppress the impact from parton–jet assignments that are inconsistent with the correct parton

flavors as follows:

$$P^{\text{sig}}(\mathbf{x}) = \frac{\sum_{k=1}^{N_p} P^{\text{sig}}_{\text{btag}}(\mathbf{x}^k) P^{\text{sig}}_{\text{kin}}(\mathbf{x}^k)}{\sum_{k=1}^{N_p} P^{\text{sig}}_{\text{btag}}(\mathbf{x}^k)}, \tag{6.5}$$

where $P^{\text{sig}}_{\text{kin}}(\mathbf{x})$ is given by Eq. 6.3 and $P^{\text{sig}}_{\text{btag}}(\mathbf{x})$ is defined as:

$$P^{\text{sig}}_{\text{btag}}(\mathbf{x}) = P_b(\text{jet}_1) P_b(\text{jet}_2) P_b(\text{jet}_3) P_{q_h}(\text{jet}_4), \tag{6.6}$$

with jet_i ($i = 1, \ldots, 4$) representing the parton–jet assignment being evaluated, and $P_f(\text{jet}_i)$ denoting the probability that jet i, characterized by its four-momentum p_{jet_i} and b-tagging weight value w_{jet_i}, originates from a parton with flavor f (b, c, or l; l for light parton).

The calibration of the b-tagging algorithm (see Sec. 4.5.1) is performed for fixed thresholds on the multivariate b-tagging discriminant variable, corresponding to different average b-tagging efficiencies in $t\bar{t}$ events of 60%, 70%, and 80% operating points (OP). The corresponding thresholds are denoted by $w^{\text{OP}}_{\text{cut}}$, with OP = 60%, 70%, or 80%. Parameterizations of the b-tagging efficiencies for different jet flavors as functions of jet p_{T} and η are available for each of these operating points, $\epsilon^{\text{OP}}_f(p_{\text{T}}, \eta)$, which can be used to compute P_f as follows: if the jet b-tagging weight falls between the thresholds for operating points OP_1 and OP_2, $w^{\text{OP}_1}_{\text{cut}} < w_{\text{jet}} \leq w^{\text{OP}_2}_{\text{cut}}$, then $P_f = \epsilon^{\text{OP}_1}_f - \epsilon^{\text{OP}_2}_f$; alternatively, if the jet b-tagging weight is below (above) the threshold corresponding to the 80% (60%) operating point, then $P_f = 1 - \epsilon^{80\%}_f$ ($P_f = \epsilon^{60\%}_f$).

6.2.2 Background Probability

The calculation of P^{bkg} follows a similar approach to that discussed in Sec. 6.2.1, although it is slightly more complicated to account for the varying fraction and different kinematic features of the $t\bar{t}$+light-jets, $t\bar{t} + c\bar{c}$ and $t\bar{t} + b\bar{b}$ backgrounds as a function of the analysis channel. This is particularly relevant in the (4 j, 3 b) and (4 j, 4 b) channels, which dominate the sensitivity of the search. While $t\bar{t}$+light-jets events often have both jets from the hadronic W boson decay among the four selected jets (see Fig. 6.4b), this is seldom the case for $t\bar{t} + b\bar{b}$ and $t\bar{t} + c\bar{c}$ events, especially in the (4 j, 4 b) channel.

In this case the four b-tagged jets typically originate from the two b-quarks from the top quark decays, the charm quark from the W boson decay, and an extra heavy-flavor quark (b or c) produced in association with the $t\bar{t}$ system, while the jet associated with the down-type quark from the W boson decay is not reconstructed (see Fig. 6.4c).

To account for this, the following kinematic variables are considered: $M_{\ell\nu b_\ell}$, $X_{q_1 j b_h}$ and $M_{q_1 j}$, with $X_{q_1 j b_h} \equiv M_{q_1 j b_h} \ominus M_{q_1 j}$, were j denotes an extra quark-jet which can either originate from the W boson decay (q_2) or from an extra heavy-quark (b or c) produced in association with the $t\bar{t}$ system. For each of these possibilities, occurring in a fraction f_j of the cases, corresponding pdfs are constructed. As a generalization

of Eq. 6.5, the expression for $P^{\rm bkg}(\mathbf{x})$ becomes:

$$P^{\rm bkg}(\mathbf{x}) = \frac{\sum_{k=1}^{N_p} \sum_{j\in\{b,c,q_2\}} f_j P^{{\rm bkg},j}_{\rm btag}(\mathbf{x}^k) P^{{\rm bkg},j}_{\rm kin}(\mathbf{x}^k)}{\sum_{k=1}^{N_p} \sum_{j\in\{b,c,q_2\}} f_j P^{{\rm bkg},j}_{\rm btag}(\mathbf{x}^k)}, \tag{6.7}$$

with

$$P^{{\rm bkg},j}_{\rm kin}(\mathbf{x}) = P^{\rm bkg}(M_{\ell\nu b_\ell}) P^{\rm bkg}(X_{q_1 j b_h}) P^{\rm bkg}(M_{q_1 j}), \tag{6.8}$$

and

$$P^{{\rm bkg},j}_{\rm btag}(\mathbf{x}) = P_b({\rm jet}_1) P_{q_1}({\rm jet}_2) P_j({\rm jet}_3) P_b({\rm jet}_4). \tag{6.9}$$

where $P_f({\rm jet}_i)$ are computed as discussed in Sec. 6.2.1. In the above expression, $P_j = P_l$ for $j = q_2$, the down-type quark in the W boson decay, and $P_{q_1} = f_c P_c + (1 - f_c) P_l$, where f_c is the fraction of events where the up-type quark from the W boson decay assigned to the jet is a charm quark. This fraction is different in each analysis channel, primarily depending on the b-tag multiplicity requirements. It varies from $\sim 50\%$ for events in the (4 j, 2 b) channel to $\sim 90\%$ for events in the (4 j, 4 b) channel.

In the case of the 4 jets channels there is only one jet left after matching the above three quarks. In the case of the 5 jets channels, there are two jets and both are considered in filling the pdfs. In the case of the ≥ 6 jets channels, only events with exactly 6 jets are used to build the pdfs, so there are three extra jets considered. At the end all pdfs are normalized to unity. Examples of the pdfs constructed for the (4 j, 4 b) channel can be found in Fig. 6.9. As can be appreciated, the pdfs for $j = q_2$ (dominant for $t\bar{t}$+light jet events) show the expected hadronic W and top mass resonances, whereas the pdfs for $j = c, b$ (more appropriate for $t\bar{t} + c\bar{c}$ and $t\bar{t} + b\bar{b}$ events) are broader.

In order to ensure the highest-possible MC statistics for the pdfs, they are derived using the $t\bar{t}$ AF2 sample (see Sec. 3.3), while the evaluation of the final discriminant is done with the $t\bar{t}$ full-simulation sample. It has been verified that the shape of the pdfs is in close agreement between AF2 and full-simulation, which ensures no loss in discrimination power.

6.2.3 PDF Smoothing

In order to treat the pdfs as probability-density functions, it is necessary to ensure that they are positive-definite over the whole kinematic range of interest. Because of the limited MC statistics, the pdf histograms may have empty bins at high mass values. On the other hand, due the preselection cut on the jet $p_{\rm T}$, there may be empty bins at very low mass values as well. In order to overcome this problem a smoothing procedure is performed:

- At low mass, starting with the first bin filled, the content of each bin before is set to one tenth of the following bin in a recursive way till arriving to the first bin in the histogram.

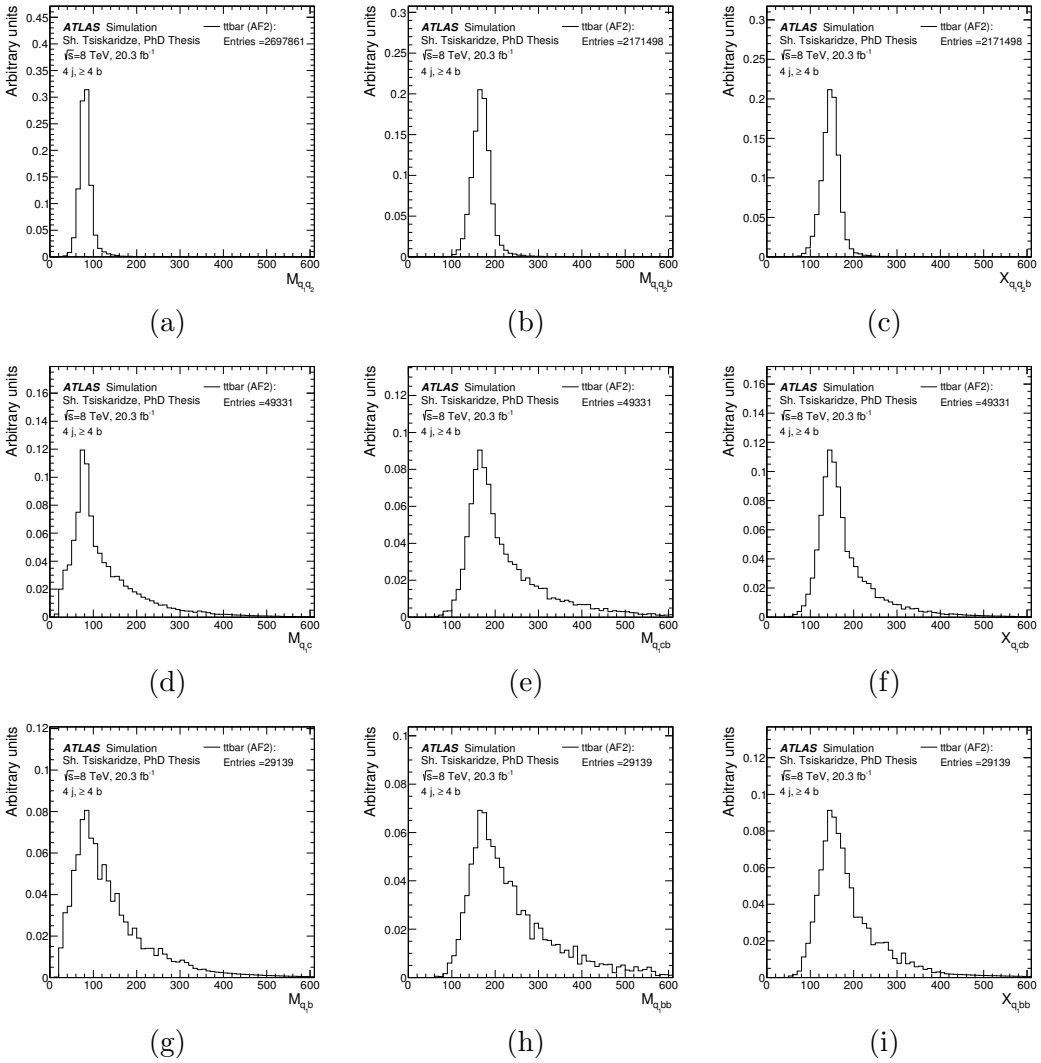

Figure 6.9: Pdfs for (a) $M_{q_1q_2}$, (b) $M_{q_1q_2b}$, (c) $X_{q_1q_2b}$, (d) M_{q_1c}, (e) M_{q_1cb}, (f) X_{q_1cb}, (g) M_{q_1b}, (h) M_{q_1bb} and (i) X_{q_1bb} for the (4 j, 4 b) channel.

- At high mass, the fluctuating distribution is replaced by an exponential function whose parameters are adjusted in order to ensure continuity just before the large fluctuations start occurring, and whose integral match the integral of the tail.

An example of a pdf before and after smoothing procedure is shown in Fig. 6.10.

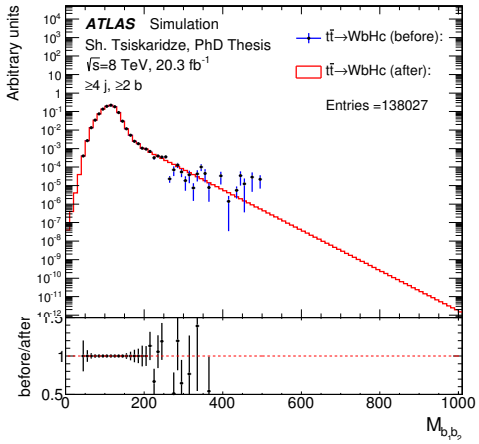

Figure 6.10: Pdf for $M_{b_1 b_2}$ in $t\bar{t} \to WbHc$ signal events with ≥ 4 jets and ≥ 2 b-tags. The bottom panel displays the ratio of the pdf before and after the smoothing procedure.

6.2.4 Final Discriminant

The final discriminant D is computed for each event as given in Eq. 6.1, using the definitions for P^{sig} and P^{bkg} given in Eq. 6.5 and Eq. 6.7. respectively. Since this analysis has higher expected sensitivity to a $t\bar{t} \to WbHc$ signal than to a $t\bar{t} \to WbHu$ signal and, in order to allow probing of the BR($t \to Hu$) versus BR($t \to Hc$) plane, the discriminant optimized for $t\bar{t} \to WbHc$ is used for both the Hc and Hu decay modes. It was verified that using the $t\bar{t} \to WbHc$ discriminant for the $t\bar{t} \to WbHu$ search does not result in a significant sensitivity loss. Figure 6.11 compares the shape of the D distribution between the $t\bar{t} \to WbHc$ and $t\bar{t} \to WbHu$ signals and the $t\bar{t} \to WbWb$ background in each of the channels considered in this analysis.

The expected distributions for $t\bar{t} \to WbHc$ signal (assuming BR($t \to Hc$) = 1%) and the different backgrounds in each of the nine analysis channels considered are shown in Fig. 6.12, along with the expected systematic uncertainties (discussed in detail in Chapter 7). The corresponding plots for $t\bar{t} \to WbHu$ signal (assuming BR($t \to Hu$) = 1%) are shown in Fig. 6.13. The data here is defined as the sum of the MC prediction of the signal and total background, also referred to as "Asimov data".

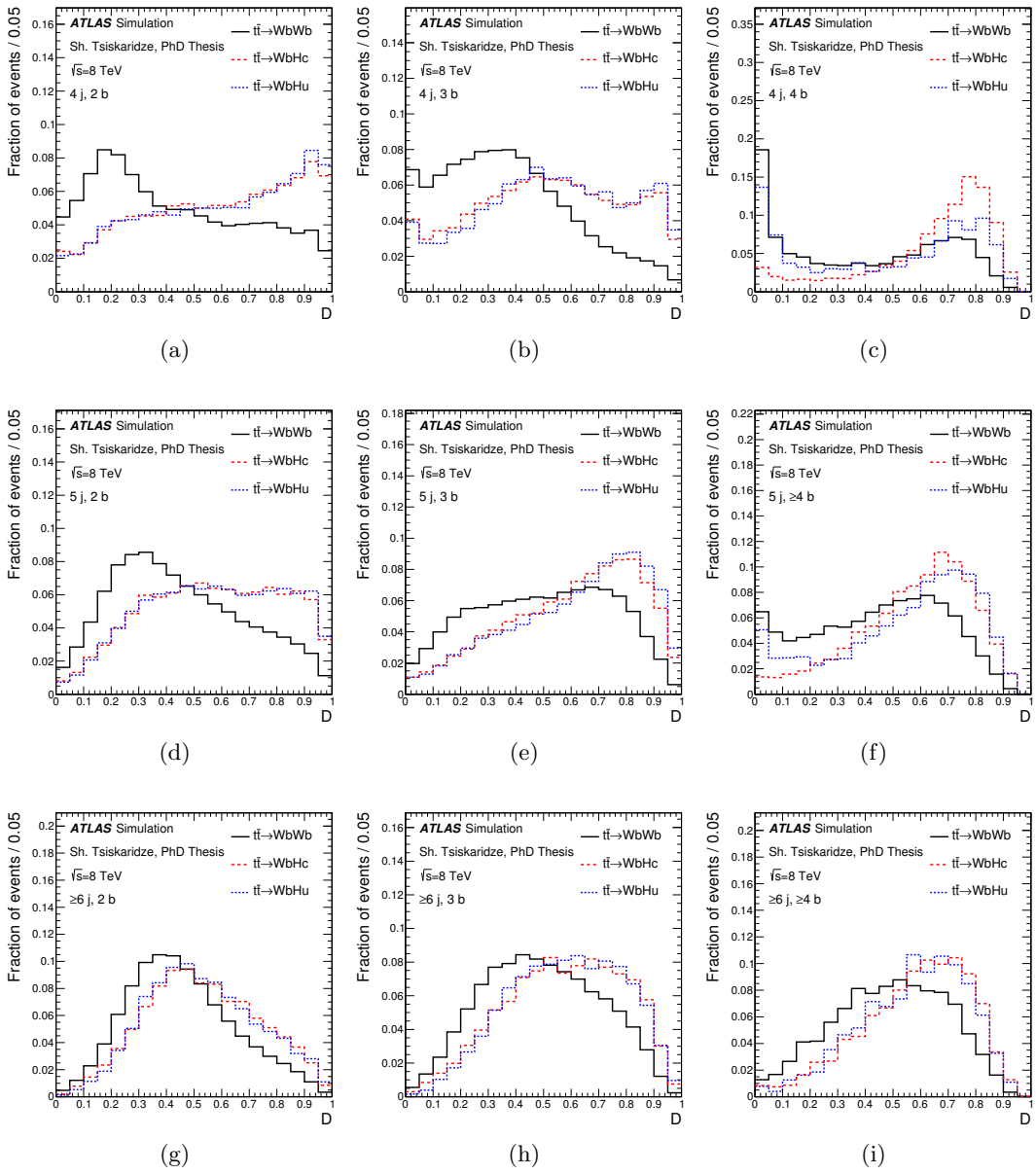

Figure 6.11: Comparison of the shape of the D discriminant distribution between the $t\bar{t} \to WbHc$ (red dashed) and $t\bar{t} \to WbHu$ (blue dotted) signals, and the $t\bar{t} \to WbWb$ background (black solid) in each of the channels considered in the analysis: (a) (4 j, 2 b), (b) (4 j, 3 b), (c) (4 j, 4 b), (d) (5 j, 2 b), (e) (5 j, 3 b), (f) (5 j, ≥4 b), (g) (≥6 j, 2 b), (h) (≥6 j, 3 b), and (i) (≥6 j, ≥4 b).

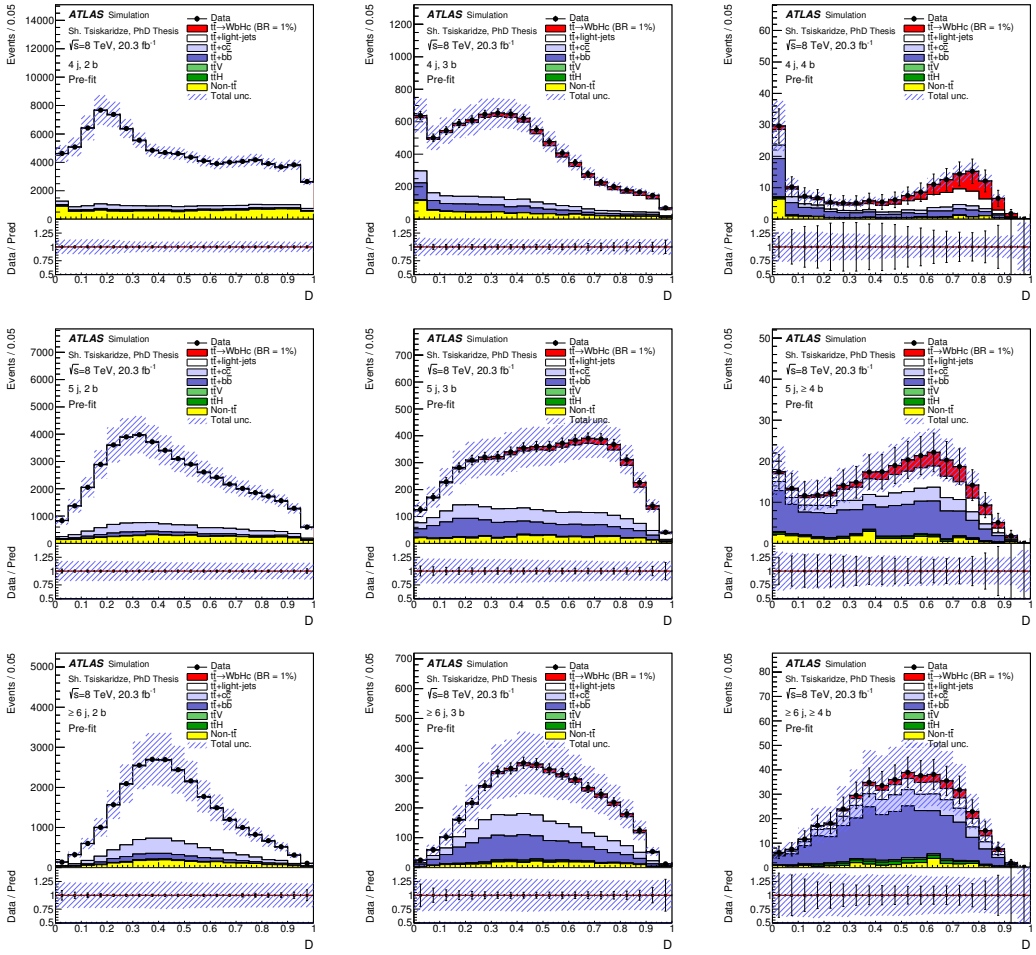

Figure 6.12: Expected $\mathcal{D}$ distribution for the combined e+jets and μ+jets selections in each of the channels considered in the analysis. From top to bottom and left to right: (4 j, 2 b), (4 j, 3 b), (4 j, 4 b), (5 j, 2 b), (5 j, 3 b), (5 j, ≥4 b), (≥6 j, 2 b), (≥6 j, 3 b), and (≥6 j, ≥4 b) channels. Shown are the pre-fit expected $t\bar{t} \to WbHc$ signal (assuming BR$(t \to Hc) = 1\%$) and backgrounds, and the Asimov data. The $t\bar{t} \to WbWb$ background has been scaled by a factor of 0.98, as discussed in Sec. 8.1. The dashed area represents the total uncertainty pre-fit and the bottom panel displays the ratio between the Asimov data and the total prediction.

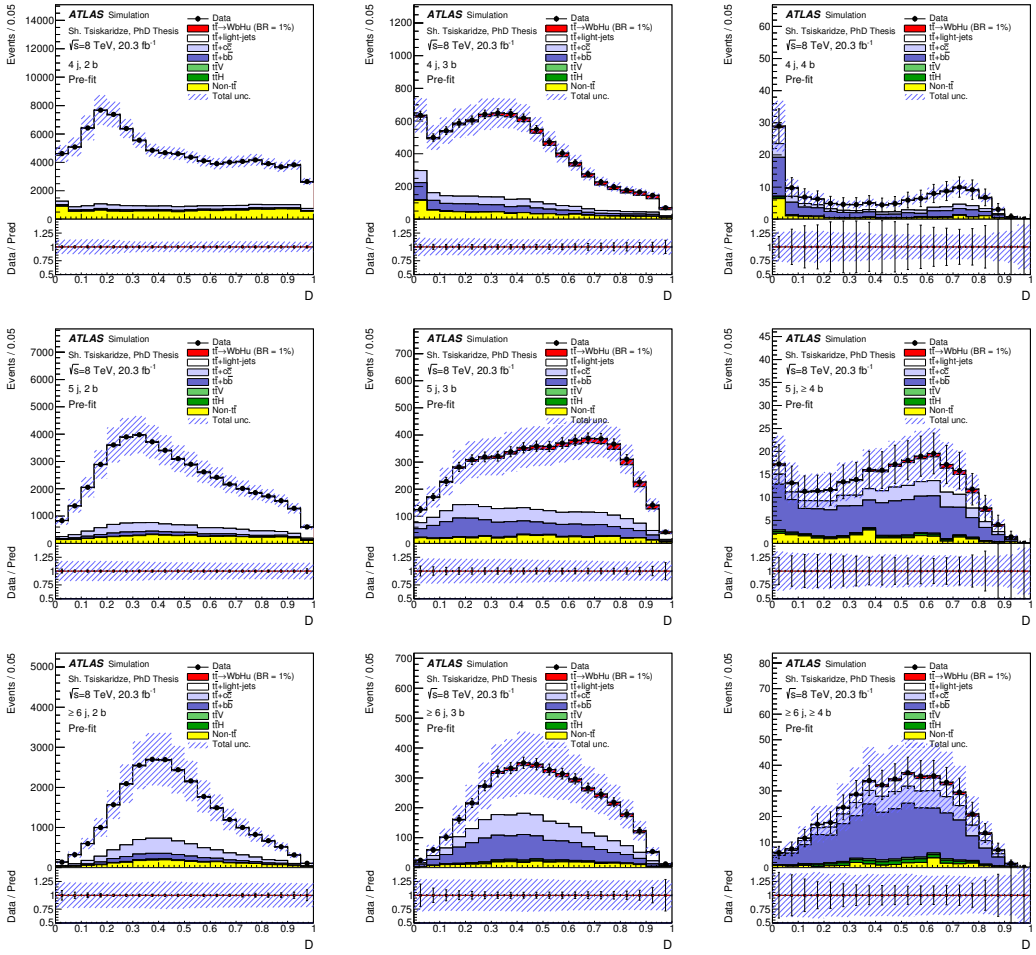

Figure 6.13: Expected $\mathcal{D}$ distribution for the combined e+jets and μ+jets selections in each of the channels considered in the analysis. From top to bottom and left to right: (4 j, 2 b), (4 j, 3 b), (4 j, 4 b), (5 j, 2 b), (5 j, 3 b), (5 j, ≥4 b), (≥6 j, 2 b), (≥6 j, 3 b), and (≥6 j, ≥4 b) channels. Shown are the pre-fit expected $t\bar{t} \to WbHu$ signal (assuming BR($t \to Hu$) = 1%) and backgrounds, and the Asimov data. The $t\bar{t} \to WbWb$ background has been scaled by a factor of 0.98, as discussed in Sec. 8.1. The dashed area represents the total uncertainty pre-fit and the bottom panel displays the ratio between the Asimov data and the total prediction.

Chapter 7

Systematic Uncertainties

There are two major types of uncertainties that affect the sensitivity of this search: *statistical* uncertainties and *systematic* uncertainties. Sources of statistical uncertainties are the limited number of events in the MC samples, that includes the Poissonian uncertainty on the event counts in the considered regions. The systematic uncertainties are coming from the finite precision of the calibration of the reconstructed objects, the non-perfect modeling of the signal and background, and the limited description of the experimental conditions, like luminosity and pile-up.

The systematic uncertainty can affect the normalization of signal and background and/or the shape of their corresponding final discriminant distributions. Each source of systematic uncertainty is considered to be uncorrelated with the other sources. Correlations of a given systematic uncertainty are maintained across processes and channels. Table 7.1 presents a list of all systematic uncertainties considered in the analysis and indicates whether they are taken to be normalization-only, or to affect both shape and normalization.

The leading sources of systematic uncertainty vary depending on the analysis channel considered, but they typically originate from $t\bar{t}$+jets modeling (including $t\bar{t}$+HF) and b-tagging. For example, the total systematic uncertainty in the background normalization in the (4 j, 4 b) channel, which dominates the sensitivity in the case of the $t\bar{t} \to WbHc$ search, is approximately 20%, with the largest contributions originating from $t\bar{t}$+HF normalization, b-tagging efficiency, c-tagging efficiency, light-jet tagging efficiency and $t\bar{t}$ cross section. However, as it will be shown in Chapter 9, the fit to data in the nine analysis channels allows the overall background uncertainty to be reduced significantly, to approximately 4.4%.

The reduced uncertainty results from the significant constraints provided by the data on some systematic uncertainties, as well as the anti-correlations among sources of systematic uncertainty resulting from the fit to the data. The total systematic uncertainty on the $t\bar{t} \to WbHc$ signal normalization in the (4 j, 4 b) channel is approximately 17%, with similar contributions from uncertainties related to b-tagging and overall signal modeling. After the fit, this uncertainty is reduced to 7.8%. Table 7.2 presents a summary of the systematic uncertainties for the $t\bar{t} \to WbHc$ search and their impact on the normalization of the signal and the main backgrounds in the (4 j, 4 b) channel.

The following sections describe each of the systematic uncertainties considered in the analyses.

Systematic uncertainty	Type	Components
Luminosity	N	1
Reconstructed Objects		
Electron	SN	5
Muon	SN	6
Jet reconstruction	SN	1
Jet vertex fraction	SN	1
Jet energy scale	SN	22
Jet energy resolution	SN	1
Missing transverse momentum	SN	2
b-tagging efficiency	SN	6
c-tagging efficiency	SN	4
Light-jet tagging efficiency	SN	12
High-p_{T} tagging	SN	1
Background Model		
$t\bar{t}$ cross section	N	1
$t\bar{t}$ modeling: p_{T} reweighting	SN	9
$t\bar{t}$ modeling: parton shower	SN	3
$t\bar{t}$+HF: normalization	N	2
$t\bar{t}$+$c\bar{c}$: p_{T} reweighting	SN	2
$t\bar{t}$+$c\bar{c}$: generator	SN	4
$t\bar{t}$+$b\bar{b}$: NLO shape	SN	8
W+jets normalization	N	3
W p_{T} reweighting	SN	1
Z+jets normalization	N	3
Z p_{T} reweighting	SN	1
Single top normalization	N	3
Single top model	SN	1
Diboson normalization	N	3
$t\bar{t}V$ cross section	N	1
$t\bar{t}V$ model	SN	1
$t\bar{t}H$ cross section	N	1
$t\bar{t}H$ model	SN	2
Multijet normalization	N	4
Signal Model		
$t\bar{t}$ cross section	N	1
Higgs boson branching ratios	N	3
$t\bar{t}$ modeling: p_{T} reweighting	SN	9
$t\bar{t}$ modeling: p_{T} reweighting non-closure	N	1
$t\bar{t}$ modeling: parton shower	N	1

Table 7.1: List of systematic uncertainties considered. An "N" means that the uncertainty is taken as affecting only the normalization for all relevant processes and channels, whereas "SN" means that the uncertainty is taken on both shape and normalization. Some of the systematic uncertainties are split into several components for a more accurate treatment.

	Pre-fit				Post-fit			
	$WbHc$	$t\bar{t}$+LJ	$t\bar{t}+c\bar{c}$	$t\bar{t}+b\bar{b}$	$WbHc$	$t\bar{t}$+LJ	$t\bar{t}+c\bar{c}$	$t\bar{t}+b\bar{b}$
Luminosity	±2.8	±2.8	±2.8	±2.8	±2.6	±2.6	±2.6	±2.6
Lepton efficiencies	±1.5	±1.5	±1.5	±1.5	±1.5	±1.5	±1.5	±1.5
Jet energy scale	±3.3	±2.9	±2.3	±5.8	±1.4	±1.2	±1.8	±4.1
Jet efficiencies	±1.2	–	±1.9	±1.7	±0.9	–	±1.4	±1.2
Jet energy resolution	–	±1.2	±2.8	±2.9	–	–	±1.0	±1.1
b-tagging eff.	±7.9	±5.5	±5.2	±10	±5.7	±3.9	±3.7	±6.6
c-tagging eff.	±7.0	±6.6	±13	±3.5	±6.3	±6.0	±11	±3.2
Light-jet tagging eff.	±0.8	±18	±3.2	±1.5	±0.6	±13	±2.3	±1.1
$t\bar{t}$: reweighting	±5.9	±2.7	±4.2	–	±3.8	±1.9	±2.3	–
$t\bar{t}$: parton shower	±5.4	±4.8	±10	±4.9	±1.7	±1.5	±6.5	±3.1
$t\bar{t}$+HF: normalization	–	–	±50	±50	–	–	±32	±16
$t\bar{t}$+HF: modeling	–	–	–	±7.7	–	–	–	±7.4
Signal modeling	±6.9	–	–	–	±6.9	–	–	–
The or. cross sections	±6.2	±6.2	±6.2	±6.2	±3.9	±3.9	±3.9	±3.9
Total	±17	±22	±54	±53	±7.8	±14	±28	±15

Table 7.2: $t\bar{t} \to WbHc, H \to b\bar{b}$ search: summary of the systematic uncertainties considered in the (4 j, 4 b) channel and their impact (in %) on the normalization of the signal and the main backgrounds, before and after the fit to data. The $t\bar{t} \to WbHc$ signal and the $t\bar{t}$+light-jets background are denoted by "$WbHc$" and "$t\bar{t}$+LJ" respectively. Only sources of systematic uncertainty resulting in a normalization change of at least 0.5% are displayed. The total post-fit uncertainty can differ from the sum in quadrature of individual sources due to the anti-correlations between them resulting from the fit to the data.

7.1 Luminosity

The uncertainty on the integrated luminosity is estimated to be 2.8%. It is estimated from a calibration of the luminosity scale derived from beam-separation scans performed in November 2012, following the same methodology as that detailed in reference [64]. This uncertainty has to be propagated to all the signal and background MC samples used, since they need to be normalized to the amount of analyzed data.

7.2 Objects Definitions

The object reconstruction and calibration introduces uncertainties associated with the definition of leptons, jets, $E_{\mathrm{T}}^{\mathrm{miss}}$ and b-, c-, and light flavor-tagging. The corresponding systematic uncertainties are discussed below.

7.2.1 Lepton Reconstruction, Identification and Trigger

The reconstruction and identification efficiency of electrons and muons, as well as the efficiency of the trigger used to record the events, differ between data and simulation. These efficiencies are measured using tag-and-probe techniques on $Z \to \ell^+\ell^-$ ($\ell = e, \mu$) data and simulated samples. The small differences found are corrected for in the simulation. Negligible sources of uncertainty originate from the corrections applied to adjust the lepton momentum scale and resolution in the simulation to match those in data. The combined effect of all these uncertainties results in an overall normalization uncertainty on the signal and background of approximately 1.5%.

7.2.2 Lepton Momentum Scale and Resolution

The accuracy of lepton momentum scale and resolution in simulation is checked using reconstructed distributions of the $Z \to \ell^+\ell^-$ and $J/\psi \to \ell^+\ell^-$ masses. In the case of electrons, E/p studies using $W \to e\nu$ events are also used. Small discrepancies are observed between data and simulation, and corrections for the lepton energy scale and resolution in the latter are implemented using the tools provided by the combined performance groups.

In the case of electrons, energy scale corrections need to be applied to data (all regions) while energy resolution corrections are applied to the simulation only. In the case of muons, momentum scale and resolution corrections are only applied to the simulation. Uncertainties on both the momentum scale and resolution are considered, and varied separately. They have a negligible impact on the signal and background normalizations.

7.2.3 Jet Reconstruction Efficiency

The jet reconstruction efficiency for calorimeter jets has been derived relative to track-jets, using a tag-and-probe technique. It is found to be about 0.2% lower in the simulation than in data for jets below 30 GeV and it is consistent with data for higher jet p_{T}. To evaluate the systematic uncertainty due to this small inefficiency 0.2% of the jets with p_{T} below 30 GeV are removed randomly and all jet-related kinematic variables (including the $E_{\mathrm{T}}^{\mathrm{miss}}$) are recomputed. The event selection is repeated using the modified selected jet list.

7.2.4 Jet Vertex Fraction Efficiency

Recalling the cut applied on the JVF variable (Sec. 4.4.5) of $|\mathrm{JVF}| > 0.5$, the per-jet efficiency is measured in $Z(\to \ell^+\ell^-)$+1-jet events in data and simulation, selecting separately events enriched in hard-scatter jets and events enriched in jets from other proton interactions in the same bunch crossing (pileup). The corresponding uncertainty is evaluated in the analysis by changing the nominal JVF cut value by 0.1 up and down and repeating the analysis using the modified cut value.

7.2.5 Jet Energy Scale

The jet energy scale (JES) and its uncertainty have been derived combining information from test-beam data, LHC collision data and simulation [186–190]. The determination of the JES uncertainty takes into account 22 uncorrelated sources of systematic uncertainty:

- Pile-up related uncertainties are assigned to the correction term in Eq. 4.4, to cover the residual mismodeling of multiple interaction in MC. The impact of the uncertainty rapidly reduces with increasing jet p_{T}.
- For very high p_{T} jets ($p_{\mathrm{T}} > 2$ TeV) in-situ techniques are limited in statistics. Therefore, studies of detector response based on MC events and extrapolated test-beam results from single-hadron response are used to assess the systematic uncertainty [191]. In order to perform this extrapolation, jets are treated as a superposition of energy deposits of single particles. The measurements of the

calorimeter response to single pions in the combined test-beam are then extrapolated to high-p_{T} jets.

- η-intercalibration uncertainties are divided into a statistical component and a MC modeling one. They are the dominant source of JES uncertainty at large η ($|\eta| > 3$).

- Uncertainties coming from in-situ techniques are divided in different categories (statistical, detector, modeling, mixed) according to their origin. Particular attention has been paid to preserving the correlation information among the various sources of uncertainty across the different p_{T} bins. The "diagonalization and reduction" method has been applied [191]. The method identifies the most relevant sources of uncertainty and organizes them into uncorrelated variations which can then be applied independently. The remaining (small) sources of uncertainty are grouped together in a residual component.

- Flavor-related uncertainties: the response of the calorimeter differs for jets initiated by quarks and jets initiated by gluons. In-situ techniques mainly measure quark-initiated jets by the nature of the process involved. The baseline uncertainty is then increased using the MC estimates of the response difference between quarks and gluons [121].

- An additional source of uncertainty in the range of 1.5% to 3% is considered for jets originating from b-quarks. The uncertainty has been obtained comparing the jet calibration to an estimate of jet p_{T} performed with track jets and evaluating the difference between an inclusive jet sample and a sample enriched in jets from b-quarks [192].

The energy of jet is varied in a correlated fashion by the assigned uncertainty corresponding to each of the 22 eigenvectors. The missing transverse momentum is corrected according to the varied p_{T} of the jets in each event. The JES uncertainty affects the normalization of signal and backgrounds by approximately 3–4% in the most sensitive search channels, (4 j, 3 b) and (4 j, 4 b), and up to 12% in the channels with $\geq$6 jets.

7.2.6 Jet Energy Resolution

The jet energy resolution (JER) has been measured separately for data and simulation using the "dijet balance" and "dijet bisector" methods [193].

The dijet balance method uses the imbalance in jet p_{T}:

$$\mathcal{A} = \frac{p_{\mathrm{T}}^{\mathrm{probe}} - p_{\mathrm{T}}^{\mathrm{ref}}}{p_{\mathrm{T}}^{\mathrm{avg}}}, \tag{7.1}$$

where $p_{\mathrm{T}}^{\mathrm{probe}}$ is the transverse momentum of the jet in the calorimeter region under investigation, $p_{\mathrm{T}}^{\mathrm{ref}}$ is the transverse momentum of a jet in a well-calibrated reference region, and $p_{\mathrm{T}}^{\mathrm{avg}} = (p_{\mathrm{T}}^{\mathrm{probe}} + p_{\mathrm{T}}^{\mathrm{ref}})/2$. The jet energy resolution can be extracted with a fit to the width of the asymmetry distribution, $\sigma(\mathcal{A})$.

The dijet bisector method relies on the decomposition of the two leading jet vectorial sum p_{T} in orthogonal directions, one of them being the bi-section of the $\Delta\phi$

angles between the two jets in dijet events. The sensitivity to jet energy resolution is different for the two since in the bisector direction the p_{T} is the sum of two small components, while in the orthogonal direction a subtraction of the much larger projection is performed.

The measured resolutions in data and simulation agree reasonably well, with some differences at high p_{T} and high η. A systematic uncertainty is defined as the quadratic difference between the jet energy resolutions for data and simulation. To estimate the corresponding systematic uncertainty in the analysis, the energy of jets in the simulation is smeared by this residual difference, and the changes in the normalization and shape of the final discriminant are compared to the default prediction.

In order to propagate the uncertainty in the p_{T} resolution, for each jet in the simulation, a random number r is drawn from a Gaussian distribution with mean 0 and sigma equal to the difference in quadrature between the fractional p_{T} resolution with the tool and the nominal one. The jet 4-momentum is then scaled by a factor $1+r$. Since jets in the simulation cannot be under-smeared, by definition the resulting uncertainty on the normalization and shape of the final discriminant is one-sided. This uncertainty is then symmetrized.

7.2.7 Missing Transverse Momentum

Beyond the propagation to $E_{\mathrm{T}}^{\mathrm{miss}}$ of uncertainties on lepton and jet energy scales and resolutions, additional uncertainties are considered related to the CellOut+SoftJet scale (SC_SOFT) and resolution (RES_SOFT). The resulting uncertainties on the total yields predicted by the simulation are at the sub-percent level.

7.2.8 *b*-tagging

The leading uncertainties associated with reconstructed objects in this analysis originate from the modeling of the b-, c-, and light-jet-tagging efficiencies in the simulation, which is corrected to match the efficiencies measured in data control samples [128,194] through dedicated scale factors.

Uncertainties on these factors include a total of six independent sources affecting b-jets and four independent sources affecting c-jets. Each of these uncertainties has a different jet-p_{T} dependence. Twelve sources of uncertainty affecting light jets are considered, which depend on jet p_{T} and η region. More information on this procedure can be found in Appendix P of reference [195]. For technical details see reference [196].

The above sources of systematic uncertainty are taken as uncorrelated between b-jets, c-jets, and light-jets. They have their largest impact in the (4 j, 4 b) channel, resulting in 10%, 13%, and 18% normalization uncertainties on the $t\bar{t}+b\bar{b}$, $t\bar{t}+c\bar{c}$, and $t\bar{t}$+light-jets background associated with the uncertainties on the b-, c-, and light-jet-tagging scale factors, respectively. An additional uncertainty is included due to the extrapolation of these scale factors to jets with p_{T} beyond the kinematic reach of the data calibration samples used ($p_{\mathrm{T}} > 300$ GeV for b- and c-jets, and $p_{\mathrm{T}} > 750$ GeV for light-jets), taken to be correlated among the three jet flavors. This uncertainty has a very small impact in this analysis (e.g. $< 0.2\%$ on the signal and background normalizations in the (4 j, 4 b) channel).

7.3 Background Modeling

7.3.1 $t\bar{t}$+jets Modeling

A number of systematic uncertainties affecting the modeling of $t\bar{t}$+jets are considered in this analysis. As discussed in Sec. 5.3.1, systematic uncertainties due to the uncertainty on the theoretical cross section, due to the choice of the parton shower and hadronization model as well as several uncertainties arising from the reweighting procedure applied to correct the $t\bar{t}$ MC are taken into account. Additional uncertainties are assigned to account for the limited knowledge of the $t\bar{t}$+HF jets production.

7.3.1.1 Theoretical Cross-Section

Uncertainties of +6.1%/-6.4% are assumed for the inclusive $t\bar{t}$ production cross section evaluated as described in Sec. 5.3.

7.3.1.2 $t\bar{t}$ Reweighting Uncertainties

As discussed in Sec. 5.3.1, a reweighting procedure based on the difference between top quark p_{T} and $t\bar{t}$ p_{T} distributions measured in data and in the simulation is applied to $t\bar{t}$ MC events. The nine largest uncertainties associated with the experimental measurement of top quark and $t\bar{t}$ p_{T} are considered, representing approximately 95% of the total experimental uncertainty. Fig. 7.1 and Fig. 7.2 show the effect of these $t\bar{t}$ uncertainties on the unfolded $p_{\mathrm{T}}^{\mathrm{top}}$ and p_{T} spectra, respectively. The largest $t\bar{t}$ uncertainties on $p_{\mathrm{T}}^{\mathrm{top}}$ and p_{T} are the choice of generator to simulate $t\bar{t}$ production (referred to as "MC generator") and the radiation modeling in $t\bar{t}$ events (referred to as "ISRFSR"), respectively. Each source is represented by a separate nuisance parameter in the fit thus making 9 nuisance parameters in total (discussed in detail in Chapter 9).

7.3.1.3 $t\bar{t} + b\bar{b}$ Modeling

As discussed in Sec. 5.3.1, the $t\bar{t} + b\bar{b}$ component of the background is reweighted to match a NLO prediction of $t\bar{t} + b\bar{b}$ including parton-showering [197], based on Sherpa+OpenLoops [97, 159]. Variations by a factor of two up and down of the default renormalization scale and two different choices for the functional form of the scales involved in the generation are considered:

- **CMMPS**. A global scale μ_{CMMPS} is used as renormalization, factorization and resummation scale, and is defined as: $\mu_{\mathrm{CMMPS}} = \prod_{i=t,\bar{t},b,\bar{b}} E_{T,i}^{1/4}$.
- **R-Mbb**. The functional form of the renormalization scale is taken to be: $\mu_R = (m_t m_{\bar{b}})^{1/2}$. This scale can adapt better to topologies where the $b\bar{b}$ pair originates from a gluon splitting.

The corresponding scale choices for the systematic uncertainties considered are summarized in Table. 7.3

The NLO uncertainties considered include: the three above scale variations, shower recoil model scheme and two alternate PDFs (MSTW and NNPDF). A fraction of the $t\bar{t} + b\bar{b}$ background originates from MPI or FSR off top decay products (such fraction is small in the channels with ≥ 4 b-tags since the extra b jets have low p_{T} and often are

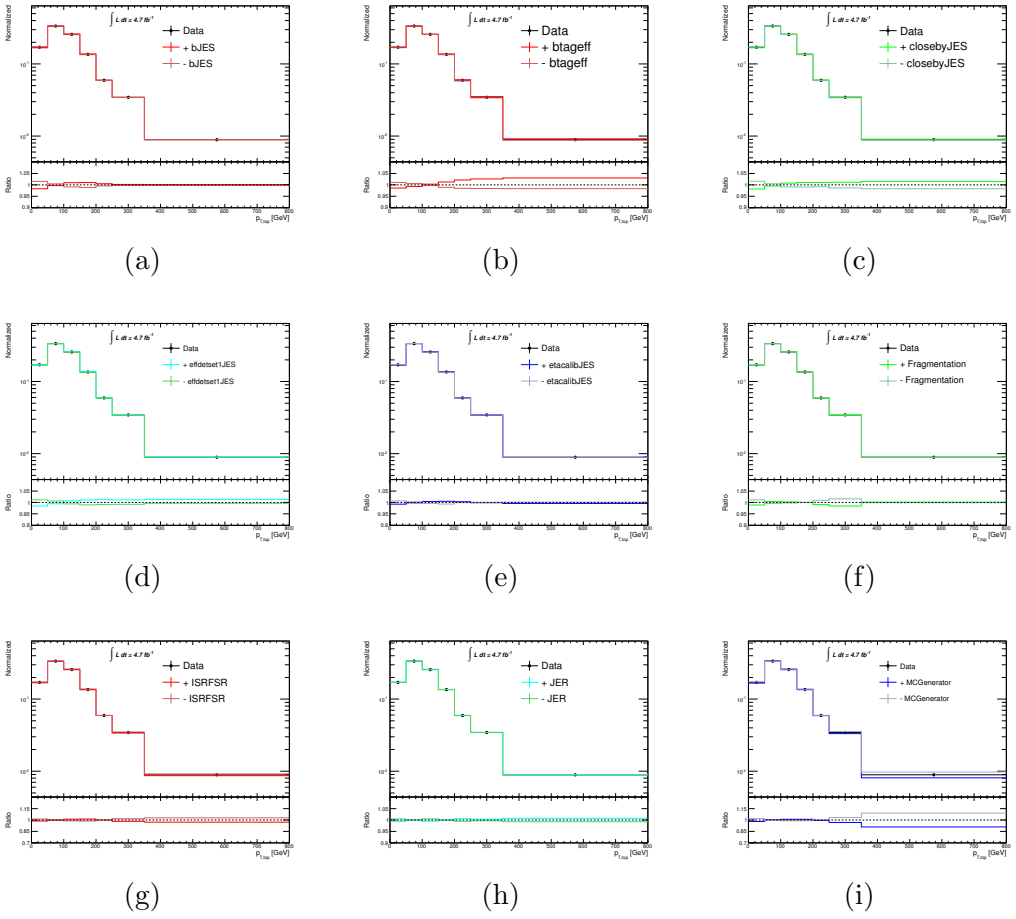

Figure 7.1: The largest individual systematic uncertainties calculated as a percentage of the normalized differential cross-section in each bin of $p_{\mathrm{T}}^{\mathrm{top}}$. Shown are up and down variations of: (a) b-quark Jets (JES), (b) b-tagging Efficiency, (c) Closeby Jets (JES), (d) Effective Detector NP Set1 (JES), (e) η-Intercalibration (JES), (f) Fragmentation, (g) ISRFSR, (h) Jet Energy Resolution and (i) MC Generator are presented. Figures taken from the reference [124].

Scale	default	CMMPS	R-Mbb
μ_R	μ_{CMMPS}	μ_{CMMPS}	$(m_t m_{\bar{b}})^{1/2}$
μ_F	$(E_{T,t} + E_{T,\bar{t}})/2$	μ_{CMMPS}	$H_{T,t}/2$
μ_Q	$(E_{T,t} + E_{T,\bar{t}})/2$	μ_{CMMPS}	$H_{T,t}/2$

Table 7.3: Variation of scales used to estimate shape uncertainties in the modeling of $t\bar{t} + b\bar{b}$ production.

below reconstruction threshold and in any case have low b-tagging efficiency). Such background cannot be calibrated to the NLO prediction and these two categories are kept separate. Additional normalization uncertainties of 25%(50%) and 40%(80%) are applied for MPI and FSR $b(b\bar{b})$ categories, respectively. The NLO corrections and associated systematics are adjusted so that the overall normalization of the $t\bar{t} + b\bar{b}$ background at the particle level is fixed (i.e. effectively only "shape effects" are taken

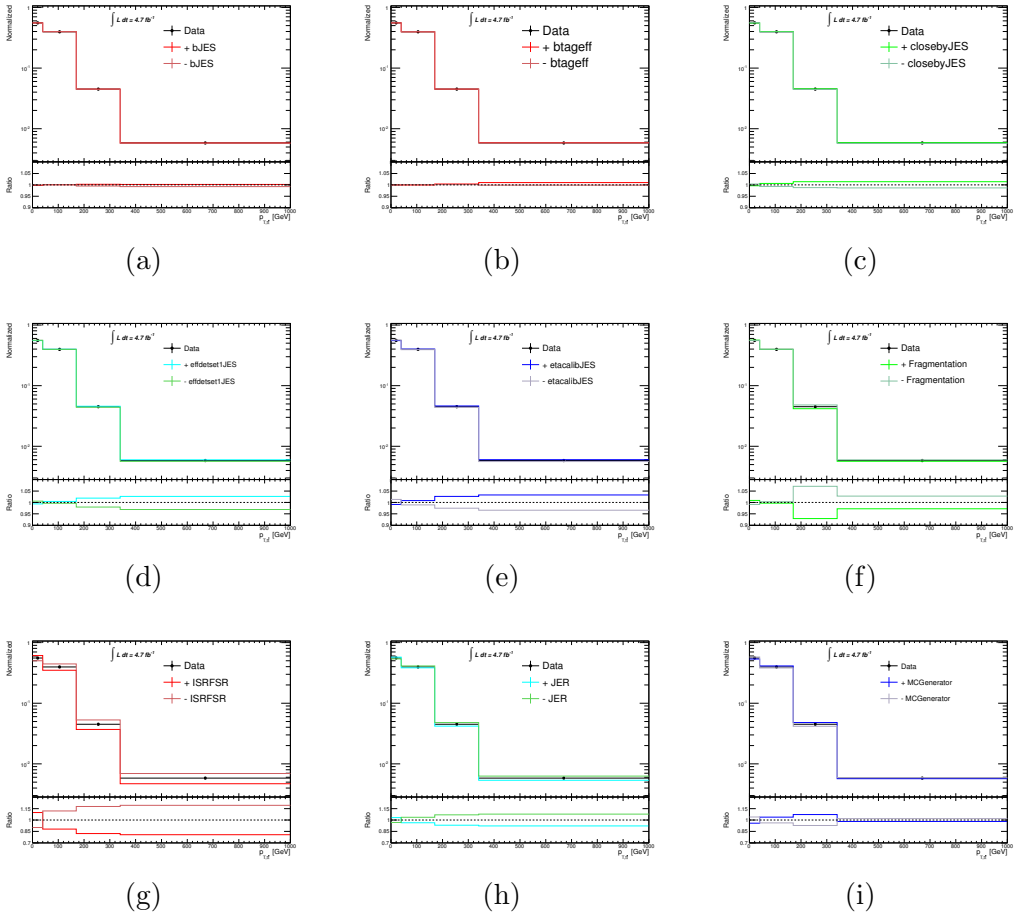

Figure 7.2: The largest individual systematic uncertainties calculated as a percentage of the normalized differential cross-section in each bin of $p_{\mathrm{T}}^{t\bar{t}}$. Shown are up and down variations of: (a) b-quark Jets (JES), (b) b-tagging Efficiency, (c) Closeby Jets (JES), (d) Effective Detector NP Set1 (JES), (e) η-Intercalibration (JES), (f) Fragmentation, (g) ISRFSR, (h) Jet Energy Resolution and (i) MC Generator are presented. Figures taken from the reference [124].

into account). The effect of these systematic uncertainties on the relative contribution of the different categories is shown in Fig. 7.3.

Detailed comparisons of $t\bar{t}$+$b\bar{b}$ between Powheg-Box+Pythia and Sherpa+OpenLoops show that the cross sections agree to better than 50%, which is taken as prior normalization uncertainty for $t\bar{t}+b\bar{b}$. The large available data statistics allows the determination of the normalizations of $t\bar{t}+b\bar{b}$ with better precision, approximately 16% (see Table 7.2) and thus, the final result does not significantly depend on the exact value for the assumed prior uncertainty, as long as it is larger than the precision with which the data can constrain it.

7.3.1.4 $t\bar{t}+c\bar{c}$ Modeling

Several systematic uncertainties are assigned to the modeling of the $t\bar{t}+c\bar{c}$ component of the background, which unfortunately cannot be calibrated to a NLO prediction, as discussed in Sec. 5.3.1.

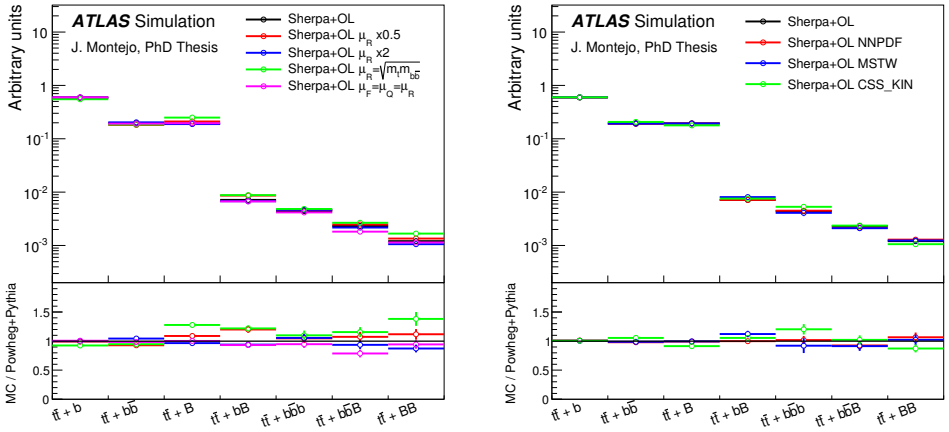

Figure 7.3: Effect of the scale variations, PDF variations and shower recoil scheme on the relative contribution across categories. Figures taken from reference [124].

The measurement of the top and $t\bar{t}$ p_{T} differential cross sections, used to reweight not only $t\bar{t}$+light jets but also the $t\bar{t}+c\bar{c}$ background, is performed for the inclusive $t\bar{t}$ sample. Through the size of the uncertainties applicable to the $t\bar{t}+c\bar{c}$ component is not known, two additional uncertainties are assigned to the $t\bar{t}+c\bar{c}$ events corresponding to the $t\bar{t}$ p_{T} and top quark p_{T} corrections being turned on/off, respectively. Figure 7.4 shows the effect of the envelope of all data-driven reweighting uncertainties on the top quark and $t\bar{t}$ p_{T}. The variation applied to $t\bar{t}+c\bar{c}$ in the analysis corresponds to the red histogram. The effect of the full size $t\bar{t}$ p_{T} variation changes significantly the jet multiplicity distribution for $t\bar{t}+c\bar{c}$.

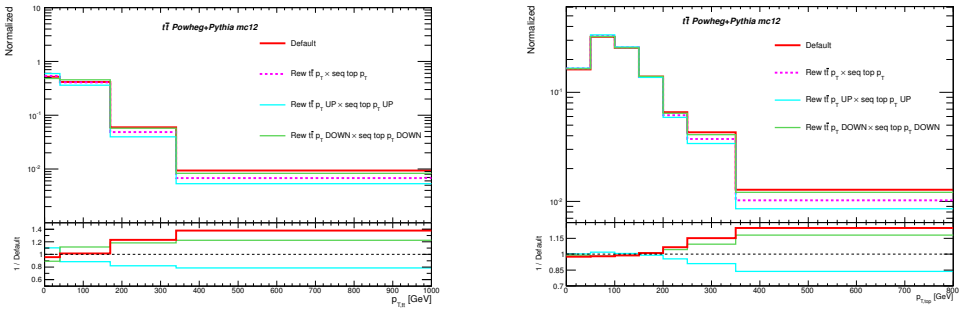

(a) (b)

Figure 7.4: The effect of the envelope of the data-driven uncertainties on (a) top and (b) $t\bar{t}$ p_{T} distributions. Figures taken from reference [124].

The systematic uncertainty on $t\bar{t}+c\bar{c}$ due to the choice of the LO generator is evaluated by comparing the POWHEG-BOX+PYTHIA and MADGRAPH+PYTHIA simulations. Three additional systematic uncertainties come from the factorization and renormalization scale variations, matching threshold and c-quark mass variations in the MADGRAPH+PYTHIA $t\bar{t}+c\bar{c}$ simulation. These uncertainties have a very small impact on the fit result. These MADGRAPH-related systematic uncertainties are ad-

justed so that the overall normalization of the $t\bar{t} + c\bar{c}$ background at the particle level is fixed (i.e. effectively only "shape effects" are taken into account). The effect of the various systematic uncertainties on the $t\bar{t} + c\bar{c}$ subcategories can be seen in Fig. 7.5.

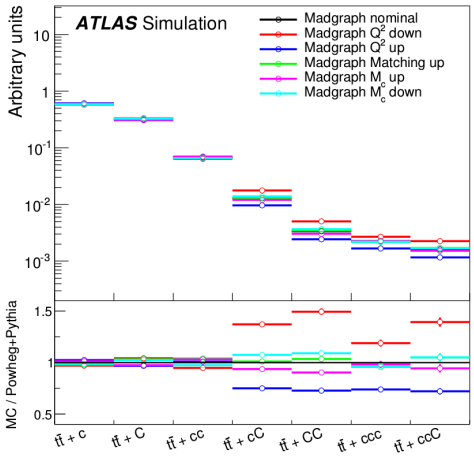

Figure 7.5: Effect of the systematic variations on MADGRAPH+PYTHIA on the $t\bar{t} + c\bar{c}$ subcategories. Figure taken from reference [124].

Finally, an overall normalization uncertainty of 50% is also assigned to the $t\bar{t} + c\bar{c}$ component, taken as uncorrelated with the same normalization uncertainty applied to $t\bar{t} + c\bar{c}$. In this case, the post-fit uncertainty on the $t\bar{t} + c\bar{c}$ normalization uncertainty is approximately 32% (see Table 7.2).

7.3.1.5 Parton Shower/Hadronization

An uncertainty due to the choice of the parton shower and hadronization model is derived by comparing events produced by POWHEG-BOX interfaced with PYTHIA or HERWIG. Both samples are processed through the AF2 ATLAS simulation. Effects on the shapes are compared, symmetrized and applied to the shapes predicted by the default model after correcting both samples to match top quark p_{T} and $t\bar{t}$ p_{T} distributions in data. Fig. 7.6 shows a comparison of the fractions of different components of $t\bar{t} + b\bar{b}$ background and the shapes of top quark p_{T} distributions between MADGRAPH+PYTHIA default and with scale variations and POWHEG-BOX+PYTHIA and POWHEG+HERWIG.

The matching to the parton shower has been observed to lead also to different predictions in the parton-level kinematics. Therefore the further reweighing is applied to the POWHEG+HERWIG sample to avoid the convolution of fragmentation and modeling uncertainties. In the case of $t\bar{t}$+light jets and $t\bar{t} + c\bar{c}$ the reweighting is performed to the differential cross section measurement, while in the case of $t\bar{t} + b\bar{b}$ the POWHEG+HERWIG sample is reweighted to the SHERPA+OPENLOOPS prediction. Since all three subcomponents of $t\bar{t}$ sample are reweighted differently, the parton shower systematic is splitted into three components which are treated as uncorrelated across flavors. These uncertainties have a significant impact on the fitted signal strength and they are constrained significantly by the fit as clearly POWHEG-BOX+PYTHIA describes data better than POWHEG+HERWIG.

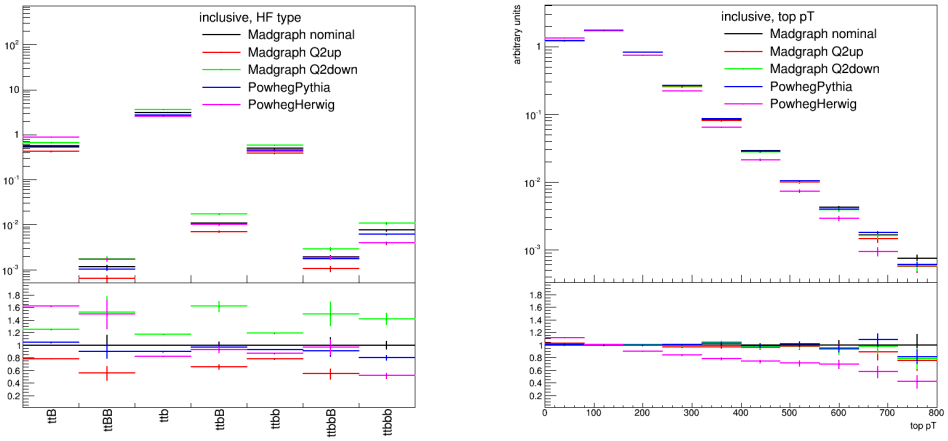

(a) (b)

Figure 7.6: Comparison of (a) the subcomponents (in *pb*) of the different components of $t\bar{t}+b\bar{b}$ background and (b) the shape of top quark p_{T} distribution between MADGRAPH+PYTHIA default and with scale variations and POWHEG-BOX+PYTHIA and POWHEG+HERWIG.

7.3.2 *W*/*Z*+jets Modeling

In the case of W+jets, which is calibrated to data in the ≥ 4 jets channel using the expected W charge asymmetry (see Sec. 3), the systematic uncertainty assigned for events with ≥ 4 jets is 7% (this is the fractional uncertainty on the correction applied to $Wb\bar{b} + Wc\bar{c}$ events, 1.50 ± 0.11, which dominate in the ≥ 2 b-tags channels). An additional 24% uncertainty is added in quadrature for each additional inclusive jet multiplicity bin: 24% uncertainty for events with ≥ 5 jets, and 24% uncertainty for events with ≥ 6 jets. This additional 24% uncertainty originates on a comparison among different algorithms for merging LO matrix-elements and parton showers [198].

As discussed in Sec. 3, the Z+jets background is calibrated to data in events with $Z+ \geq 2$ jets. A 5% uncertainty is assigned to such calibration, and an additional 24% uncertainty is added in quadrature for each additional inclusive jet multiplicity (following the same procedure as in W+jets). Therefore, a total normalization uncertainty of $5\% \oplus 24\% \oplus 24\% = 34\%$ is assigned for events with ≥ 4 jets, an additional 24% uncertainty for events with ≥ 5 jets, and an additional 24% uncertainty for events with ≥ 6 jets.

These normalization uncertainties are in general believed to be conservative given the fairly good agreement found at higher jet multiplicities in the sample with exactly 0 b-tagged jets, which is enriched in W+jets.Finally, the full size of the W and Z p_{T} correction, after symmetrization, is taken as systematic uncertainty. All above uncertainties are taken as uncorrelated between W+jets and Z+jets.

7.3.3 Other Physics Backgrounds

Uncertainties affecting the modeling of the single top quark background include a +5%/-4% uncertainty on the total cross section estimated as a weighted average of the theoretical uncertainties on t-, Wt- and s-channel production [166–168]. Similar to the case of W/Z+jets, an additional 24% normalization uncertainty is added in quadra-

ture for each additional inclusive jet multiplicity bin. Therefore, a total normalization uncertainty of $4.5\% \oplus 24\% = 24.4\%$ is assigned for events with ≥ 4 jets, an additional 24% uncertainty for events with ≥ 5 jets, and an additional 24% uncertainty for events with ≥ 6 jets. An additional systematic uncertainty on Wt-channel production concerning the separation between $t\bar{t}$ and Wt at NLO [199] is assigned. This uncertainty is estimated by comparing the nominal sample, which uses the so-called "diagram subtraction" scheme, with an alternative sample using the "diagram removal" scheme.

Uncertainties on the diboson background normalization include 5% from the NLO theoretical cross sections [169]. Similar to the case of W/Z+jets, an additional 24% normalization uncertainty is added in quadrature for each additional inclusive jet multiplicity bin. Therefore, a total normalization uncertainty of $5\% \oplus 24\% \oplus 24\% = 34\%$ is assigned for events with ≥ 4 jets, an additional 24% uncertainty for events with ≥ 5 jets, and an additional 24% uncertainty for events with ≥ 6 jets.

Uncertainties on the $t\bar{t}V$ and $t\bar{t}H$ normalizations are 15% and +9%/-12%, respectively, from the uncertainties on their respective NLO theoretical cross sections [171, 183, 200]. In addition, dedicated NLO POWHEL samples are used to evaluate the impact of the choice of factorization and renormalization scale on $t\bar{t}H$ signal kinematics. In these samples the default scale is varied by a factor of two up and down. The effect of the variations on $t\bar{t}H$ distributions was studied at the truth level and the nominal POWHEL $t\bar{t}H$ sample was reweighted to reproduce these variations. In a similar way as above, the nominal $t\bar{t}H$ sample is reweighted to reproduce the effect of changing functional form of the scale from the default static to a dynamic one.

7.3.4 Multijet Background

Systematic uncertainties on the multijet background estimate via the MM receive contributions from the limited data statistics, particularly at high jet and b-tag multiplicities, as well as from the uncertainty on the fake rates, estimated in different control regions. A combined conservative uncertainty of 50% due to all these effects is assigned, which is taken as correlated across jet and b-tag multiplicity bins, but uncorrelated between electron and muon channels. No shape uncertainty is assigned but due to a very limited statistics in high jet and b-tag multiplicity bins there is a large uncertainty coming from the limited template statistics which has a significant effect on the template shape.

7.4 Signal Modeling

Several normalization and shape uncertainties are taken into account for the FCNC signal. The uncertainty on total uncertainty on the $t\bar{t}$ cross section (see Sec. 7.3.1.1) is taken fully correlated with the $t\bar{t} \to WbWb$ background. Uncertainties on the $H \to b\bar{b}$ branching ratio are taken into account following the recommendation of the LHC Higgs Cross Section Working Group [183]: $\pm 1.1\%$ ($\Delta\alpha_S$), $\pm 1.4\%$ (Δm_b) and $\pm 0.8\%$ (theory).

The same sequential reweighting on $t\bar{t}$ p_{T} and top quark p_{T} as applied to the $t\bar{t} \to WbWb$ background is also applied to the FCNC signal, after some additional reweighting to improve the agreement between PROTOS+PYTHIA and the original POWHEG+PYTHIA. As a result, the same nine uncertainties related to the sequential reweighting (see Sec. 7.3.1) are applied to the FCNC signal and fully correlated with those for the $t\bar{t} \to WbWb$ background. Slight imperfections in the reweighting

applied to match PROTOS+PYTHIA and the original POWHEG+PYTHIA are taken as additional normalization uncertainties affecting the signal acceptance in each of the jet multiplicity bins: 6.6% for 4 jets, 11.4% for 5 jets and 7.6% for $\geq$6 jets (independent on the b-tag multiplicity).

Finally, an uncertainty associated to parton shower and hadronization model is estimated by comparing the $t\bar{t} \rightarrow WbWb$ yields between POWHEG+PYTHIA and POWHEG+HERWIG in the 2 b-tags channel, which is enriched in the $t\bar{t}$+light jets, and thus taken to be representative of what would be the signal acceptance uncertainty due to differences in extra jet radiation between both parton shower/hadronization models. The assigned uncertainty is 5.4% for 4 jets, 11.8% for 5 jets and 16.2% for $\geq$6 jets (independent on the b-tag multiplicity) and taken to be fully correlated with the parton shower and hadronization model systematic associated to the $t\bar{t}$+light jets background (see Sec. 7.3.1).

Chapter 8

Statistical Analysis

This chapter describes the statistical interpretation of the results to make statements about the presence or absence of the FCNC signals. In Sec. 8.1 the general methodology is explained. Sec. 8.2 introduces the CL_s method, while Sec. 8.3 describes the likelihood function and profile likelihood ratio. The appropriate approximate distributions are presented in Sec. 8.4.

8.1 Hypothesis Testing

To discover or exclude a new physics model in particle physics a *statistical test* is performed, involving the comparison of two hypotheses are considered:

- **Null Hypothesis, $\mathbf{H_0}$**. The hypothesis that describes the known physical processes. In the case of this analysis it corresponds to the SM decay of the top quark, $t \to Wb$ in 100% of the cases, i.e. $\mathrm{BR}(t \to Wb) = 1$. This is often referred to as the background-only (B) hypothesis.
- **Test Hypothesis, $\mathbf{H_1}$**. The hypothesis that in addition includes a new physical process. For this analysis it corresponds to the presence of $t \to Hq$ $(q = u, c)$ decays in addition to the SM $t \to Wb$ decay , such that $\mathrm{BR}(t \to Wb) + \mathrm{BR}(t \to Hq) = 1$. For this reason, this is often referred to as the signal-plus-background (S+B) hypothesis.

The two hypotheses can be generalized by introducing a signal strength modifier, μ, which acts as a multiplicative factor to the signal yield. In the case of this analysis it's defined as a multiplicative factor to the yield for $t\bar{t} \to WbHq$ signal events that have been normalized to a reference branching ratio $\mathrm{BR}_{\mathrm{ref}}(t \to Hq) = 1\%$. The relationship between μ and the corresponding $\mathrm{BR}(t \to Hq)$ is given by equation:

$$\mu = \frac{\mathrm{BR}(t \to Hq)[1 - \mathrm{BR}(t \to Hq)]}{\mathrm{BR}_{\mathrm{ref}}(t \to Hq)[1 - \mathrm{BR}_{\mathrm{ref}}(t \to Hq)]}. \tag{8.1}$$

For a given μ value, the SM $t\bar{t} \to WbWb$ background contribution is scaled accordingly in order to preserve the inclusive $t\bar{t}$ cross section. The corresponding multiplicative factor would be $[1 - \mathrm{BR}(t \to Hq)]^2$, with $\mathrm{BR}(t \to Hq)$ being a function of μ as can be derived from Eq. 8.1:

$$\mathrm{BR}(t \to Hq) = \frac{1 - \sqrt{1 - 4\mathrm{BR}_{\mathrm{ref}}(t \to Hq)(1 - \mathrm{BR}_{\mathrm{ref}}(t \to Hq))\mu}}{2}. \tag{8.2}$$

Therefore, the background-only hypothesis corresponds to $\mu = 0$, whereas the signal-plus-background hypothesis, assuming $\mathrm{BR}(t \to Hq) = 1\%$, corresponds to $\mu = 1$.

The agreement between the observed data and the background expectation is quantified by the p-value: the probability that the observed data originates from a model with signal strength μ. As a particular case, the p_0-value quantifies the agreement of the data with the background-only hypothesis. The p-value can be converted into the significance Z (see Fig. 8.1a), which represents the number of standard deviations from the mean of a Gaussian distributed variable needed to have an upper-tail probability equal to p_μ:

$$Z = \Phi^{-1}(1 - p_\mu), \tag{8.3}$$

where Φ^{-1} is the quantile (inverse of the cumulative distribution) of the standard Gaussian.

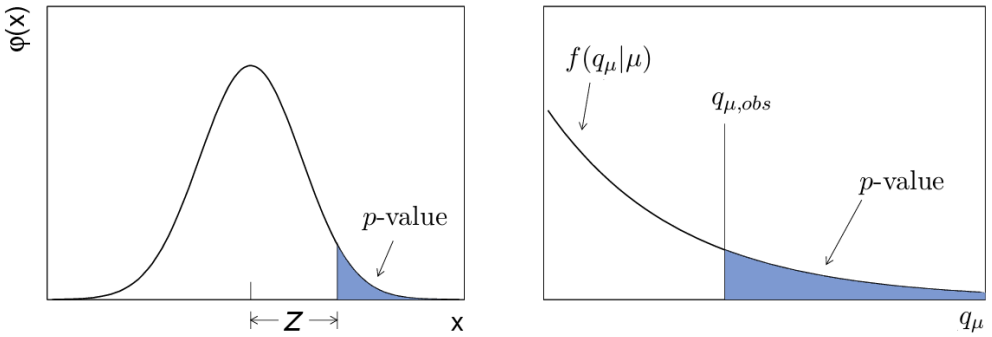

Figure 8.1: (a) The standard normal distribution $\phi(x) = \frac{1}{\sqrt{2}} \exp\left(-\frac{x^2}{2}\right)$ showing the relation between the significance Z and the p-value. (b) Illustration of the determination of the p-value from an observed value of the test statistic q_μ.

If a sufficiently low value of p_μ is found, it can be claimed that the tested hypothesis is false.[1] The threshold to consider a probability low enough as to refute a hypothesis is arbitrary and a prescription has to be chosen. In experimental particle physics, the convention has been adopted that a probability p_μ of less than 5%, equivalent to a significance of $Z = 1.64$, is low enough as to exclude the existence of new physics producing a signal with strength μ times the predicted one. If $\mu = 1$ is excluded then the new physics model can be considered to be falsified. This convention is also referred to as 95% confidence level (CL).

The convention to claim the presence of a new signal is much more stringent.[2] If the background-only hypothesis is rejected with a $p_0 = 1.3 \times 10^{-3}$, equivalent to a significance $Z = 3$, an evidence for new physics is announced. A discovery is claimed for $Z = 5$, corresponding to $p_0 = 2.9 \times 10^{-7}$.

[1] Unless the two hypotheses that are being tested are mutually exclusive, and the union of both covers all the spectrum of possibilities, the rejection of one hypothesis doesn't imply an affirmation of the second one.

[2] Note that with the 5% prescription and assuming Gaussian statistics, one in every twenty experiments would lead to the claim of excluding the SM.

8.2 CL_s Method

The CL_s method is introduced in order to have a protection against the possibility to exclude or discover signals to which an analysis is not sensitive [201]. The CL_s is defined as the ratio of the confidence levels of the signal-plus-background hypothesis, CL_{s+b}, to the background only hypothesis, CL_b:

$$CL_s = \frac{CL_{s+b}}{CL_b}. \tag{8.4}$$

The confidence levels CL_{s+b} and CL_b are the probabilities to obtain a value of the test statistic, q_μ, as low or lower than the observed value, q_μ^{obs}, under the corresponding hypotheses:

$$\begin{aligned} CL_{s+b} =& P_1(q_\mu < q_\mu^{\text{obs}}|H_1) = \int_{q_\mu^{\text{obs}}}^{\infty} f(q_\mu|\mu)dq_\mu = p_\mu, \\ CL_b =& P_0(q_\mu < q_\mu^{\text{obs}}|H_0) = \int_{q_\mu^{\text{obs}}}^{\infty} f(q_\mu|\mu=0)dq_\mu = 1-p_0. \end{aligned} \tag{8.5}$$

A signal is considered excluded at a certain confidence level CL when $1 - CL_s < CL$. If $CL_s < 0.05$, the signal-plus-background hypothesis with a signal strength μ is excluded at 95% CL.

A small CL_{s+b} is an indication of a bad compatibility of the data with the signal-plus-background hypothesis, which would then favor the background-only hypothesis, while a CL_b close to 1 means a poor compatibility with the background hypothesis. In particular, the limits obtained with the CL_s method are conservative, but allow to treat correctly situations with very low background rates where it is not always possible to disentangle clearly the background-only from the signal-plus-background hypotheses.

8.3 Likelihood Function and Profile Likelihood Ratio

The statistical test generally chosen by the ATLAS collaboration is the *profile likelihood ratio* [202], which allows to incorporate the uncertainties in the limit calculation.

First, the likelihood function, $L(\mu, \theta)$, is constructed as a product of Poisson probability terms over all bins, N_{bins}, and over all regions considered in the search:

$$L(\mu,\theta) = \prod_{i=1}^{N_{bins}} \frac{(\mu s_i + b_i)^{n_i}}{n_i!} e^{-(\mu s_i + b_i)} \prod_{j=1}^{N_{NP}} \rho(\theta_j), \tag{8.6}$$

where μ is the strength of the signal process, s_i and b_i indicates the number of expected signal and background events, respectively, in the i-th bin, and are functions of θ. θ is a vector of parameters, the *nuisance parameters* (NP), that encodes the effect of systematic uncertainties.

Each NP is characterized by a pdf, $\rho(\theta)$, encoding the information about its best estimate and width, which is related to the size of the uncertainty. The pdfs for each systematic uncertainty are determined beforehand by auxiliary measurements. Depending on the NP, different functional forms for the pdf are used in this analysis:

- A Gaussian pdf is the common assumption for most systematic uncertainties. Systematic uncertainties that change the shape of the final discriminant are assumed to have a Gaussian prior:

$$\rho(\theta) = \frac{1}{\sqrt{2\pi}\sigma} \exp\left(-\frac{(\theta - \hat{\theta})^2}{2\sigma^2}\right). \tag{8.7}$$

  where $\hat{\theta}$ is the measured value and σ is the calculated uncertainty.

- A log-normal pdf is used for normalization uncertainties, given its property that the effect on the estimation is bounded to positive values:

$$\rho(\theta) = \frac{1}{\sqrt{2\pi}\ln(\sigma)} \exp\left(-\frac{(\ln(\theta/\hat{\theta}))^2}{2(\ln(\sigma))^2}\right)\frac{1}{\theta}, \tag{8.8}$$

  where parameter σ characterizes the width of the log-normal distribution.

- A Gamma pdf is used to describe statistical uncertainties associated with the number of selected MC events. The event rate n in a certain region is related to the number of events N in MC using the relation $n = \alpha \cdot N$. The gamma distribution, as a function of these variables, is expressed as follow:

$$\rho(n) = \frac{1}{\alpha}\frac{(n/\alpha)^N}{N!}e^{(-n/\alpha)}. \tag{8.9}$$

A powerful property of the likelihood function is that independent regions can be easily combined by just multiplying the Poissonian terms of the new regions considered with the original one-channel likelihood. This is important since, by combining different analysis channels, the statistical power and sensitivity of the analysis can be significantly improved.

The profile likelihood ratio, depending on the signal strength μ, can now be written as:

$$\lambda(\mu) = \frac{L(\mu, \hat{\hat{\theta}})}{L(\hat{\mu}, \hat{\theta})}. \tag{8.10}$$

where $\hat{\mu}$ and $\hat{\theta}$ are the values of μ and θ that maximize the likelihood, while $\hat{\hat{\theta}}$ in the numerator denotes the value of θ that maximizes L for the chosen μ. The maximization of the likelihood over θ leads to adjustment in the NPs in order to improve the agreement of the expectation with data.

In order to simplify the analysis, all NP are redefined in order to be centered at zero and with a width of one. In the case of a Gaussian NP this is equivalent to:

$$\theta' = \frac{\theta - \hat{\theta}}{\sigma}. \tag{8.11}$$

In this way, a fitted value close to 0 and a fitted error close to 1 indicates that the data does not have enough statistical power to induce a pull in the nuisance parameter and reduce the original uncertainty. Fitted values away from 0 indicate that the modified MC is in better agreement with the observed data. Reduced errors indicate

that the assigned prior is too large, and the observed data allows reducing the allowed range for the systematic variation.

As can be appreciated, $0 \leq \lambda \leq 1$, where λ near 1 implying a good agreement between the data and the hypothesized value of μ. The test statistic used is defined as:

$$q_\mu = -2 \ln \lambda(\mu). \tag{8.12}$$

An important special case of the statistic q_μ is q_0, which is obtained by setting $\mu = 0$ in the profile likelihood ratio:

$$q_0 = -2 \ln \frac{L(0, \hat{\hat{\theta}}_0)}{L(\hat{\mu}, \hat{\theta})}. \tag{8.13}$$

Rejecting the $\mu = 0$ hypothesis effectively leads to the discovery of a new signal. Therefore, q_0 is used to measure the compatibility of the observed data with the background-only hypothesis.

Given the values q_μ for the test statistics, the p-values can be obtained by integrating the q_μ probability density function between the observed q_μ value and infinity:

$$p_\mu = \int_{q_\mu^{\text{obs}}}^{\infty} f(q_\mu|\mu) dq_\mu. \tag{8.14}$$

In the absence of any significant excess above the background expectation, Eq. 8.14 is used to set upper limits on μ, and thus on $\text{BR}(t \to Hq)$ via Eq. 8.2. The relation between the p-value and the observed q_μ is illustrated in Fig. 8.1b.

Usually, the pdf $f(q_\mu|\mu')$ with $\mu \neq \mu'$ is also needed in order to test the compatibility of an hypothesis μ when the data is originated from a model with μ'. This "off-diagonal" hypothesis testing is useful to characterize the expected performance of an analysis. The median significance for a discovery is computed using $f(q_0|1)$, whereas the expected 95% CL in the absence of a signal is computed from $f(q_1|0)$.

8.4 Approximation for the Profile Likelihood Ratio

As can be appreciated from Eq. 8.14, the computation of a p-value requires the full distribution of the test statistic. The estimation of $f(q_\mu|\mu)$ with MC methods is very computationally expensive (for example, for $p_0 \sim 10^{-7}$ about 10^8 pseudo-experiments have to be simulated). In the limit of large statistics or "asymptotic limit", an approximation can be employed to estimate $f(q_\mu|\mu)$.

Let us assume, that the statistical test is given with a signal strength parameter μ, while data are distributed according to a strength parameter μ'. Then, the desired distribution $f(q_\mu|\mu')$ can be obtained using Wald's approximation of a single parameter of interest [203]:

$$q_\mu = \frac{(\mu - \hat{\mu})^2}{\sigma^2} + \mathcal{O}\left(\frac{1}{\sqrt{N}}\right), \tag{8.15}$$

where $\hat{\mu}$ follows a Gaussian distribution with a mean μ' and standard deviation σ, and N represents the data sample size.

The standard deviation σ is obtained from the covariance matrix of the estimators for all the parameters, $V_{ij} = cov[\hat{\theta}_i, \hat{\theta}_j]$, where θ_i represents both μ as well as the

nuisance parameters (e.g. take $\theta_0 = \mu$, and $\sigma^2 = V_{00}$). To estimate these values, the "Asimov" data set, which is defined as the sum of the MC prediction of the signal and total background [202], is used.

Assuming that μ' is also Gaussian distributed, one can neglect the term $\mathcal{O}\left(\frac{1}{\sqrt{N}}\right)$, and show that the statistic q_μ follows a *non-central chi-square distribution* for one degree of freedom:

$$f(q_\mu|\mu') = \frac{1}{2\sqrt{q_\mu}}\frac{1}{2\sqrt{\pi}}\left[\exp\left(-\frac{1}{2}(\sqrt{q_\mu}+\sqrt{\Lambda})^2\right) + \exp\left(-\frac{1}{2}(\sqrt{q_\mu}-\sqrt{\Lambda})^2\right)\right], \quad (8.16)$$

where the non-centrality parameter Λ is given by:

$$\Lambda = \frac{(\mu-\mu')^2}{\sigma^2}. \quad (8.17)$$

This asymptotic approximation is used to compute the relevant p-values in this dissertation.

The statistical framework used to extract the final results of the analyses is the HistFitter package [204], which uses the HistFactory [205] and RooStats [206] softwares based on RooFit [207] and ROOT [208, 209]. This framework allows to build models that contain the description of complex analyses in terms of control and signal regions, where the uncertainties on the background and signal samples, as well as their correlations, are treated coherently.

Chapter 9

Results

This chapter presents the results obtained from the search for $t\bar{t} \to WbHq$, $H \to b\bar{b}$, which is the main subject of this dissertation. It also summarizes the results from the ATLAS searches exploiting other Higgs boson decay modes, $H \to \gamma\gamma$ and $H \to WW^*, \tau\tau$, as well as the combination of all ATLAS searches. These results are compared with the corresponding results from the CMS collaboration.

9.1 Search for $t\bar{t} \to WbHq$, $H \to b\bar{b}$

Following the statistical analysis discussed in Chapter 8, a binned likelihood fit under the signal-plus-background hypothesis is performed on the distributions of the final discriminant in the nine analysis channels considered. Figures 9.1–9.3 show a comparison of the data and prediction of the final discriminant in each of the analysis channels, for both pre- and post-fit to data, in the case of the $t\bar{t} \to WbHc$ search. As can be appreciated, the total background uncertainty is significantly reduced after the fit in both signal-rich and background-dominated channels, resulting in an increase in the search sensitivity. The corresponding post-fit yields for $t\bar{t} \to WbHc$ search are shown in Table 9.1. The corresponding figures and table for the $t\bar{t} \to WbHc$ search can be found in App. D.

The fitted nuisance parameters for the $t\bar{t} \to WbHc$ and $t\bar{t} \to WbHu$ searches are shown in Fig. 9.4. The corresponding correlation matrices among nuisance parameters are presented in Fig. 9.5. A glossary for the nuisance parameters can be found in App. G. The validation of the fitting procedure has been performed on an Asimov dataset including $t\bar{t} \to WbHc$ and $t\bar{t} \to WbHu$ signals and is presented in App. E.

The best-fit branching ratio obtained is $\mathrm{BR}(t \to Hc) = [0.17 \pm 0.12\,(\mathrm{stat.}) \pm 0.17\,(\mathrm{syst.})]\%$, assuming that $\mathrm{BR}(t \to Hu) = 0$. A similar fit is performed for the $t\bar{t} \to WbHu$ search, yielding $\mathrm{BR}(t \to Hu) = [-0.07 \pm 0.17\,(\mathrm{stat.}) \pm 0.28\,(\mathrm{syst.})]\%$, assuming that $\mathrm{BR}(t \to Hc) = 0$. Figure 9.6 shows the evolution of $-2\Delta \ln L = -2 \ln L(\mathrm{BR}) - 2 \ln L(\hat{\mathrm{BR}})$, where $\hat{\mathrm{BR}}$ is the maximum likelihood estimator of the branching ratio, separately as a function of $\mathrm{BR}(t \to Hc)$ and $\mathrm{BR}(t \to Hu)$. The different measured values for the two branching ratios is the result of the different sensitivities of the $t\bar{t} \to WbHc$ and $t\bar{t} \to WbHu$ searches, as discussed in Sec. 6.1.

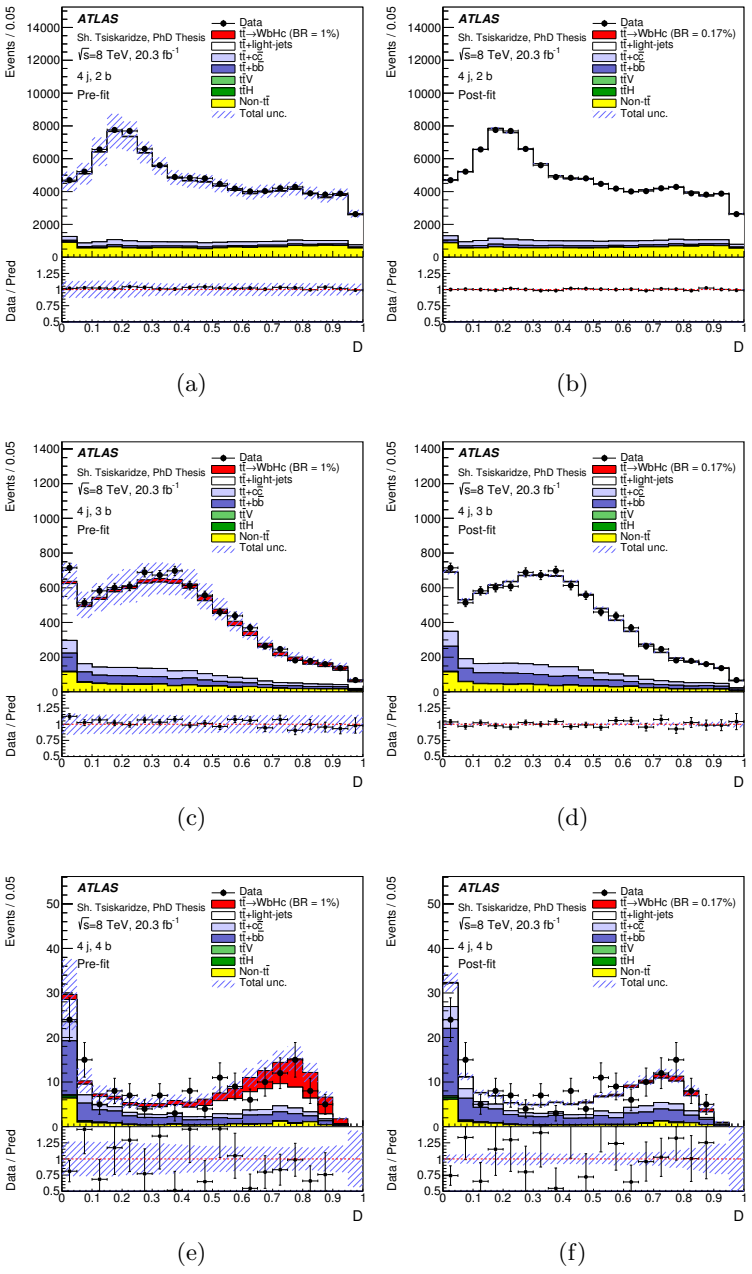

Figure 9.1: $t\bar{t} \to WbHc, H \to b\bar{b}$ search: comparison between the data and prediction for the distribution of the D discriminant used in the (4 j, 2 b) channel (a) before the fit and (b) after the fit, in the (5 j, 2 b) channel (c) before the fit and (d) after the fit, and in the ($\geq$6 j, 2 b) channel (e) before the fit and (f) after the fit. The fit is performed on data under the signal-plus-background hypothesis. In the pre-fit distributions the $t\bar{t} \to WbHc$ signal (solid red) is normalized to BR($t \to Hc$) = 1% and the $t\bar{t} \to WbWb$ background is normalized to the SM prediction, while in the post-fit distributions both signal and $t\bar{t} \to WbWb$ background are normalized using the best-fit BR($t \to Hc$). The small contributions from W/Z+jets, single top, diboson and multijet backgrounds are combined into a single background source referred to as "Non-$t\bar{t}$". The bottom panels display the ratios of data to the total signal-plus-background prediction after the fit ("Pred"). The hashed area represents the total uncertainty on the background.

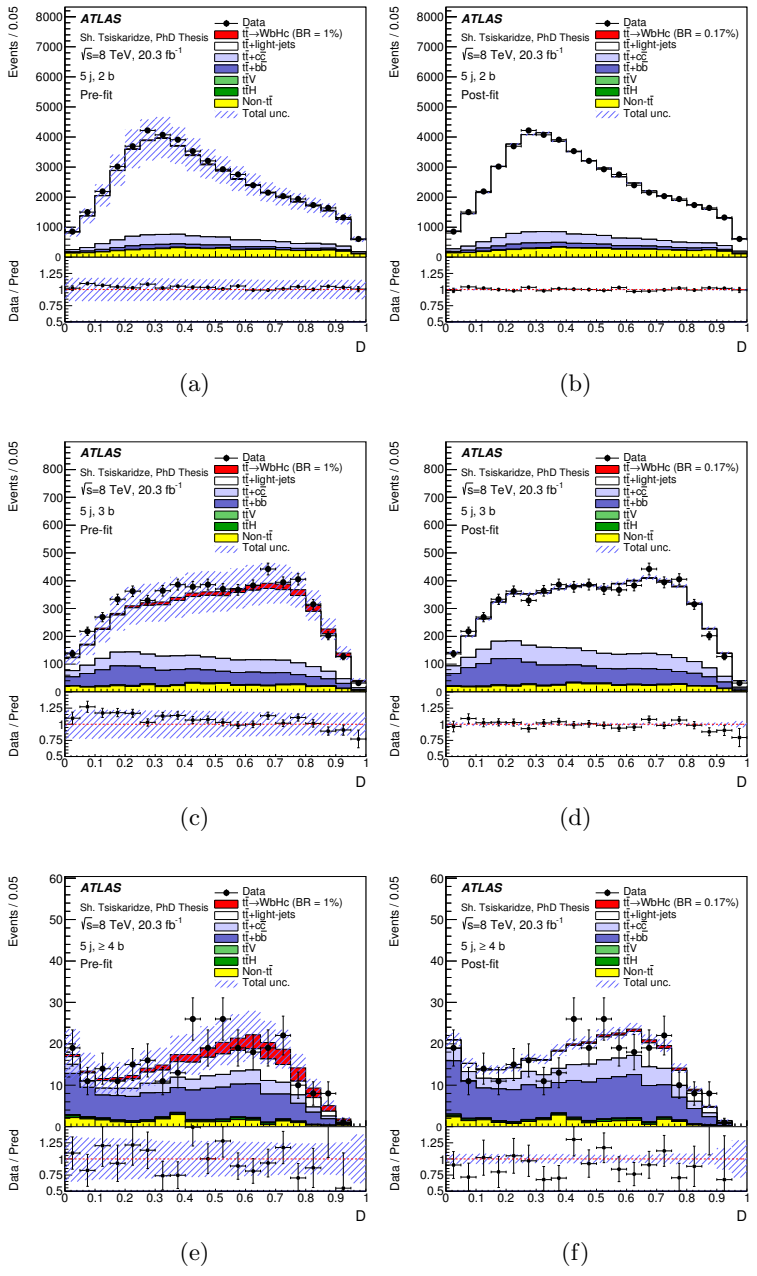

Figure 9.2: $t\bar{t} \to WbHc, H \to b\bar{b}$ search: comparison between the data and prediction for the distribution of the D discriminant used in the (4 j, 3 b) channel (a) before the fit and (b) after the fit, in the (5 j, 3 b) channel (c) before the fit and (d) after the fit, and in the ($\geq$6 j, 3 b) channel (e) before the fit and (f) after the fit. The fit is performed on data under the signal-plus-background hypothesis. In the pre-fit distributions the $t\bar{t} \to WbHc$ signal (solid red) is normalized to BR($t \to Hc$) = 1% and the $t\bar{t} \to WbWb$ background is normalized to the SM prediction, while in the post-fit distributions both signal and $t\bar{t} \to WbWb$ background are normalized using the best-fit BR($t \to Hc$). The small contributions from W/Z+jets, single top, diboson and multijet backgrounds are combined into a single background source referred to as "Non-$t\bar{t}$". The bottom panels display the ratios of data to the total signal-plus-background prediction after the fit ("Pred"). The hashed area represents the total uncertainty on the background.

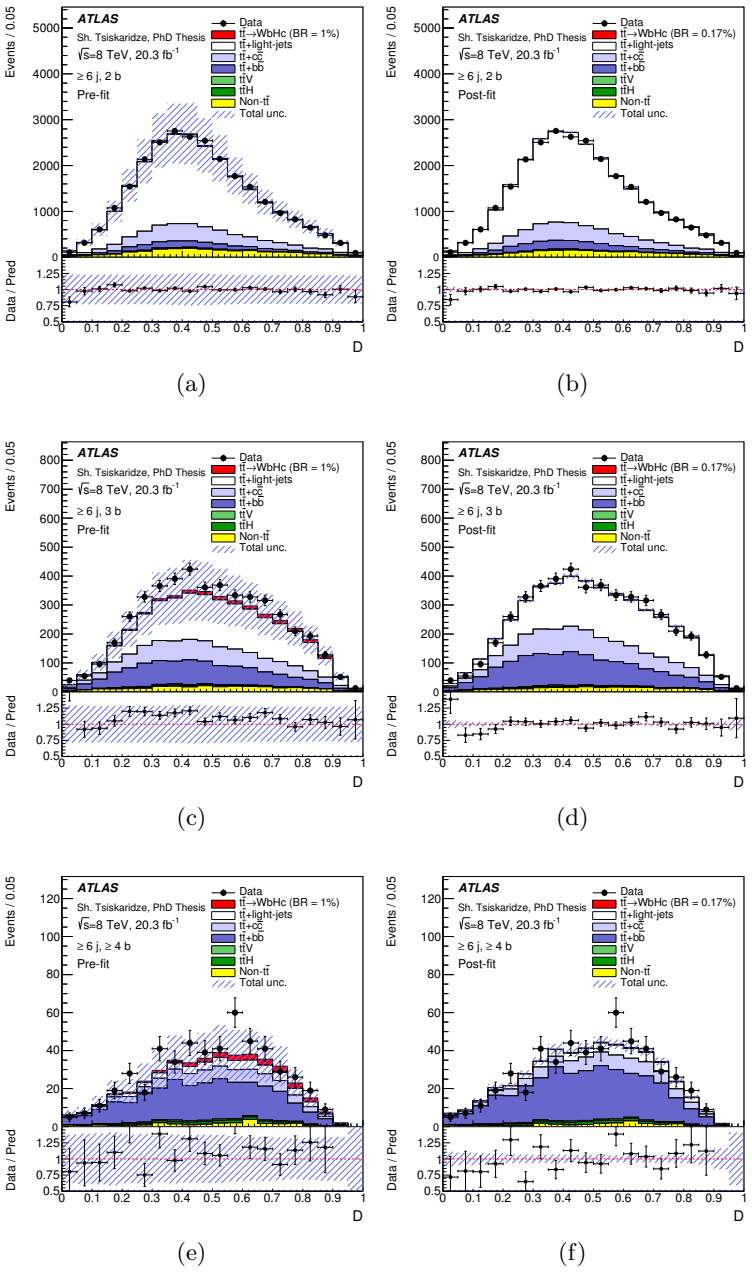

Figure 9.3: $t\bar{t} \to WbHc, H \to b\bar{b}$ search: comparison between the data and prediction for the distribution of the D discriminant used in the (4 j, 4 b) channel (a) before the fit and (b) after the fit, in the (5 j, ≥4 b) channel (c) before the fit and (d) after the fit, and in the (≥6 j, ≥4 b) channel (e) before the fit and (f) after the fit. The fit is performed on data under the signal-plus-background hypothesis. In the pre-fit distributions the $t\bar{t} \to WbHc$ signal (solid red) is normalized to $\mathrm{BR}(t \to Hc) = 1\%$ and the $t\bar{t} \to WbWb$ background is normalized to the SM prediction, while in the post-fit distributions both signal and $t\bar{t} \to WbWb$ background are normalized using the best-fit $\mathrm{BR}(t \to Hc)$. The small contributions from W/Z+jets, single top, diboson and multijet backgrounds are combined into a single background source referred to as "Non-$t\bar{t}$". The bottom panels display the ratios of data to the total signal-plus-background prediction after the fit ("Pred"). The hashed area represents the total uncertainty on the background.

	4 j, 2 b	4 j, 3 b	4 j, 4 b
$t\bar{t} \to WbHc$	155 ± 11	68.5 ± 5.0	7.23 ± 0.56
$t\bar{t}$+light-jets	77300 ± 1700	6240 ± 190	56.1 ± 7.3
$t\bar{t} + c\bar{c}$	5600 ± 1500	810 ± 210	23.4 ± 6.0
$t\bar{t} + b\bar{b}$	2420 ± 360	890 ± 130	54.1 ± 7.5
$t\bar{t}V$	122 ± 19	15.6 ± 2.5	0.90 ± 0.15
$t\bar{t}H$	30.9 ± 3.6	12.8 ± 1.6	1.92 ± 0.26
W+jets	4900 ± 1100	231 ± 55	5.8 ± 1.5
Z+jets	1040 ± 390	48 ± 18	0.78 ± 0.32
Single top	5100 ± 1000	352 ± 71	7.1 ± 1.5
Diboson	209 ± 72	11.6 ± 4.0	0.22 ± 0.08
Multijet	1120 ± 320	75 ± 22	2.41 ± 0.70
Total	98070 ± 370	8756 ± 98	159.9 ± 7.4
Data	98049	8752	161

	5 j, 2 b	5 j, 3 b	5 j, ≥4 b
$t\bar{t} \to WbHc$	85 ± 10	42.4 ± 5.1	6.17 ± 0.77
$t\bar{t}$+light-jets	37600 ± 1200	3570 ± 160	66.4 ± 8.1
$t\bar{t} + c\bar{c}$	4700 ± 1200	970 ± 240	59 ± 16
$t\bar{t} + b\bar{b}$	2140 ± 310	1150 ± 160	144 ± 17
$t\bar{t}V$	145 ± 23	26.6 ± 4.2	3.12 ± 0.50
$t\bar{t}H$	41.0 ± 4.5	22.4 ± 2.6	5.98 ± 0.74
W+jets	1940 ± 560	140 ± 41	6.0 ± 1.8
Z+jets	380 ± 170	27.6 ± 12.4	1.38 ± 0.63
Single top	2090 ± 630	219 ± 66	10.1 ± 3.1
Diboson	93 ± 39	7.8 ± 3.3	0.37 ± 0.16
Multijet	332 ± 96	46 ± 13	6.2 ± 1.9
Total	49570 ± 250	6223 ± 66	308 ± 11
Data	49699	6199	286

	≥6 j, 2 b	≥6 j, 3 b	≥6 j, ≥4 b
$t\bar{t} \to WbHc$	46.1 ± 4.2	25.0 ± 2.3	5.41 ± 0.52
$t\bar{t}$+light-jets	18590 ± 800	2080 ± 140	54.2 ± 8.4
$t\bar{t} + c\bar{c}$	3820 ± 920	980 ± 240	85 ± 20
$t\bar{t} + b\bar{b}$	1860 ± 270	1260 ± 170	320 ± 35
$t\bar{t}V$	178 ± 27	43.7 ± 6.8	8.3 ± 1.3
$t\bar{t}H$	64.0 ± 7.2	39.6 ± 4.5	15.9 ± 1.8
W+jets	680 ± 220	75 ± 24	7.0 ± 2.7
Z+jets	159 ± 78	16.8 ± 8.3	1.48 ± 0.75
Single top	740 ± 270	108 ± 40	10.6 ± 4.0
Diboson	48 ± 23	5.7 ± 2.7	0.51 ± 0.25
Multijet	120 ± 34	13.9 ± 4.0	1.12 ± 0.65
Total	26300 ± 160	4652 ± 62	508 ± 22
Data	26185	4701	516

Table 9.1: $t\bar{t} \to WbHc, H \to b\bar{b}$ search: predicted and observed yields in each of the analysis channels considered. The background prediction is shown after the fit to data under the signal-plus-background hypothesis. The quoted uncertainties are the sum in quadrature of statistical and systematic uncertainties on the yields, computed taking into account correlations among nuisance parameters and among processes.

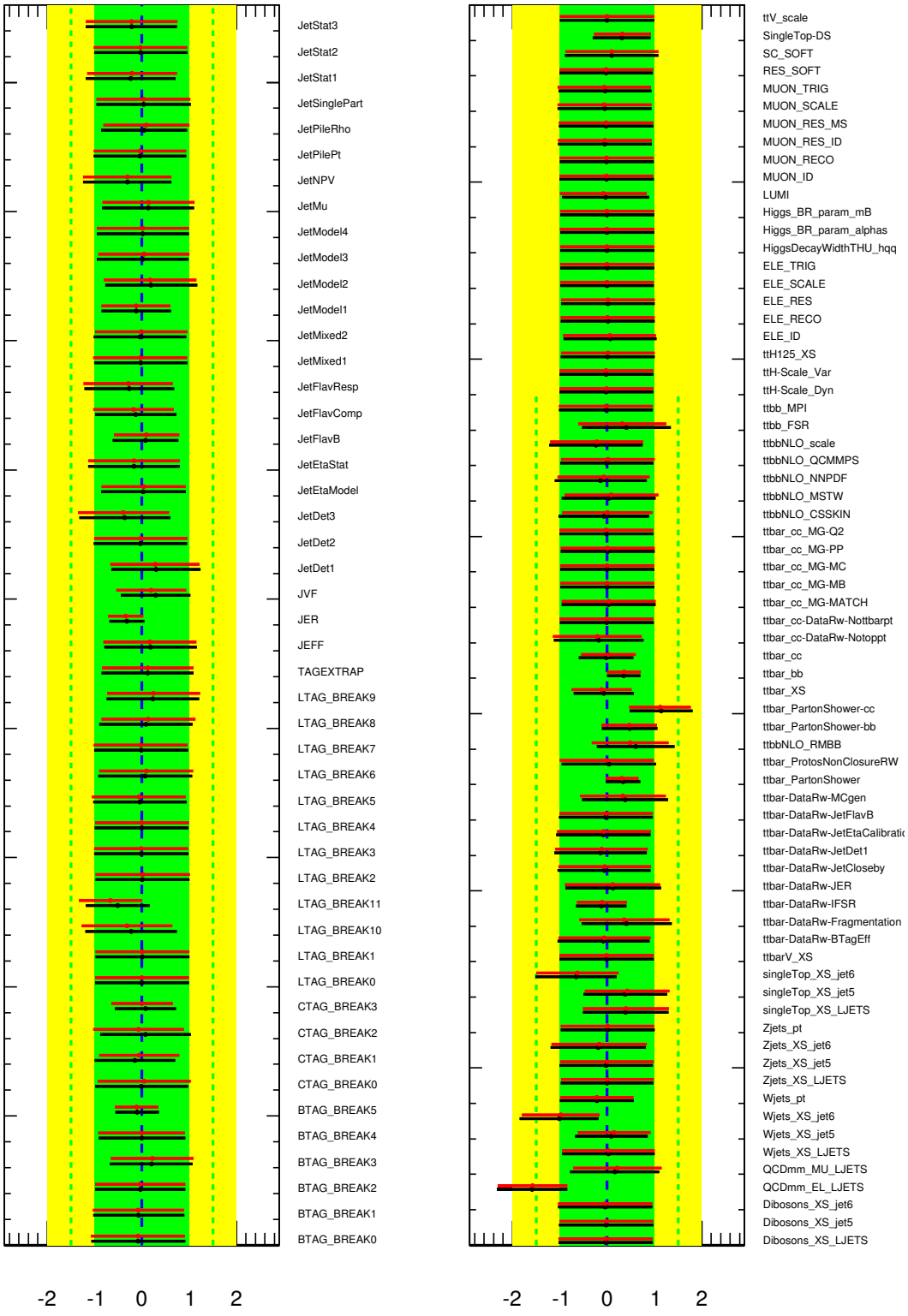

Figure 9.4: Comparison of the fitted nuisance parameters between the fit to the data under the signal+background hypothesis in (red) the $t\bar{t} \to WbHc$ and (black) $t\bar{t} \to WbHu$ analyses. A glossary can be found in App. G.

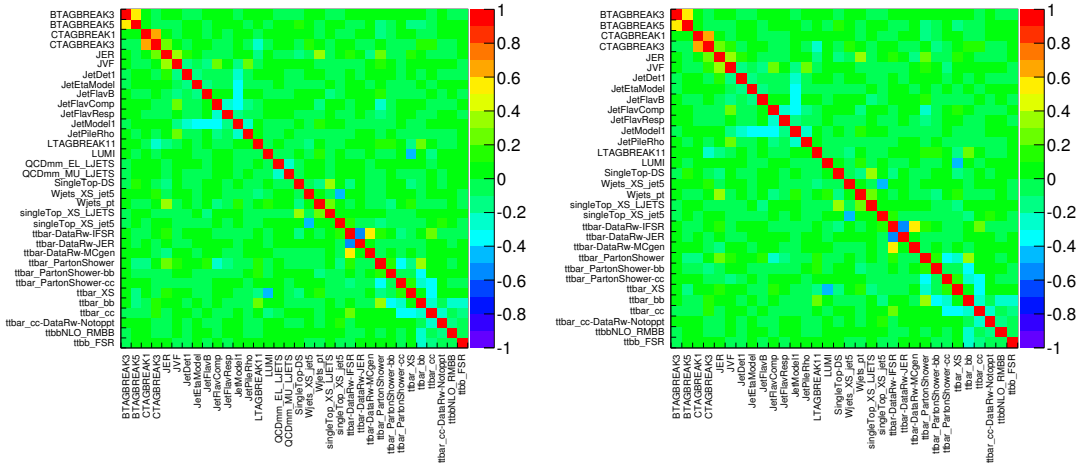

(a) (b)

Figure 9.5: Correlation matrix corresponding to the fit to the data under the signal+background hypothesis in the (a) $t\bar{t} \to WbHc$ and (b) $t\bar{t} \to WbHu$ analyses. Only nuisance parameters with a correlation coefficient of at least 20% with any other parameter are displayed.

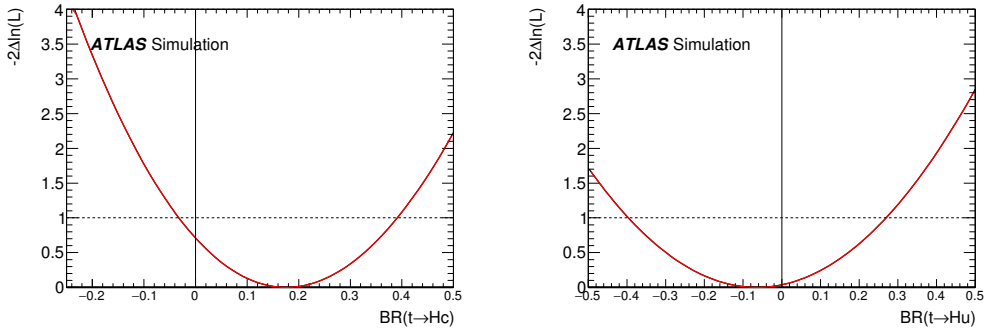

(a) (b)

Figure 9.6: Evolution of $-2\Delta \ln L$ as a function of (a) BR($t \to Hc$) and as a function of (b) BR($t \to Hu$).

9.1.1 Discussion of the Fit

The large number of events in the analysis channels considered, together with their different background compositions, allows the fit to place constraints on the nuisance parameters. Each fitted nuisance parameter value represents the preferred shift with respect to the nominal prediction in units of its prior uncertainty. The fitted error represents the post-fit uncertainty in units of the prior uncertainty. Therefore, a fitted value close to 0 and a fitted error close to 1 indicates that the data did not have enough statistical power to induce a pull in the nuisance parameter and reduce the original uncertainty.

Only few of the nuisance parameters are expected to be pulled and somewhat constrained by the data. For example, an improved background prediction is obtained with significantly reduced uncertainty, not only in the signal-depleted channels, but also in the most sensitive analysis channels for this search, (4 j, 3 b) and (4 j, 4 b). The channels with two b-tags are used to constrain the leading uncertainties affecting the $t\bar{t}$+light-jets background prediction, while the channels with $\geq$5 jets and $\geq$3 b-tags are sensitive to the uncertainties affecting the $t\bar{t}$+HF background prediction. The most relevant pulls and constrains are discussed in the following:

- LTAG_BREAK11: this uncertainty corresponds to the largest eigenvector after diagonalization of the light-tagging uncertainties. This systematic is slightly pulled and significantly overconstrained. The channels with $\geq$4 b-tag jets are particular very sensitive to the light-tagging uncertainty, as shown in Fig. 9.1–D.3(e-f), since this region is dominated by $t\bar{t}$+light-jet events. The high statistics of this region and different shape for $t\bar{t}$+light and $t\bar{t}+$HF for the D discriminant allow the reduction of the uncertainty. The effect of this systematic uncertainty on the $t\bar{t}$+light-jet background in the (5 j, $\geq$4 b) region is shown in Fig. 9.7a.

- CTAG_BREAK3: this uncertainty corresponds to the largest eigenvector after diagonalization of the c-tagging uncertainties. This systematic is not pulled, but somewhat overconstrained. The channels with 2 and 3 b-tagged jets are in particular sensitive to the c-tagging systematic uncertainty via the $t\bar{t}$+light background component, since the channels with 3 b-tagged jets are dominated with $W \to cs$ decays. The effect of this systematic uncertainty on the $t\bar{t}$+light-jet background in the (4 j, 3 b) region is shown in Fig. 9.7b. The high statistics of this region allows the reduction of the uncertainty, which was derived on a sample of $D^{\star+}$ events.

- ttbar_XS: the $t\bar{t}$ cross section uncertainty is $\sim$ 6.2% and is significant for the $t\bar{t} \to WbHu$ search. This systematic is not pulled and is slightly overconstrained (down to $\sim$ 4% normalization uncertainty). The exact mechanism is still unclear, however, it is possibly related to its anticorrelation with the $t\bar{t}+c\bar{c}$ normalization uncertainty. This nuisance parameter cannot be interpreted as a cross section measurement since the $t\bar{t}$+HF normalization nuisance parameters do not have a meaning of fractions and can not therefore modify the total $t\bar{t}$ normalization.

- ttbar_PartonShower: the three nuisance parameters related to the choice of fragmentation model are slightly pulled and significantly overconstrained and, therefore, deserve further attention. The nuisance parameter affecting $t\bar{t}$+light-jets is heavily constrained and fitted at its nominal value. The fitted value indicates that

data supports the prediction of POWHEG-BOX+PYTHIA, while the prediction of POWHEG+HERWIG is in disagreement with data in the high-statistics channels and, since the full difference to POWHEG-BOX+PYTHIA is taken as systematic uncertainty, the fit constrains the allowed variation to a smaller range. The effect on the $t\bar{t}$+light-jets background in the ($\geq$6 j, 2 b) region is shown in Fig. 9.7c. The nuisance parameter related to $t\bar{t}+b\bar{b}$ is in agreement with the nominal prediction, indicating that NLO prediction of SHERPA+OPENLOOPS agrees with data. The effect of the fragmentation uncertainty is again too large and data can constrain this systematic uncertainty to a fraction of its pre-fit value. The pull on $t\bar{t}+c\bar{c}$ is difficult to study since there is no NLO prediction to compare to and both predictions, POWHEG-BOX+PYTHIA or POWHEG+HERWIG could be equally valid. The only possible evidence supporting this pull is that the $t\bar{t}+C$ component in POWHEG+HERWIG is 40% higher than in POWHEG-BOX+PYTHIA, thus the pull towards POWHEG+HERWIG would introduce the same effect as the leading correction on the $t\bar{t}+B$ component, where the NLO prediction is observed to be 40% higher than in POWHEG-BOX+PYTHIA.

- $t\bar{t}+b\bar{b}$ and $t\bar{t}+c\bar{c}$ normalizations: the normalization of the $t\bar{t}+b\bar{b}$ ($t\bar{t}+c\bar{c}$) component is fitted to a value $\sim$ 34% ($\sim$ 18%) higher than its nominal prediction, and the uncertainty is reduced from the very conservative 50% to 16% (32%). Simultaneous analysis of the channels with 2, 3 and $\geq$4 b-tagged jets can resolve the $t\bar{t}+b\bar{b}$ and $t\bar{t}+c\bar{c}$ normalizations. This systematic is mostly measured at high jet multiplicity (the natural topology for $t\bar{t}+b\bar{b}$ and $t\bar{t}+c\bar{c}$ evets). The normalization uncertainty of the $t\bar{t}+b\bar{b}$ background is also reduced, although to a smaller extent since there is no region where it is the dominant background.

- ttbbNLO_RMBB: this uncertainty corresponds to the NLO uncertainty on $t\bar{t}+b\bar{b}$ that cause the migration across $t\bar{t}+b$, $t\bar{t}+B$, $t\bar{t}+b\bar{b}$ categories, and thus introduces shape effects. This systematic is somewhat pulled and slightly overconstrained.

- JER: the JER uncertainty is very large due to very conservative approach to estimate the resolution uncertainty at low jet p_{T}. This uncertainty is slightly pulled and constrained to about half of its pre-fit value. The origin of this constrain is the high-statistics in the channels with 2 b-tagged jets. Since the bulk of the contribution originates from low-p_{T} jets, this uncertainty can be reduced by the fit to data. The effect of this uncertainty is shown in Fig. 9.7d for the $t\bar{t}$+light-jets background in the (4 j, 2 b) region.

- BTAG_BREAK5: this uncertainty corresponds to the largest eigenvector after diagonalization of the b-tagging uncertainties. This systematic is not pulled and is slightly overconstrained. The origin of this constrain is the shape effect in the high-statistics in the channels with 2 b-tagged jets. It introduces a $\sim$ 2% variation per b-tagged jet that is amplified to $\sim$ 8% in the 4 b-tag regions. The simultaneous fit of different b-tag multiplicities allows reducing this uncertainty. The effect of this uncertainty is shown in Fig. 9.7e for the $t\bar{t}$+light-jets background in the (4 j, 2 b) region.

- ttbar-DataRw-IFSR: this uncertainty corresponds to the largest uncertainty out of nine components of the $t\bar{t}$ reweighting. It is associated to initial- and final-state radiation in the differential cross section measurement. The variation of

this uncertainty has the largest effect on the $p_{\mathrm{T}}^{t\bar{t}}$ spectrum, which propagates to the reconstructed jet multiplicity. This variation is not supported by the data and can be constrained. This constraint is in fact expected since the differential cross section measurement is performed with the 7 TeV, which has a factor of four less statistics than the data-set used for this analysis. The effect of this uncertainty is shown in Fig. 9.7f for the $t\bar{t}$+light-jets background in the (4 j, 2 b) region.

Other systematic uncertainties are not discussed since their pulls and constrains are less significant or they do not affect appreciably the sensitivity of the analysis.

A summary of the leading 15 systematic uncertainties affecting the $t\bar{t} \to WbHc$ and $t\bar{t} \to WbHu$ searches are provided in Fig. 9.8. This summary quantifies the impact on the signal strength μ, both before and after the fit, displaying the constraints provided by the data on the associated nuisance parameters. The pre-fit impact on μ is estimated by fixing the corresponding nuisance parameter at $\theta_0 \pm \Delta\theta$, where θ_0 is the nominal value of the nuisance parameter and $\Delta\theta$ is its pre-fit uncertainty, and performing the fit again. The difference between the default and modified μ, $\Delta\mu$, represents the effect of the systematic uncertainty in question on μ. The same procedure is followed to estimate the post-fit impact on μ, but the corresponding nuisance parameter is instead fixed at $\hat{\theta} \pm \sigma_\theta$, where $\hat{\theta}$ is the fitted value of the nuisance parameter and σ_θ is its post-fit uncertainty. For reference, $\Delta\mu = 0.05$ corresponds to $\Delta\mathrm{BR}(t \to Hc) \simeq 0.05\%$.

As expected, the leading systematic uncertainties for the $t\bar{t} \to WbHc$ search are those associated with the main backgrounds in the (4 j, $\geq$4 b) channel. The systematic uncertainties with the largest impact on μ are the leading uncertainty for light-jet tagging and the uncertainty on the $t\bar{t}$ background associated with the choice of parton shower and hadronization models. The significant impact from light-jet tagging results from the large fraction of $t\bar{t}$+light-jets background present in the (4 j, 4 b) channel, which peaks at high values of the final discriminant, like the signal, and thus cannot be strongly constrained by the fit. Because of this, this uncertainty remains the leading one after the fit. In contrast, the uncertainty related to $t\bar{t}$ modeling is significantly constrained by the fit since it has a large impact ($\sim$5–16%) on the $t\bar{t}$+light-jets background normalization in the highly populated channels with two b-tags. As a result, this uncertainty is ranked only fourth in importance after the fit, becoming comparable to uncertainties such as the choice of renormalization scale for $t\bar{t} + b\bar{b}$, the leading uncertainty for c-jet tagging and the $t\bar{t} + c\bar{c}$ normalization. Of these, the nuisance parameter associated with the choice of the renormalization scale for $t\bar{t} + b\bar{b}$ is slightly pulled (by half of the prior uncertainty) to improve agreement with the data in the (4 j, 4 b) and (5 j, 4 b) channels. In these channels, this uncertainty causes variations of up to $\sim$5% in the bin contents in some regions of the final discriminant, i.e. distorting its shape compared to that of the nominal prediction, but the sensitivity is not sufficient to constrain it significantly. The leading uncertainty from c-tagging causes small (few percent) distortions in the shape of the background, and also cannot be constrained by the fit. In contrast, the fit is sensitive to the $t\bar{t} + c\bar{c}$ normalization and the second-leading uncertainty for c-tagging,[1] through the comparison of data and predictions across channels with different b-tag multiplicity, yielding results in agreement with the nominal predictions but with half the initial uncertainties. Other nuisance

[1] The main effect of this uncertainty is a change in normalization for the background with almost no effect on its shape in the final discriminant.

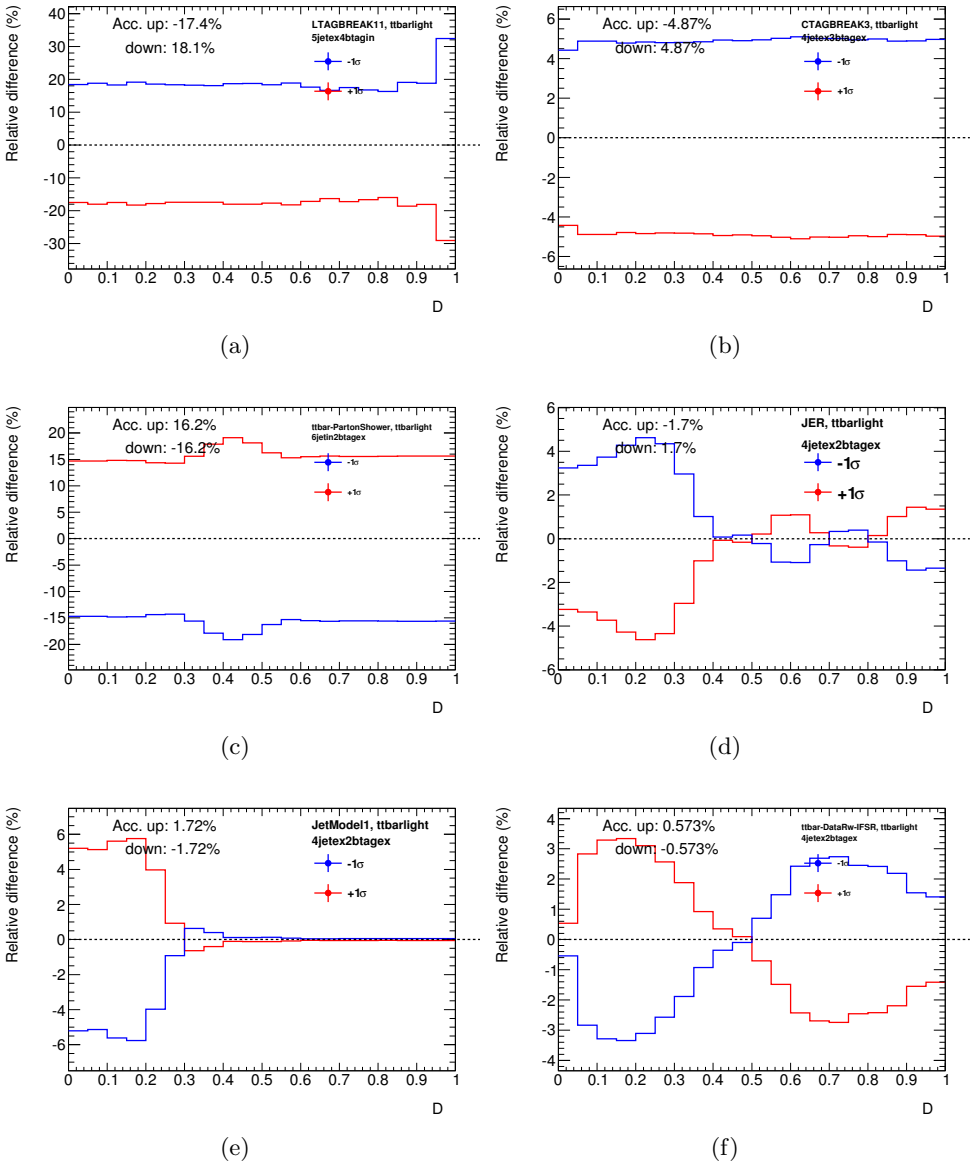

Figure 9.7: Effect of different systematic uncertainties on the $t\bar{t}$+light-jets background (a) Light-tagging eigenvector 11 in the (5 j, $\geq$ 4 b) region, (b) c-tagging eigenvector 3 in the (4 j, 3 b) region, (c) ttbar PartonShower in the ($\geq$ 6 j, 2 b) region, (d) JER in the (4 j, 2 b) region, (e) JetModel1 in the (4 j, 2 b) region and (f) DataRw-IFSR in the (4 j, 2 b) region. Relative differences between the nominal and $\pm 1\sigma$ distributions of the D discriminant are shown.

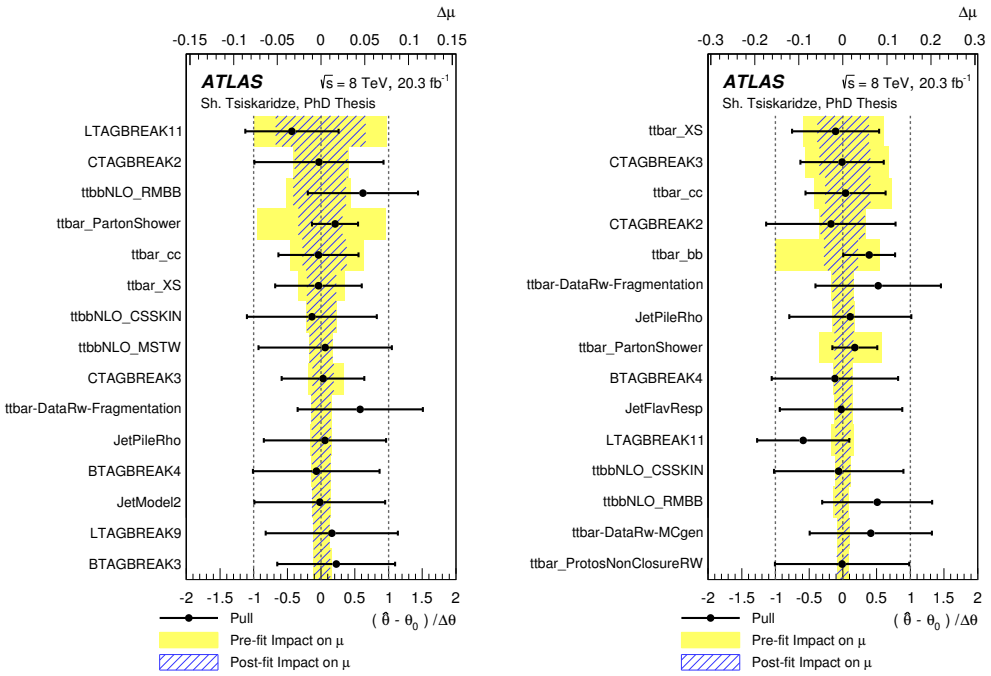

Figure 9.8: The fitted values of the nuisance parameters for the most important sources of systematic uncertainty and their impact on the measured signal strength for (a) the $t\bar{t} \to WbHc$, $H \to b\bar{b}$ search and (b) the $t\bar{t} \to WbHu$, $H \to b\bar{b}$ search. The points, which are drawn conforming to the scale of the bottom axis, show the deviation of each of the fitted nuisance parameters, $\hat{\theta}$, from θ_0, which is the nominal value of that nuisance parameter, in units of the pre-fit standard deviation $\Delta\theta$. The error bars show the post-fit uncertainties, σ_θ, which are close to 1 if the data do not provide any further constraint on that uncertainty. Conversely, a value of σ_θ much smaller than 1 indicates a significant reduction with respect to the original uncertainty. The nuisance parameters are sorted according to their post-fit effect on μ (hashed blue area), conforming to the scale of the top axis, with those with the largest impact at the top.

parameters have a smaller impact on the signal extraction and typically have small pulls or constraints.

In the case of the $t\bar{t} \to WbHu$ search, the leading uncertainties are similar, but the normalization uncertainty on the $t\bar{t}$ cross section is ranked high due to the significantly worse signal-to-background ratio in the (4 j, 3 b) channel, which dominates the $t\bar{t} \to WbHu$ sensitivity. On the other hand, a slight pull is obtained for the nuisance parameter associated with one of the uncertainties for the top quark p_{T} and $t\bar{t}$ system p_{T} reweightings, which is used by the fit to improve agreement between data and prediction in the channels with two b-tags but which has very small effect on the background prediction in the signal region.

9.1.2 Limits on BR($t \to Hq$)

In the absence of a significant excess in data above the background expectation, 95% CL limits are set on BR($t \to Hc$) and BR($t \to Hu$). Fig. 9.15a and Fig. 9.15b show the observed and expected $\mathrm{CL_s}$ as a function of BR($t \to Hc$) and BR($t \to Hu$) respectively. The observed (expected) 95% CL upper limits on the branching ratios are BR($t \to Hc$) $< 0.56\%\,(0.42\%)$ and BR($t \to Hu$) $< 0.61\%\,(0.64\%)$. These limits are obtained considering the complete set of nine analysis channels discussed previously. Detailed studies were performed to assess the impact on the expected sensitivity from considering particular subsets of the nine analysis channels, and are described in App. F.

The upper limits on the branching ratios BR($t \to Hq$) ($q = u, c$) can be translated to upper limits on the non-flavor-diagonal Yukawa couplings λ_{tqH} appearing in the following lagrangian [210]:

$$\mathcal{L}_{FCNC} = \lambda_{tcH}\bar{t}Hc + \lambda_{tuH}\bar{t}Hu + h.c. \tag{9.1}$$

The branching ratio for BR($t \to Hq$) is estimated as the ratio of its partial width to the SM $t \to Wb$ partial width, which is assumed to be dominant. Following the calculation in reference [211], the following expression is obtained:

$$\mathrm{BR}(t \to Hq) = \lambda_{tqH}^2/(g^2 \cdot |V_{tb}|^2 \cdot \chi^2), \tag{9.2}$$

where $g = 2m_W/v$ is the weak coupling constant, $|V_{tb}|$ is taken equal to 1, and χ^2 is a a kinematic factor given by $\chi^2 = (1 - 3x^4 + 2x^6)(1 - y^2)^{-2}x^{-2}/2$. In the expression of χ^2 the variables x and y are defined as $x = m_W/m_t$, $y = m_H/m_t$, where m_W, m_t and m_H are the W-boson, top-quark and Higgs-boson masses respectively, and the masses of the lighter quarks have been neglected. Using PDG averages [19] and applying NLO corrections to both the $t \to Hq$ decay width [212] and the top quark total decay width [213] leads to $g\chi = 1.92 \pm 0.02$, which is used in the extraction of the coupling. Therefore, the coupling can be extracted as:

$$|\lambda_{tqH}| = 1.92\sqrt{\mathrm{BR}(t \to Hq)}. \tag{9.3}$$

The above branching ratio limits can be translated to median expected limits on the couplings of $|\lambda_{tcH}| < 0.14\,(0.12)$ and $|\lambda_{tuH}| < 0.15\,(0.15)$.

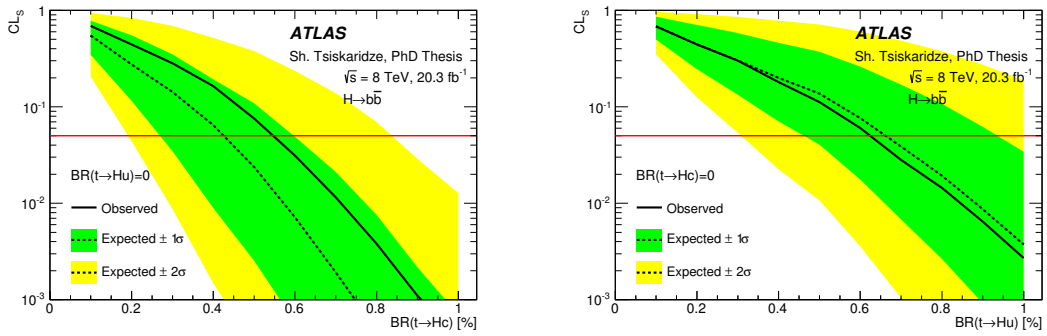

(a) (b)

Figure 9.9: (a) CL_s versus $BR(t \to Hc)$ (b) CL_s versus $BR(t \to Hu)$ for the $H \to \bar{b}$ search, assuming that the other branching ratio is zero. The observed CL_s values (solid black lines) are compared to the expected (median) CL_s values under the background-only hypothesis (dotted black lines). The surrounding shaded bands correspond to the 68% and 95% CL intervals around the expected CL_s values, denoted by $\pm 1\sigma$ and $\pm 2\sigma$, respectively. The solid red line at CL_s=0.05 denotes the value below which the hypothesis is excluded at 95% CL.

9.2 Combination with Other ATLAS Searches

This section reviews the results obtained for $H \to \gamma\gamma$ and $H \to W^+W^-, \tau^+\tau^-$ searches. A combination between the three ATLAS searches, $H \to b\bar{b}$, $H \to \gamma\gamma$ and $H \to W^+W^-, \tau^+\tau^-$, is also performed.

9.2.1 $H \to \gamma\gamma$

The first search for $t \to Hq$, published by the ATLAS Collaboration, was based on the $H \to \gamma\gamma$ decay mode [3]. In this search the $t\bar{t}$ production is undertaken using the pp collision data-set corresponding to an integrated luminosity of 4.5 fb^{-1} at $\sqrt{s} = 7$ TeV and 20.3 fb^{-1} at $\sqrt{s} = 8$ TeV.

The FCNC decay of one of the top quarks with further $H \to \gamma\gamma$ decay introduces the requirement of at least two reconstructed photon candidates. The remaining top quark in the event is searched for in two final states: leptonic and hadronic, depending on the W boson decay modes. The leptonic channel selects events with exactly one lepton (e or μ), at least two jets, and at least one b-tagged jet. The hadronic channel selects events with no reconstructed lepton, at least four jets, and at least one b-tagged jet. In both channels, additional requirements are made to select events compatible with $t\bar{t} \to WbHq$ production by exploiting the invariant masses of the reconstructed top quark candidates. Finally, the diphoton mass ($m_{\gamma\gamma}$) distribution of the selected events is analyzed using a sideband technique in order to estimate the background in the signal region, defined to be 122 GeV $\leq m_{\gamma\gamma} \leq$ 129 GeV. The diphoton mass spectrum in the hadronic channel is shown in Fig. 9.10a.

In comparison with the $H \to b\bar{b}$ search, this analysis does not distinguish between the $t\bar{t} \to WbHc$ and $t\bar{t} \to WbHu$ signals, because their selection acceptances are very close, although not identical. In order to combine it with the other searches discussed in this paper, minor modifications to the inputs were made with respect to the published result, all having a negligible impact on the result. The $t\bar{t}$ cross-section uncertainty

and the uncertainty model for Higgs branching ratios, as well as the separate treatment of $t\bar{t} \to WbHc$ and $t\bar{t} \to WbHu$ signals, are updated taking into account their slightly different acceptances.

The best-fit branching ratios obtained are $\mathrm{BR}(t \to Hc) = [0.22 \pm 0.26\,(\mathrm{stat.}) \pm 0.10\,(\mathrm{syst.})]\%$ and $\mathrm{BR}(t \to Hu) = [0.23 \pm 0.27\,(\mathrm{stat.}) \pm 0.10\,(\mathrm{syst.})]\%$ assuming that $\mathrm{BR}(t \to Hu) = 0$ and $\mathrm{BR}(t \to Hc) = 0$ respectively.

No significant signal is observed and an upper limit is set on the $t \to Hq$ branching ratio. The observed (expected) 95% CL upper limits on the branching ratios are $\mathrm{BR}(t \to Hq) < 0.79\%\,(0.51\%)$, where $\mathrm{BR}(t \to Hq) \equiv \mathrm{BR}(t \to Hc) + \mathrm{BR}(t \to Hu)$. Fig. 9.10b shows the observed and expected $\mathrm{CL_s}$ as a function of $\mathrm{BR}(t \to Hq)$. The corresponding limits on the couplings are $|\lambda_{tqH}| < 0.17\,(0.14)$, where $|\lambda_{tqH}| \equiv \sqrt{|\lambda_{tcH}|^2 + |\lambda_{tuH}|^2}$. These limits can also be understood as applying only to one of the decay modes, if the other decay mode is assumed to have a branching ratio equal to zero.

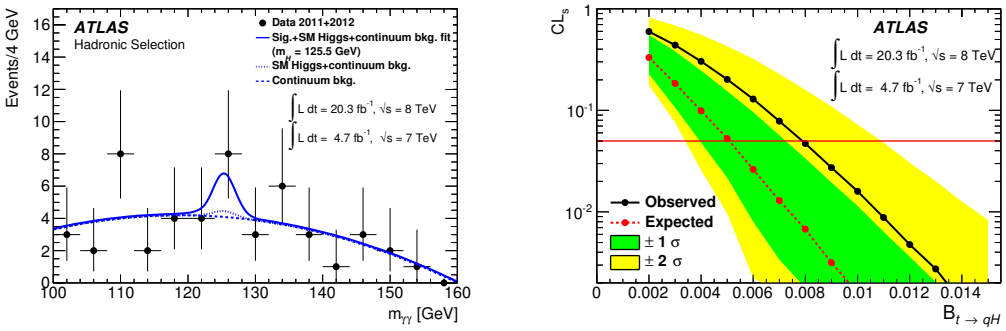

(a) (b)

Figure 9.10: (a) Distribution of $m_{\gamma\gamma}$ for the selected events in the hadronic channel. The result of a fit to the data of the sum of a signal component with the mass of the Higgs boson fixed to $m_H = 125.5$ GeV and a background component (dashed) described by a second-order polynomial is superimposed. The small contribution from SM Higgs boson production, included in the fit, is also shown (difference between the dotted and dashed lines). (b) $\mathrm{CL_s}$ versus $\mathrm{BR}(t \to Hq)$ for the $H \to \gamma\gamma$ search. The observed $\mathrm{CL_s}$ values (solid black lines) are compared to the expected (median) $\mathrm{CL_s}$ values under the background-only hypothesis (dotted black lines). The surrounding shaded bands correspond to the 68% and 95% CL intervals around the expected $\mathrm{CL_s}$ values, denoted by $\pm 1\sigma$ and $\pm 2\sigma$, respectively. The solid red line at $\mathrm{CL_s}$=0.05 denotes the value below which the hypothesis is excluded at 95% CL. Figures taken from reference [3].

9.2.2 $H \to W^+W^-, \tau^+\tau^-$

The ATLAS collaboration has performed a search for $t\bar{t}H$ associated production, with $H \to WW^*$, ZZ^*, $\tau\tau$, resulting in multilepton final states [6]. This search has been reinterpreted in the context of $t\bar{t} \to WbHq$ [10]. According the Table 1.6, the $H \to WW^*$ and $H \to \tau\tau$ decay modes have significant branching ratios, of 21.5% and 6.3% respectively. The event topology for signal events, $t\bar{t} \to WbHq \to W^\pm W^\pm W^\mp bq$ and $t\bar{t} \to WbHq \to W^\pm \tau^\pm \tau^\mp bq$, can be effectively exploited to suppress backgrounds in the case of multilepton final states.

The search considered five separate event categories depending on the number of reconstructed electrons or muons and hadronic τ candidates, of which the following three are considered for a reinterpretation in the context of the $t\bar{t} \to WbHq$ search:

- $2\ell 0\tau_{\text{had}}$: two same-charge light leptons (e or μ) with no hadronic τ candidates (τ_{had}) and $\geq$4 jets with $\geq$1 b-tagged jets. This channel is sensitive to the process $t\bar{t} \to WbHq \to \ell^{\pm}\ell^{\pm}qqqb2\nu$. To further improve the sensitivity, this category is further subdivided into six subcategories depending on the flavor of the leptons and the number of jets: (ee, $\mu\mu$, $e\mu$)$\times$(4 jets, $\geq$5 jets).

- 3ℓ: three light leptons with either $\geq$3 jets of which $\geq$2 are b-tagged, or $\geq$4 jets of which $\geq$1 are b-tagged. This channel is sensitive to the process $t\bar{t} \to WbHq \to \ell^{\pm}\ell^{\pm}\ell^{\mp}qb3\nu$.

- $2\ell 1\tau_{\text{had}}$: two same-charge light leptons (e or μ), one τ_{had} candidate, and $\geq$4 jets with $\geq$1 b-tagged jets. This channel is sensitive to the process $t\bar{t} \to WbHq \to \ell^{\pm}\ell^{\pm}\tau^{\mp}qb3\nu$.

The two other categories considered in the $t\bar{t}H$ search in multilepton final states but not in this reinterpretation are: 4ℓ (four light leptons with $\geq$2 jets and $\geq$1 b-tagged jets) and $1\ell 2\tau_{\text{had}}$ (one light lepton and two opposite-charge τ_{had} candidates, with $\geq$3 jets and $\geq$1 b-tagged jets), which have very small signal acceptance and/or poor signal-to-background ratio due to the large number of jets misidentified as τ_{had} candidates. The minimum number of jets required in the $2\ell 0\tau_{\text{had}}$ category is well matched to the number of partons expected from $t\bar{t} \to WbHq \to W^{\pm}W^{\pm}W^{\mp}bq$ signal events, while the 3ℓ and $2\ell 1\tau_{\text{had}}$ categories effectively require one or two jets beyond leading order. Because of this, and the gain in branching ratio resulting from only requiring two, as opposed to three, W bosons decaying leptonically, the $2\ell 0\tau_{\text{had}}$ category dominates the sensitivity.

The largest background in the most sensitive category, $2\ell 4$ j, is $t\bar{t}$ or single-top production with one of the leptons originating from a decay of a heavy-flavor hadron ("non-prompt lepton"), followed by $t\bar{t}W$ production. Smaller contributions arise from $t\bar{t}(Z/\gamma^*)$, $t\bar{t}H$, and diboson (primarily WZ) production, and dilepton events from $t\bar{t}$ and Z/γ^* with the wrong charge sign measured for one electron. In the remaining categories the non-prompt lepton background decreases in importance, relative to the prompt-lepton contributions. The prompt contributions are estimated using the simulation, as typically the relevant processes (e.g., $t\bar{t}V$, $V = W, Z$) have not been measured at an accuracy exceeding that of theoretical predictions. The non-prompt lepton background predictions are computed or validated using data control regions with similar lepton kinematic selections but with fewer jets (two or three). Further details are provided in references [8, 10]. Figure 9.11 shows the event yields in each of the categories, which are used as input to the statistical analysis.

The best-fit branching ratio obtained is $\text{BR}(t \to Hc) = [0.27 \pm 0.18\,(\text{stat.}) \pm 0.21\,(\text{syst.})]\%$ assuming that $\text{BR}(t \to Hu) = 0$. A similar fit is performed for the $t\bar{t} \to WbHu$ search, yielding $\text{BR}(t \to Hu) = [0.23 \pm 0.18\,(\text{stat.}) \pm 0.21\,(\text{syst.})]\%$, assuming that $\text{BR}(t \to Hc) = 0$. Fig. 9.12a and Fig. 9.12b show the observed and expected CL_s as a function of $\text{BR}(t \to Hc)$ and $\text{BR}(t \to Hu)$ respectively. The observed (expected) 95% CL upper limits on the branching ratios are $\text{BR}(t \to Hc) < 0.79\%\,(0.54\%)$ and $\text{BR}(t \to Hu) < 0.78\%\,(0.57\%)$. The corresponding observed (expected) limits on the couplings are $|\lambda_{tcH}| < 0.17\,(0.14)$ and $|\lambda_{tuH}| < 0.17\,(0.14)$ at 95% CL.

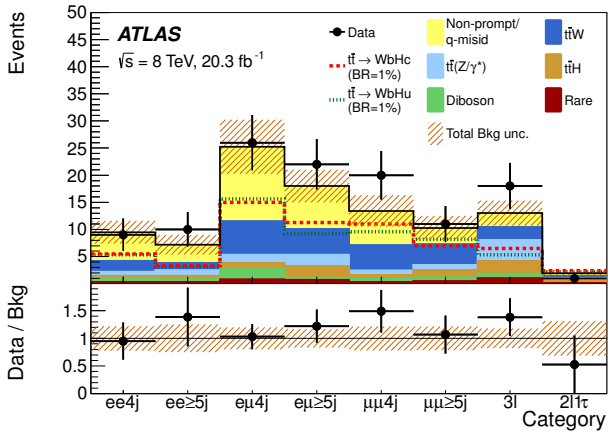

Figure 9.11: $t\bar{t} \to WbHq, H \to WW^*, \tau\tau$ search: comparison between the data and background prediction for the yields in each of the analysis channels considered before the fit to data. The expected $t\bar{t} \to WbHc$ and $t\bar{t} \to WbHu$ signals (dashed histograms) are shown separately normalized to BR$(t \to Hq) = 1\%$. The sum of instrumental backgrounds originating from non-prompt leptons and lepton charge misidentification is denoted by "Non-prompt/q-misid". The small contribution from rare processes such as tZ, $t\bar{t}WW$, triboson, $t\bar{t}t\bar{t}$ and tH production are combined into a single background source denoted by "Rare". The bottom panel displays the ratio of data to the SM background ("Bkg") prediction. The hashed area represents the total uncertainty on the background.

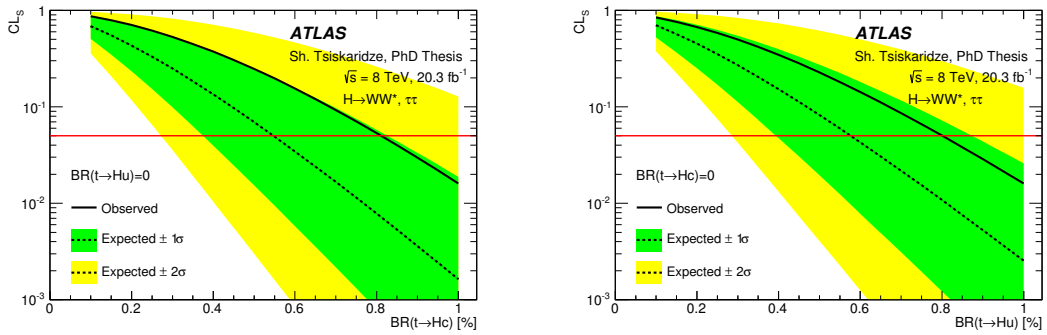

(a) (b)

Figure 9.12: (a) CL_s versus BR$(t \to Hc)$ (b) CL_s versus BR$(t \to Hu)$ for the $H \to W^+W^-, \tau^+\tau^-$ search, assuming that the other branching ratio is zero. The observed CL_s values (solid black lines) are compared to the expected (median) CL_s values under the background-only hypothesis (dotted black lines). The surrounding shaded bands correspond to the 68% and 95% CL intervals around the expected CL_s values, denoted by $\pm 1\sigma$ and $\pm 2\sigma$, respectively. The solid red line at CL_s=0.05 denotes the value below which the hypothesis is excluded at 95% CL.

9.2.3 ATLAS Combined Results

The three searches discussed in previous sections are combined using the statistical analysis discussed in Chapter 8. In this combination, the only systematic uncertainties taken to be fully correlated among the three searches are the $t\bar{t}$ cross section and the

integrated luminosity for $\sqrt{s} = 8$ TeV data. The dominant uncertainties on the Higgs boson branching ratios primarily affect the $t\bar{t} \to WbHq, H \to \gamma\gamma$ and $t\bar{t} \to WbHq$, $H \to b\bar{b}$ searches. Other uncertainties such as those associated with leptons, JES and b-tagging should be partially correlated between the $t\bar{t} \to WbHq$, $H \to \gamma\gamma$ search and the other two searches, but the differences in treatment between analyses (different lepton selection and p_{T} cuts, no uncertainty breakdown for JES and b-tagging in the $t\bar{t} \to WbHq$, $H \to \gamma\gamma$ search) make it difficult to account for correlations. However, given that the $t\bar{t} \to WbHq$, $H \to \gamma\gamma$ search is completely dominated by the data statistics, the effect of this simplification is negligible. The uncertainties taken as correlated between the $t\bar{t} \to WbHq$, $H \to b\bar{b}$ and $t\bar{t} \to WbHq$, $H \to WW^*, \tau\tau$ searches include those associated with lepton isolation, the leading b-tagging and JES uncertainties, and the reweighting of top quark p_{T} and $t\bar{t}$ system p_{T}. The rest of the uncertainties are taken to be uncorrelated among the searches. This correlation scheme closely follows the procedure adopted in the combination of $t\bar{t}H$ searches and the Higgs couplings combination [214].

The first set of combined results obtained are for each of the branching ratios at a time, taking the other branching ratio equal to zero. The best-fit combined branching ratios are $\mathrm{BR}(t \to Hc) = [0.22 \pm 0.10\,(\mathrm{stat.}) \pm 0.10\,(\mathrm{syst.})]\%$ and $\mathrm{BR}(t \to Hu) = [0.16 \pm 0.11\,(\mathrm{stat.}) \pm 0.12\,(\mathrm{syst.})]\%$ respectively. A comparison of the best fit branching ratios for the individual searches and their combination can be found in Fig. 9.13.

Figure 9.14 summarizes the observed (expected) 95% CL upper limits on the branching ratios, which are $\mathrm{BR}(t \to Hc) < 0.46\%\,(0.25\%)$ and $\mathrm{BR}(t \to Hu) < 0.45\%\,(0.29\%)$. The corresponding observed (expected) upper limits on the λ_{tcH} and λ_{tuH} couplings are 0.13 (0.10) and 0.13 (0.10) respectively. A comparison to other existing results can be found in Table 9.2. The $H \to b\bar{b}$ search discussed in this dissertation has the best expected sensitivity to $\mathrm{BR}(t \to Hc)$ among all individual searches, and about a factor two better than the corresponding CMS search.

Collab.	Higgs boson decay mode	95% CL upper limits on $\mathrm{BR}(t \to Hc)$		95% CL upper limits on $\mathrm{BR}(t \to Hu)$		Reference
		Observed	Expected	Observed	Expected	
CMS	$H \to \gamma\gamma$ (1)	0.69%	0.81%	–	–	[4]
	$H \to \gamma\gamma$ (2)	0.47%	0.71%	0.42%	0.65%	[5]
	$H \to WW^*, \tau^+\tau^-$ (3ℓ, 4ℓ)	1.28%	1.17%	–	–	[4]
	$H \to WW^*, \tau^+\tau^-$ (SS 2ℓ, 3ℓ)	0.93%	0.89%	–	–	[7]
	$H \to b\bar{b}$	1.16%	0.89%	1.92%	0.85%	[215]
	Combination $\gamma\gamma$ (1), 3ℓ, 4ℓ	0.56%	0.65%	–	–	[4]
ATLAS	$H \to \gamma\gamma$	0.79%	0.51%	0.79%	0.51%	[3]
	$H \to WW^*, \tau^+\tau^-$ (SS 2ℓ, 3ℓ)	0.79%	0.54%	0.78%	0.57%	[6]
	$H \to b\bar{b}$	0.56%	0.42%	0.61%	0.64%	[10]
	Combination	0.46%	0.25%	0.45%	0.29%	[10]

Table 9.2: Summary of 95% CL upper limits on $\mathrm{BR}(t \to Hq)$ from LHC experiments. The results quoted for each branching ratio assumes the other branching ratio equal to zero.

A similar set of results can be obtained by releasing the assumption of one branching ratio equal to zero at a time, and varying simultaneously both branching ratios. Although the $t\bar{t} \to WbHq$, $H \to \gamma\gamma$ and $t\bar{t} \to WbHq$, $H \to WW^*, \tau\tau$ searches are basi-

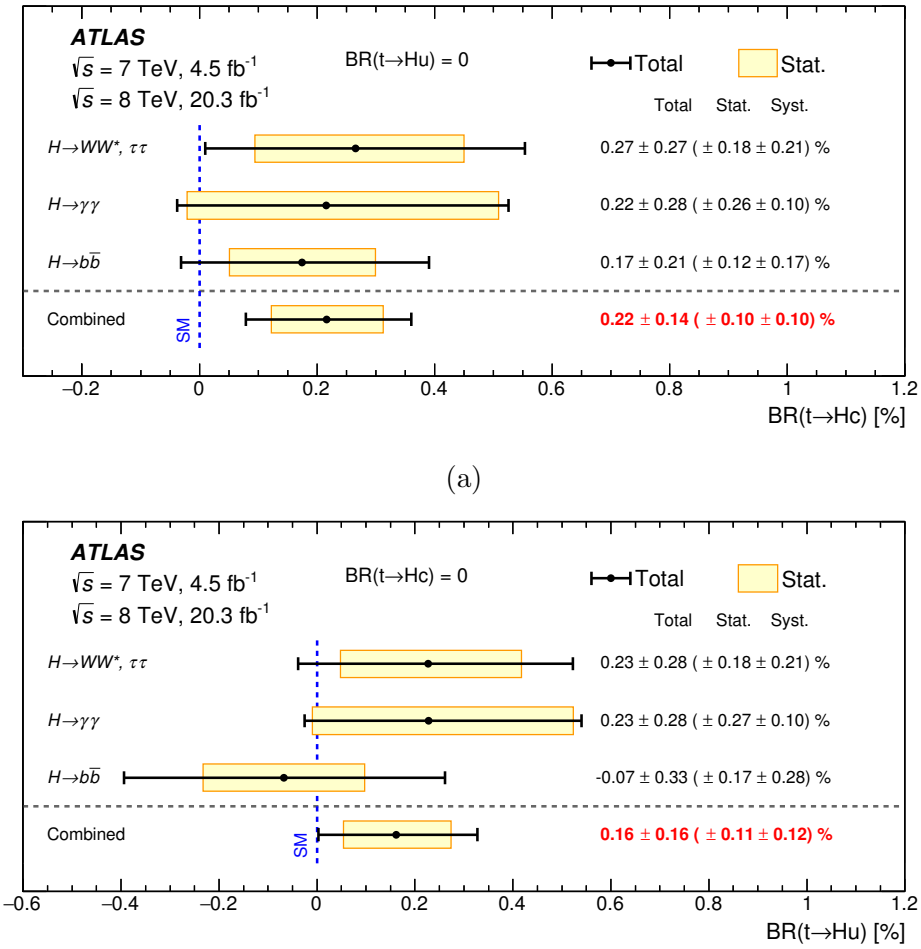

Figure 9.13: Summary of the best-fit (a) BR($t \to Hc$) and (b) BR($t \to Hu$) for the individual searches as well as their combination, under the assumption that other branching ratio is zero.

cally only sensitive to the sum of both branching ratios, the $t\bar{t} \to WbHq$, $H \to b\bar{b}$ search has different sensitivity to each of them and a simultaneous fit can be performed. The best-fit branching ratios obtained from the simultaneous fit are BR($t \to Hc$) = [0.34 ± 0.22 (stat.) ± 0.15 (syst.)]% and BR($t \to Hu$) = [−0.17 ± 0.25 (stat.) ± 0.17 (syst.)]%, with a correlation coefficient of −0.84, as shown in Fig. 9.16.

Figure 9.17a shows the 95% CL upper limits on the branching ratios in the BR($t \to Hu$) versus BR($t \to Hc$) plane. The corresponding upper limits on the coupling plane of $|\lambda_{tuH}|$ vs $|\lambda_{tcH}|$ can be found in Fig. 9.17b. The observed (expected) 95% CL upper limits on each of the branching ratios (profiled over the other branching ratio, required to be non-zero) are BR($t \to Hc$) < 0.47% (0.37%) and BR($t \to Hu$) < 0.45% (0.50%). As can be appreciated, the expected limits are in this case significantly worse than when assuming the other branching ratio equal to zero. This comes from the strong anticorrelation between both parameters (see Fig. 9.16). Also, the observed and expected limits are closer in this case. This comes from the excess in data: when generating the background-only Asimov dataset following the standard procedure, the

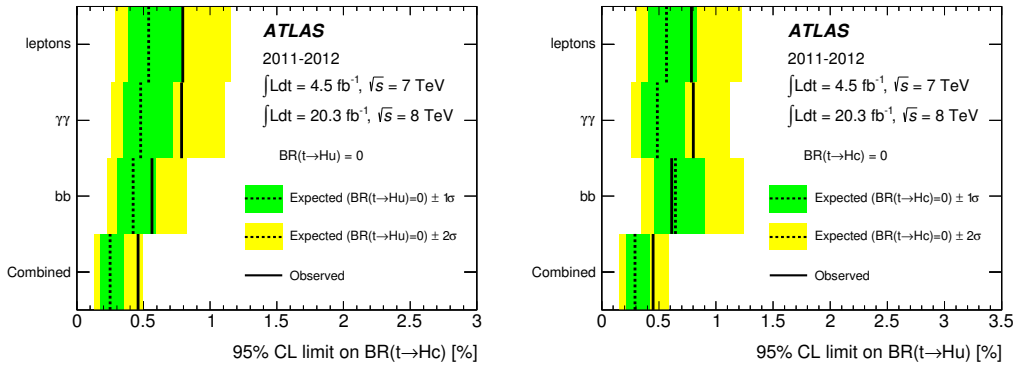

(a) (b)

Figure 9.14: 95% CL upper limits on (a) BR($t \to Hc$) and (b) BR($t \to Hu$) for the individual searches as well as their combination, under the assumption that the other branching ratio is zero. The observed limits (solid lines) are compared to the expected (median) limits under the background-only hypothesis. The surrounding shaded bands correspond to the 68% and 95% CL intervals around the expected limits, denoted as $\pm 1\sigma$ and $\pm 2\sigma$, respectively.

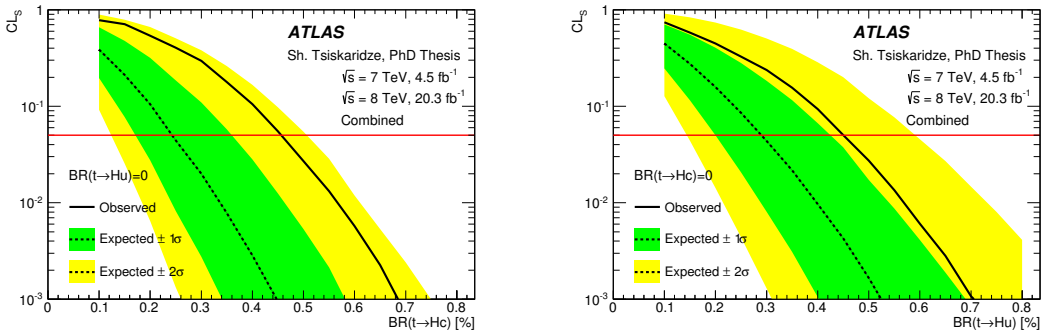

(a) (b)

Figure 9.15: (a) CL_s versus BR($t \to Hc$) (b) CL_s versus BR($t \to Hu$) for the combination of searches, assuming that the other branching ratio is zero. The observed CL_s values (solid black lines) are compared to the expected (median) CL_s values under the background-only hypothesis (dotted black lines). The surrounding shaded bands correspond to the 68% and 95% CL intervals around the expected CL_s values, denoted by $\pm 1\sigma$ and $\pm 2\sigma$, respectively. The solid red line at CL_s=0.05 denotes the value below which the hypothesis is excluded at 95% CL.

other branching ratio is profiled as a (free) nuisance parameter which matches and propagates the excess to the background-only expectation, resulting in weaker expected limits.

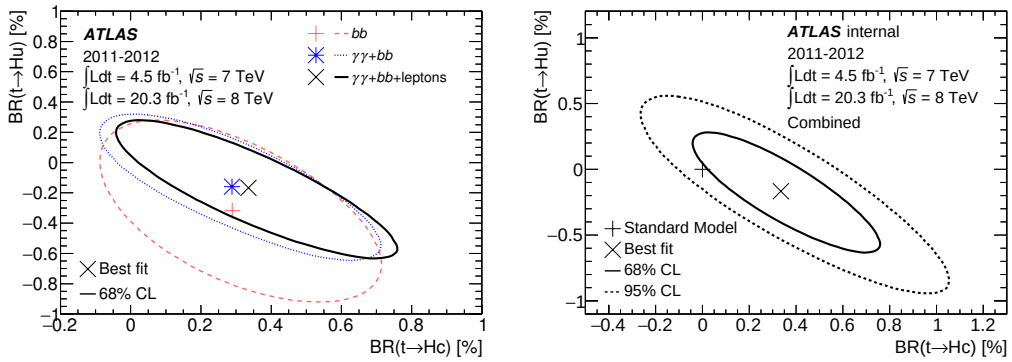

(a) (b)

Figure 9.16: ATLAS Combination: (a) Best-fit BR($t \to Hc$) and BR($t \to Hu$) and the corresponding 68% CL regions for several combinations with the $t\bar{t} \to WbHq$, $H \to b\bar{b}$ search. (b) Best-fit BR($t \to Hc$) and BR($t \to Hu$) and the corresponding 68% CL (solid) and 95% CL (dotted) regions for the full combination.

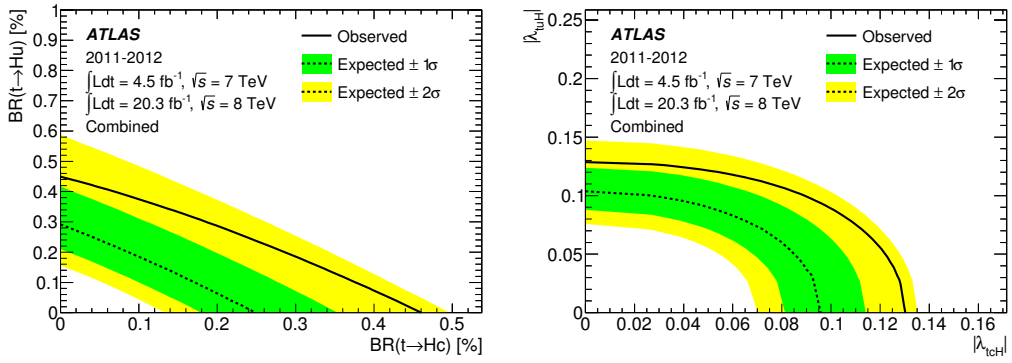

(a) (b)

Figure 9.17: ATLAS Combination: 95% CL upper limits (a) on the plane of BR($t \to Hu$) vs BR($t \to Hc$) and (b) on the plane of $|\lambda_{tuH}|$ vs $|\lambda_{tcH}|$. The observed limits (solid lines) are compared to the expected (median) limits under the background-only hypothesis. The surrounding shaded bands correspond to the 68% and 95% CL intervals around the expected limits, denoted as $\pm 1\sigma$ and $\pm 2\sigma$, respectively.

Chapter 10

Prospects

In this chapter the prospects for future improvements in the sensitivity of the $t\bar{t} \to WbHq$, $H \to b\bar{b}$ search, based on the method of analysis presented in this dissertation, are discussed. In short, four main areas of improvement can be identified: statistical uncertainty, systematic uncertainties, event categorization and discriminating variable. Each of these areas are discussed below.

10.1 Statistical Uncertainty

After the 2013-2014 shutdown, the LHC has resumed operations in 2015 and has started providing pp collisions at a center-of-mass energy of $\sqrt{s} = 13$ TeV. At this higher energy, the $t\bar{t}$ production cross section increases by factor of about 3.2, from 257 pb to 829 pb [44] (see Fig. 1.13). Therefore, for the same integrated luminosity the statistical sensitivity of the search is expected to improve by a factor of about 1.8 in Run 2, compared to Run 1. The expected integrated luminosity for the whole Run 2 (2015-2018) is about 100 fb^{-1}, a factor of five larger than that recorded at $\sqrt{s} = 8$ TeV. Beyond Run 2, an integrated luminosity of 300 fb^{-1} is expected by the end of Run 3 (2019-2022) and up to 3 ab^{-1} by the end of the high-luminosity LHC (2024-2035).

10.2 Systematic Uncertainties

The sensitivity of the search can be increased by reducing systematic uncertainties. In particular, over the next few years further theoretical developments are expected in the modeling of $t\bar{t}$-related backgrounds, that should lead to smaller uncertainties. In addition, the increased data statistics will also help placing constraints on some of the leading background modeling uncertainties through the fitting procedure. Finally, further refinements to experimental techniques such as b-tagging, whose uncertainties play a significant role as shown in Fig. 9.8, are also expected to improve the sensitivity.

The default b-tagging algorithm for Run 1 analysis is MV1 (see Sec. 4.5.1). The track impact parameter resolution will improve during Run 2 due to the installation of the Insertable B-Layer (IBL) [216] during the 2012-2014 LHC shutdown. Thus, for Run 2 an improved b-tagging algorithm, so-called MV2c00, has been developed [217]. A comparison between the performance of MV1 and MV2c00 b-tagging algorithms is presented in Fig. 10.1. Both multivariate algorithms are trained with only light-flavor jets as background. As can be appreciated, the light-flavor jet rejection is improved

by a factor of 4-5 and the c-jet rejection by about a factor 1.1 for a 70% operating point. Alternatively for the same light-flavor jet rejection obtained in Run 1 for the 70% operating point, a relative 10% improvement in the b-jet efficiency is achieved. Therefore, for Run 2 the improved b-tagging will result in better signal-to-background and smaller impact from background related uncertainties, including those associated with charm and light-jet tagging.

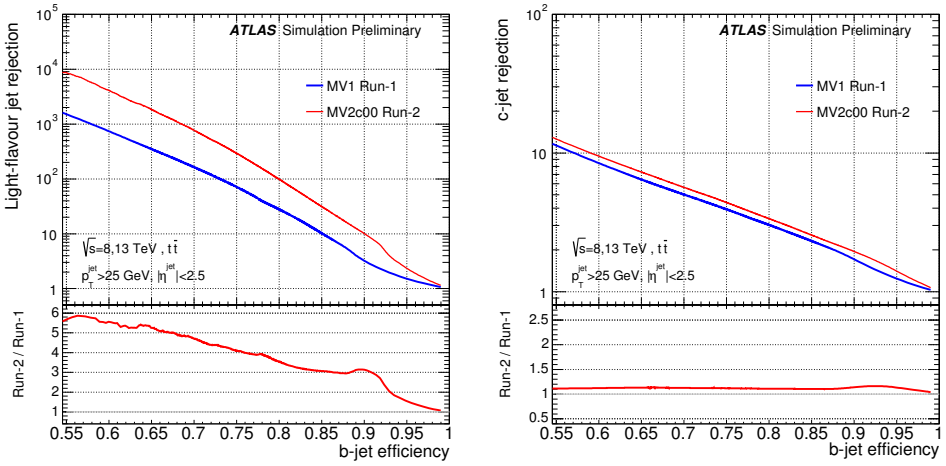

(a) (b)

Figure 10.1: (a) Light-jet rejection versus b-jet efficiency and (b) c-jet rejection versus b-jet efficiency for the MV1 b-tagging algorithm using the Run 1 detector and reconstruction software (blue) compared to the MV2c00 b-tagging algorithm using the Run 2 setup (red). Figures taken from reference [217].

10.3 Event Categorization

As discussed in Sec. 6.1, the preselected events are categorized into nine channels depending on the number of jets (4, 5 and $\geq$6) and on the number of b-tagged jets (2, 3 and $\geq$4) using the 70% b-tagging operating point. However, more refined event categorizations are possible, leading to analysis channels with improved signal-to-background ratio and/or better final discriminant separation.

Exploiting the fact that jets in signal events have higher b-tagging weights than in background events, the events can be characterized by two jet counters, number of "loose" jets, L, and number of "tight" jets, T, defined for each event as follows:

- L: number of jets with the MV1 weight between the 80% and 70% operating points;
- T: number of jets with the MV1 weight above the 60% operating point.

Given these counters, the following splitting on sub-channels is possible:

- Channels with exactly 2 b-tagged jets are split on sub-channels with $L < 2$ and $L \geq 2$;

- Channels with exactly 3 b-tagged jets are split on sub-channels with $L < 1$ and $L \geq 1$;

- Channels with $\geq$4 b-tagged jets are split on sub-channels with $T < 4$ and $T \geq 4$;

An example of the shape comparison of the D discriminating variable before and after the channel splitting is shown in Fig. 10.2 for the most sensitive (4 j, 4 b) channel of the $t\bar{t} \to WbHc$ search. For numerical comparisons the measure of the signal-to-background discrimination, quantified by the so-called "separation" variable,[1] is also presented. As can be appreciated, the separation between the $t\bar{t} \to WbHc$ signal and the $t\bar{t}$ background is improved by about 50% for the (4 j, 4 b) sub-channel with T$\geq$4. The expected signal and background in the (4 j, 4b) channel before and after the channel splitting are shown in Table 10.1. The (4 j, 4 b) sub-channel with T$\geq$4 shows a significantly improved signal-to-background compared to the unsplit (4 j, 4 b) channel, which should result in an improved sensitivity as the analysis is less and less limited by the statistical uncertainty.

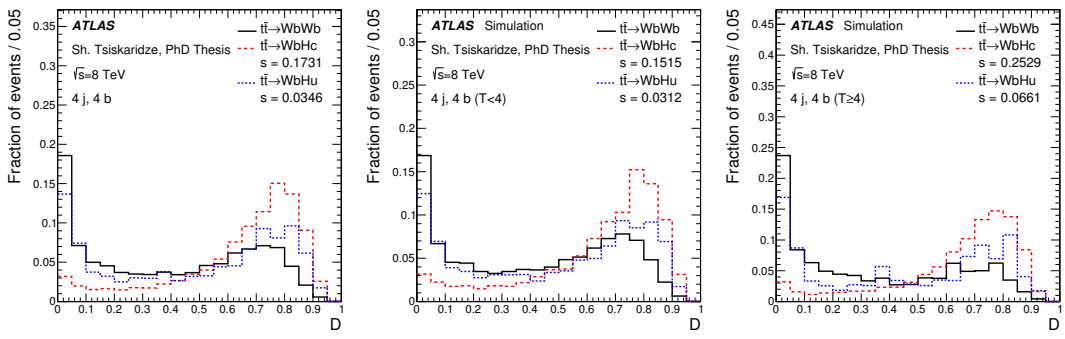

(a) (b) (c)

Figure 10.2: The shape comparison of the D discriminating variable between the $t\bar{t} \to WbHc$ (red dashed) and $t\bar{t} \to WbHu$ (blue dotted) signals, and the $t\bar{t} \to WbWb$ background (black solid) in the (4 j, 4 b) channel: (a) before and after the channel splitting (see text for details) into sub-channels with (b) $T < 4$ and (c) $T \geq 4$. Also shown is the "separation" S between signal and background, defined in Eq. 10.1.

While a-priori promising, the channel splitting introduces additional difficulties. After the splitting the statistics may fall down significantly causing overestimation of systematic uncertainties due to statistical fluctuations and fit instabilities. It also requires the availability of a "pseudo-continuous b-tagging" calibration, including proper treatment of correlations in b-tagging uncertainties across b-tagging operating points.

[1] The "separation" between the signal and background histograms is calculated as:

$$S = \sum_{i=1}^{N_{bins}} \frac{1}{2} \frac{\left(\frac{s_i}{\Sigma_s} - \frac{b_i}{\Sigma_b}\right)^2}{\left(\frac{s_i}{\Sigma_s} + \frac{b_i}{\Sigma_b}\right)} \tag{10.1}$$

where s_i and b_i are the per bin content of the signal and background histograms, respectively, $\Sigma_s = \sum_{i=1}^{N_{bins}} s_i$ and $\Sigma_b = \sum_{i=1}^{N_{bins}} b_i$. The value of this variable is 0 if signal and background distributions are identical and 1 if they do not overlap.

Channel	$t\bar{t} \to WbHc$	$t\bar{t}$+light-jets	$t\bar{t} + c\bar{c}$	$t\bar{t} + b\bar{b}$	Total Bkg.	S/B	$S/\sqrt{B}$
Default	41.58	52.07	20.86	43.21	116.15	0.36	3.86
T<4	25.93	45.78	15.97	23.29	85.03	0.30	2.81
T≥4	15.80	6.29	4.90	19.93	31.11	0.51	2.83

Table 10.1: Predicted signal (assuming BR($t \to Hc$) = 1%) and background yields for the (4j, 4b) channel before and after splitting according to the T counter (see text for details). Also shown are the S/B and $S/\sqrt{B}$ ratios.

Due to the above, this channel splitting was not adopted in the current analysis but may lead to significant improvement with the 13 TeV data.

10.4 Discriminating Variable

Finally, one may improve the discriminating variable by including additional information to suppress the impact from combinatorial background and/or to achieve better signal-to-background separation. Examples include the addition of new terms to the probability calculation: a "pseudo-continuous b-tagging term" and "jet charge information", discussed below.

10.4.1 Pseudo-continuous *b*-tagging Term

One can exploit the fact that jets in signal and background events have different b-tagging weights, by adding an additional term to the signal and the background probabilities in Eq. 6.5 and Eq. 6.7, respectively. As a first step, the jets in the events are sorted according to their MV1 weight and, for each weight position i ($i \in \{1 \cdots N_{\text{jets}}\}$), the corresponding signal and background pdfs (P_i^{sig} and P_i^{bkg}) are constructed. Examples of the pdfs constructed for the (4 j, 4 b) channel can be found in Fig. 10.3.

Given these per-jet pdfs, the per-event b-tagging probabilities for signal and background are computed as:[2]

$$\begin{aligned} P_{\text{evt}}^{\text{sig}}(\mathbf{x}) &= \prod_{i=1}^{N_{\text{jets}}} P_i^{\text{sig}}(w_{\text{jet}_i}), \\ P_{\text{evt}}^{\text{bkg}}(\mathbf{x}) &= \prod_{i=1}^{N_{\text{jets}}} P_i^{\text{bkg}}(w_{\text{jet}_i}). \end{aligned} \tag{10.2}$$

where w_{jet_i} is the MV1 weight of i-th jet and N_{jets} is the total number of jets in the event.

Since $P_{\text{evt}}^{\text{sig}}(\mathbf{x})$ and $P_{\text{evt}}^{\text{bkg}}(\mathbf{x})$ are not affected by the jet permutations in the event,

[2] For events with ≥6 jets only the first six jets with the highest b-tagging weights are considered.

one can define new signal and background probabilities as follows:

$$\begin{aligned} P^{\text{sig}}_{\text{new}}(\mathbf{x}) =& P^{\text{sig}}_{\text{evt}}(\mathbf{x}) \cdot P^{\text{sig}}(\mathbf{x}), \\ P^{\text{bkg}}_{\text{new}}(\mathbf{x}) =& P^{\text{bkg}}_{\text{evt}}(\mathbf{x}) \cdot P^{\text{bkg}}(\mathbf{x}), \end{aligned} \tag{10.3}$$

where $P^{\text{sig}}(\mathbf{x})$ and $P^{\text{bkg}}(\mathbf{x})$ are given by Eq. 6.5 and Eq. 6.7, respectively. The new discriminating variable is defined as:

$$D_{\text{new}}(\mathbf{x}) = \frac{P^{\text{sig}}_{\text{new}}(\mathbf{x})}{P^{\text{sig}}_{\text{new}}(\mathbf{x}) + P^{\text{bkg}}_{\text{new}}(\mathbf{x})}. \tag{10.4}$$

In general, $P^{\text{sig}}_{\text{evt}}(\mathbf{x})$ is larger than $P^{\text{bkg}}_{\text{evt}}(\mathbf{x})$ and thus it helps to pull the distribution of the D_{new} discriminating variable to 1 for signal and to 0 for background (particularly $t\bar{t}$+light-jets), improving the separation. The shape comparison of the distributions for the D and D_{new} discriminating variables are shown in Fig. 10.4. In Fig. 10.5 the corresponding comparison of the data and prediction is presented. This procedure improves the separation between signal and background by about 20% in most of the analysis channels. However, as discussed previously, exploiting this information requires a pseudo-continuous b-tagging calibration instead of the calibration one for a fixed operating point, which was not available in Run 1 for the analysis discussed in this dissertation.

10.4.2 Jet Charge Information

Flavor jet identification is an important task in particle physics. The charge information of the tracks inside the jet can also be used to estimate the charge of the initial parton. For the analysis presented in this dissertation, this additional jet information (especially on the b-tagged jets) could have helped reduce the impact from combinatorial background on the final discriminant, and thus improve the signal-to-background discrimination.

There are different methods for estimating the jet charge [218–221] based on the reconstructed track information. The *momentum weighted jet charge* (MWJQ) method [219] had been studied in the early stages of this analysis. In this case, the jet charge is defined as:

$$Q_{jet} = \frac{\sum_{i=1}^{N_{tracks}} q_i \cdot |\overrightarrow{j} \cdot \overrightarrow{p_i}|^{\kappa}}{\sum_{i=1}^{N_{tracks}} |\overrightarrow{j} \cdot \overrightarrow{p_i}|^{\kappa}} \tag{10.5}$$

where q_i and p_i are the charge and momentum of the i^{th} track, $\overrightarrow{j}$ defines the unit vector along the jet axis and κ is a parameter whose value can be chosen to optimize the performance of the jet charge variable.

The performance of the jet charge also depends on the selection of tracks used in Eq. 10.5. Therefore, an optimization procedure based on the combination of two quantities, *efficiency* (ε) and *purity* (P), is introduced. If N_+ and N_- are the number of jets corresponding to two different charge hypotheses ($Q > 0$ and $Q < 0$), then the measured asymmetry can be defined as:

$$A_m = \frac{N^m_+ - N^m_-}{N^m_+ + N^m_-} \rightarrow \sigma_{A_m} = \sqrt{\frac{1 - A^2_m}{N^m_+ + N^m_-}} = \sqrt{\frac{1 - A^2_m}{N_m}}, \tag{10.6}$$

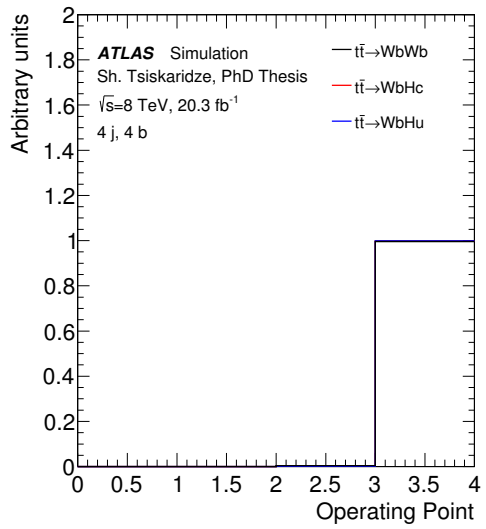

(a) 1st leading jet

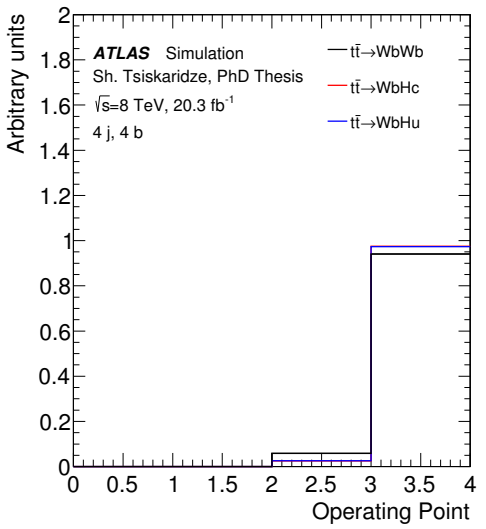

(b) 2nd leading jet

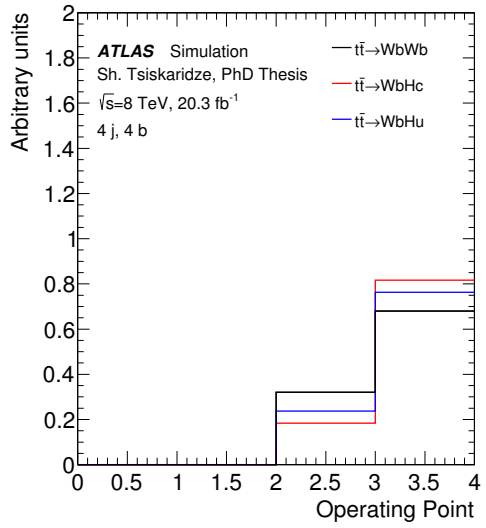

(c) 3rd leading jet

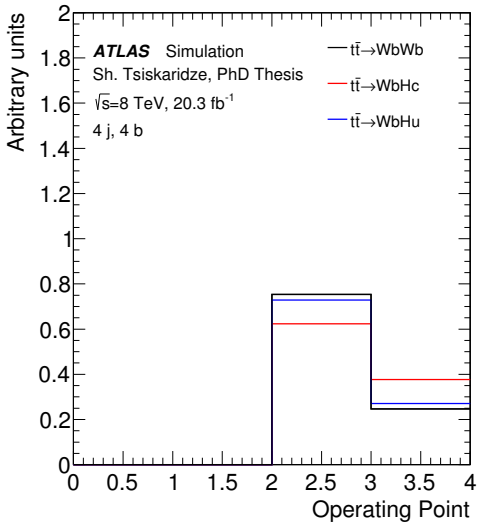

(d) 4th leading jet

Figure 10.3: Pdfs for $P_i^{\text{sig/bkg}}$ ($i \in \{1 \cdots N_{\text{jets}}\}$) for the first leading jets (in MV1 weight) in the (4 j, 4 b) channel.

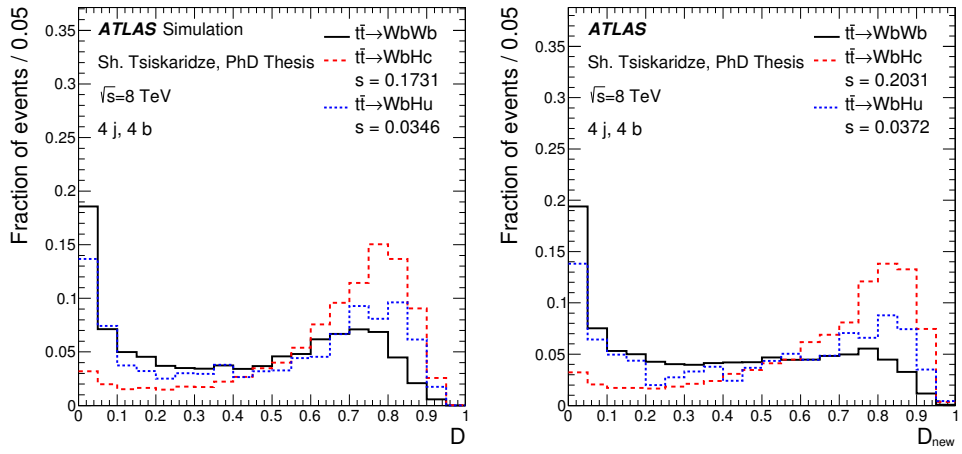

(a) (b)

Figure 10.4: Comparison of the shape of (a) the default discriminating variable D and (b) the new discriminating variable D_{new} (see text for details) between the $t\bar{t} \to WbHc$ (red dashed) and $t\bar{t} \to WbHu$ (blue dotted) signals, and the $t\bar{t} \to WbWb$ background (black solid) in (4 j, 4 b) channel. Also shown is the "separation" S between signal and background, defined in Eq. 10.1.

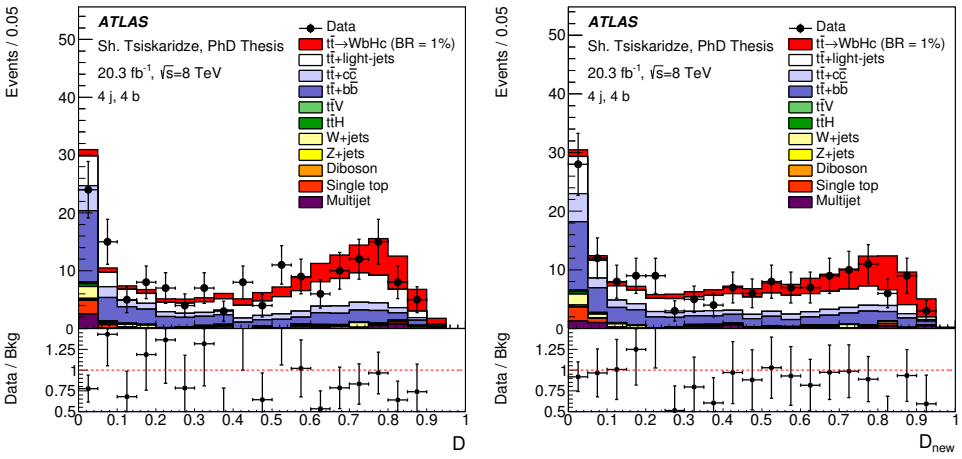

(a) (b)

Figure 10.5: Comparison between the data and prediction for (a) default discriminating variable D and (b) discriminating variable D_{new} with pseudo-continuous b-tagging for the (4 j, 4 b) channel. Shown are the pre-fit distributions. The $t\bar{t} \to WbHc$ signal (solid red) is normalized to BR($t \to Hc$) = 1% and the $t\bar{t} \to WbWb$ background is normalized to the SM prediction. The bottom panels display the ratios of data to the SM background prediction before the fit ("Bkg").

while the truth asymmetry is given by:

$$A_t = \frac{N_+^t - N_-^t}{N_+^t + N_-^t}. \tag{10.7}$$

The *dilution* D is defined as:

$$D = \frac{N_{\text{right}} - N_{\text{wrong}}}{N_{\text{right}} + N_{\text{wrong}}} \equiv 2P - 1 \rightarrow D = \frac{A_m}{A_t}, \tag{10.8}$$

where N_{right} and N_{wrong} are the number of correctly and incorrectly assigned jets and P is a purity. The statistical uncertainty on the true asymmetry is given by:

$$\sigma_{A_t} = \frac{\sigma_{A_m}}{D} = \sqrt{\frac{1 - A_m^2}{D^2 N_m}} = \sqrt{\frac{1 - D^2 A_t^2}{\varepsilon D^2 N}}. \tag{10.9}$$

The decision on the optimal method is based on choosing the one with the largest εD^2 [221].

Since the dominant fraction of the jets considered in this analysis are b-jets from $t\bar{t}$+jets events, the $t\bar{t}$ sample generated with MC@NLO (the only MC sample available at the time) is used for optimization studies. To optimize the algorithm for b-jets one needs to adjust the efficiency and purity definitions. For simplicity, five different sub-selections are considered:

- J_0 - set of all considered jets in the $t\bar{t}$ sample;
- J_1 - jets with assigned jet charge (subset of J_0);
- J_2 - jets that are matched to the truth b-jets only (subset of J_1);
- J_3 - intersection of sets J_1 and J_2 i.e. b-jets with assigned charge;
- J_4 - jets with charge correctly assigned. (subset of J_3);

Given the above sub-selections, the efficiency and purity are defined as:

$$\varepsilon = \frac{|J_3|}{|J_2|}, \quad P = \frac{|J_4|}{|J_3|}. \tag{10.10}$$

The optimal κ value and track selection parameters for b-jets are presented in the Table 10.2. The default choice used in ATLAS is also shown for comparison. As can be appreciated, the track selection is the same, except the number of selected tracks, N_{tracks}, and the cut on the matching criteria for the track and jet, ΔR.

The jet charge asymmetry between the quark and anti-quark for b-, c- and u-quarks are shown in Fig. 10.6, using the optimal track selection for b-jets. A table summarizing the purity for different jet flavors is also presented. The jet charge assignment efficiency obtained for preselected events is above 99%, while the b-jet charge assignment purity is about 63%. As can be appreciated, the MWJC method shows a good charge assignment also for the other jet flavors.

The calculation of $P^{\text{sig}}(\mathbf{x})$ and $P^{\text{bkg}}(\mathbf{x})$ in Eq. 6.5 and Eq. 6.7, respectively, could be extended to weight each of the jet permutations by the combined probability based on b-tagging and jet charge information.

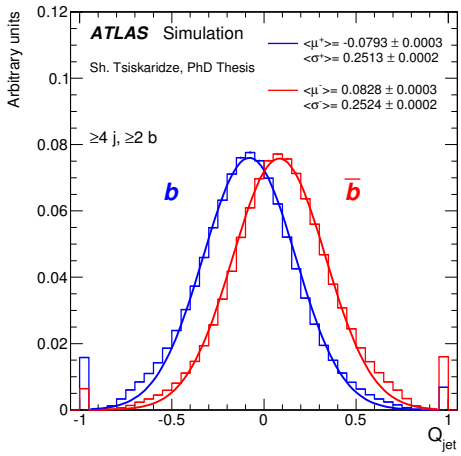

(a)

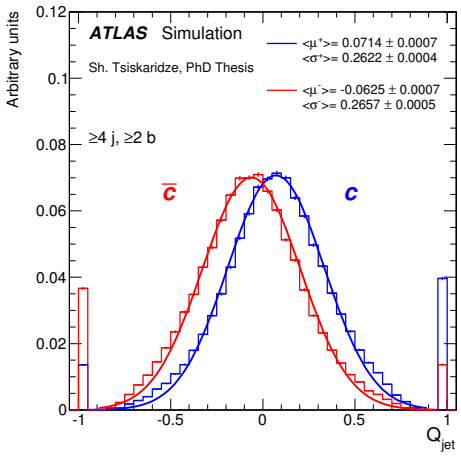

(b)

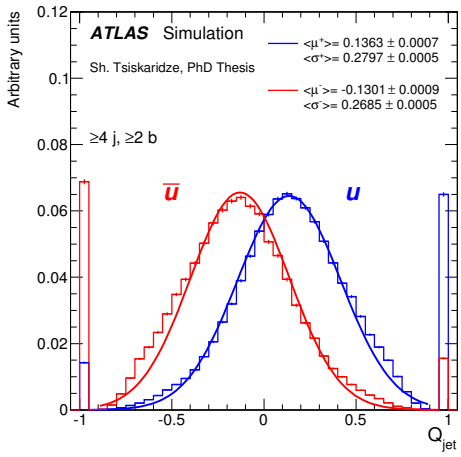

(c)

Quark	Purity P
b	63%
c	61%
s	70%
u	73%
d	65%

(d)

Figure 10.6: Jet charge asymmetry for (a) b- and $\bar{b}$-quarks, (b) c- and $\bar{c}$-quarks, and (c) u- and $\bar{u}$-quarks for events with $\geq$ 4 jets and $\geq$ 2 b-tags. The mean and sigma values of the Gaussian fit on the interval (-1, 1) is also shown. (+) and (-) values corresponds to the quark and anti-quark, respectively. (d) Purity obtained for different jet flavors.

Parameter	Optimal value	Values used in ATLAS
Parameter κ	0.5	0.5
Number of tracks, N_{tracks}	$N_{tracks} \geq 1$	$10 \geq N_{tracks} \geq 2$
Track distance to jet axis, ΔR	$\Delta R < 0.35$	$\Delta R < 0.25$
Track p_{T}	> 1 GeV	> 1 GeV
Impact parameter $\lvert d_0 \rvert$	≥ 2.0	≥ 2.0
Impact parameter $\lvert z_0 \cdot \sin\theta \rvert$	≥ 10.0	≥ 10.0
Number of hits in the PD	≥ 1	≥ 1
Number of hits in the SCT	≥ 6	≥ 6

Table 10.2: The best track selection for the b-jets obtained during the optimization studies. The track selection used in ATLAS [221] is also shown for comparison.

Chapter 11

Summary

This dissertation presents a novel search for flavor-changing neutral currents in the decay of a top quark to an up-type quark ($q = u, c$) and a Higgs boson, with the Higgs boson decaying to $b\bar{b}$. The search is based on $t\bar{t}$ final states, where one top quark is required to decay into Wb, with the W boson decaying leptonically, while the other top quark decays into Hq, yielding $t\bar{t} \to WbHq \to l\nu bb\bar{b}q$. The analysis is performed using pp collision data at center-of-mass energies of $\sqrt{s} = 8$ TeV recorded in 2012 with the ATLAS detector at the LHC and corresponding to an integrated luminosity of 20.3 fb^{-1}.

The lepton+jets final state is characterized by one isolated electron or muon with moderately high transverse momentum, at least four jets and a large missing transverse energy. The search exploits the high multiplicity of b jets characteristic of signal events to separate the signal from the background. In order to optimize the sensitivity of the search, $t\bar{t}$ events are categorized into nine different channels depending on the number of jets (4, 5 and $\geq$6) and on the number of b-tagged jets (2, 3 and $\geq$4).

After event categorization, the signal-to-background ratio is very low even in the most sensitive analysis regions. A suitable discriminating variable between signal and background, based on a per-event likelihood function, is constructed. The main background for the analysis is $t\bar{t}$+jets production, accounting for more than 90% of the background in all regions. The systematic uncertainties on the modeling of the $t\bar{t}$+HF background constitute the main source of sensitivity degradation. In order to reduce the impact of the systematic uncertainties, both theoretical and experimental, the analysis uses a profile likelihood fit exploiting high-statistics control regions to constrain in-situ the leading uncertainties and improve the background modeling.

The analysis is performed separately for $t \to Hc$ and $t \to Hu$ searches and, in the absence of a significant excess in data above the background expectation, 95% CL limits are set on BR($t \to Hc$) and BR($t \to Hu$). The observed (expected) upper limits on the $t \to Hc$ and $t \to Hu$ branching ratios are 0.55% (0.42%) and 0.60% (0.65%) respectively, at the 95% CL. The analysis presented in this dissertation constitutes the single most sensitive search for $t \to Hc$ decays to date.

The results from other ATLAS searches (as well as from CMS searches) are summarized, including a previous search probing $H \to \gamma\gamma$ decays, and a reinterpretation of a search for $t\bar{t}H$ production in multilepton final states, which exploits the $H \to WW^*, \tau\tau$ decay modes. All ATLAS searches discussed in this dissertation have comparable sensitivity, and they have been combined, significantly improving upon the individual searches. The observed (expected) 95% CL combined upper limits on the $t \to Hc$

and $t \to Hu$ branching ratios are 0.46% (0.25%) and 0.45% (0.29%) respectively. The corresponding observed (expected) upper limits on the $|\lambda_{tcH}|$ and $|\lambda_{tuH}|$ couplings are 0.13 (0.10) and 0.13 (0.10) respectively. Upper limits in the $t \to Hc$ versus $t \to Hu$ branching ratio plane, as well as best-fit branching ratios, are also reported. The combination of the three ATLAS searches yields the most sensitive direct bounds on tqH ($q = u, c$) interactions measured so far.

After the 2013-2014 shutdown, the LHC has resumed operations in 2015 and have started providing pp collisions at a center-of-mass energy of $\sqrt{s} = 13$ TeV. At this higher energy the production cross sections for FCNC processes increases significantly, and a large integrated luminosity is expected to be collected over the next years. The sophisticated $t\bar{t} \to WbHq$ search, discussed in this dissertation has demonstrated the potential of the $H \to b\bar{b}$ decay channel, and represents a stepping stone for further refined searches in Run 2. In particular, a number of possible improvements have been identified in this dissertation. Therefore, significant gains in sensitivity to tqH interactions are expected in the near future, opening the door to the observation of new phenomena beyond the SM.

Appendix A

Signal Modeling

As discussed in Sec. 5.3.5, the $t\bar{t} \to WbHq$ signal is simulated using the PROTOS+PYTHIA LO generator, while the $t\bar{t} \to WbWb$ background is modeled using the POWHEG-BOX+PYTHIA NLO generator with further sequential reweighting on the partonic $t\bar{t}$ p_{T} and top quark p_{T} in order to match differential cross section measurements at 7 TeV. Ideally, the FCNC signal would be modeled with the same generator and reweighting corrections as the $t\bar{t} \to WbWb$ background, since they both originate from $t\bar{t}$ production. In order to achieve an improved description of the FCNC signal, and a means to implement a treatment of $t\bar{t}$ modeling systematics affecting both signal and background as consistent as possible, the following strategy is followed.

First, a sequential reweighting of $t\bar{t}$ p_{T} followed by reweighting of top quark p_{T} is applied to the FCNC signal in PROTOS+PYTHIA in order to match the distributions in the original POWHEG-BOX+PYTHIA (prior to application of reweighting to match the differential cross section measurements). The goal is to bring PROTOS+PYTHIA to a level as close as possible to the original POWHEG-BOX+PYTHIA, so that the common set of reweighting corrections to match the differential cross section measurements and associated systematics are applied in a unified way to both signal and background. This first set of corrections for PROTOS+PYTHIA is derived using two samples of $t\bar{t} \to WbWb$ [1] generated with PROTOS+PYTHIA and with POWHEG-BOX+PYTHIA. The comparison of the $t\bar{t}$ and top quark p_{T} in PROTOS+PYTHIA to that in POWHEG-BOX+PYTHIA before and after applying this sequential reweighting is shown in Fig. A.1. After the sequential reweighting, the agreement is significantly improved up to p_{T} values of approximately 300 GeV. Although the agreement is not perfect at high p_{T} values, we consider it sufficient for our purpose.

After this first reweighting, it is assumed that the PROTOS+PYTHIA $t\bar{t}$ sample is for all practical purposes equivalent to the original POWHEG-BOX+PYTHIA $t\bar{t}$ sample. Next, a second sequential reweighting on $t\bar{t}$ and top quark p_{T} is applied, the same one used in POWHEG-BOX+PYTHIA to match the differential cross section measurements. It is checked that after the two-step reweighting an improved agreement is obtained in reco-level distributions between PROTOS+PYTHIA $t\bar{t} \to WbWb$ and the standard reweighted POWHEG-BOX+PYTHIA $t\bar{t} \to WbWb$. Comparisons for several lepton plus $\geq$4 jets selections with exactly 2 b-tags are shown in Figs. A.2–A.4. While the agreement is significantly improved after reweighting, some small residual shape differences can be observed. Probably more importantly, some residual differences in the yields

[1] To derive this correction only the partonic top kinematics is used and the top decay products are of no relevance.

for the different jet multiplicity regions remain: 6.6% for 4 jets, 11.4% for 5 jets and 7.6% for ≥6 jets, which will be taken as uncertainties on the signal acceptance for each of the jet multiplicity bins (independent on b-tag multiplicity).

Finally, the two-step sequential reweightings on $t\bar{t}$ and top quark p_{T} are applied to the FCNC signal. A comparison on the yields and final discriminant variable between original and reweighted $t\bar{t} \to WbHc$ signal in each of the analysis channels is shown in Fig. A.5. The main effect is a few percent increase of the signal yield in the 4 jets channels, and a similar decrease at higher jet multiplicity. This is expected since the original Protos was predicting a slightly harder $t\bar{t}$ p_{T} spectrum than reweighted POWHEG-BOX+PYTHIA, which is correlated with the jet multiplicity and corrected by the two-step reweighting.

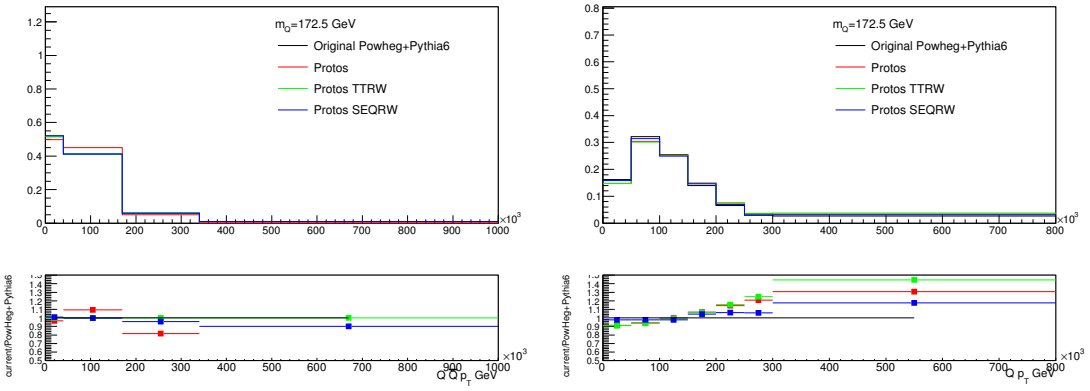

(a) (b)

Figure A.1: Comparison of the distributions of (a) $t\bar{t}$ p_{T} and (b) top quark p_{T} between original POWHEG-BOX+PYTHIA (black), nominal PROTOS+PYTHIA (red), PROTOS+PYTHIA after $t\bar{t}$ p_{T} reweighting (green) and PROTOS+PYTHIA after sequential $t\bar{t}$ p_{T} plus top quark p_{T} reweighting (blue).

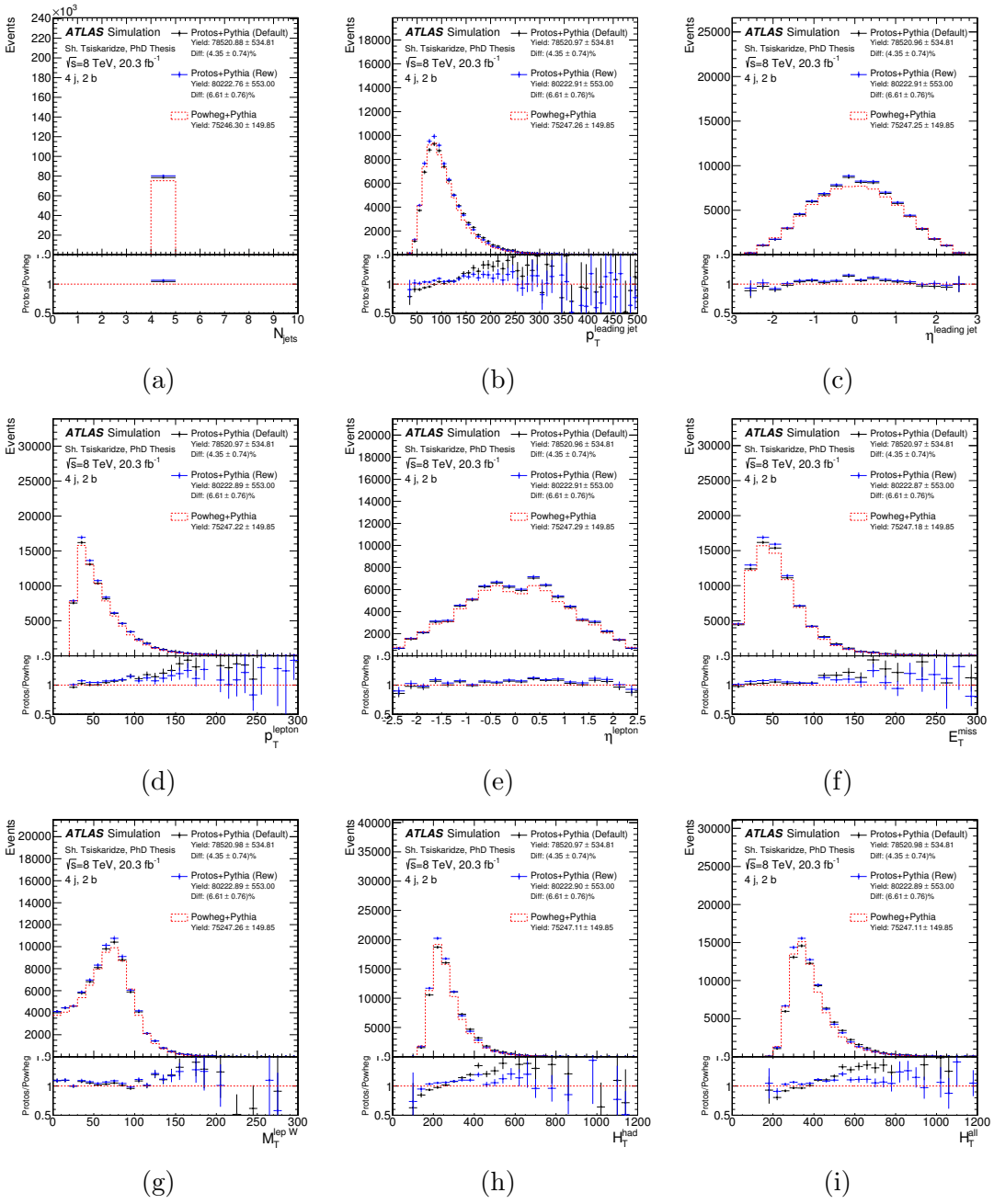

Figure A.2: Comparison between the default $t\bar{t} \to WbWb$ POWHEG-BOX+PYTHIA prediction (reweighted to the differential cross section measurements at 7 TeV) and $t\bar{t} \to WbWb$ PROTOS+PYTHIA before and after the two-step reweighting procedure (see text for details) to better approximate the top and $t\bar{t}$ kinematics of the default POWHEG-BOX+PYTHIA prediction. The comparison is made for the combined e+jets and μ+jets channels in the (4 j, 2 b) region for a number of kinematic variables: (a) jet multiplicity, (b) leading jet p_{T}, (c) leading jet η, (d) lepton p_{T}, (e) lepton η, (f) missing transverse energy, (g) W transverse mass, (h) $H_{\mathrm{T}}^{\mathrm{had}}$ and (i) H_{T} (defined as the scalar sum of the lepton p_{T}, $E_{\mathrm{T}}^{\mathrm{miss}}$ and $H_{\mathrm{T}}^{\mathrm{had}}$). Only statistical uncertainties are being shown.

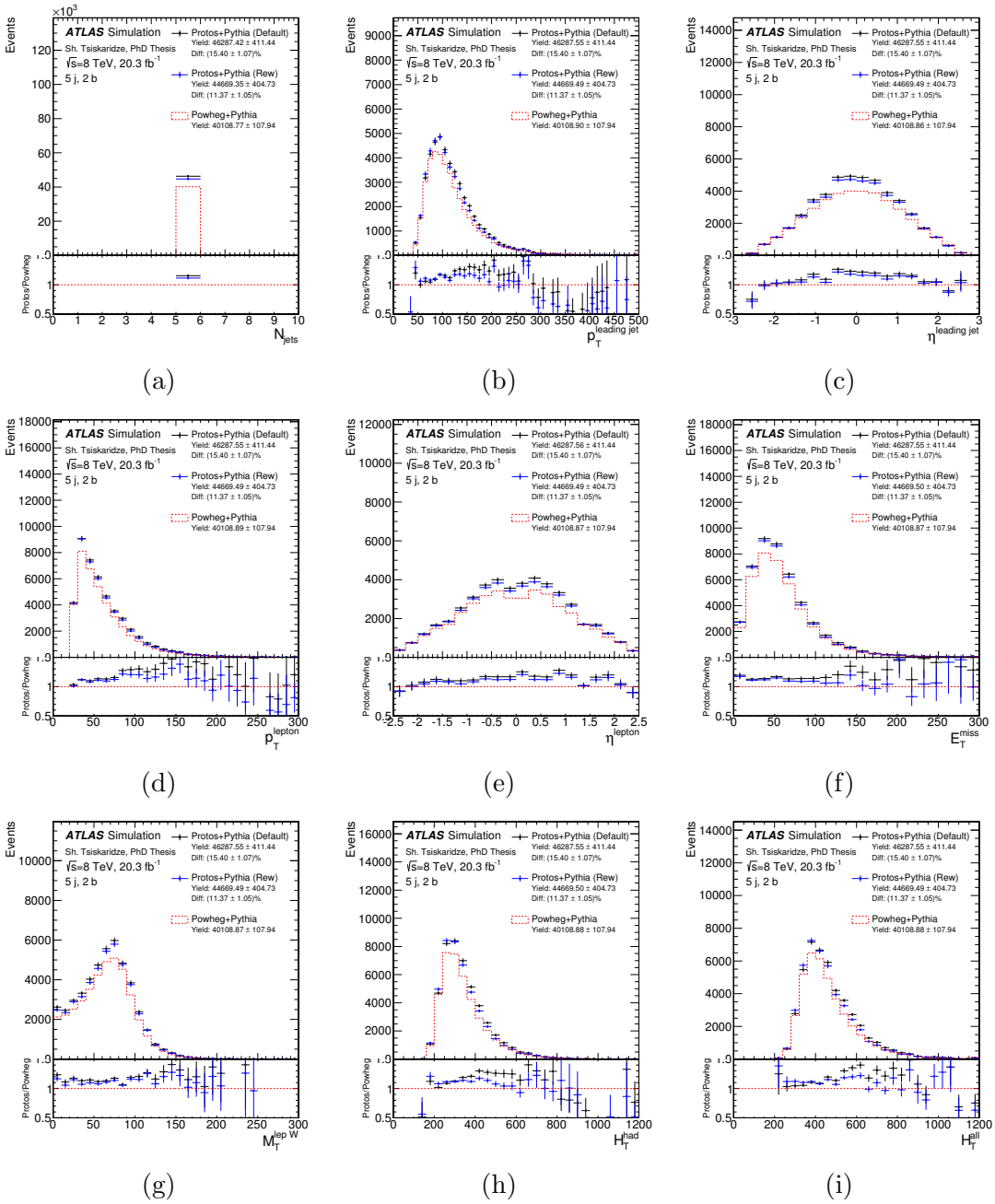

(a) (b) (c)

(d) (e) (f)

(g) (h) (i)

Figure A.3: Comparison between the default $t\bar{t} \to WbWb$ POWHEG-BOX+PYTHIA prediction (reweighted to the differential cross section measurements at 7 TeV) and $t\bar{t} \to WbWb$ PROTOS+PYTHIA before and after the two-step reweighting procedure (see text for details) to better approximate the top and $t\bar{t}$ kinematics of the default POWHEG-BOX+PYTHIA prediction. The comparison is made for the combined e+jets and μ+jets channels in the (5 j, 2 b) region for a number of kinematic variables: (a) jet multiplicity, (b) leading jet p_{T}, (c) leading jet η, (d) lepton p_{T}, (e) lepton η, (f) missing transverse energy, (g) W transverse mass, (h) $H_{\mathrm{T}}^{\mathrm{had}}$ and (i) H_{T} (defined as the scalar sum of the lepton p_{T}, $E_{\mathrm{T}}^{\mathrm{miss}}$ and $H_{\mathrm{T}}^{\mathrm{had}}$). Only statistical uncertainties are being shown.

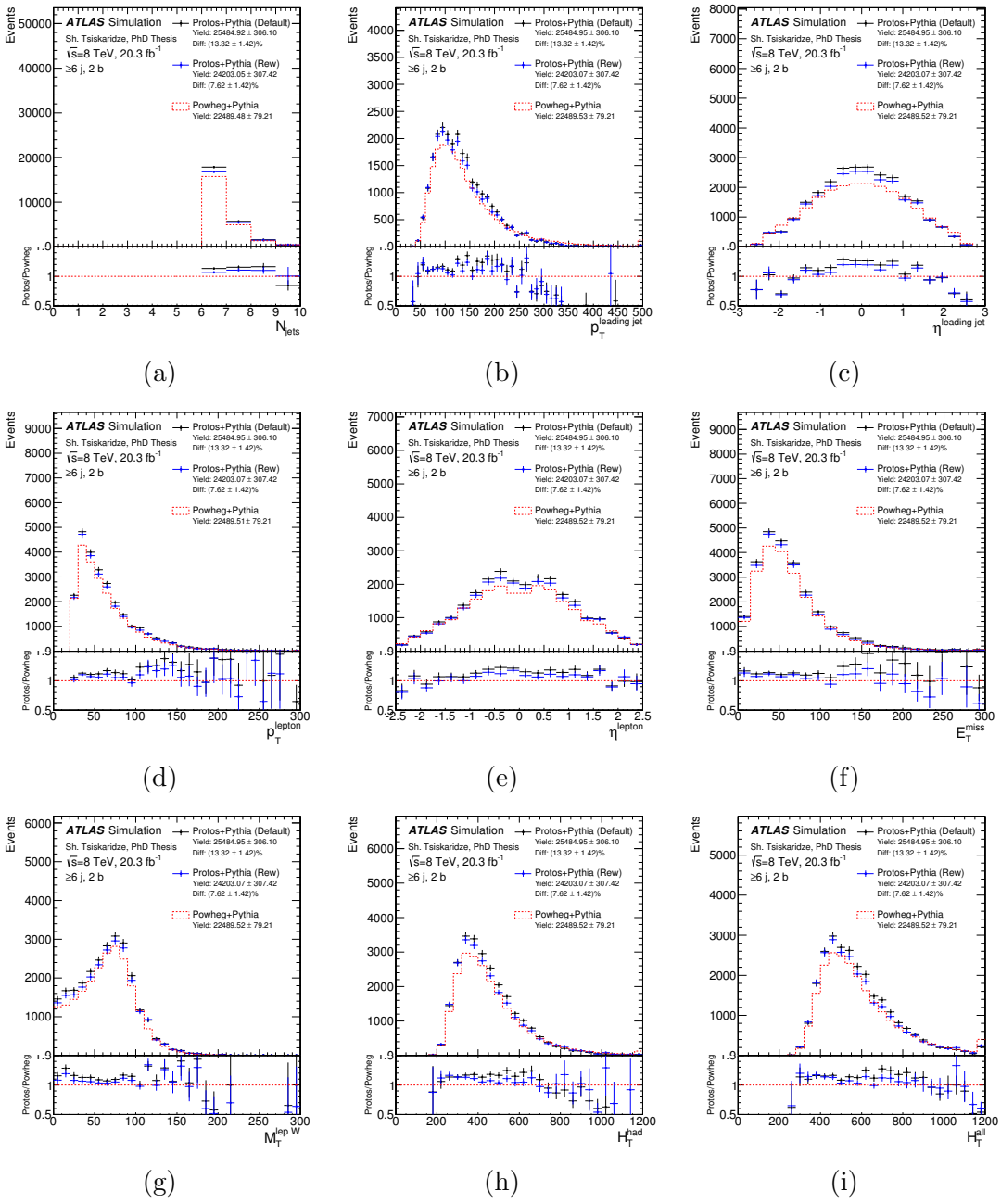

Figure A.4: Comparison between the default $t\bar{t} \to WbWb$ POWHEG-BOX+PYTHIA prediction (reweighted to the differential cross section measurements at 7 TeV) and $t\bar{t} \to WbWb$ PROTOS+PYTHIA before and after the two-step reweighting procedure (see text for details) to better approximate the top and $t\bar{t}$ kinematics of the default POWHEG-BOX+PYTHIA prediction. The comparison is made for the combined e+jets and μ+jets channels in the ($\geq$6 j, 2 b) region for a number of kinematic variables: (a) jet multiplicity, (b) leading jet p_{T}, (c) leading jet η, (d) lepton p_{T}, (e) lepton η, (f) missing transverse energy, (g) W transverse mass, (h) $H_{\mathrm{T}}^{\mathrm{had}}$ and (i) H_{T} (defined as the scalar sum of the lepton p_{T}, $E_{\mathrm{T}}^{\mathrm{miss}}$ and $H_{\mathrm{T}}^{\mathrm{had}}$). Only statistical uncertainties are being shown.

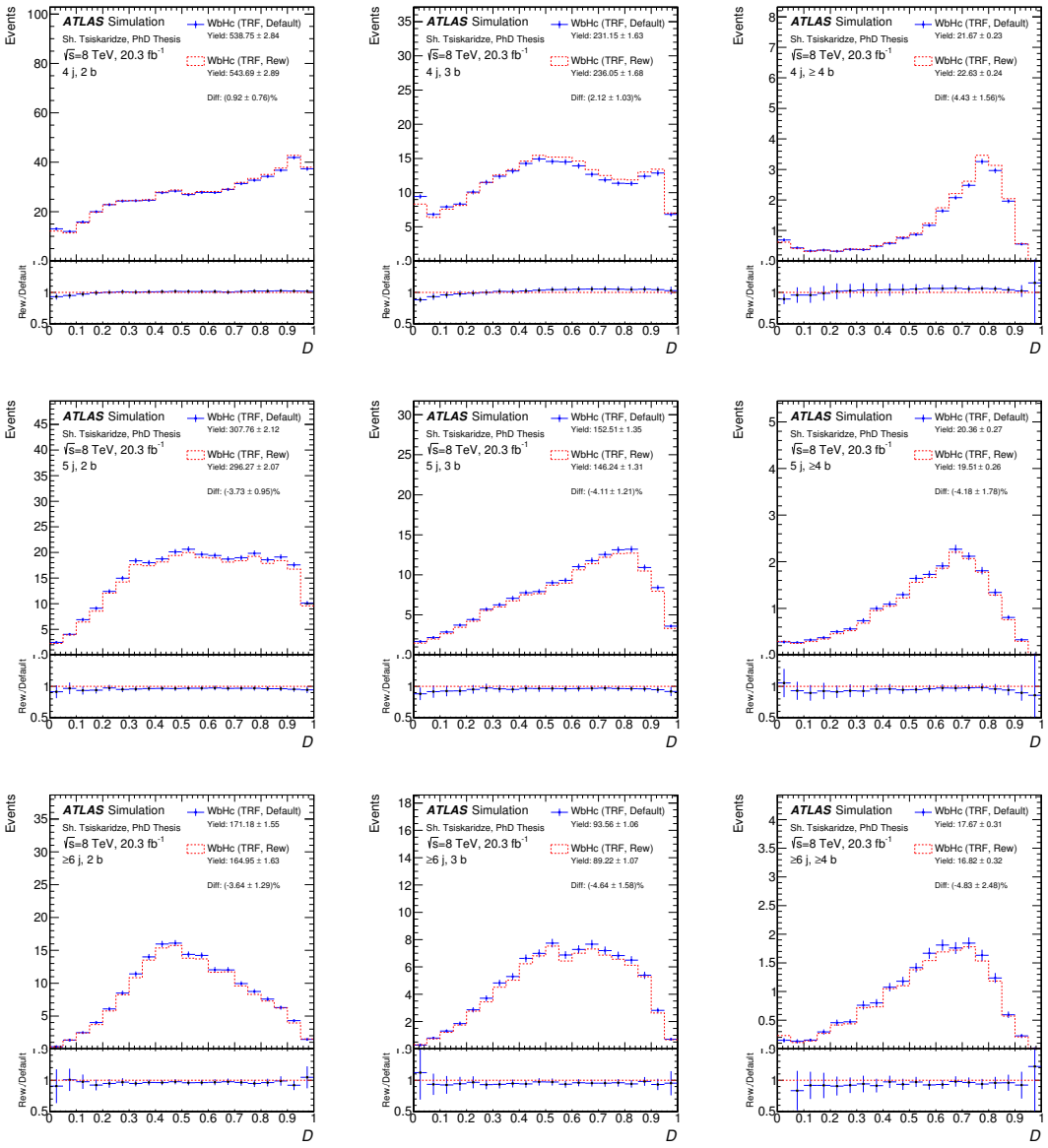

Figure A.5: Comparison of the $\mathcal{D}$ distribution in $WbHc$ signal before and after reweighting for the combined e+jets and μ+jets selections in each of channels considered in the analysis. In both cases the signal distributions are obtained using the TRF method. From top to bottom and left to right: (4j, 2b), (4j, 3b), (4j, 4b), (5j, 2b), (5j, 3b), (5j, ≥4b), (≥6j, 2b), (≥6j, 3b), and (≥6j, ≥4b) channels.

Appendix B

Tag Rate Function Validation

The TRF method relies on the correct parametrization of the flavor tagging efficiency in MC samples. A careful validation of the efficiencies used is performed by checking the compatibility of normalization and shape for relevant kinematic distributions obtained after the standard cut on the b-tagging output variable and the prediction based on the TRF method.

The fractional differences between the DT-based and TRF-based predicted normalizations for FCNC signals and $t\bar{t}$ backgrounds in each of the analysis channels considered are summarized in Tables B.1 and B.2, respectively. The corresponding shape comparisons for the D discriminant are shown in Figs. B.1-B.5.

Channel	$t\bar{t} \to WbHc$	$t\bar{t} \to WbHu$
4 j, 2 b	0.57 ± 0.99 % (0.58)	-0.77 ± 1.01 % (0.77)
4 j, 3 b	2.78 ± 1.46 % (1.91)	2.13 ± 1.57 % (1.35)
4 j, 4 b	13.22 ± 4.37 % (3.02)	-28.96 ± 8.99 % (3.22)
5 j, 2 b	0.59 ± 1.32 % (0.45)	-0.79 ± 1.32 % (0.60)
5 j, 3 b	1.87 ± 1.79 % (1.04)	1.48 ± 1.90 % (0.78)
5 j, ≥4 b	10.98 ± 4.55 % (2.41)	-5.84 ± 8.18 % (0.71)
≥6 j, 2 b	-0.04 ± 1.87 % (0.02)	-0.22 ± 1.87 % (0.12)
≥6 j, 3 b	-0.01 ± 2.36 % (0.01)	-0.19 ± 2.52 % (0.08)
≥6 j, ≥4 b	13.97 ± 5.68 % (2.46)	-13.73 ± 6.93 % (1.98)

Table B.1: Fractional difference, including the statistical uncertainty, between DT and TRF-based predictions for the normalization of the $t\bar{t} \to WbHc$ and $t\bar{t} \to WbHu$ signals in each of the analysis channels considered. The number in parentheses denotes the number of statistical standard deviations.

Channel	$t\bar{t} + b\bar{b}$	$t\bar{t} + c\bar{c}$	$t\bar{t}$+ light
4 j, 2 b	-1.90 ± 1.54 % (1.23)	-1.54 ± 0.91 % (1.69)	-1.00 ± 0.24 % (4.20)
4 j, 3 b	-0.59 ± 2.47 % (0.24)	-3.37 ± 2.00 % (1.68)	2.46 ± 0.69 % (3.55)
4 j, 4 b	-4.01 ± 8.64 % (0.46)	-9.01 ± 9.54 % (0.94)	-0.15 ± 8.20 % (0.02)
5 j, 2 b	-1.94 ± 1.63 % (1.19)	-1.56 ± 0.97 % (1.61)	-0.74 ± 0.34 % (2.19)
5 j, 3 b	3.13 ± 2.27 % (1.38)	-1.81 ± 1.90 % (0.95)	4.32 ± 0.90 % (4.79)
5 j, ≥4 b	1.49 ± 5.62 % (0.26)	-11.32 ± 6.90 % (1.64)	-0.78 ± 7.52 % (0.10)
≥6 j, 2 b	-1.17 ± 1.70 % (0.69)	-0.37 ± 1.04 % (0.36)	-0.34 ± 0.47 % (0.72)
≥6 j, ≥4 b	1.32 ± 4.02 % (0.33)	0.89 ± 5.59 % (0.16)	-11.68 ± 7.19 % (1.63)

Table B.2: Fractional difference, including the statistical uncertainty, between DT and TRF-based predictions for the normalization of the different $t\bar{t}$ background components in each of the analysis channels considered. The number in parentheses denotes the number of statistical standard deviations.

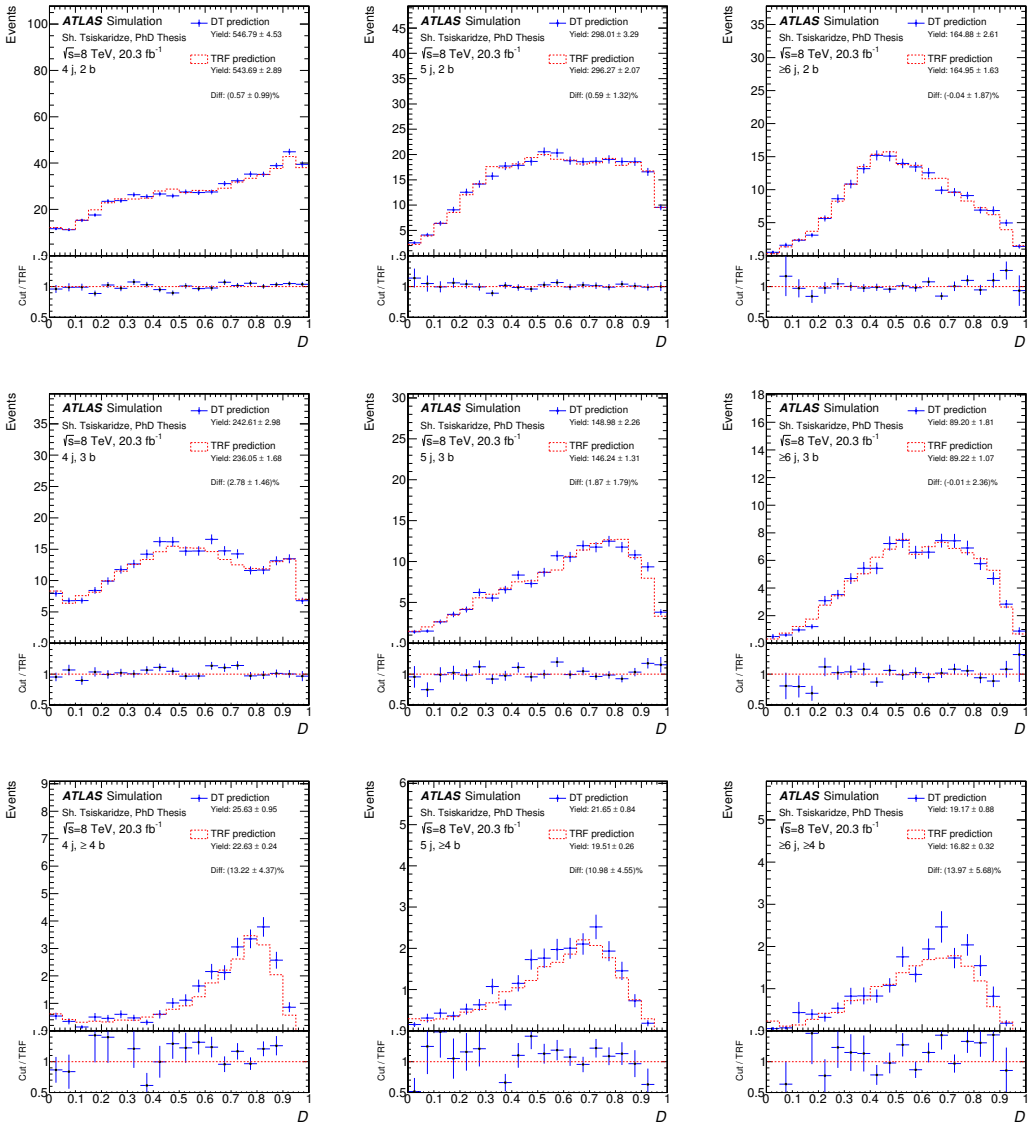

Figure B.1: Comparison between the DT- and TRF-based predictions for the final discriminant variable D corresponding to the $t\bar{t} \to WbHc$ signal in each of the analysis channels considered.

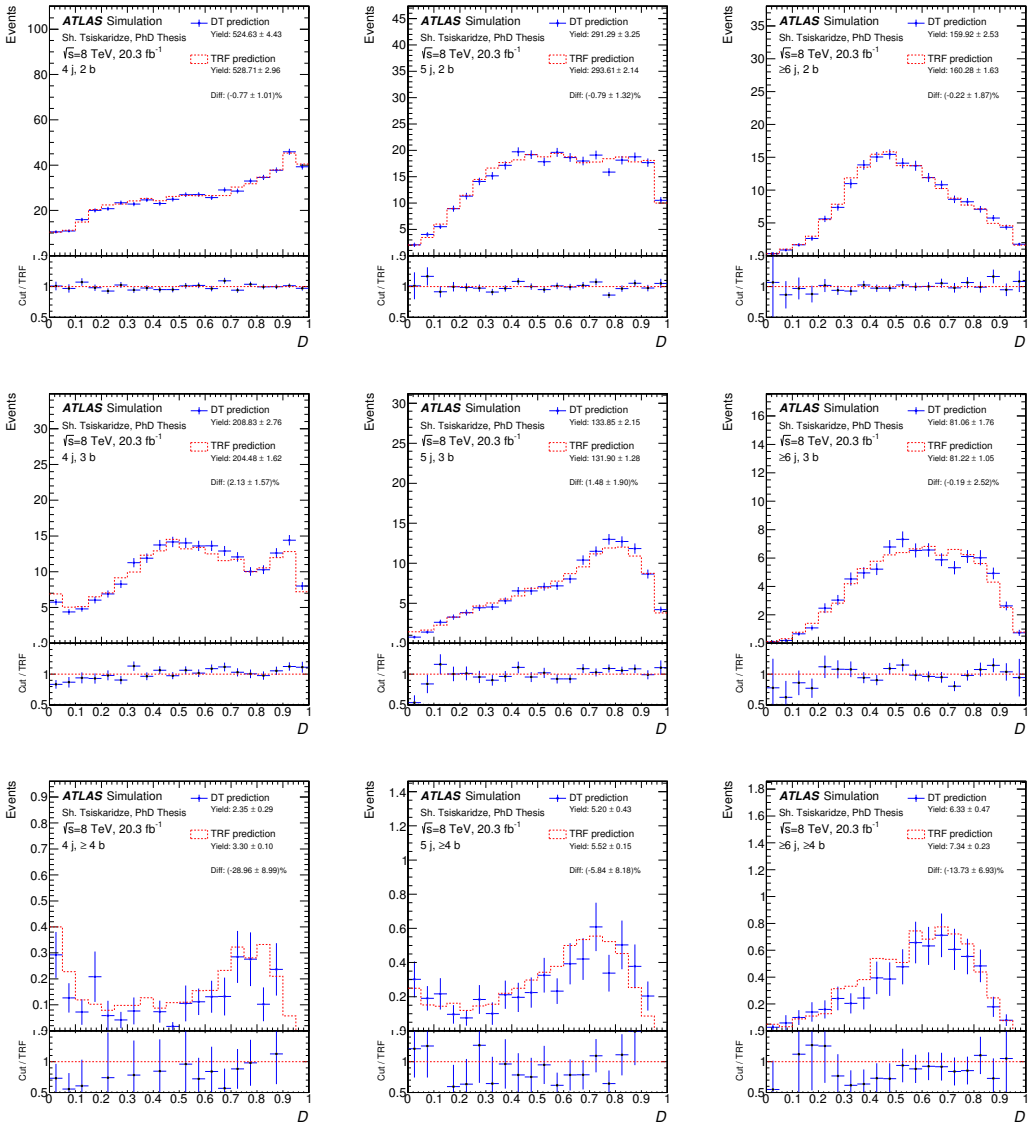

Figure B.2: Comparison between the DT- and TRF-based predictions for the final discriminant variable D corresponding to the $t\bar{t} \to WbHu$ signal in each of the analysis channels considered.

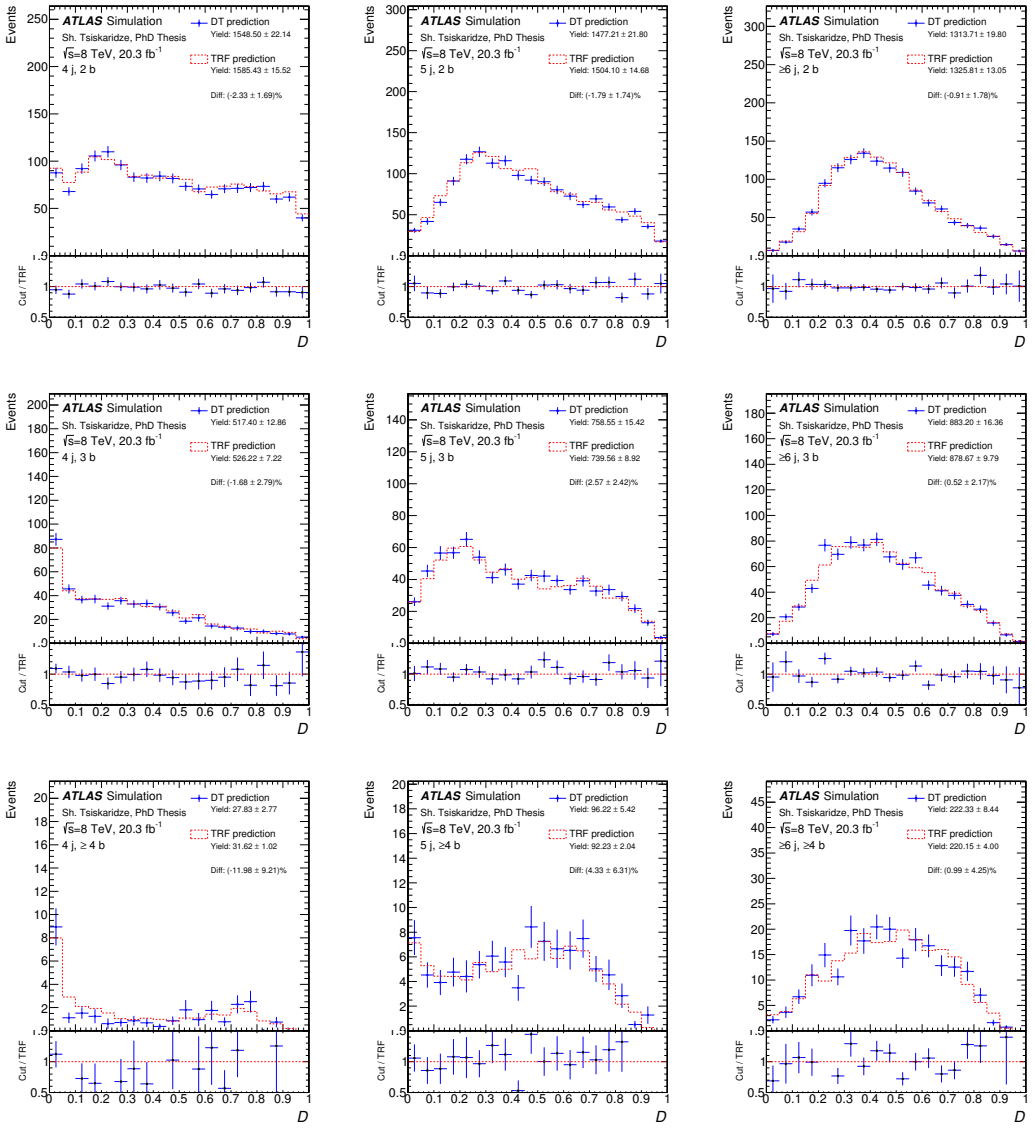

Figure B.3: Comparison between the DT- and TRF-based predictions for the final discriminant variable D corresponding to the $t\bar{t}$+$b\bar{b}$ background in each of the analysis channels considered.

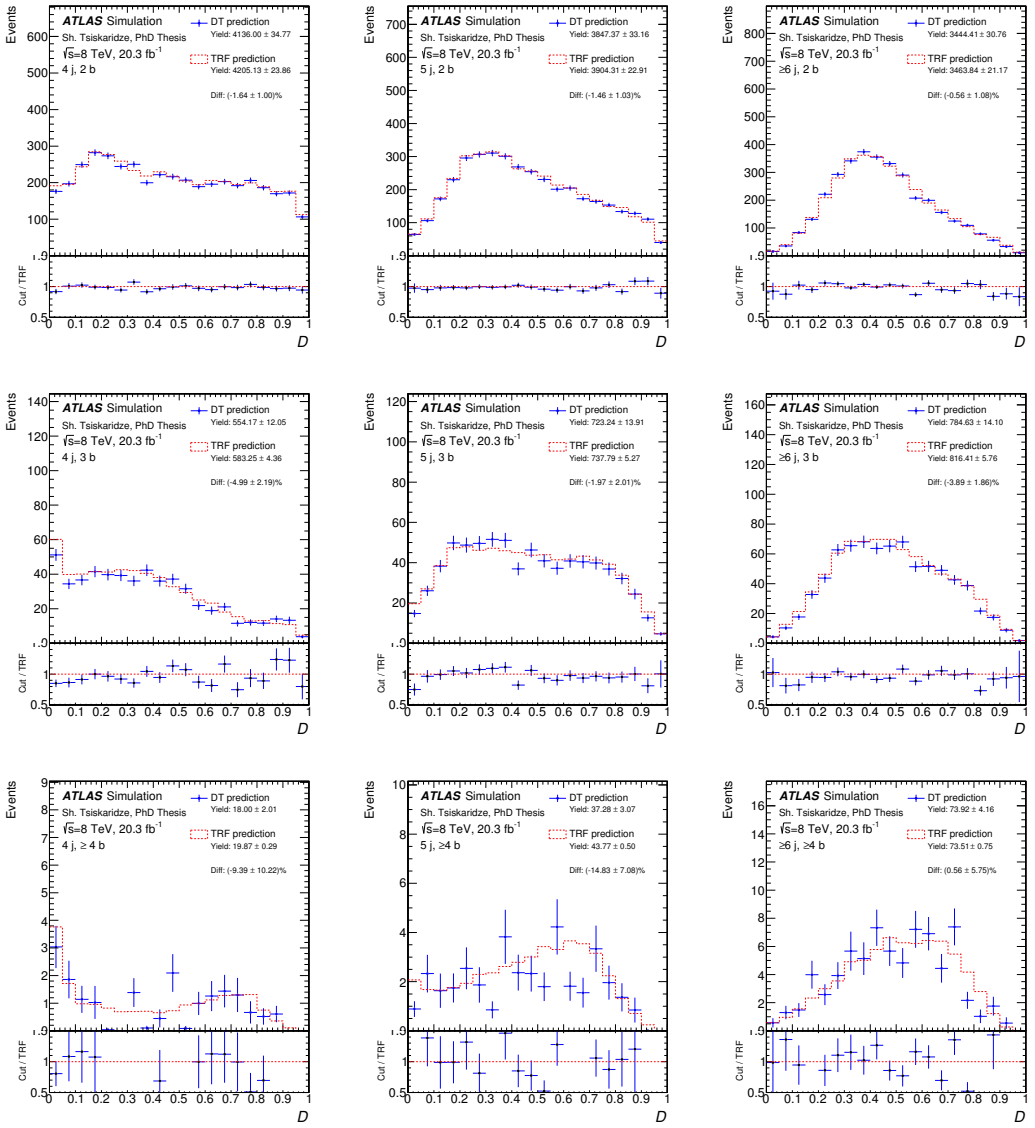

Figure B.4: Comparison between the DT- and TRF-based predictions for the final discriminant variable D corresponding to the $t\bar{t}$+$c\bar{c}$ background in each of the analysis channels considered.

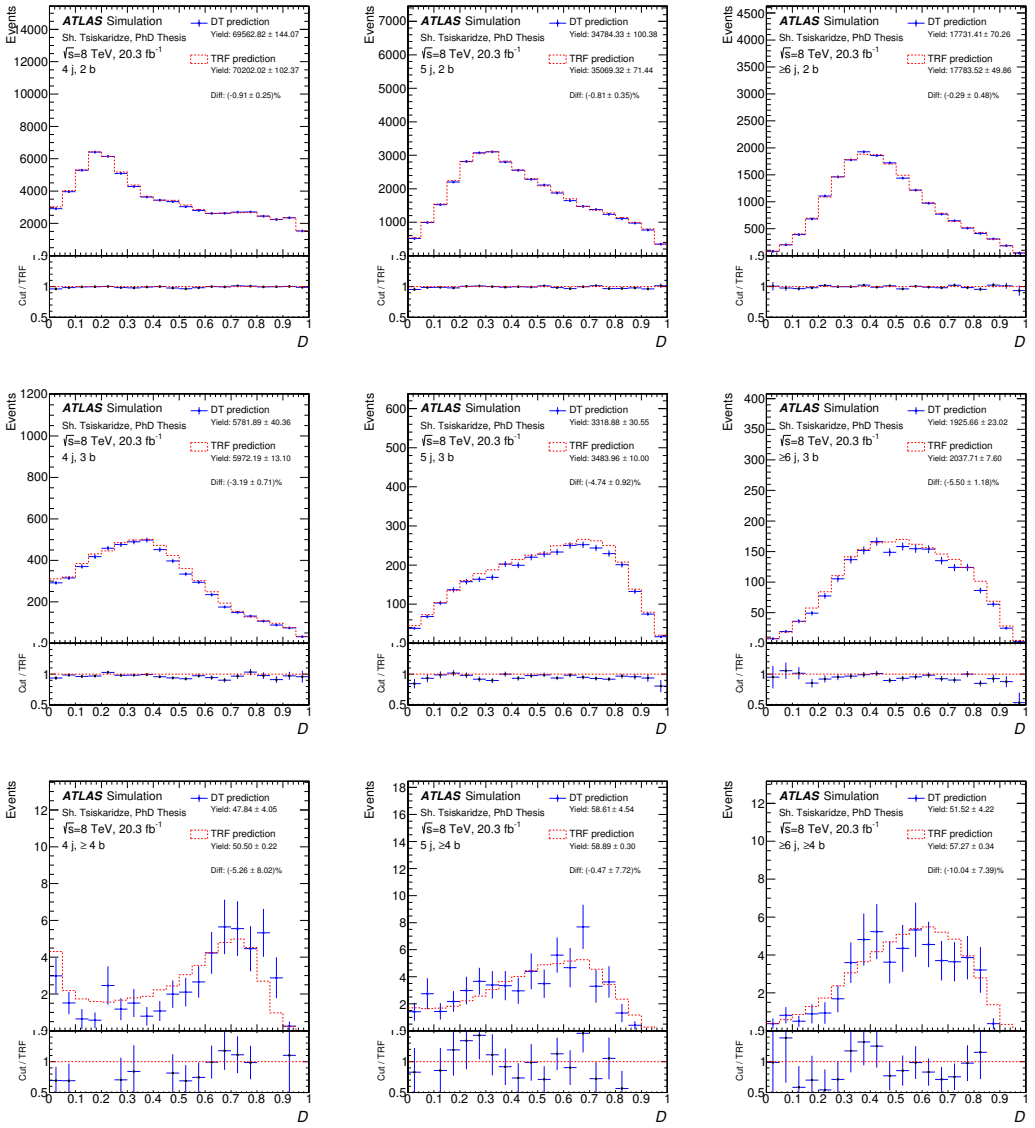

Figure B.5: Comparison between the DT- and TRF-based predictions for the final discriminant variable D corresponding to the $t\bar{t}$+light background in each of the analysis channels considered.

Appendix C

Data-to-MC Comparisons

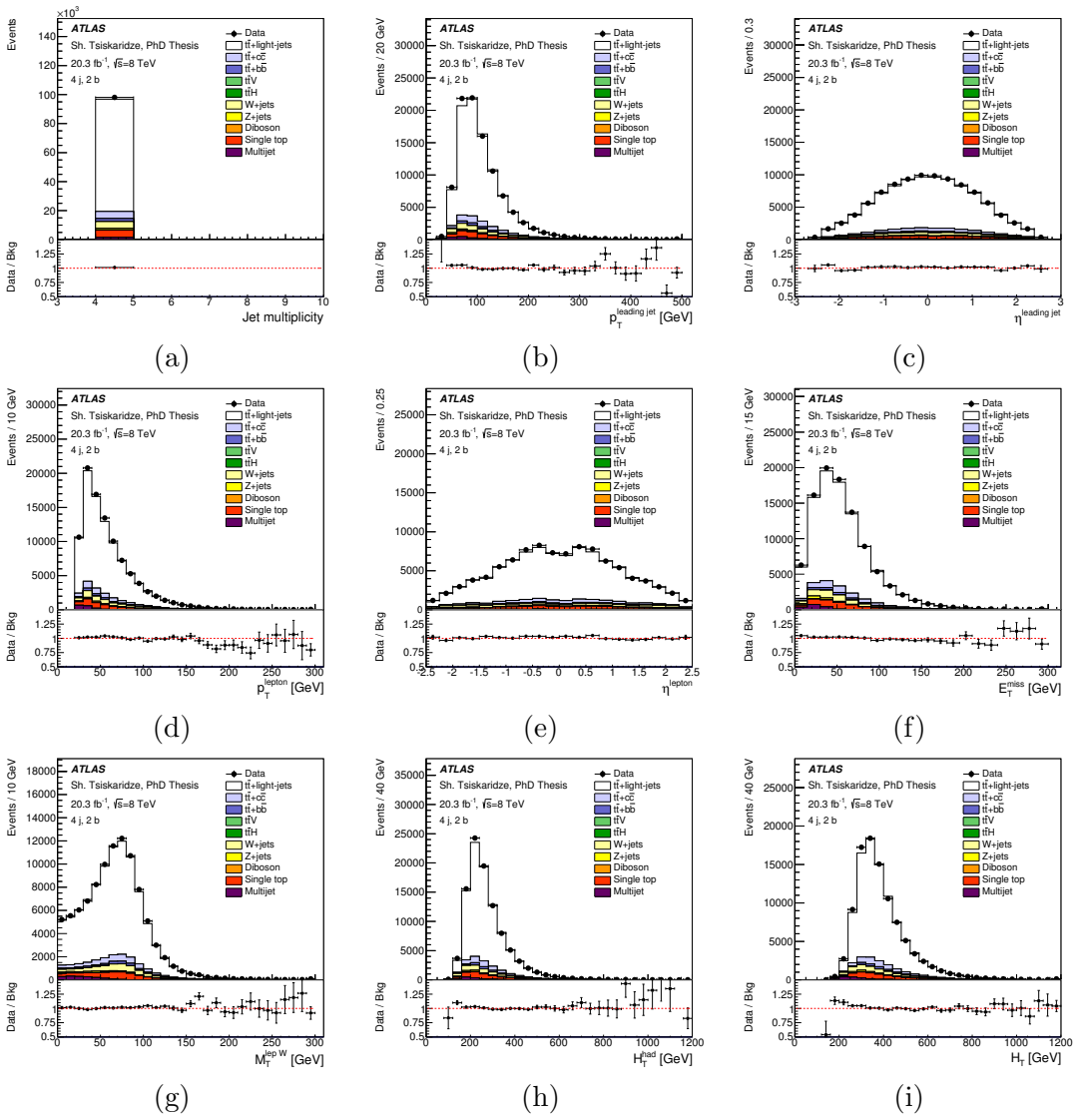

Figure C.1: Comparison between data and prediction in the combined e+jets and μ+jets channels in the (4 j, 2 b) region for a number of kinematic variables: (a) jet multiplicity, (b) leading jet p_{T}, (c) leading jet η, (d) lepton p_{T}, (e) lepton η, (f) missing transverse energy, (g) W transverse mass, (h) $H_{\mathrm{T}}^{\mathrm{had}}$ and (i) H_{T} (defined as the scalar sum of the lepton p_{T}, $E_{\mathrm{T}}^{\mathrm{miss}}$ and $H_{\mathrm{T}}^{\mathrm{had}}$). Only statistical uncertainties are being shown.

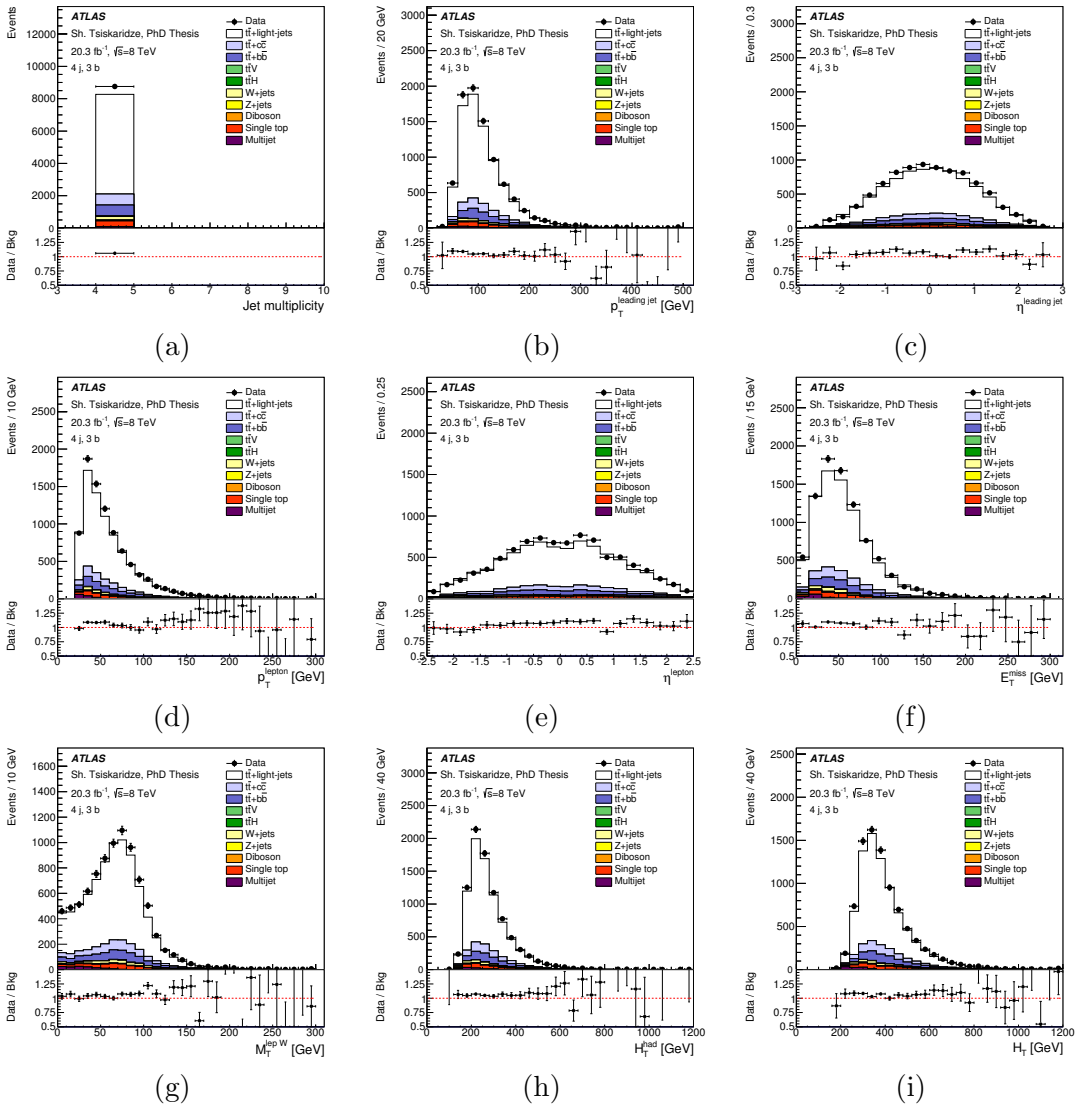

Figure C.2: Comparison between data and prediction in the combined e+jets and μ+jets channels in the (4 j, 3 b) region for a number of kinematic variables: (a) jet multiplicity, (b) leading jet p_{T}, (c) leading jet η, (d) lepton p_{T}, (e) lepton η, (f) missing transverse energy, (g) W transverse mass, (h) $H_{\mathrm{T}}^{\mathrm{had}}$ and (i) H_{T} (defined as the scalar sum of the lepton p_{T}, $E_{\mathrm{T}}^{\mathrm{miss}}$ and $H_{\mathrm{T}}^{\mathrm{had}}$). Only statistical uncertainties are being shown.

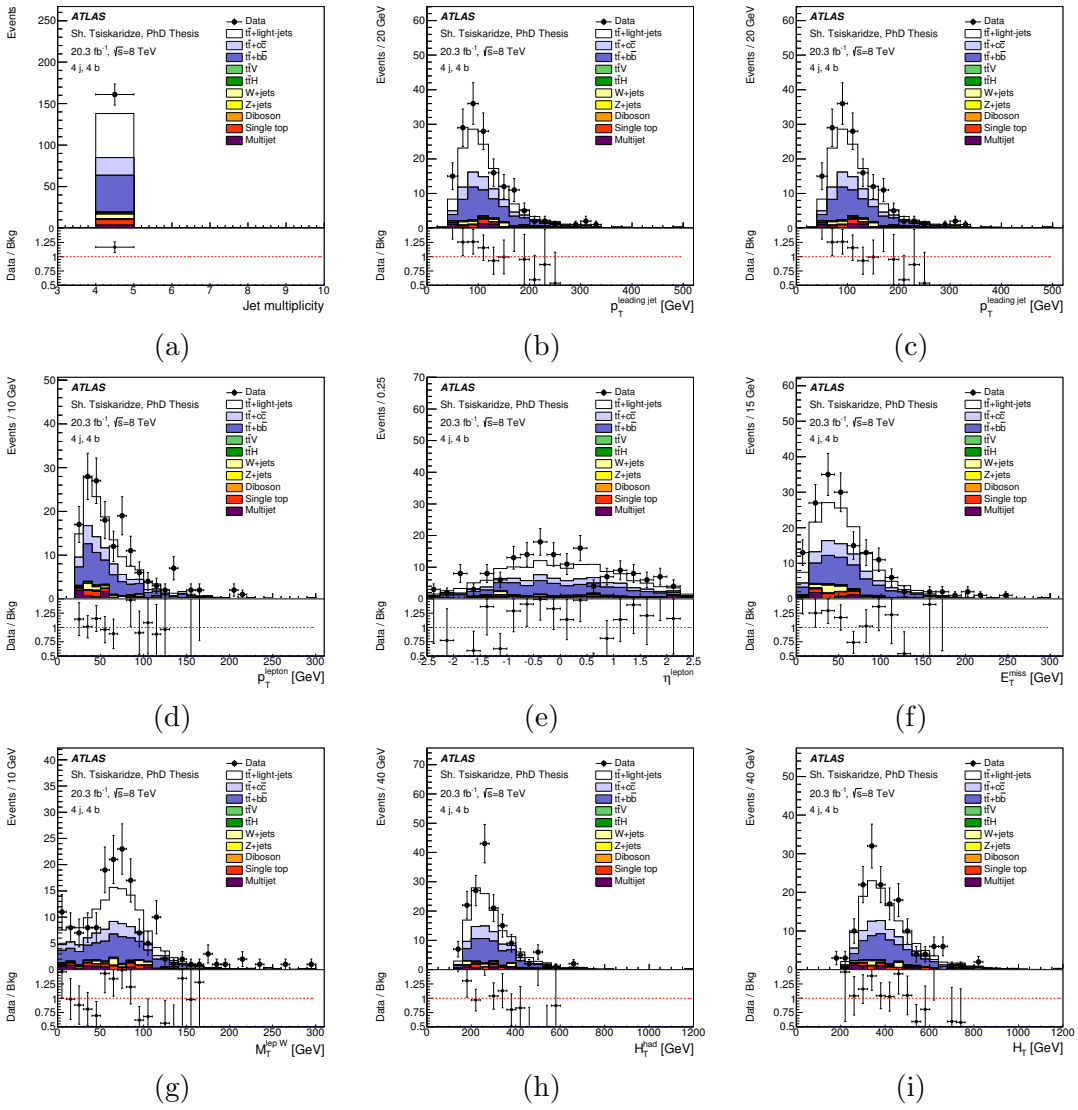

Figure C.3: Comparison between data and prediction in the combined e+jets and μ+jets channels in the (4 j, 4 b) region for a number of kinematic variables: (a) jet multiplicity, (b) leading jet p_{T}, (c) leading jet η, (d) lepton p_{T}, (e) lepton η, (f) missing transverse energy, (g) W transverse mass, (h) $H_{\mathrm{T}}^{\mathrm{had}}$ and (i) H_{T} (defined as the scalar sum of the lepton p_{T}, $E_{\mathrm{T}}^{\mathrm{miss}}$ and $H_{\mathrm{T}}^{\mathrm{had}}$). Only statistical uncertainties are being shown.

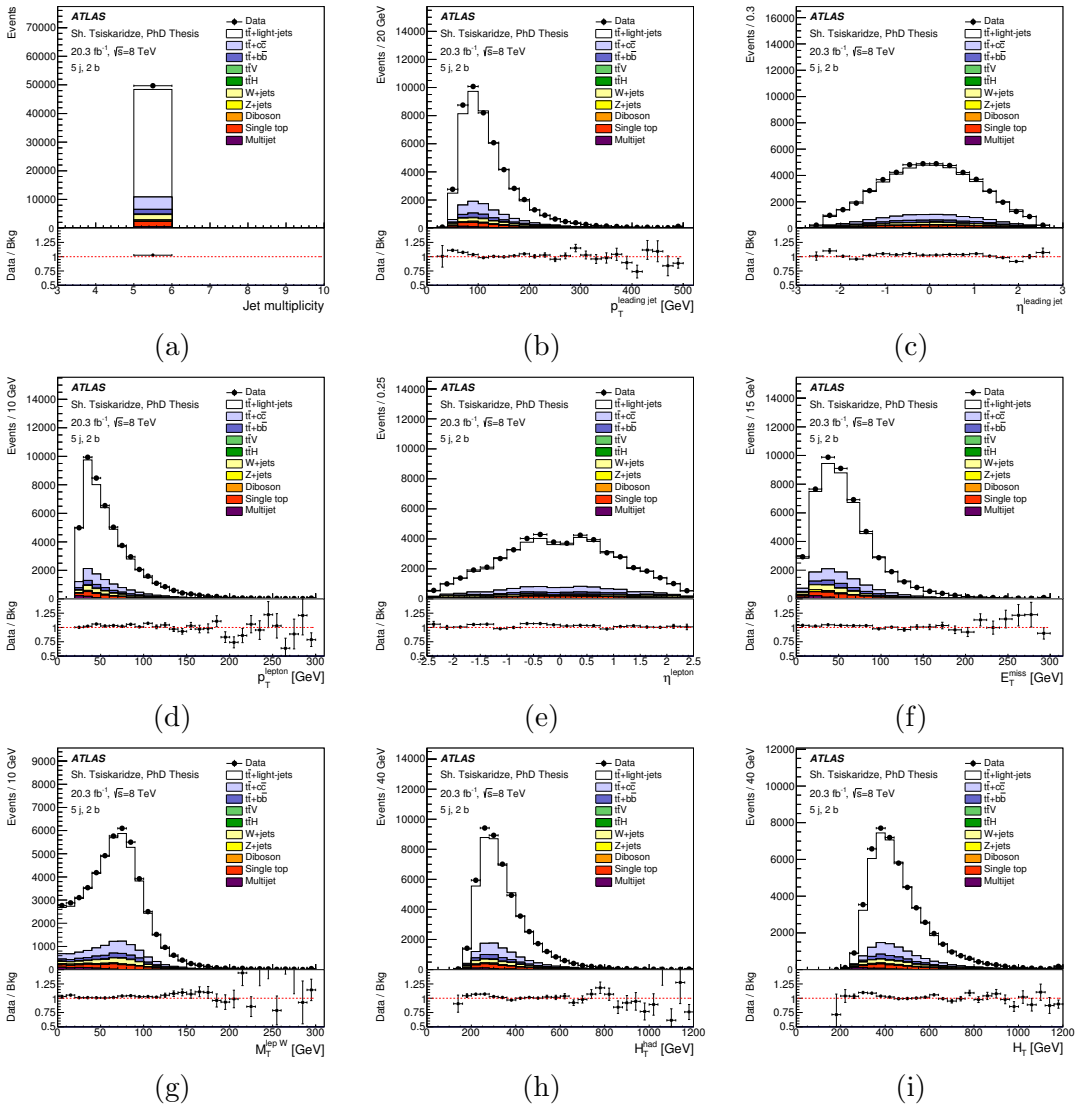

Figure C.4: Comparison between data and prediction in the combined e+jets and μ+jets channels in the (5 j, 2 b) region for a number of kinematic variables: (a) jet multiplicity, (b) leading jet p_{T}, (c) leading jet η, (d) lepton p_{T}, (e) lepton η, (f) missing transverse energy, (g) W transverse mass, (h) $H_{\mathrm{T}}^{\mathrm{had}}$ and (i) H_{T} (defined as the scalar sum of the lepton p_{T}, $E_{\mathrm{T}}^{\mathrm{miss}}$ and $H_{\mathrm{T}}^{\mathrm{had}}$). Only statistical uncertainties are being shown.

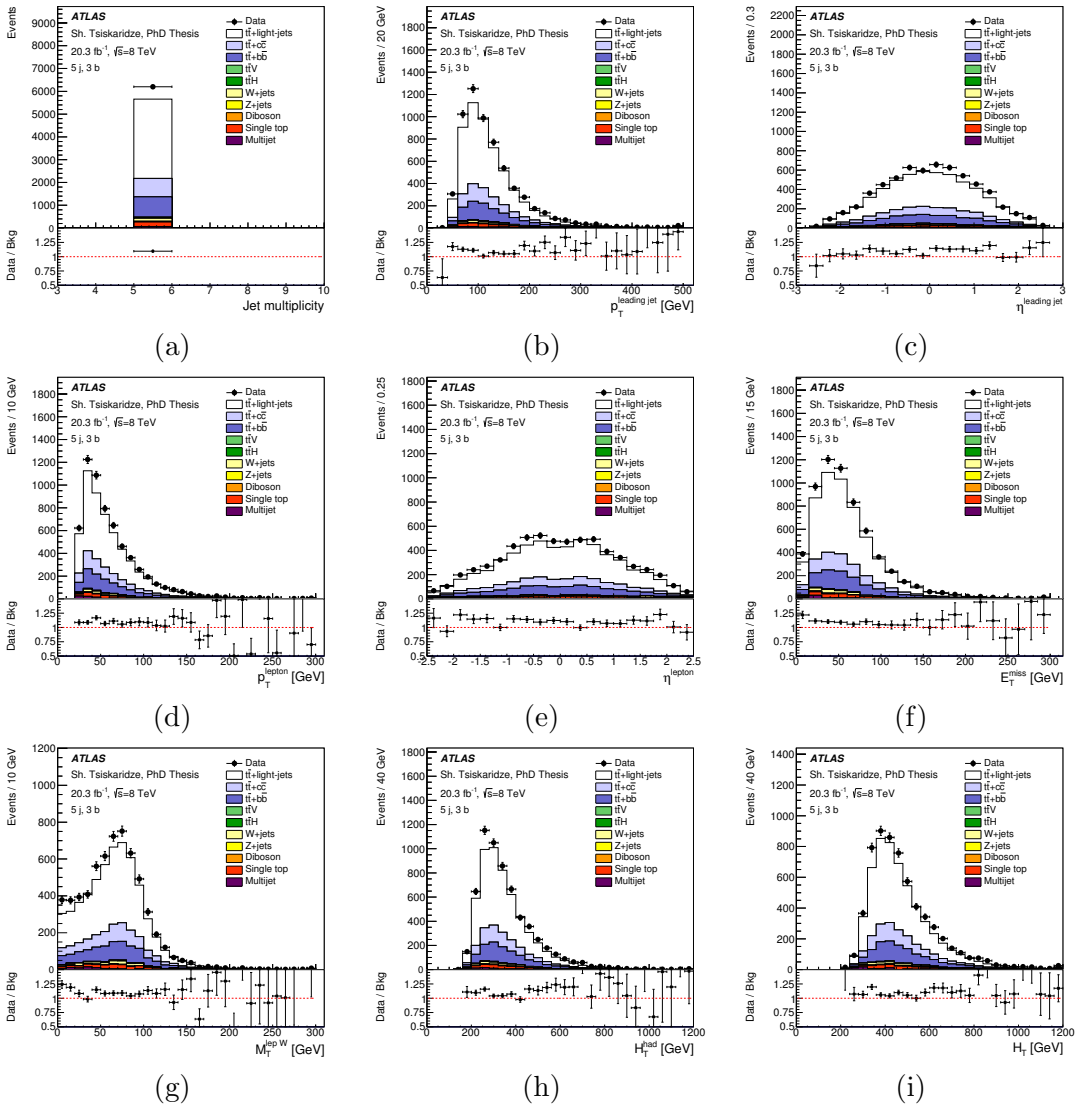

Figure C.5: Comparison between data and prediction in the combined e+jets and μ+jets channels in the (5 j, 3 b) region for a number of kinematic variables: (a) jet multiplicity, (b) leading jet p_{T}, (c) leading jet η, (d) lepton p_{T}, (e) lepton η, (f) missing transverse energy, (g) W transverse mass, (h) $H_{\mathrm{T}}^{\mathrm{had}}$ and (i) H_{T} (defined as the scalar sum of the lepton p_{T}, $E_{\mathrm{T}}^{\mathrm{miss}}$ and $H_{\mathrm{T}}^{\mathrm{had}}$). Only statistical uncertainties are being shown.

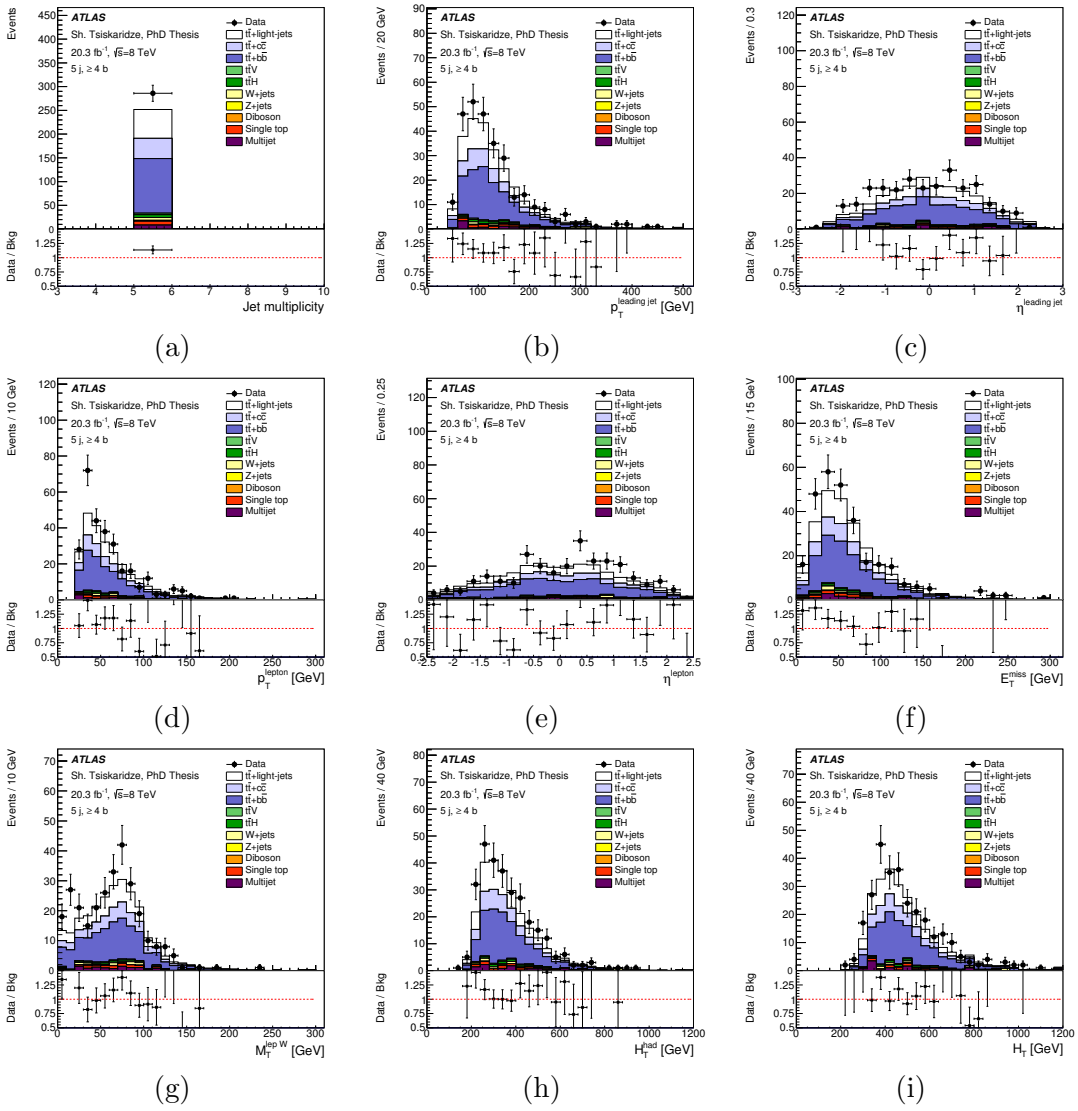

Figure C.6: Comparison between data and prediction in the combined e+jets and μ+jets channels in the (5 j, ≥4 b) region for a number of kinematic variables: (a) jet multiplicity, (b) leading jet p_{T}, (c) leading jet η, (d) lepton p_{T}, (e) lepton η, (f) missing transverse energy, (g) W transverse mass, (h) $H_{\mathrm{T}}^{\mathrm{had}}$ and (i) H_{T} (defined as the scalar sum of the lepton p_{T}, $E_{\mathrm{T}}^{\mathrm{miss}}$ and $H_{\mathrm{T}}^{\mathrm{had}}$). Only statistical uncertainties are being shown.

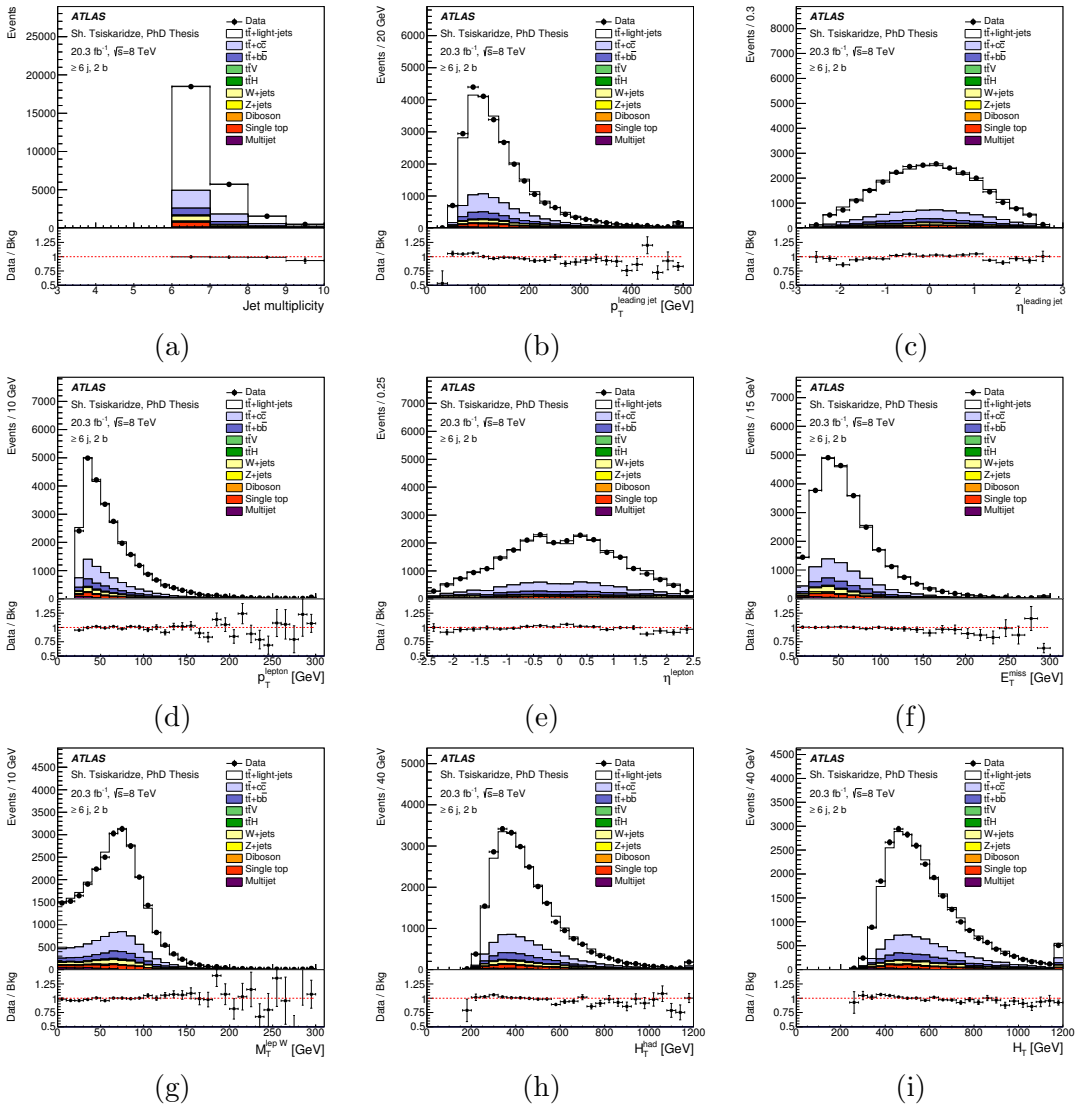

Figure C.7: Comparison between data and prediction in the combined e+jets and μ+jets channels in the (≥6 j, 2 b) region for a number of kinematic variables: (a) jet multiplicity, (b) leading jet p_{T}, (c) leading jet η, (d) lepton p_{T}, (e) lepton η, (f) missing transverse energy, (g) W transverse mass, (h) $H_{\mathrm{T}}^{\mathrm{had}}$ and (i) H_{T} (defined as the scalar sum of the lepton p_{T}, $E_{\mathrm{T}}^{\mathrm{miss}}$ and $H_{\mathrm{T}}^{\mathrm{had}}$). Only statistical uncertainties are being shown.

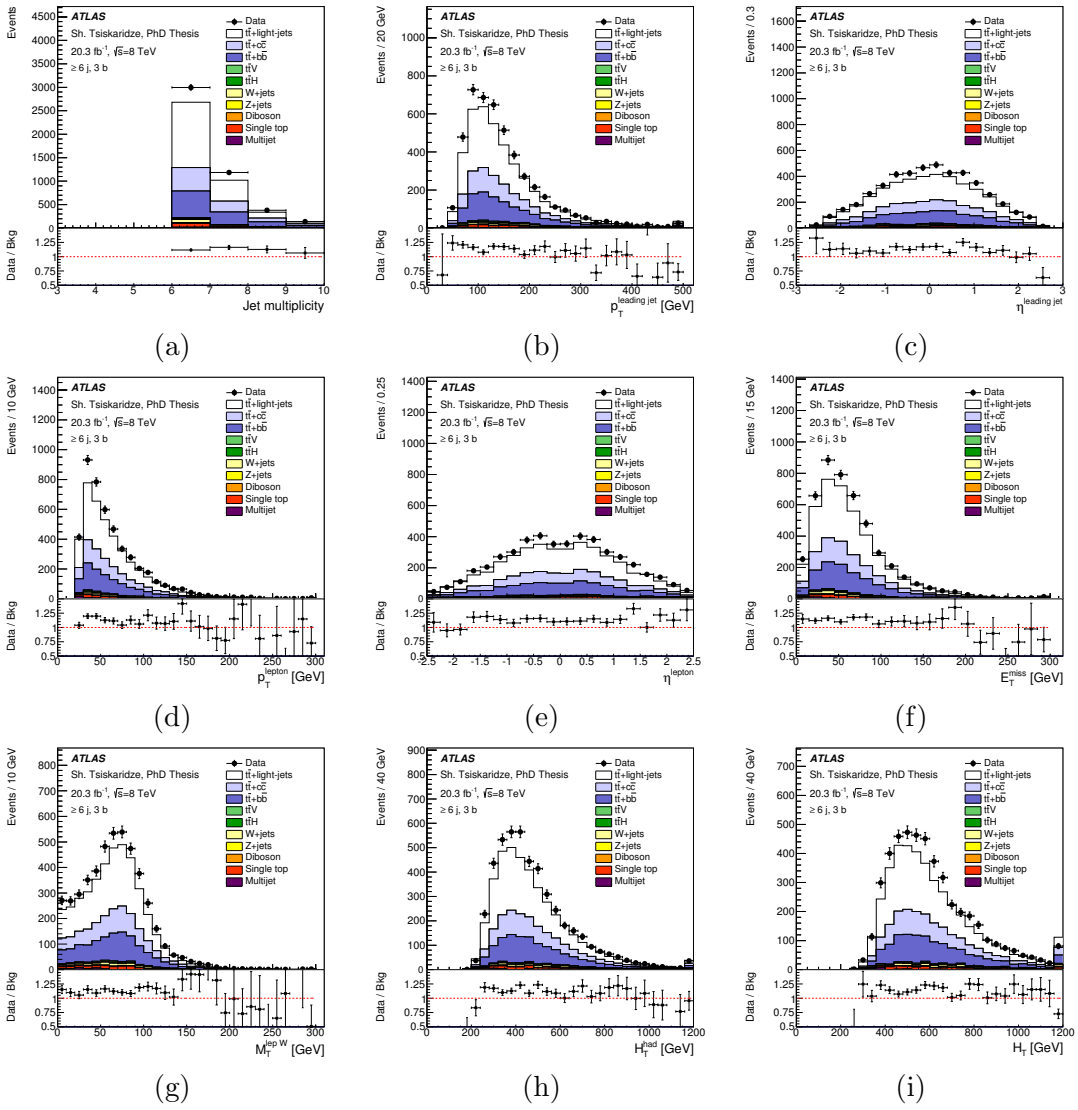

Figure C.8: Comparison between data and prediction in the combined e+jets and μ+jets channels in the ($\geq$6 j, 3 b) region for a number of kinematic variables: (a) jet multiplicity, (b) leading jet p_{T}, (c) leading jet η, (d) lepton p_{T}, (e) lepton η, (f) missing transverse energy, (g) W transverse mass, (h) $H_{\mathrm{T}}^{\mathrm{had}}$ and (i) H_{T} (defined as the scalar sum of the lepton p_{T}, $E_{\mathrm{T}}^{\mathrm{miss}}$ and $H_{\mathrm{T}}^{\mathrm{had}}$). Only statistical uncertainties are being shown.

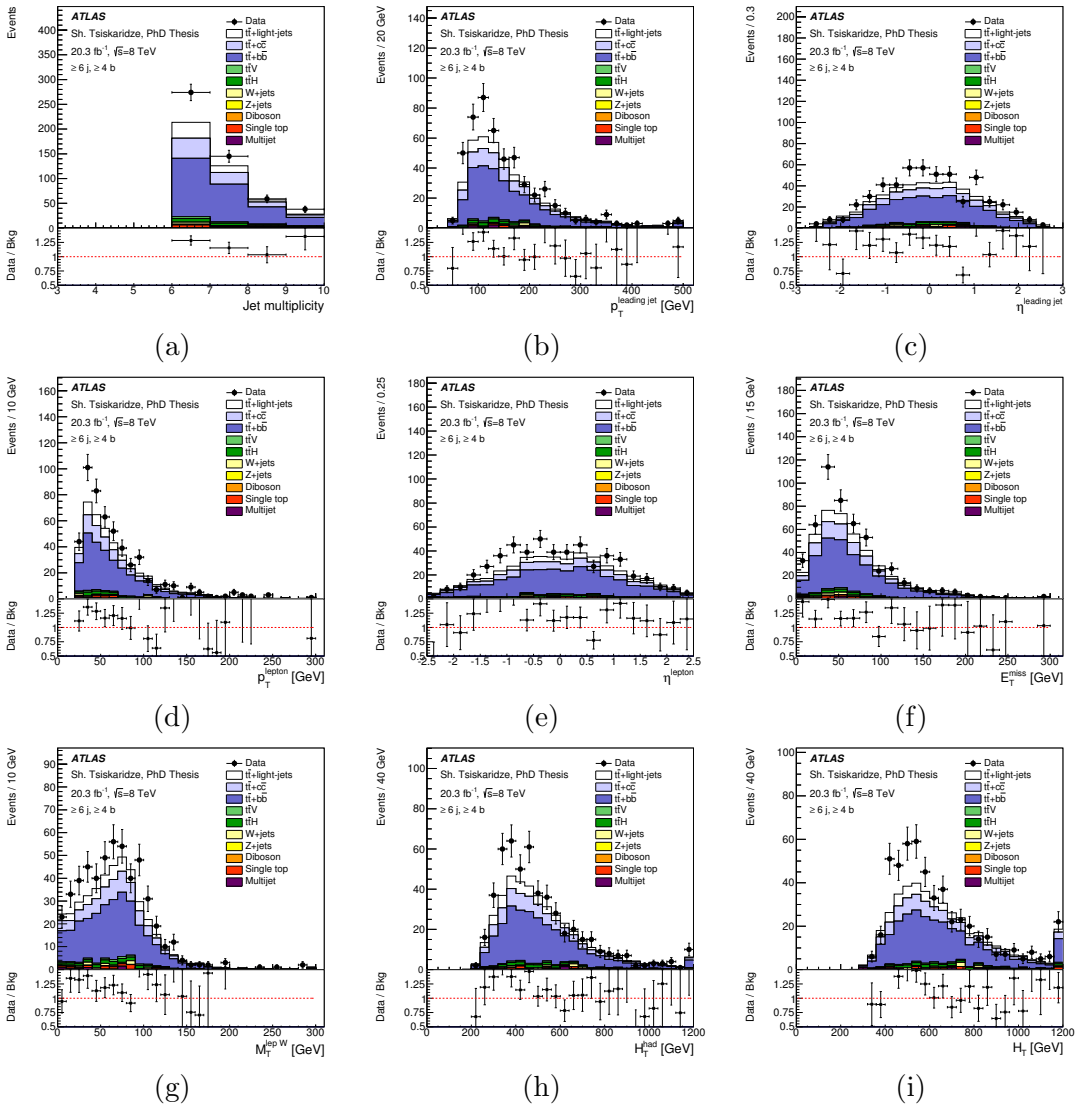

Figure C.9: Comparison between data and prediction in the combined e+jets and μ+jets channels in the (≥6 j, ≥4 b) region for a number of kinematic variables: (a) jet multiplicity, (b) leading jet p_{T}, (c) leading jet η, (d) lepton p_{T}, (e) lepton η, (f) missing transverse energy, (g) W transverse mass, (h) $H_{\mathrm{T}}^{\mathrm{had}}$ and (i) H_{T} (defined as the scalar sum of the lepton p_{T}, $E_{\mathrm{T}}^{\mathrm{miss}}$ and $H_{\mathrm{T}}^{\mathrm{had}}$). Only statistical uncertainties are being shown.

Appendix D

Pre- and Post-fit Distributions for the $t\bar{t} \to WbHu$, $H \to b\bar{b}$ Search

Figures D.1-D.3 show a comparison of the data and prediction of the final discriminant in each of the analysis channels, for both pre- and post-fit to data,in the case of the $t\bar{t} \to WbHu$ search. The corresponding pre-fit and post-fit yields are shown in Tables 6.1 and D.1 respectively.

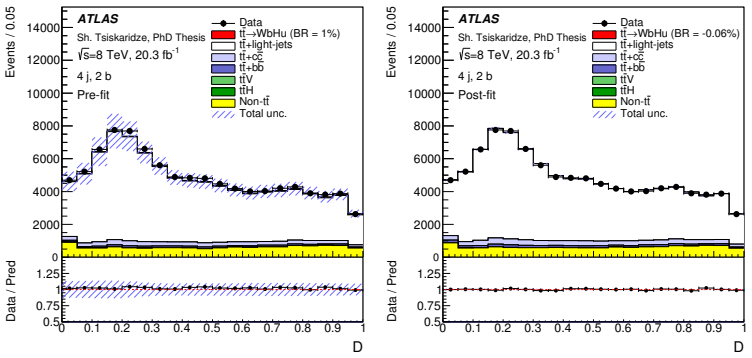

(a) (b)

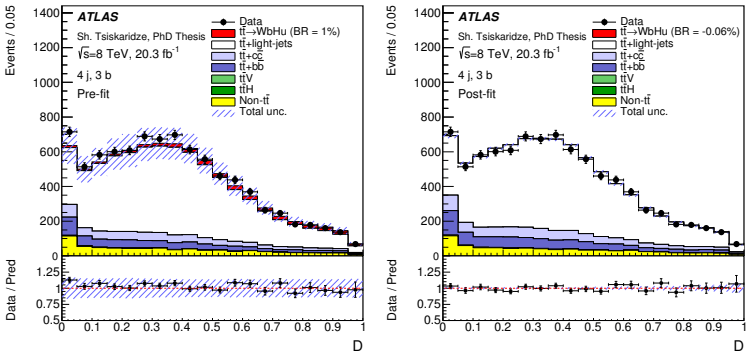

(c) (d)

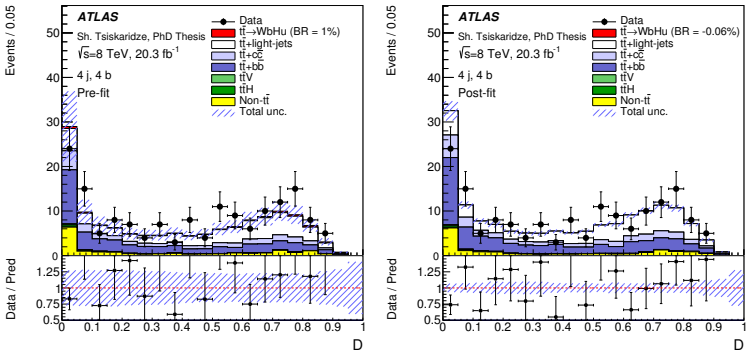

(e) (f)

Figure D.1: $t\bar{t} \to WbHu, H \to b\bar{b}$ search: comparison between the data and prediction for the distribution of the D discriminant used in the (4 j, 2 b) channel (a) before the fit and (b) after the fit, in the (5 j, 2 b) channel (c) before the fit and (d) after the fit, and in the ($\geq$6 j, 2 b) channel (e) before the fit and (f) after the fit. The fit is performed on data under the signal-plus-background hypothesis. In the pre-fit distributions the $t\bar{t} \to WbHu$ signal (solid red) is normalized to BR($t \to Hu$) = 1% and the $t\bar{t} \to WbWb$ background is normalized to the SM prediction, while in the post-fit distributions both signal and $t\bar{t} \to WbWb$ background are normalized using the best-fit BR($t \to Hu$). The small contributions from W/Z+jets, single top, diboson and multijet backgrounds are combined into a single background source referred to as "Non-$t\bar{t}$". The bottom panels display the ratios of data to the total signal-plus-background prediction after the fit ("Pred"). The hashed area represents the total uncertainty on the background.

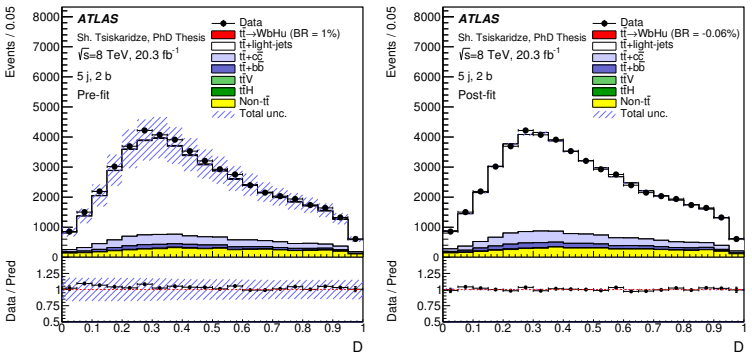

(a) (b)

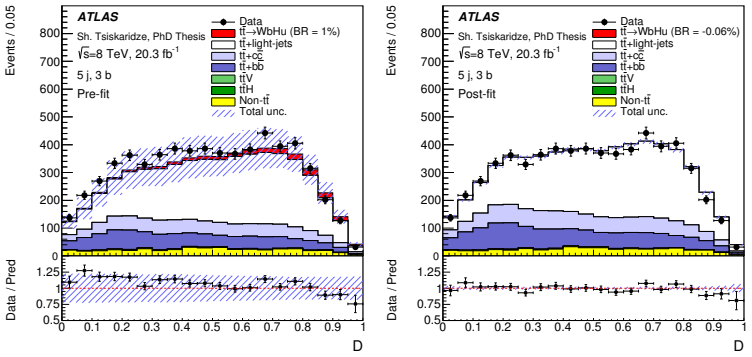

(c) (d)

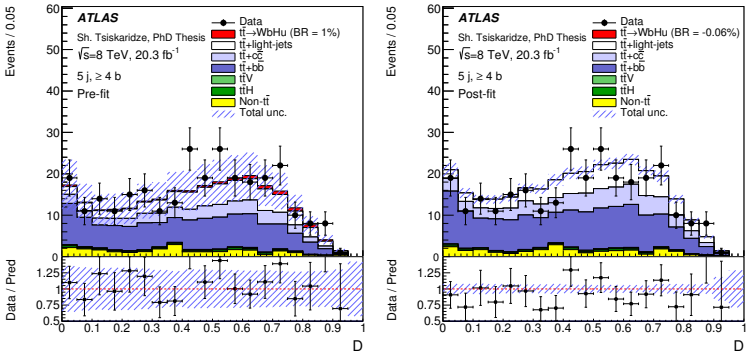

(e) (f)

Figure D.2: $t\bar{t} \to WbHu, H \to b\bar{b}$ search: comparison between the data and prediction for the distribution of the D discriminant used in the (4 j, 3 b) channel (a) before the fit and (b) after the fit, in the (5 j, 3 b) channel (c) before the fit and (d) after the fit, and in the ($\geq$6 j, 3 b) channel (e) before the fit and (f) after the fit. The fit is performed on data under the signal-plus-background hypothesis. In the pre-fit distributions the $t\bar{t} \to WbHu$ signal (solid red) is normalized to BR($t \to Hu$) = 1% and the $t\bar{t} \to WbWb$ background is normalized to the SM prediction, while in the post-fit distributions both signal and $t\bar{t} \to WbWb$ background are normalized using the best-fit BR($t \to Hu$). The small contributions from W/Z+jets, single top, diboson and multijet backgrounds are combined into a single background source referred to as "Non-$t\bar{t}$". The bottom panels display the ratios of data to the total signal-plus-background prediction after the fit ("Pred"). The hashed area represents the total uncertainty on the background.

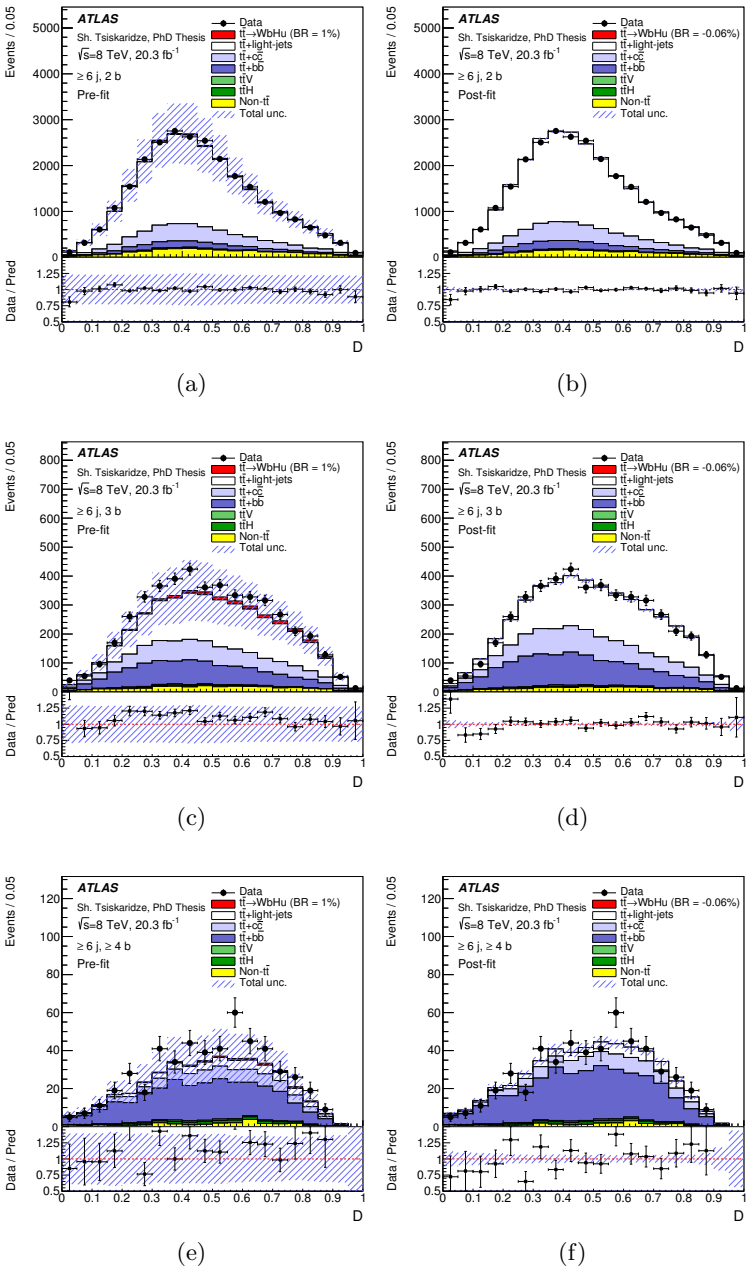

Figure D.3: $t\bar{t} \to WbHu, H \to b\bar{b}$ search: comparison between the data and prediction for the distribution of the D discriminant used in the (4 j, 4 b) channel (a) before the fit and (b) after the fit, in the (5 j, ≥4 b) channel (c) before the fit and (d) after the fit, and in the (≥6 j, ≥4 b) channel (e) before the fit and (f) after the fit. The fit is performed on data under the signal-plus-background hypothesis. In the pre-fit distributions the $t\bar{t} \to WbHu$ signal (solid red) is normalized to $\mathrm{BR}(t \to Hu) = 1\%$ and the $t\bar{t} \to WbWb$ background is normalized to the SM prediction, while in the post-fit distributions both signal and $t\bar{t} \to WbWb$ background are normalized using the best-fit $\mathrm{BR}(t \to Hu)$. The small contributions from W/Z+jets, single top, diboson and multijet backgrounds are combined into a single background source referred to as "Non-$t\bar{t}$". The bottom panels display the ratios of data to the total signal-plus-background prediction after the fit ("Pred"). The hashed area represents the total uncertainty on the background.

	4 j, 2 b	4 j, 3 b	4 j, 4 b
$t\bar{t} \to WbHu$	-54.4 ± 4.0	-21.5 ± 1.6	-0.26 ± 0.03
$t\bar{t}$+light-jets	77300 ± 1700	6300 ± 190	58.5 ± 7.3
$t\bar{t} + c\bar{c}$	5800 ± 1500	840 ± 210	24.5 ± 6.2
$t\bar{t} + b\bar{b}$	2400 ± 370	880 ± 130	54.3 ± 7.7
$t\bar{t}V$	122 ± 19	15.6 ± 2.5	0.91 ± 0.15
$t\bar{t}H$	30.8 ± 3.6	12.8 ± 1.6	1.92 ± 0.26
W+jets	5000 ± 1100	236 ± 56	5.9 ± 1.5
Z+jets	1040 ± 400	49 ± 19	0.80 ± 0.33
Single top	5200 ± 1100	356 ± 72	7.3 ± 1.5
Diboson	210 ± 72	11.8 ± 4.1	0.22 ± 0.08
Multijet	1140 ± 320	76 ± 22	2.47 ± 0.71
Total	98070 ± 420	8800 ± 100	156.6 ± 6.7
Data	98049	8752	161

	5 j, 2 b	5 j, 3 b	5 j, $\geq$4 b
$t\bar{t} \to WbHu$	-30.3 ± 3.6	-14.0 ± 1.7	-0.56 ± 0.07
$t\bar{t}$+light-jets	37500 ± 1200	3600 ± 160	68.7 ± 8.2
$t\bar{t} + c\bar{c}$	4800 ± 1200	1000 ± 240	61 ± 17
$t\bar{t} + b\bar{b}$	2110 ± 310	1140 ± 160	144 ± 18
$t\bar{t}V$	145 ± 22	26.7 ± 4.2	3.13 ± 0.51
$t\bar{t}H$	41.0 ± 4.5	22.4 ± 2.6	5.98 ± 0.74
W+jets	1990 ± 560	145 ± 42	6.2 ± 1.8
Z+jets	380 ± 170	28 ± 12	1.39 ± 0.64
Single top	2110 ± 630	222 ± 67	10.4 ± 3.2
Diboson	94 ± 39	7.9 ± 3.3	0.37 ± 0.16
Multijet	340 ± 97	47 ± 13	6.3 ± 1.9
Total	49570 ± 260	6226 ± 66	310 ± 10
Data	49699	6199	286

	$\geq$6 j, 2 b	$\geq$6 j, 3 b	$\geq$6 j, $\geq$4 b
$t\bar{t} \to WbHu$	-16.2 ± 1.5	-8.29 ± 0.74	-0.67 ± 0.07
$t\bar{t}$+light-jets	18530 ± 790	2090 ± 140	56.5 ± 8.4
$t\bar{t} + c\bar{c}$	3940 ± 930	1020 ± 240	90 ± 21
$t\bar{t} + b\bar{b}$	1820 ± 270	1240 ± 170	316 ± 36
$t\bar{t}V$	178 ± 27	43.8 ± 6.8	8.3 ± 1.3
$t\bar{t}H$	63.8 ± 7.1	39.5 ± 4.5	15.8 ± 1.8
W+jets	700 ± 230	77 ± 25	7.3 ± 2.8
Z+jets	161 ± 79	17.1 ± 8.5	1.52 ± 0.77
Single top	750 ± 280	110 ± 41	10.8 ± 4.1
Diboson	48 ± 23	5.8 ± 2.8	0.51 ± 0.25
Multijet	122 ± 34	14.2 ± 4.0	1.17 ± 0.68
Total	26300 ± 170	4650 ± 63	508 ± 21
Data	26185	4701	516

Table D.1: $t\bar{t} \to WbHu, H \to b\bar{b}$ search: predicted and observed yields in each of the analysis channels considered. The background prediction is shown after the fit to data under the signal-plus-background hypothesis. The quoted uncertainties are the sum in quadrature of statistical and systematic uncertainties on the yields, computed taking into account correlations among nuisance parameters and among processes.

Appendix E

Fit Validation

To validate the fitting procedure, a signal injection test was performed whereby the Asimov dataset was generated including $t\bar{t} \to WbHc$ or $t\bar{t} \to WbHu$ signal corresponding to different input branching ratios (0%, 1%, 2%, and 4%) and a signal-plus-background fit was performed. The fitted branching ratio was found to agree well with the input one, as shown in Fig. E.1, while all other nuisance parameters are fitted at 0. A summary for the fitted branching ratios and their total expected uncertainty can be found in Table E.1. Not only the fitted value but also the constraints on the nuisance parameters are found to be independent of the input branching ratio (see Figs. E.2 and E.3), thus confirming the unbiasedness of the full fit.

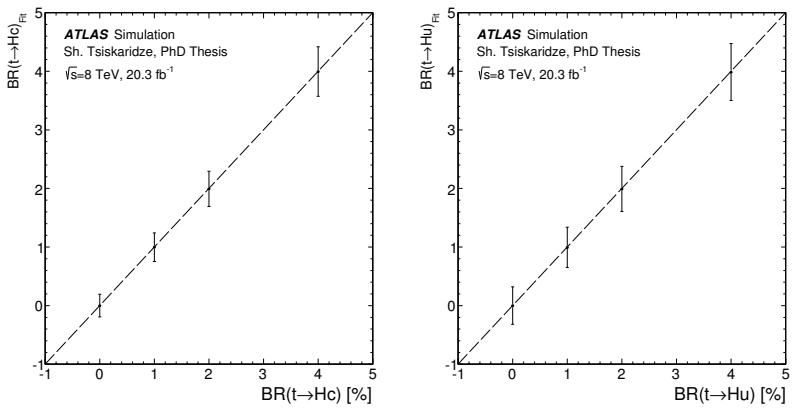

(a) (b)

Figure E.1: Linearity test for (a) $t\bar{t} \to WbHc$ and (b) $t\bar{t} \to WbHu$. Shown is the fitted branching ratio for Asimov datasets with different input branching ratios.

Input BR($t \to Hq$)	0%	1%	2%	4%
Fitted BR($t \to Hc$)	(0.00 ± 0.19)%	(1.00 ± 0.24)%	(1.99 ± 0.30)%	(3.99 ± 0.42)%
Fitted BR($t \to Hu$)	(0.00 ± 0.32)%	(0.99 ± 0.35)%	(1.99 ± 0.39)%	(3.98 ± 0.49)%

Table E.1: Fitted values for BR($t \to Hc$) and BR($t \to Hu$) for different input values including the total estimated uncertainty.

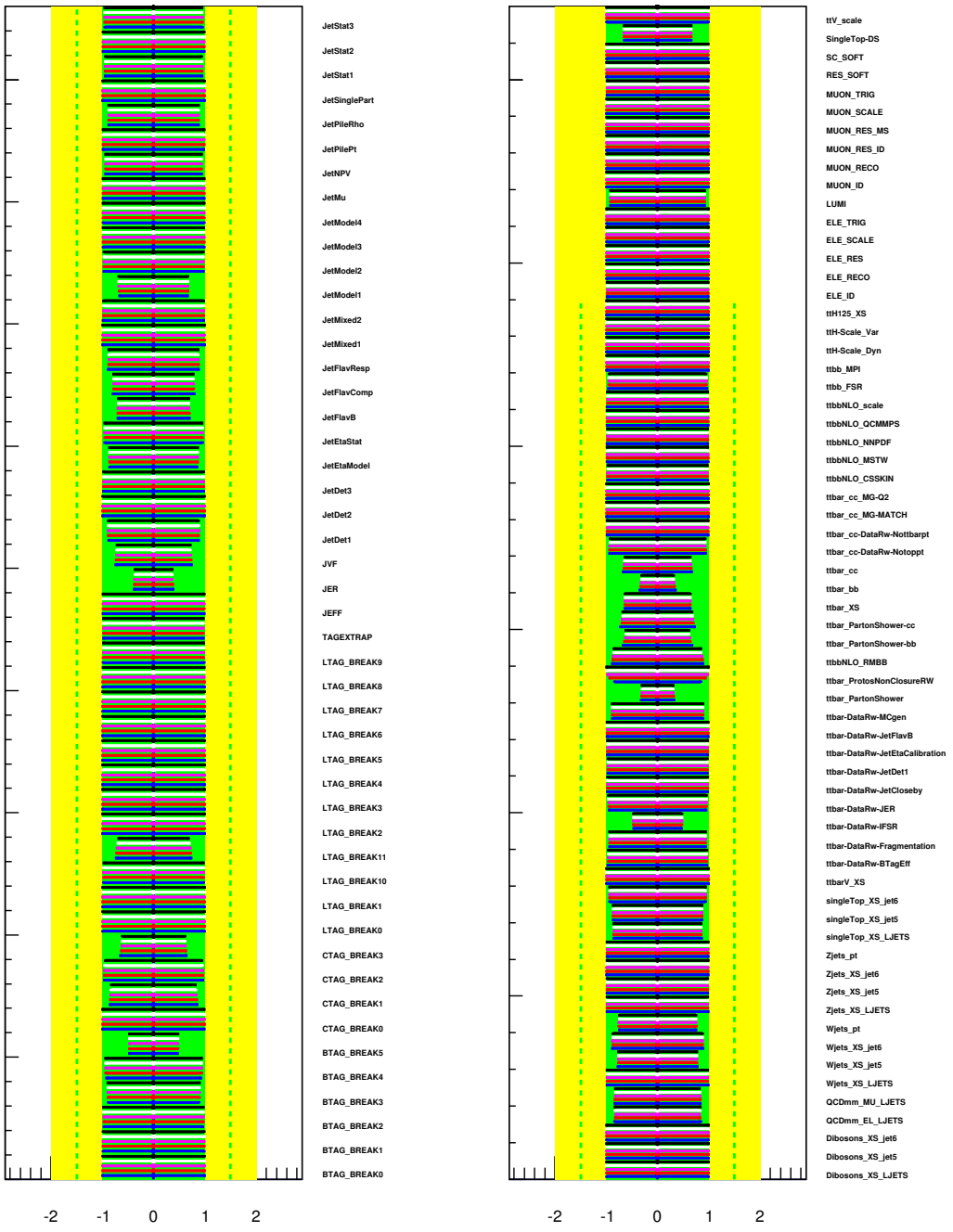

Figure E.2: Nuisance parameter fits to Asimov datasets with different input branching ratios: Black: input BR($t \to Hc$) = 0% and fit to background-only hypothesis, White: input BR($t \to Hc$) = 0% and fit to signal+background hypothesis, Magenta: input BR($t \to Hc$) = 1% and fit to signal+background hypothesis, Red: input BR($t \to Hc$) = 2% and fit to signal+background hypothesis, Blue: input BR($t \to Hc$) = 4% and fit to signal+background hypothesis.

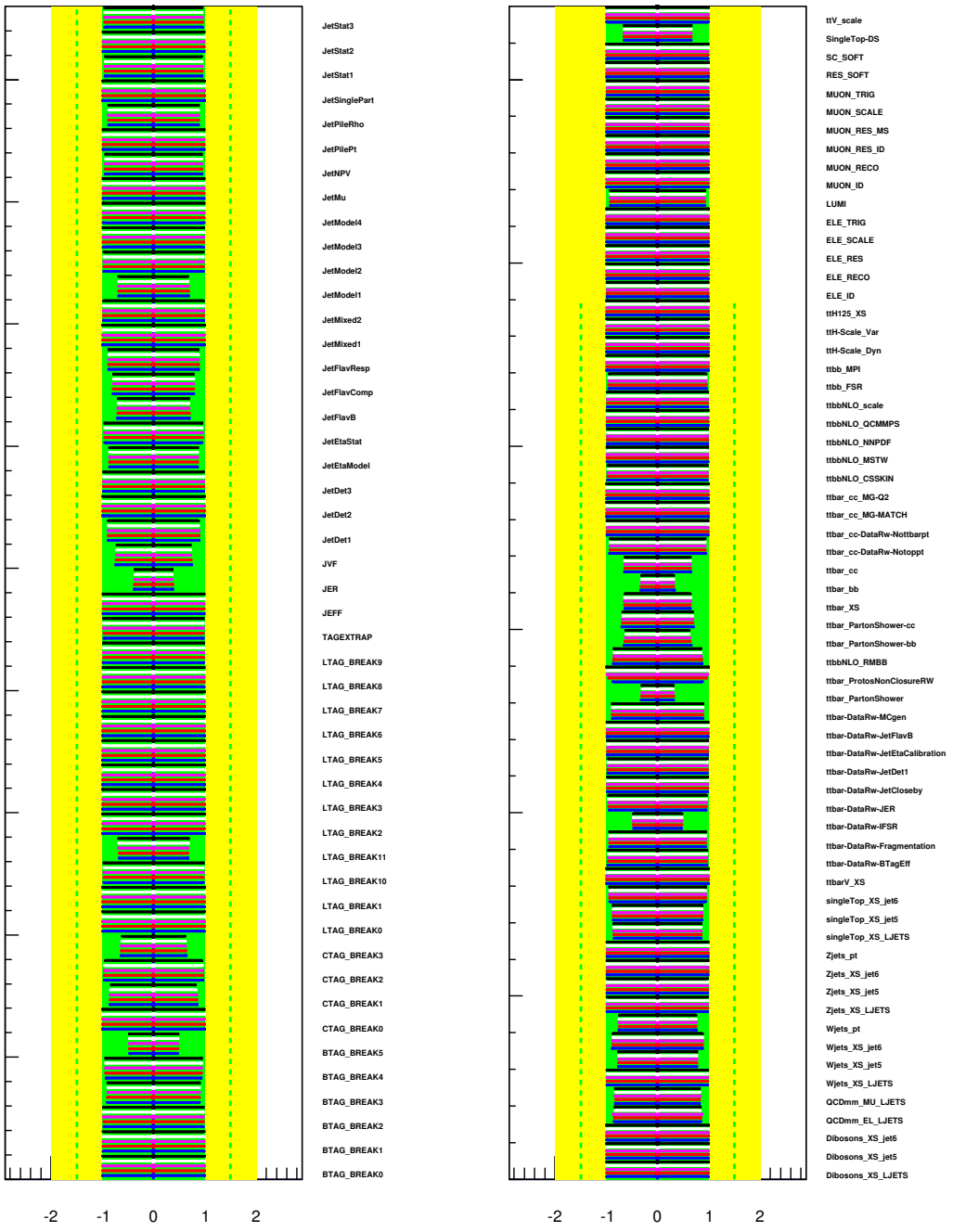

Figure E.3: Nuisance parameter fits to Asimov datasets with different input branching ratios: Black: input BR($t \to Hu$) = 0% and fit to background-only hypothesis, White: input BR($t \to Hu$) = 0% and fit to signal+background hypothesis, Magenta: input BR($t \to Hu$) = 1% and fit to signal+background hypothesis, Red: input BR($t \to Hu$) = 2% and fit to signal+background hypothesis, Blue: input BR($t \to Hu$) = 4% and fit to signal+background hypothesis.

Appendix F

Expected Sensitivity Studies

Figures F.1a and F.1b show the expected CL_s as a function of BR($t \to Hc$) and BR($t \to Hu$), respectively, taking into account systematic uncertainties. The median expected limits are: BR($t \to Hc$) $< 0.40\%$ at 95% CL and BR($t \to Hu$) $< 0.63\%$ at 95% CL. Note that the expected limits obtained with the Asimov dataset are slightly better than those reported in Sec. 9.1. The reason is that these expected limits are obtained from the pre-fit backgrounds, which is slightly lower than the post-fit backgrounds.

Table F.1 shows the expected limits on BR($t \to Hc$) and BR($t \to Hu$) for different combinations of analysis channels to demonstrate the impact from considering some of the background-dominated channels. As expected, the most sensitive individual channels are (4 j, 4 b) and (4 j, 3 b) in the case of the $t\bar{t} \to WbHc$ and $t\bar{t} \to WbHu$ searches respectively. Considering only the combination of (4 j, 3 b) and (4 j, 4 b) channels, the expected limits on BR($t \to Hc$) and BR($t \to Hu$) are worse than the nominal limits from the nine analysis channels by factors of 1.35 and 1.65 respectively. Adding the (5 j, 3 b) and (5 j, $\geq$4 b) channels, for a total of four analysis channels, brings the degradation down to factors of 1.25 and 1.43 for BR($t \to Hc$) and BR($t \to Hu$) respectively. Adding also the (4 j, 2 b) and (5 j, 2 b) channels, for a total of six analysis channels, helps further, bringing the degradation down to factors of 1.03 and 1.03 for BR($t \to Hc$) and BR($t \to Hu$) respectively. Therefore, the consideration of the $\geq$6 jets channels improves the sensitivity by only 3%, but it is useful to better calibrate the $t\bar{t}$+HF background.

The median expected limits without taking into account systematic uncertainties are BR($t \to Hc$) $< 0.25\%$ at 95% CL and BR($t \to Hu$) $< 0.36\%$ at 95% CL. These limits are to be compared to 0.40% and 0.63%, respectively. Despite the profiling, systematic uncertainties do have a significant impact on the sensitivity. However, through the profiling the expected sensitivity should continue to improve as $1/\sqrt{L}$, where L is the integrated luminosity.

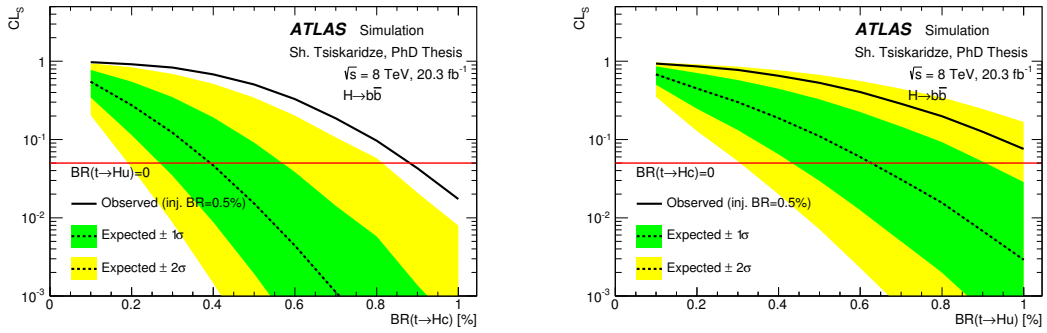

(a) (b)

Figure F.1: (a) CL_s versus $BR(t \to Hc)$ (b) CL_s versus $BR(t \to Hu)$ for the $H \to \bar{b}$ search, assuming that the other branching ratio is zero. The observed CL_s values (solid black lines) are compared to the expected (median) CL_s values under the background-only hypothesis (dotted black lines). The surrounding shaded bands correspond to the 68% and 95% CL intervals around the expected CL_s values, denoted by $\pm 1\sigma$ and $\pm 2\sigma$, respectively. Also shown is the median observed CL_s for an injected signal of $BR(t \to Hq) = 0.5\%$. The solid red line at CL_s=0.05 denotes the value below which the hypothesis is excluded at 95% CL.

Channel	-2σ	$-\sigma$	$BR_{exp}(t \to Hc)$	$+\sigma$	$+2\sigma$	-2σ	$-\sigma$	$BR_{exp}(t \to Hu)$	$+\sigma$	$+2\sigma$
(4, 5, ≥6 jets)x(2, 3, ≥4 b-tags)	0.22	0.29	0.40	0.56	0.77	0.34	0.46	0.64	0.90	1.23
(4, 5 jets)x(2, 3, ≥4 b-tags)	0.22	0.30	0.42	0.58	0.81	0.35	0.47	0.66	0.92	1.26
(4, 5 jets)x(3, ≥4 b-tags)	0.27	0.36	0.50	0.71	0.98	0.49	0.66	0.91	1.29	1.81
(4 jets)x(3, ≥4 b-tags)	0.29	0.39	0.54	0.77	1.07	0.56	0.75	1.04	1.48	2.06
(4 jets, 2 b-tags)	2.41	3.23	4.49	6.13	8.07	2.19	2.93	4.07	5.58	7.39
(4 jets, 3 b-tags)	0.57	0.76	1.06	1.50	2.08	0.58	0.78	1.09	1.54	2.15
(4 jets, 4 b-tags)	0.39	0.52	0.72	1.07	1.61	8.86	11.89	16.50	24.36	37.90
(5 jets, 2 b-tags)	2.89	3.88	5.38	7.44	10.02	2.69	3.62	5.02	6.97	9.46
(5 jets, 3 b-tags)	1.08	1.45	2.01	2.93	4.25	0.91	1.23	1.70	2.47	3.58
(5 jets, ≥4 b-tags)	0.96	1.29	1.78	2.67	4.02	4.30	5.77	8.01	12.12	18.34
(≥6 jets, 2 b-tags)	3.40	4.57	6.34	8.53	11.12	3.52	4.73	6.56	8.94	11.80
(≥6 jets, 3 b-tags)	2.38	3.20	4.44	6.67	9.96	2.62	3.51	4.88	7.32	10.92
(≥6 jets, ≥4 b-tags)	1.71	2.29	3.18	4.79	7.39	6.15	8.25	11.45	16.74	22.94

Table F.1: Expected limits (in %) on $BR(t \to Hc)$ and $BR(t \to Hu)$ for different combinations of analyses channels taking into account systematic uncertainties.

Appendix G

Glossary

This section describes the naming of nuisance parameters corresponding to various systematic uncertainties in the fit output.

- Luminosity: LUMI
- Electron:
  - identification: ELE_ID
  - reconstruction: ELE_RECO
  - resolution: ELE_RES
  - energy scale: ELE_SCALE
  - trigger: ELE_TRIG
- Muon:
  - identification: MUON_ID
  - reconstruction: MUON_RECO
  - resolution in the tracker: MUON_RES_ID
  - resolution in the muon system: MUON_RES_MS
  - momentum scale: MUON_SCALE
  - trigger: MUON_TRIG
- Jet reconstruction efficiency: JEFF
- Jet vertex fraction: JVF
- Jet energy scale:
  22 independent components provided by JES group and related to the overall JES, jet η intercalibration, jet flavor, pile-up effects and data statistics for data-driven methods: JetDet1, JetDet2, JetDet3, JetEtaModel, JetEtaStat, JetFlavB, JetFlavComp, JetFlavResp, JetMixed1, JetMixed2, JetModel1, JetModel2, JetModel3, JetModel4, JetMu, JetNPV, JetPilePt, JetPileRho, JetSinglePart, JetStat1, JetStat2, JetStat3
- Jet resolution: JER

- Missing transverse momentum: SC_SOFT, RES_SOFT
- b-tagging uncertainties:
  6 eigenvectors corresponding to b-jet p_{T} bins ordered from the smallest to the largest: BTAGBREAK0, BTAGBREAK1, BTAGBREAK2, BTAGBREAK3, BTAGBREAK4, BTAGBREAK5
- c-tagging uncertainties:
  4 eigenvectors corresponding to c-jet p_{T} bins ordered from the smallest to the largest: CTAGBREAK0, CTAGBREAK1CTAGBREAK2, CTAGBREAK3
- light-tagging uncertainties:
  12 eigenvectors corresponding to 6 light jet p_{T} bins and two jet ηregions ordered from the smallest to the largest: LTAGBREAK0, LTAGBREAK1, LTAGBREAK2, LTAGBREAK3, LTAGBREAK4, LTAGBREAK5, LTAGBREAK6, LTAGBREAK7, LTAGBREAK8, LTAGBREAK9, LTAGBREAK10, LTAGBREAK11
- high-p_{T} extrapolation uncertainty for b-, c- and light-tagging: TAGEXTRAP
- $t\bar{t}$ normalization:
  - $t\bar{t}$ inclusive cross section: ttbar_XS
  - $t\bar{t} + b\bar{b}$ normalization: ttbar_bb
  - $t\bar{t} + c\bar{c}$ normalization: ttbar_cc
- $t\bar{t}$ inclusive production:
  Uncertainties associated with the measurement of the differential cross section for $t\bar{t}$ and top p_{T} used to correct $t\bar{t}$ MC model:
  - Detector: ttbar-DataRw-BTagEff, ttbar-DataRw-Fragmentation, ttbar-DataRw-JER, ttbar-DataRw-JetCloseby, ttbar-DataRw-JetDet1, ttbar-DataRw-JetEtaCalibration, ttbar-DataRw-JetFlavB
  - Model: initial and final state radiation - ttbar-DataRw-IFSR, MC generator - ttbar-DataRw-MCgen
- $t\bar{t}$+light:
  Parton shower model: ttbar_PartonShower
- $t\bar{t}$+$c\bar{c}$: MC modeling
  - Matching parameter variation in Madgraph: ttbar_cc_MG-MATCH
  - c-mass variation in Madgraph:ttbar_cc_MG-MC
  - scale variation in Madgraph:ttbar_cc_MG-Q2
  - generator choice (Powheg vs Madgraph): ttbar_cc_MG
  - parton shower model: ttbar_PartonShower-cc
  - reweighting: Uncertainties corresponding to switching top p_{T} (ttbar_cc-DataRw-Notoppt) and $t\bar{t}$ p_{T} (ttbar_cc-DataRw-Nottbarpt) reweighting off
- $t\bar{t}$+$b\bar{b}$: MC modeling
  - scale variation in Sherpa: ttbbNLO_scale

  - scale functional form choice in Sherpa: ttbbNLO_QCMMPS
  - PDF uncertainties: tttbbNLO_NNPDF, ttbbNLO_MSTW
  - uncertainty due to MPI model: ttbbNLO_MPI
  - uncertainty due to FSR model: ttbbNLO_FSR
  - parton shower model: ttbar_PartonShower-bb

- Small backgrounds:
  - cross section for W+jets with ≥ 4 jets: Wjets_XS_LJETS
  - cross section for W+jets with ≥ 5 jets: Wjets_XS_jet5
  - cross section for W+jets with ≥ 6 jets: Wjets_XS_jet6
  - W p_{T} correction for W+jets : Wjets_pt
  - cross section for Z+jets with ≥ 4 jets: Zjets_XS_LJETS
  - cross section for Z+jets with ≥ 5 jets: Zjets_XS_jet5
  - cross section for Z+jets with ≥ 6 jets: Zjets_XS_jet6
  - Z p_{T} correction for Z+jets : Zjets_pt
  - cross section for single top production with ≥ 4 jets: singleTop_XS_LJETS
  - cross section for single top production with ≥ 5 jets: singleTop_XS_jet5
  - cross section for single top production with ≥ 6 jets: singleTop_XS_jet6
  - cross section diboson production with ≥ 4 jets: Dibosons_XS_LJETS
  - cross section diboson production with ≥ 5 jets: Dibosons_XS_jet5
  - cross section diboson production with ≥ 6 jets: Dibosons_XS_jet6
  - modeling of Wt single top production (diagram subtraction scheme): SingleTop-DS
  - cross section for $t\bar{t}V, (V = Z, W, WW)$ production: ttbarV_XS
  - modeling of $t\bar{t}V, (V = Z, W)$: scale variation (ttV_scale)
  - cross section for $t\bar{t}H$ production: ttH125_XS
  - modeling of $t\bar{t}H$: scale variation (ttH-Scale_Var) and choice of functional form of scale (ttH-Scale_Dyn)
  - multijet normalization: QCDmm_EL_LJETS (e+jets) and QCDmm_MU_LJETS (μ+jets)

- Signal modeling:
  - Protos reweighting non-closure: ttbar_ProtosNonClosureRW
  - uncertainty in Higgs branching ratios from $\Delta\alpha_s$: BR_param_alphaS
  - uncertainty in Higgs branching ratios from Δm_b: BR_param_mB
  - uncertainty on Higgs decay with from higher-order QCD corrections: BR_HiggsDecayWidthTHU_hqq

Bibliography

[1] ATLAS Collaboration, *Observation of a new particle in the search for the Standard Model Higgs boson with the ATLAS detector at the LHC*, Phys. Lett. B **716** (2012) 1, arXiv:1207.7214 [hep-ex].

[2] CMS Collaboration, *Observation of a new boson at a mass of 125 GeV with the CMS experiment at the LHC*, Phys. Lett. B **716** (2012) 30, arXiv:1207.7235 [hep-ex].

[3] ATLAS Collaboration, *Search for top quark decays $t \to qH$ with $H \to \gamma\gamma$ using the ATLAS detector*, JHEP **1406** (2014) 008, arXiv:1403.6293 [hep-ex].

[4] CMS Collaboration, *Searches for heavy Higgs bosons in two-Higgs-doublet models and for $t \to ch$ decay using multilepton and diphoton final states in pp collisions at 8 TeV*, Phys. Rev. D **90** (2014) 112013, arXiv:1410.2751 [hep-ex].

[5] CMS Collaboration, *Search for top quark decays $t \to qH$ with $H \to \gamma\gamma$ in pp collisions at $\sqrt{s} = 8$ TeV*, CMS-PAS-TOP-14-019 (2015) . https://cds.cern.ch/record/2034227.

[6] ATLAS Collaboration, *Search for the associated production of the Higgs boson with a top quark pair in multilepton final states with the ATLAS detector*, Phys. Lett. B **749** (2015) 519, arXiv:1506.05988.

[7] CMS Collaboration, *Search for top quark decays via Higgs-boson-mediated flavor changing neutral currents in pp collisions at $\sqrt{s} = 8$* TeV, CMS-PAS-TOP-13-017 (2015) . https://cds.cern.ch/record/2001934.

[8] ATLAS Collaboration, *Search for the Standard Model Higgs boson produced in association with top quarks and decaying into $b\bar{b}$ in pp collisions at $\sqrt{s} = 8$ TeV with the ATLAS detector*, Eur. Phys. J. C **75** (2015) 349, arXiv:1503.05066 [hep-ex].

[9] ATLAS Collaboration, *Search for production of vector-like quark pairs and of four top quarks in the lepton-plus-jets final state in pp collisions at $\sqrt{s} = 8$ TeV with the ATLAS detector*, JHEP **08** (2015) 105, arXiv:1505.04306 [hep-ex].

[10] ATLAS Collaboration, *Search for flavour-changing neutral current top quark decays $t \to Hq$ in pp collisions at $\sqrt{s} = 8$ TeV with the ATLAS detector*, JHEP **12** (2015) 061, arXiv:1509.06047 [hep-ex].

[11] ATLAS IBL Collaboration, *Prototype ATLAS IBL Modules using the FE-I4A Front-End Readout Chip*, JINST **7** (2012) P11010, `arXiv:1209.1906 [physics.ins-det]`.

[12] S. Glashow, *Partial Symmetries of Weak Interactions*, Nucl. Phys. B **22** (1961) 579.

[13] S. Weinberg, *A Model of Leptons*, Phys. Rev. Lett. **19** (1967) 1264.

[14] A. Salam, *Gauge Unification of Fundamental Forces*, Rev. Mod. Phys. **52** (1980) 525.

[15] Y. Fukuda, *Evidence for Oscillation of Atmospheric Neutrinos*, Phys. Rev. Lett. **81** (1998) 1562, `arXiv:hep-ex/9807003 [hep-ex]`.

[16] S. Glashow, J. Iliopoulos, and L. Maiani, *Weak Interactions with Lepton-Hadron Symmetry*, Phys. Rev. D **2** (1970) 1285.

[17] M. M. H. Luk and U. Heintz, *The Search for a Heavy Top-Like Quark*, Brown U. (2013) . https://cds.cern.ch/record/1569839.

[18] M. E. Peskin and D. V. Schroeder, *An introduction to quantum field theory.* Advanced book program. Westview Press Reading (Mass.), Boulder (Colo.), 1995. http://opac.inria.fr/record=b1131978.

[19] Particle Data Group, W. Yao et al., *Review of Particle Physics*, J. Phys. G **33** (2006) 1.

[20] SLAC Collaboration, *Discovery of a Narrow Resonance in e^+e^- Annihilation*, Phys. Rev. Lett. **33** (1974) 1406.

[21] MIT Collaboration, *Experimental Observation of a Heavy Particle J*, Phys. Rev. Lett. **33** (1974) 1404.

[22] S. Herb, D. Hom, L. Lederman, J. Sens, H. Snyder, et al., *Observation of a Dimuon Resonance at 9.5-GeV in 400-GeV Proton-Nucleus Collisions*, Phys. Rev. Lett. **39** (1977) 252.

[23] UA1 Collaboration, G. Arnison et al., *Experimental Observation of Isolated Large Transverse Energy Electrons with Associated Missing Energy at $\sqrt{s} = 540$ GeV*, Phys. Lett. B **122** (1983) 103.

[24] UA2 Collaboration, M. Banner et al., *Observation of Single Isolated Electrons of High Transverse Momentum in Events with Missing Transverse Energy at the CERN $\bar{p}p$ Collider*, Phys. Lett. B **122** (1983) 476.

[25] UA1 Collaboration, G. Arnison et al., *Experimental Observation of Lepton Pairs of Invariant Mass Around 95 GeV/c^2 at the CERN SPS Collider*, Phys. Lett. B **126** (1983) 398.

[26] UA2 Collaboration, P. Bagnaia et al., *Evidence for $Z^0 \to e^+e^-$ at the CERN $\bar{p}p$ Collider*, Phys. Lett. B **129** (1983) 130.

[27] CDF Collaboration, F. Abe et al., *Observation of top quark production in $\bar{p}p$ collisions*, Phys. Rev. Lett. **74** (1995) 2626, arXiv:hep-ex/9503002 [hep-ex].

[28] D0 Collaboration, S. Abachi et al., *Observation of the top quark*, Phys. Rev. Lett. **74** (1995) 2632, arXiv:hep-ex/9503003 [hep-ex].

[29] M. Baak and R. Kogler, *The global electroweak Standard Model fit after the Higgs discovery*, arXiv:1306.0571 [hep-ph].

[30] ATLAS and CMS Collaborations, *Combined Measurement of the Higgs Boson Mass in pp Collisions at $\sqrt{s} = 7$ and 8 TeV with the ATLAS and CMS Experiments*, Phys. Rev. Lett. **114** (2015) 191803, arXiv:1503.07589 [hep-ex].

[31] ATLAS Collaboration, *Evidence for the spin-0 nature of the Higgs boson using ATLAS data*, Phys. Lett. B **726** (2013) 120, arXiv:1307.1432 [hep-ex].

[32] J. Oort, *The force exerted by the stellar system in the direction perpendicular to the galactic plane and some related problems*, Bulletin of the Astronomical Institutes of the Netherlands **6** (1932) 249.

[33] K. Begeman, A. Broeils, and R. Sanders, *Extended rotation curves of spiral galaxies Dark haloes and modified dynamics*, Mon. Not. Roy. Astron. Soc. **249** (1991) 523.

[34] Planck Collaboration, P. A. R. Ade, N. Aghanim, and C. Armitage-Caplan, *Planck 2013 results. I. Overview of products and scientific results*, Astronomy and Astrophysics **1303** (2013) 5062, arXiv:1303.5062.

[35] S. P. Martin, *A Supersymmetry primer*, Adv. Ser. Direct. High Energy Phys. **18** (1998) 1, arXiv:hep-ph/9709356 [hep-ph].

[36] J. Aguilar-Saavedra, *Top flavour-changing neutral interactions: theoretical expectations and experimental detection*, Acta Phys. Pol. B **35** (2004) 2695, arXiv:hep-ph/0409342.

[37] J. Aguilar-Saavedra and B. Nobre, *Rare top decays $t \to c\gamma$, $t \to cg$ and CKM unitarity*, Phys. Lett. B **553** (2003) 251, arXiv:hep-ph/0210360 [hep-ph].

[38] BNL E871 Collaboration, D. Ambrose et al., *Improved Branching Ratio Measurement for the Decay $K_L^0 \to \mu^+\mu^-$*, Phys. Rev. Lett. **84** (2000) 1389.

[39] R. Ammar et al., *Evidence for penguin-diagram decays: First observation of $B \to K^*\gamma$*, Phys. Rev. Lett. **71** (1993) 674.

[40] The Belle Collaboration, K. Abe et al., *Observation of the Decay $B \to Kl^+l^-$*, Phys. Rev. Lett. **88** (2001) 021801.

[41] ATLAS, CDF, CMS and D0 Collaborations, *First combination of Tevatron and LHC measurements of the top-quark mass*, arXiv:1403.4427 [hep-ex].

[42] J. Aguilar-Saavedra, *Top flavor-changing neutral interactions: Theoretical expectations and experimental detection*, Acta Phys. Polon. B **35** (2004) 2695, arXiv:hep-ph/0409342 [hep-ph].

[43] J. Yang, B. Young, and X. Zhang, *Flavor-changing top quark decays in R-parity violating SUSY*, Phys. Rev. D **58** (1998) 055001, arXiv:hep-ph/9705341.

[44] ATLAS Collaboration, *Measurements of the $t\bar{t}$ production cross-section in the dilepton and lepton-plus-jets channels and of the ratio of the $t\bar{t}$ and Z boson cross-sections in pp collisions at $\sqrt{s} = 13$ TeV with the ATLAS detector*, ATLAS-CONF-2015-049 (2015) . https://cds.cern.ch/record/2052605.

[45] F. Fiedler, *Precision Measurements of the Top Quark Mass*, arXiv:1003.0521.

[46] L. Wu, *Enhancing thj Production from Top-Higgs FCNC Couplings*, JHEP **02** (2015) 061, arXiv:1407.6113 [hep-ph].

[47] A. Greljo, J. Kamenik, and J. Kopp, *Disentangling Flavor Violation in the Top-Higgs Sector at the LHC*, JHEP **1407** (2014) 046, arXiv:1404.1278 [hep-ph].

[48] LHC Higgs Cross Section Working Group, J. Andersen et al., *Handbook of LHC Higgs Cross Sections: 3. Higgs Properties*, arXiv:1307.1347 [hep-ph].

[49] L. Evans and P. Bryant, *LHC Machine*, JINTS **3** (2008) S08001.

[50] ALICE Collaboration, *The ALICE experiment at the CERN LHC*, JINTS **3** (2008) S08002.

[51] ATLAS Collaboration, *The ATLAS Experiment at the CERN Large Hadron Collider*, JINST **3** (2008) S08003.

[52] CMS Collaboration, *The CMS experiment at the CERN LHC*, JINTS **3** (2008) S08004.

[53] LHCb Collaboration, *The LHCb Detector at the LHC*, JINTS **3** (2008) S08005.

[54] *The CERN accelerator complex*, . http://cds.cern.ch/record/2119882.

[55] *Integrated luminosity summary plots for 2011-2012 data taking*, . https://twiki.cern.ch/twiki/bin/view/AtlasPublic/LuminosityPublicResults.

[56] *Illustration of particle detection in the subsystems of the ATLAS detector*, . http://www.interactions.org/imagebank/images/CE0155M.jpg.

[57] M. Schott and M. Dunford, *Review of single vector boson production in pp collisions at $\sqrt{s} = 7$ TeV*, Eur. Phys. J. C **74** (2014) 2916, arXiv:1405.1160 [hep-ex].

[58] ATLAS Collaboration, *ATLAS magnet system: Technical design report, 1*, ATLAS-TDR-6; CERN-LHCC-97-018 (1997) . http://cds.cern.ch/record/338080.

[59] ATLAS Collaboration, *Studies of the performance of the ATLAS detector using cosmic-ray muons*, Eur. Phys. J. C **71** (2011) 1593, arXiv:1011.6665 [physics.ins-det].

[60] ATLAS Collaboration, *ATLAS liquid-argon calorimeter : Technical Design Report*, ATLAS-TDR-2; CERN-LHCC-96-041 (1996) . https://cds.cern.ch/record/331061.

[61] ATLAS Collaboration, *Readiness of the ATLAS Tile calorimeter for LHC collisions*, Eur. Phys. J. C **70** (2010) 1193, arXiv:1007.5423 [physics.ins-det].

[62] ATLAS Collaboration, *ATLAS: Tile Calorimeter Technical Design Report*, CERN-LHCC-96-042 (1996) . https://cds.cern.ch/record/331062.

[63] ATLAS Collaboration, *ATLAS: Muon Spectrometer Technical Design Report*, CERN-LHCC-97-022 (1997) . https://cds.cern.ch/record/333970.

[64] ATLAS Collaboration, *Improved luminosity determination in pp collisions at $\sqrt{s} = 7$ TeV using the ATLAS detector at the LHC*, Eur. Phys. J. C **73** (2013) 2518, arXiv:1302.4393 [hep-ex].

[65] S. Van der Meer, *Calibration of the effective beam height in the ISR*, CERN-ISR-PO-68-31 (1968) .

[66] K. Kordas et al., *The ATLAS Data Acquisition and Trigger : concept, design and status*, Nucl. Phys. Proc. Suppl. **172** (2007) 178.

[67] ATLAS Collaboration, *Performance of the ATLAS Trigger System in 2010*, Eur. Phys. J. C **72** (2012) 1849, arXiv:1110.1530 [hep-ex].

[68] M. A. Dobbs et al., *Les Houches guidebook to Monte Carlo generators for hadron collider physics*, in *Physics at TeV colliders. Proceedings, Workshop, Les Houches, France, May 26-June 3, 2003*, p. 411. 2004. arXiv:hep-ph/0403045 [hep-ph].

[69] J. C. Collins, D. E. Soper, and G. F. Sterman, *Factorization of Hard Processes in QCD*, Adv. Ser. Direct. High Energy Phys. **5** (1989) 1, arXiv:hep-ph/0409313 [hep-ph].

[70] H. Lai, M. Guzzi, J. Huston, Z. Li, P. Nadolsky, et al., *New parton distributions for collider physics*, Phys. Rev. D **82** (2010) 074024, arXiv:1007.2241 [hep-ph].

[71] J. Pumplin et al., *New generation of parton distributions with uncertainties from global QCD analysis*, JHEP **0207** (2002) 012, arXiv:hep-ph/0201195 [hep-ph].

[72] A. Martin, W. Stirling, R. Thorne, and G. Watt, *Parton distributions for the LHC*, Eur. Phys. J. C **63** (2009) 189, arXiv:0901.0002 [hep-ph].

[73] M. Whalley, D. Bourilkov, and R. Group, *The Les Houches accord PDFs (LHAPDF) and LHAGLUE*, arXiv:hep-ph/0508110 [hep-ph].

[74] NNPDF Collaboration, R. Ball et al., *Unbiased global determination of parton distributions and their uncertainties at NNLO and at LO*, Nucl. Phys. B **855** (2012) 153, arXiv:1107.2652 [hep-ph].

[75] NNPDF Collaboration, *NNPDF web site*, . https://nnpdf.hepforge.org/.

[76] T. D. Lee and M. Nauenberg, *Degenerate Systems and Mass Singularities*, Phys. Rev. **133** (1964) 1549.

[77] T. Kinoshita, *Mass Singularities of Feynman Amplitudes*, J. Math. Phys. **3** (1962) 650.

[78] F. Ambroglini, R. Armillis, P. Azzi, G. Bagliesi, A. Ballestrero, et al., *Proceedings of the Workshop on Monte Carlos, Physics and Simulations at the LHC. Part I*, arXiv:0902.0293 [hep-ph].

[79] S. Catani, F. Krauss, R. Kuhn, and B. Webber, *QCD matrix elements + parton showers*, JHEP **0111** (2001) 063, arXiv:hep-ph/0109231 [hep-ph].

[80] M. Mangano, M. Moretti, F. Piccinini, and M. Treccani, *Matching matrix elements and shower evolution for top-quark production in hadronic collisions*, JHEP **0701** (2007) 013, arXiv:hep-ph/0611129 [hep-ph].

[81] B. Andersson, G. Gustafson, G. Ingelman, and T. Sjostrand, *Parton Fragmentation and String Dynamics*, Phys. Rept. **97** (1983) 31.

[82] T. Sjostrand, *Jet Fragmentation of Nearby Partons*, Nucl. Phys. B **248** (1984) 469.

[83] B. Webber, *A QCD Model for Jet Fragmentation Including Soft Gluon Interference*, Nucl. Phys. B **238** (1984) 492.

[84] G. Marchesini and B. Webber, *Monte Carlo Simulation of General Hard Processes with Coherent QCD Radiation*, Nucl. Phys. B **310** (1988) 461.

[85] M. Mangano and T. Stelzer, *Tools for the simulation of hard hadronic collisions*, Ann. Rev. Nucl. Part. Sci. **55** (2005) 555.

[86] ATLAS Collaboration, *Measurement of the underlying event in jet events from 7 TeV proton-proton collisions with the ATLAS detector*, Eur. Phys. J. C **74** (2014) 2965, arXiv:1406.0392 [hep-ex].

[87] T. Sjöstrand, S. Mrenna, and P. Skands, *PYTHIA 6.4 Physics and Manual*, JHEP **0605** (2006) 026, arXiv:hep-ph/0603175 [hep-ph].

[88] J. Butterworth, J. R. Forshaw, and M. Seymour, *Multiparton interactions in photoproduction at HERA*, Z. Phys. C **72** (1996) 637, arXiv:hep-ph/9601371 [hep-ph].

[89] G. Corcella, I. Knowles, G. Marchesini, S. Moretti, K. Odagiri, et al., *HERWIG 6: An Event generator for hadron emission reactions with interfering gluons (including supersymmetric processes)*, JHEP **0101** (2001) 010, arXiv:hep-ph/0011363 [hep-ph].

[90] M. Mangano, M. Moretti, F. Piccinini, R. Pittau, and A. Polosa, *ALPGEN, a generator for hard multiparton processes in hadronic collisions*, JHEP **0307** (2003) 001, arXiv:hep-ph/0206293 [hep-ph].

[91] J. Alwall, M. Herquet, F. Maltoni, O. Mattelaer, and T. Stelzer, *MadGraph 5 : Going Beyond*, JHEP **1106** (2011) 128, arXiv:1106.0522 [hep-ph].

[92] T. Gleisberg, S. Hoeche, F. Krauss, M. Schonherr, S. Schumann, et al., *Event generation with SHERPA 1.1*, JHEP **0902** (2009) 007, arXiv:0811.4622 [hep-ph].

[93] S. Schumann and F. Krauss, *A Parton shower algorithm based on Catani-Seymour dipole factorisation*, JHEP **0803** (2008) 038, arXiv:0709.1027 [hep-ph].

[94] S. Hoeche, F. Krauss, S. Schumann, and F. Siegert, *QCD matrix elements and truncated shower*, JHEP **0905** (2009) 053, arXiv:0903.1219 [hep-ph].

[95] S. Frixione and B. Webber, *The MC@NLO 3.2 Event Generator*, CERN-PH-TH/2006-012 , arXiv:hep-ph/0601192 [hep-ph].

[96] S. Frixione, P. Nason, and C. Oleari, *Matching NLO QCD computations with parton shower simulations: the POWHEG method*, JHEP **11** (2007) 070, arXiv:0709.2092 [hep-ph].

[97] F. Cascioli, P. Maierhofer, and S. Pozzorini, *Scattering Amplitudes with Open Loops*, Phys. Rev. Lett. **108** (2012) 111601, arXiv:1111.5206 [hep-ph].

[98] ATLAS Collaboration, *The ATLAS Simulation Infrastructure*, Eur. Phys. J. C **70** (2010) 823, arXiv:1005.4568 [physics.ins-det].

[99] M. Dobbs and J. B. Hansen, *The HepMC C++ Monte Carlo event record for High Energy Physics*, Comput. Phys. Commun. **134** (2001) 41.

[100] P. Calafiura, W. Lavrijsen, C. Leggett, M. Marino, and D. Quarrie, *The Athena Control Framework in Production, New Developments and Lessons Learned*, . https://cds.cern.ch/record/865624.

[101] GEANT4, S. Agostinelli et al., *GEANT4: A Simulation toolkit*, Nucl. Instr. Meth. A **506** (2003) 250.

[102] W. Lukas, *Fast Simulation for ATLAS: Atlfast-II and ISF*, Journal of Physics: Conference Series **396** (2012) 022031. http://stacks.iop.org/1742-6596/396/i=2/a=022031.

[103] B. Acharyia et al., *Object selection and calibration, background estimations and MC samples for top quark analyses using the full 2012 data set*, ATL-COM-PHYS-2013-1016 (2013) .

[104] B. Acharyia et al., *Object selection and calibration, background estimations and MC samples for the Winter 2013 Top Quark analyses with 2012 data*, ATL-COM-PHYS-2013-088 (2013) .

[105] T. Cornelissen, M. Elsing, S. Fleischmann, W. Liebig, E. Moyse, and A. Salzburger, *Concepts, Design and Implementation of the ATLAS New Tracking (NEWT)*, ATL-SOFT-PUB-2007-007, (2007) .

[106] R. Frühwirt, *Application of kalman filtering to track and vertex fitting*, Nucl. Instr. Meth. A **262** (1987) 444.

[107] ATLAS Collaboration, *Tracking Results and Comparison to Monte Carlo simulation at* $\sqrt{s} = 900$ *GeV*, ATLAS-CONF-2010-011. https://cds.cern.ch/record/1276323.

[108] ATLAS Collaboration, *Performance of the ATLAS Inner Detector Track and Vertex Reconstruction in the High Pile-Up LHC Environment*, ATLAS-CONF-2012-042 (2012) . https://cds.cern.ch/record/1435196.

[109] ATLAS Collaboration, *Performance of the ATLAS Electron and Photon Trigger in pp Collisions at* $\sqrt{s} = 7$ *TeV in 2011*, ATLAS-CONF-2012-048 (2012) . https://cds.cern.ch/record/1450089.

[110] W. Lampl et al., *Calorimeter clustering algorithms: Description and performance*, ATL-LARG-PUB-2008-002 (2012) . https://cdsweb.cern.ch/record/1099735.

[111] ATLAS Collaboration, *Electron efficiency measurements with the ATLAS detector using the 2012 LHC proton-proton collision data*, ATLAS-CONF-2014-032 (2012) . https://cds.cern.ch/record/1706245.

[112] ATLAS Collaboration, *Electron Efficiency Measurements for 2012 and 2011 Data*, ATL-COM-PHYS-2013-1287.

[113] ATLAS Collaboration, *Object selection and calibration, background estimations and MC samples for top quark analyses using the full 2012 data set*, ATL-COM-PHYS-2013-1016 (2013) .

[114] ATLAS Collaboration, *Measurement of the muon reconstruction performance of the ATLAS detector using 2011 and 2012 LHC proton-proton collision data*, Eur. Phys. J. C **74** (2014) 3130, `arXiv:1407.3935 [hep-ex]`.

[115] ATLAS Collaboration, *Measurement of the muon reconstruction performance of the ATLAS detector using 2011 and 2012 LHC proton-proton collision data*, Eur. Phys. J. C **74** (2014) 3130, `arXiv:1407.3935 [hep-ex]`.

[116] M. Cacciari, G. P. Salam, and G. Soyez, *The anti-k_t jet clustering algorithm*, JHEP **0804** (2008) 063, `arXiv:0802.1189v2 [hep-ph]`.

[117] M. Cacciari and G. P. Salam, *Dispelling the N^3 myth for the k_t jet-finder*, Phys. Lett. B **641** (2006) 57, `arXiv:hep-ph/0512210 [hep-ph]`.

[118] M. Cacciari, G. P. Salam, and G. Soyez, *FastJet User Manual*, Eur. Phys. J. C **72** (2012) 1896, `arXiv:1111.6097 [hep-ph]`.

[119] G. P. Salam, *Towards Jetography*, Eur. Phys. J. C **67** (2010) 637, `arXiv:0906.1833 [hep-ph]`.

[120] ATLAS Collaboration, *Jet energy measurement with the ATLAS detector in proton-proton collisions at* $\sqrt{s} = 7$ *TeV*, Eur. Phys. J. C **73** (2013) 2304, `arXiv:1112.6426 [hep-ex]`.

[121] ATLAS Collaboration, *Jet energy measurement and its systematic uncertainty in proton-proton collisions at $\sqrt{s} = 7$ TeV with the ATLAS detector*, Eur. Phys. J. C **75** (2015) 17, arXiv:1406.0076 [hep-ex].

[122] ATLAS Collaboration, *Pile-up subtraction and suppression for jets in ATLAS*, ATLAS-CONF-2013-083 (2013) . http://cds.cern.ch/record/1570994.

[123] M. Cacciari, G. P. Salam, and G. Soyez, *The Catchment Area of Jets*, JHEP **0804** (2008) 005, arXiv:0802.1188 [hep-ph].

[124] J. Montejo Berlingen and A. Juste Rozas, *Search for new physics in $t\bar{t}$ final states with additional heavy-flavor jets with the ATLAS detector*, Barcelona, Autonoma U. (2015) . https://cds.cern.ch/record/2053769/.

[125] ATLAS Collaboration, *b-tagging in dense environments*, ATL-PHYS-PUB-2014-014 (2014) . https://cds.cern.ch/record/1750682.

[126] ATLAS Collaboration, *Performance of b-Jet Identification in the ATLAS Experiment*, JINST **11** (2016) P04008, arXiv:1512.01094 [hep-ex].

[127] ATLAS Collaboration, *Performance and Calibration of the JetFitterCharm Algorithm for c-Jet Identification*, ATL-PHYS-PUB-2015-001, (2015) . http://cds.cern.ch/record/1980463.

[128] ATLAS Collaboration, *Calibration of b-tagging using dileptonic top pair events in a combinatorial likelihood approach with the ATLAS experiment*, ATLAS-CONF-2014-004 (2014) . http://cds.cern.ch/record/1664335.

[129] ATLAS Collaboration, *b-jet tagging calibration on c-jets containing D^{*+} mesons*, ATLAS-CONF-2012-039 (2012) . https://cds.cern.ch/record/1435193.

[130] ATLAS Collaboration, *Measurement of the mistag rate of b-tagging algorithms with 5 fb^{-1} of data collected by the ATLAS detector*, ATLAS-CONF-2012-040 (2012) . https://cds.cern.ch/record/1435194.

[131] ATLAS Collaboration, *Performance of Missing Transverse Momentum Reconstruction in ATLAS studied in Proton-Proton Collisions recorded in 2012 at 8 TeV*, ATLAS-CONF-2013-082, (2013) . http://cds.cern.ch/record/1570993.

[132] ATLAS Collaboration, *Measurement of the top quark-pair production cross section with ATLAS in pp collisions at $\sqrt{s} = 7$ TeV*, Eur. Phys. J. C **71** (2011) 1577, arXiv:1012.1792 [hep-ex].

[133] P. Golonka and Z. Was, *PHOTOS Monte Carlo: A Precision tool for QED corrections in Z and W decays*, Eur. Phys. J. C **45** (2006) 97, arXiv:hep-ph/0506026.

[134] S. Jadach, J. H. Kühn, and Z. Waąs, *TAUOLA - a library of Monte Carlo programs to simulate decays of polarized τ leptons*, Comput. Phys. Commun. **64** (1991) 275.

[135] S. Agostinelli et al., *Geant4: a simulation toolkit*, Nucl. Instr. Meth. A **506** (2003) 250.

[136] ATLAS Collaboration, *Summary of ATLAS Pythia 8 tunes*, ATL-PHYS-PUB-2012-003 (2012) . http://cds.cern.ch/record/1474107.

[137] S. Frixione, P. Nason, and G. Ridolfi, *A Positive-weight next-to-leading-order Monte Carlo for heavy flavour hadroproduction*, JHEP **0709** (2007) 126, arXiv:0707.3088.

[138] P. Nason, *A New method for combining NLO QCD with shower Monte Carlo algorithms*, JHEP **0411** (2004) 040, arXiv:hep-ph/0409146.

[139] S. Frixione, P. Nason, and C. Oleari, *Matching NLO QCD computations with Parton Shower simulations: the POWHEG method*, JHEP **0711** (2007) 070, arXiv:0709.2092 [hep-ph].

[140] S. Alioli, P. Nason, C. Oleari, and E. Re, *A general framework for implementing NLO calculations in shower Monte Carlo programs: the POWHEG BOX*, JHEP **1006** (2010) 043, arXiv:1002.2581 [hep-ph].

[141] H.-L. Lai, M. Guzzi, J. Huston, Z. Li, P. M. Nadolsky, et al., *New parton distributions for collider physics*, Phys. Rev. D **82** (2010) 074024, arXiv:1007.2241 [hep-ph].

[142] T. Sjöstrand, S. Mrenna, and P. Z. Skands, *PYTHIA 6.4 Physics and Manual*, JHEP **0605** (2006) 026, arXiv:hep-ph/0603175 [hep-ph].

[143] P. Z. Skands, *Tuning Monte Carlo Generators: The Perugia Tunes*, Phys. Rev. D **82** (2010) 074018, arXiv:1005.3457 [hep-ph].

[144] M. Czakon and A. Mitov, *Top++: A Program for the Calculation of the Top-Pair Cross-Section at Hadron Colliders*, Comput. Phys. Commun. **185** (2014) 2930, arXiv:1112.5675 [hep-ph].

[145] M. Cacciari, M. Czakon, M. Mangano, A. Mitov, and P. Nason, *Top-pair production at hadron colliders with next-to-next-to-leading logarithmic soft-gluon resummation*, Phys. Lett. B **710** (2012) 612, arXiv:1111.5869 [hep-ph].

[146] P. Bärnreuther, M. Czakon, and A. Mitov, *Percent Level Precision Physics at the Tevatron: First Genuine NNLO QCD Corrections to $q\bar{q} \to t\bar{t} + X$*, Phys. Rev. Lett. **109** (2012) 132001, arXiv:1204.5201 [hep-ph].

[147] M. Czakon and A. Mitov, *NNLO corrections to top-pair production at hadron colliders: the all-fermionic scattering channels*, JHEP **1212** (2012) 054, arXiv:1207.0236 [hep-ph].

[148] M. Czakon and A. Mitov, *NNLO corrections to top pair production at hadron colliders: the quark-gluon reaction*, JHEP **1301** (2013) 080, arXiv:1210.6832 [hep-ph].

[149] M. Czakon, P. Fiedler, and A. Mitov, *Total Top-Quark Pair-Production Cross Section at Hadron Colliders Through $O(\alpha_S^4)$*, Phys. Rev. Lett. **110** (2013) 252004, arXiv:1303.6254 [hep-ph].

[150] A. Martin, W. Stirling, R. Thorne, and G. Watt, *Parton distributions for the LHC*, Eur. Phys. J. C **63** (2009) 189, arXiv:0901.0002 [hep-ph].

[151] A. Martin, W. Stirling, R. Thorne, and G. Watt, *Uncertainties on alpha(S) in global PDF analyses and implications for predicted hadronic cross sections*, Eur. Phys. J. C **64** (2009) 653, arXiv:0905.3531 [hep-ph].

[152] M. Botje, J. Butterworth, A. Cooper-Sarkar, A. de Roeck, J. Feltesse, et al., *The PDF4LHC Working Group Interim Recommendations*, arXiv:1101.0538 [hep-ph].

[153] J. Gao, M. Guzzi, J. Huston, H.-L. Lai, Z. Li, et al., *CT10 next-to-next-to-leading order global analysis of QCD*, Phys. Rev. D **89** (2014) 033009, arXiv:1302.6246 [hep-ph].

[154] R. D. Ball, V. Bertone, S. Carrazza, C. S. Deans, L. Del Debbio, et al., *Parton distributions with LHC data*, Nucl. Phys. B **867** (2013) 244, arXiv:1207.1303 [hep-ph].

[155] ATLAS Collaboration, *Measurements of normalized differential cross-sections for ttbar production in pp collisions at sqrt(s) = 7 TeV using the ATLAS detector*, Phys. Rev. D **90** (2014) 072004, arXiv:1407.0371 [hep-ex].

[156] A. Bredenstein, A. Denner, S. Dittmaier, and S. Pozzorini, *NLO QCD corrections to pp → t anti-t b anti-b + X at the LHC*, Phys. Rev. Lett. **103** (2009) 012002, arXiv:0905.0110 [hep-ph].

[157] A. Bredenstein, A. Denner, S. Dittmaier, and S. Pozzorini, *NLO QCD Corrections to Top Anti-Top Bottom Anti-Bottom Production at the LHC: 2. full hadronic results*, JHEP **1003** (2010) 021, arXiv:1001.4006 [hep-ph].

[158] G. Bevilacqua, M. Czakon, C. Papadopoulos, R. Pittau, and M. Worek, *Assault on the NLO Wishlist: pp t anti-t b anti-b*, JHEP **0909** (2009) 109, arXiv:0907.4723 [hep-ph].

[159] T. Gleisberg, S. Hoeche, F. Krauss, M. Schonherr, S. Schumann, et al., *Event generation with SHERPA 1.1*, JHEP **0902** (2009) 007, arXiv:0811.4622 [hep-ph].

[160] M. L. Mangano, M. Moretti, and R. Pittau, *Multijet matrix elements and shower evolution in hadronic collisions: $Wb\bar{b}$ + n jets as a case study*, Nucl. Phys. B **632** (2002) 343, arXiv:hep-ph/0108069.

[161] K. Melnikov and F. Petriello, *Electroweak gauge boson production at hadron colliders through O(alpha(s)**2)*, Phys. Rev. D **74** (2006) 114017, arXiv:hep-ph/0609070.

[162] ATLAS Collaboration, *Measurement of the charge asymmetry in top-quark pair production in the lepton-plus-jets final state in pp collision data at $\sqrt{s} = 8$ TeV with the ATLAS detector*, Eur. Phys. J. C **76** (2015) 87, arXiv:1509.02358.

[163] S. Alioli, P. Nason, C. Oleari, and E. Re, *NLO single-top production matched with shower in POWHEG: s- and t-channel contributions*, JHEP **0909** (2009) 111, arXiv:0907.4076 [hep-ph].

[164] E. Re, *Single-top Wt-channel production matched with parton showers using the POWHEG method*, Eur. Phys. J. C **71** (2011) 1547, arXiv:1009.2450 [hep-ph].

[165] S. Frixione, E. Laenen, P. Motylinski, and B. R. Webber, *Single-top production in MC@NLO*, JHEP **0603** (2006) 092, arXiv:hep-ph/0512250.

[166] N. Kidonakis, *Next-to-next-to-leading-order collinear and soft gluon corrections for t-channel single top quark production*, Phys. Rev. D **83** (2011) 091503, arXiv:1103.2792 [hep-ph].

[167] N. Kidonakis, *Two-loop soft anomalous dimensions for single top quark associated production with a W- or H-*, Phys. Rev. D **82** (2010) 054018, arXiv:1005.4451 [hep-ph].

[168] N. Kidonakis, *NNLL resummation for s-channel single top quark production*, Phys. Rev. D **81** (2010) 054028, arXiv:1001.5034 [hep-ph].

[169] J. M. Campbell and R. K. Ellis, *An Update on vector boson pair production at hadron colliders*, Phys. Rev. D **60** (1999) 113006, arXiv:hep-ph/9905386.

[170] ATLAS Collaboration, *ATLAS tunes of PYTHIA6 and PYTHIA8 for MC11*, ATL-PHYS-PUB-2011-008 (2011) . https://cds.cern.ch/record/1363300.

[171] M. Garzelli, A. Kardos, C. Papadopoulos, and Z. Trocsanyi, *$t\,\bar{t}\,W^{+-}$ and $t\,\bar{t}\,Z$ Hadroproduction at NLO accuracy in QCD with Parton Shower and Hadronization effects*, JHEP **1211** (2012) 056, arXiv:1208.2665 [hep-ph].

[172] M. V. Garzelli, A. Kardos, C. Papadopoulos, and Z. Trocsanyi, *Standard Model Higgs boson production in association with a top anti-top pair at NLO with parton showering*, Europhys. Lett. **96** (2011) 11001, arXiv:1108.0387 [hep-ph].

[173] G. Bevilacqua, M. Czakon, M. Garzelli, A. van Hameren, A. Kardos, et al., *HELAC-NLO*, Comput. Phys. Commun. **184** (2013) 986, arXiv:1110.1499 [hep-ph].

[174] T. Sjostrand, S. Mrenna, and P. Z. Skands, *A Brief Introduction to PYTHIA 8.1*, Comput. Phys. Commun. **178** (2008) 852, arXiv:0710.3820 [hep-ph].

[175] ATLAS Collaboration, *New ATLAS event generator tunes to 2010 data*, ATL-PHYS-PUB-2011-009 (2011) . https://cds.cern.ch/record/1345343.

[176] S. Dawson, C. Jackson, L. Orr, L. Reina, and D. Wackeroth, *Associated Higgs production with top quarks at the Large Hadron Collider: NLO QCD corrections*, Phys. Rev. D **68** (2003) 034022, arXiv:hep-ph/0305087 [hep-ph].

[177] W. Beenakker et al., *NLO QCD corrections to $t\bar{t}H$ production in hadron collisions*, Nucl. Phys. B **653** (2003) 151, arXiv:hep-ph/0211352 [hep-ph].

[178] W. Beenakker et al., *Higgs radiation off top quarks at the Tevatron and the LHC*, Phys. Rev. Lett. **87** (2001) 201805, arXiv:hep-ph/0107081 [hep-ph].

[179] A. Djouadi, J. Kalinowski, and M. Spira, *HDECAY: A Program for Higgs boson decays in the standard model and its supersymmetric extension*, Comput. Phys. Commun. **108** (1998) 56, arXiv:hep-ph/9704448 [hep-ph].

[180] A. Bredenstein, A. Denner, S. Dittmaier, and M. Weber, *Precise predictions for the Higgs-boson decay $H \to WW/ZZ \to 4$ leptons*, Phys. Rev. D **74** (2006) 013004, arXiv:hep-ph/0604011 [hep-ph].

[181] S. Actis, G. Passarino, C. Sturm, and S. Uccirati, *NNLO Computational Techniques: The Cases $H \to \gamma\gamma$ and $H \to gg$*, Nucl. Phys. B **811** (2009) 182, arXiv:0809.3667 [hep-ph].

[182] A. Denner, S. Heinemeyer, I. Puljak, D. Rebuzzi, and M. Spira, *Standard Model Higgs-Boson Branching Ratios with Uncertainties*, Eur. Phys. J. C **71** (2011) 1753, arXiv:1107.5909 [hep-ph].

[183] LHC Higgs Cross Section Working Group, *Handbook of LHC Higgs Cross Sections: 1. Inclusive Observables*, arXiv:1101.0593 [hep-ph].

[184] J. A. Aguilar-Saavedra, *PROTOS, a Program for Top Simulations*, . http://jaguilar.web.cern.ch/jaguilar/protos/.

[185] J. A. Aguilar-Saavedra, *A Minimal set of top-Higgs anomalous couplings*, Nucl. Phys. B **821** (2009) 215, arXiv:0904.2387 [hep-ph].

[186] ATLAS Collaboration, *Jet energy measurement with the ATLAS detector in proton-proton collisions at $\sqrt{s} = 7$ TeV*, Eur. Phys. J. C **73** (2013) 2304, arXiv:1112.6426 [hep-ex].

[187] ATLAS Collaboration, *In-situ jet energy scale and jet shape corrections for multiple interactions in the first ATLAS data at the LHC*, ATLAS-CONF-2011-030 (2011) . https://cds.cern.ch/record/1337780.

[188] ATLAS Collaboration, *In-situ pseudorapidity intercalibration for evaluation of jet energy scale uncertainty using dijet events in proton-proton collisions at $\sqrt{s} = 7$ TeV*, ATLAS-CONF-2011-014 (2011) . https://cds.cern.ch/record/1334876.

[189] ATLAS Collaboration, *Jet energy resolution and reconstruction efficiencies from in-situ techniques with the ATLAS Detector Using Proton-Proton Collisions at a Center of Mass Energy $\sqrt{s} = 7$ TeV*, ATLAS-CONF-2010-054 (2011) . https://cds.cern.ch/record/1281311.

[190] ATLAS Collaboration, *In-situ pseudorapidity intercalibration to evaluate jet energy scale uncertainty and calorimeter performance in the forward region*, ATLAS-CONF-2010-055 (2011) . https://cds.cern.ch/record/1281312.

[191] ATLAS Collaboration, *Single hadron response measurement and calorimeter jet energy scale uncertainty with the ATLAS detector at the LHC*, Eur. Phys. J. C **73** (2013) 2305, arXiv:1203.1302 [hep-ex].

[192] ATLAS Collaboration, *Light-quark and Gluon Jets: Calorimeter Response, Jet Energy Scale Systematics and Properties*, ATLAS-CONF-2012-138, (2012) . https://cds.cern.ch/record/1480629.

[193] ATLAS Collaboration, *Data-driven determination of the energy scale and resolution of jets reconstructed in the ATLAS calorimeters using dijet and multijet events at* $\sqrt{s} = 8\ TeV$, ATLAS-CONF-2015-017, (2015) . https://cds.cern.ch/record/200867.

[194] ATLAS Collaboration, *Calibration of the performance of b-tagging for c and light-flavour jets in the 2012 ATLAS data*, ATLAS-CONF-2014-046 (2014) . http://cds.cern.ch/record/1741020.

[195] F. Ahmadow et al., *Search for the Standard Model Higgs boson produced in association with a vector boson and decaying to a b-quark pair using up to 4.7* fb^{-1} *of pp collision data at* $\sqrt{s} = 7$ TeV *with the ATLAS detector at the LHC*, ATL-COM-PHYS-2011-1648 (2011) .

[196] *Eigenvector Variation Method Twiki:*, . `https://twiki.cern.ch/twiki/bin/viewauth/AtlasProtected/BTaggingCalibrationDataInterface#Eigenvector_variation_method`.

[197] F. Cascioli, P. Maierhfer, N. Moretti, S. Pozzorini, and F. Siegert, *NLO matching for* $t\bar{t}b\bar{b}$ *production with massive b-quarks*, Phys. Lett. B **734** (2014) 210, `arXiv:1309.5912 [hep-ph]`.

[198] J. Alwall, S. Hoche, F. Krauss, N. Lavesson, L. Lonnblad, et al., *Comparative study of various algorithms for the merging of parton showers and matrix elements in hadronic collisions*, Eur. Phys. J. C **53** (2008) 473, `arXiv:0706.2569 [hep-ph]`.

[199] S. Frixione, E. Laenen, P. Motylinski, B. R. Webber, and C. D. White, *Single-top hadroproduction in association with a W boson*, JHEP **0807** (2008) 029, `arXiv:0805.3067 [hep-ph]`.

[200] J. M. Campbell and R. K. Ellis, $t\bar{t}W^{+-}$ *production and decay at NLO*, JHEP **1207** (2012) 052, `arXiv:1204.5678 [hep-ph]`.

[201] T. Junk, *Confidence level computation for combining searches with small statistics*, Nucl. Instr. Meth. A **434** (1999) 435, `arXiv:hep-ex/9902006`.

[202] G. Cowan, K. Cranmer, E. Gross, and O. Vitells, *Asymptotic formulae for likelihood-based tests of new physics*, Eur. Phys. J. C **71** (2011) 1554, `arXiv:1007.1727 [physics.data-an]`.

[203] A. Wald, *Tests of Statistical Hypotheses Concerning Several Parameters When the Number of Observations is Large*, Transactions of the American Mathematical Society **54** (1943) 426.

[204] M. Baak, G. J. Besjes, D. Cte, A. Koutsman, J. Lorenz, and D. Short, *HistFitter software framework for statistical data analysis*, Eur. Phys. J. C **75** (2015) 153, `arXiv:1410.1280 [hep-ex]`.

[205] ROOT Collaboration, *HistFactory: A tool for creating statistical models for use with RooFit and RooStats*, CERN-OPEN-2012-016 (2012) . https://cds.cern.ch/record/1456844.

[206] L. Moneta, K. Belasco, K. Cranmer, S. Kreiss, A. Lazzaro, et al., *The RooStats Project*, arXiv:1009.1003 [physics.data-an].

[207] W. Verkerke and D. P. Kirkby, *The RooFit toolkit for data modeling*, eConf **C0303241** (2003) MOLT007, arXiv:physics/0306116 [physics].

[208] R. Brun and F. Rademakers, *ROOT: An object oriented data analysis framework*, Nucl. Instr. Meth. A **389** (1997) 81.

[209] I. Antcheva, M. Ballintijn, B. Bellenot, M. Biskup, R. Brun, et al., *ROOT: A C++ framework for petabyte data storage, statistical analysis and visualization*, Comput. Phys. Commun. **182** (2011) 1384.

[210] M. Buchkremer, G. Cacciapaglia, A. Deandrea, and L. Panizzi, *Feynrules for Top FCNC Model*, . http://feynrules.irmp.ucl.ac.be/wiki/TFCNC/.

[211] J.-B. de Vivie and D. Fournier, *Search for Flavour Changing Neutral Currents in $t \to qH$, with $H \to \gamma\gamma$ and limit on the tcH coupling*, ATL-COM-PHYS-2013-1455 (2013) .

[212] C. Zhang and F. Maltoni, *Top-quark decay into Higgs boson and a light quark at next-to-leading order in QCD*, Phys. Rev. D **88** (2013) 054005, arXiv:1305.7386 [hep-ph].

[213] A. Denner and T. Sack, *The Top width*, Nucl. Phys. B **358** (1991) 46.

[214] ATLAS Collaboration, *Measurements of the Higgs boson production and decay rates and coupling strengths using pp collision data at $\sqrt{s}$ = 7 and 8 TeV in the ATLAS experiment*, ATLAS-CONF-2015-007, (2015) . https://cds.cern.ch/record/2002212.

[215] CMS Collaboration, *Search for the Flavor-Changing Neutral Current Decay $t \to Hq$ Where the Higgs Decays to $b\bar{b}$ Pairs at $\sqrt{s} = 8$ TeV*, CMS-PAS-TOP-14-020 (2015) . https://cds.cern.ch/record/2104020.

[216] M. Capeans, G. Darbo, K. Einsweiller, M. Elsing, T. Flick, M. Garcia-Sciveres, C. Gemme, H. Pernegger, O. Rohne, and R. Vuillermet, *ATLAS Insertable B-Layer Technical Design Report*, CERN-LHCC-2010-013. ATLAS-TDR-19, (Sep, 2010) . https://cds.cern.ch/record/1291633.

[217] ATLAS Collaboration, *Expected performance of the ATLAS b-tagging algorithms in Run-2*, ATL-PHYS-PUB-2015-022, (Jul, 2015) . https://cds.cern.ch/record/2037697.

[218] D. Krohn, T. Lin, M. Schwartz, and W. Waalewijn, *Jet Charge at the LHC*, Phys. Rev. Lett. **110** (2013) 212001, arXiv:1209.2421 [hep-ph].

[219] ALEPH Collaboration, *Determination of A_{FB}^b using jet charge measurements in Z decays*, Phys. Lett. B **426** (1998) 217.

[220] ATLAS Collaboration, *A new tagger for the charge identification of b-jets*, ATL-PHYS-PUB-2015-040 (2015) . http://cds.cern.ch/record/2048132.

[221] ATLAS, G. Aad et al., *Measurement of the top quark charge in pp collisions at $\sqrt{s} = 7$ TeV with the ATLAS detector*, JHEP **11** (2013) 031, arXiv:1307.4568 [hep-ex].

Acknowledgements

First of all I want to thank my supervisors Sebastian and Aurelio for all the hard work, support and wise guidance. Thanks for finding the time for me even in the busiest periods, to discuss together doubts and results, and actually help me to learn how to become a researcher. I want to thank Sebastian for giving the opportunity to do a PhD at IFAE, for the continued help during these years and for all good you have done for me. I want to thank Aurelio who inspired me to do this analysis and offering another point of view every time when I was not able to see a problem from a different perspective. Thank you both for your smiles that made everything easier. I really enjoyed working in IFAE Pixel and Top analysis groups, and in the ATLAS Collaboration in general.

I want to give a special thanks to Mr. Matteo Cavalli-Sforza and Mrs. Martine Bosman for all the nice words and for the moral support in the difficult moments.

Appreciation also goes to Ilya Korolkov, for being like a "Godfather" for me during all these years, who suggested to do the PhD in the High Energy Physics and in particular at IFAE, and who always provided assistance in the moments when no one else could help.

A particular acknowledgement goes to the IFAE Top group, present and former members, for their fundamental contributions to the common analysis framework used for this search. Big thanks to Eve, Javier, Clement, Antonella, Francesco, Mirko and Jordi for the help, support and fruitful collaboration. Thanks for always greeting me with a smile when I had yet another question.

Thanks to the complete IFAE members that warmly welcomed me from the first day I arrived, who helped me through the paperwork and university rules.

I also want to thank warmly all the people from ATLAS community I worked with, especially Hongtao Yang from University of Wisconsin-Madison, who helped to perform the combined ATLAS results.

Finally, the biggest "thank you" of all goes to my family for being there for me in the good and in the stressful times, sharing sleepless work nights, for the faith in me even when I was almost to gave up. Thank you all for the following every step toward this thesis with great enthusiasm. You gave me the strength to finish the PhD program successfully. I promise, the future is going to be even better.